MULTI-SCALE, MULTI-PHYSICS RELIABILITY MODELING OF MODERN ELECTRONIC DEVICES AND SYSTEM

A Dissertation

Submitted to the Faculty

of

Purdue University

by

Woojin Ahn

In Partial Fulfillment of the

Requirements for the Degree

of

Doctor of Philosophy

August 2019

Purdue University

West Lafayette, Indiana

THE PURDUE UNIVERSITY GRADUATE SCHOOL
STATEMENT OF DISSERTATION APPROVAL

Dr. Muhammad A. Alam, Chair
School of Electrical and Computer Engineering

Dr. Mark S. Lundstrom
School of Electrical and Computer Engineering

Dr. Peide P. Ye
School of Electrical and Computer Engineering

Dr. Ganesh Subbarayan
School of Mechanical Engineering

Approved by:

Dr. Dimitrios Peroulis
School of Electrical and Computer Engineering

To my parents,
my daughter, Sua,
and my wife, Inkyung

ACKNOWLEDGMENTS

I would like to express my deepest appreciation to my advisor, Professor Muhammad Ashraful Alam for his vision and motivation in guiding me to explore the bridge among transistor, circuit, and system for developing modeling framework of modern ICs reliability issues. I have learned various analytical, and numerical skills that can help me to attack the most challenging issues in the field. I also learned a lot in person, his patience, and leadership that will give a great influence on my future life. I am very fortunate to have him as my advisor.

I would also like to express my sincere thanks to Professor Ganesh Subbarayan in mechanical engineering department. He has offered me much advice and insights on effective medium model and homogenization models and I have had much helpful advice from his group as well. I would like to thank his graduate students, Pavan Kumar Vaitheeswaran and Huanyu Liao. My special thanks Professor Mark Lundstrom for having interest in my work and particularly like to thank him to be his teaching assistant for edX course which gave me much insights into nano-transistors and device physics. Also, I would like to thank Prof. Peide D. Ye for serving in my doctoral advisory committee and providing valuable feedbacks.

Thanks to Dr. Srikanth Krishnan (TI), Dr. Dhanoop Varghese (TI), Dr. Luu Nguyen (TI), Dr. Patrick Justison (Globalfoundries), Dr. Haojun Zhang (Globalfoundries), Dr. Tian Shen (IBM), Hao Tian (Purdue), Professor Susanna Reggiani (Bologna University), and her student Davide Cornigli for many useful discussions, and most importantly, for providing experimental data to validate my compact models. Without them, this work would not have been possible.

I would like to extend my thanks to many former and current members of Professor Alams research group. Special thanks to my past group-mates: Chunsheng Jiang, Hai Jiang, SangHoon Shin, Xingshu Sun, Aida Ebrahimi, Ryyan Khan, Raghu Chavali,

and Piyush Dak for giving me always kind and insightful replies whenever I ask them a question, I would like to thank all my current members: Xin Jin, Reza Asadpour, Tahir Patel, Yen-Pu Chen, Bikram Mahajan, Nicolo Zagni, Ratul Baruah, Levi Davies, and Marco Fratus, and office colleagues: Evan Witkoske, Xufeng Wang, Yubo Sun, for valuable discussions on many interesting research topics. Furthermore, I wish to thank all my friends at Purdue: Weeseong Seo, Euisuk Sung, Jaehoon Bang, Jonghoon Ahn, Younghoon Kim, Min Ku Kim, Donghyun Seo, Hagyoul Bae, Doosan Back, Soonam Lee, Chankyu Lee, Wonil Cheong, Weonchan Sung, Bong Joong Kim, Jinhyun Noh, Haejun Chung, Chiho Choi, for making my stay at Purdue enjoyable. Also, I would like thank to Vicki Johnson, Matt Golden, Elisheba Vanwinkle, Debra Bowman for their administrative assistance.

Last but not least, a special word of thanks must go to my wife Inkyung Ryu for her endless devotion and encouragement. I am greatly indebted to her and all the achievements at Purdue would not have been possible without her sacrifice, and dedication. I also would like to express my gratitude towards my parents: Kee Hong Ahn, and Sookja Ban for their unconditional love and unparalleled support that made it possible for me to pursue Ph.D. I would also like to thank my sister, Sungji Ahn for the encouragement, and inspiration throughout my life. Finally, special thanks to my daughter Sua for being a bright and healthy baby.

TABLE OF CONTENTS

Page

Page

Page

Page

LIST OF TABLES

LIST OF FIGURES

Figure Page

Figure Page

Figure Page

Figure Page

ABSTRACT

Ahn, Woojin Ph.D., Purdue University, August 2019. Multi-Scale, Multi-Physics Reliability Modeling of Modern Electronic Devices and System. Major Professor: Muhammad Ashraful Alam.

Electronics have now become a part of our daily life and therefore the reliability of microelectronics cannot be overlooked. As the Moore's law era comes to an end, various new system-level innovations (e.g., 3D packaging, evolution of packaging material to molding compounds) with constant scaling of transistors have resulted in increasingly complicated integrated circuits (ICs) configurations. The reliability modeling of complex ICs is a nontrivial concern for a variety of reasons. For example, ever since 2004, self-heating effect (SHE) has become an important reliability concern for ICs. Currently, many groups have developed thermal predictive models for transistors, circuits, and systems. In order to describe SHE self-consistently, the modeling framework must account for correlated self-heating within the ICs. This multi-scales nature of the self-consistency problem is one of the difficult factors poses an important challenge to self-consistent modeling. In addition, coupling between different physical effects within IC further complicates the problem.

In this thesis, we discuss three challenges, and their solutions related to an IC's reliability issues. We (i) generalize the classical effective medium theory (EMT) to account for anisotropic, heterogeneous system; (ii) develop computationally efficient a physics-based thermal compact model for a packaged ICs to predict junction temperature in the transistor based on the EMT model, and image charge theory. Our thermal compact model bridges different length scales among the sources and rest of the system. Finally (iii) propose the modeling framework of electrical chip package interaction (CPI) due to charge transport within mold compounds by coupling

moisture diffusion, electric distribution, and ions transport. The proposed modeling framework not only addresses the three major modeling challenges discussed earlier, but also provides deep and fundamental insights regarding the performance and reliability of modern ICs.

1. INTRODUCTION

1.1 Semiconductor industry trend

Since the beginning of the 21st century, the integration of computing power and communication infrastructures have led to the explosion of digital data traffic across the world. Fig. 1.1 shows that the number of devices integrated (e.g. 6.4 billion by 2017) is expected to experience an accelerated growth to meet the increasing demand for artificial intelligence systems, such as autonomous vehicles, IoT devices, and machine learning applications. Soon every aspect of our daily life will involve interaction with these integrated circuits. From the server to IoT devices, each class of computing infrastructure must balance its application-specific performance-power trade-off, see Fig. 1.2. For example, a high-end server can consume high-power necessary to achieve the target performance because integrated active cooling can

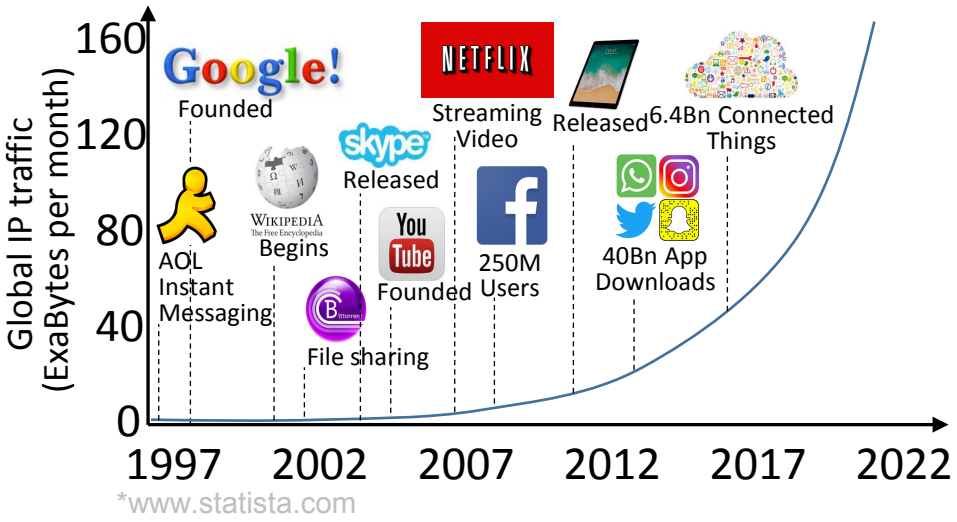

Fig. 1.1. The amount of data transfer per week trend

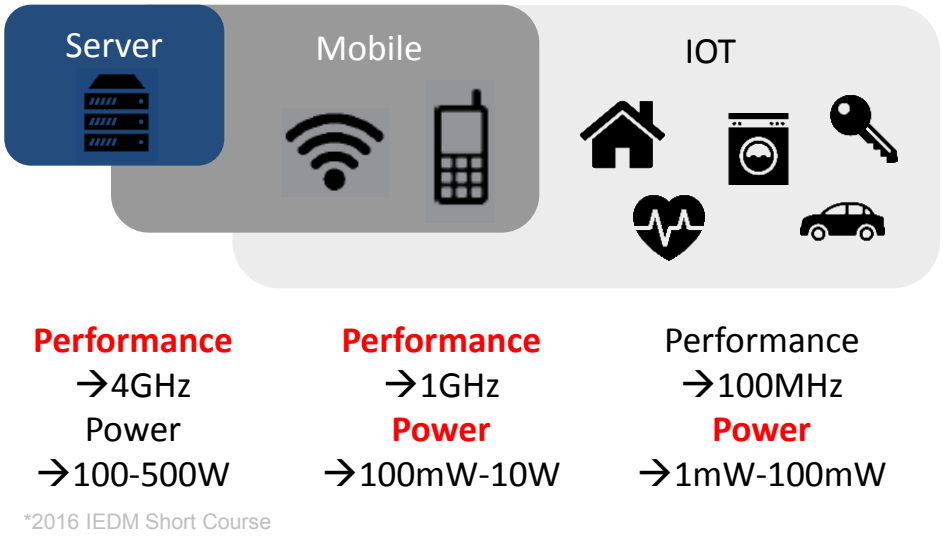

Fig. 1.2. Concept chart of dominant factor between performance and power for three main applications

be used to manage thermal runaway. On the other hand, IoT devices with passive cooling must minimize power dissipation to avoid self-heating and frequent battery replacement. The IoT functionality is limited by the available power-budget. In the case of mobile devices, the processor must co-optimize for power (i.e., for reduced self-heating and frequent charging) and performance (i.e., running multiple apps).

The semiconductor industry has met these diverse requirements by continuously scaling down the transistors. This strategy has been effective for the following reasons: (i) when the intrinsic capacitance is reduced, the corresponding decrease in gate delay translates to higher clock frequency and improved performance; (ii) the simultaneous decrease in current and voltage translates to reduced power dissipation per transistor.

1.1.1 The evolution of transistors during the Moore's law era

In addition to the previous reasons, the scaling down transistors size reduces the manufacturing cost of an individual transistor. Moore's law is the well-known

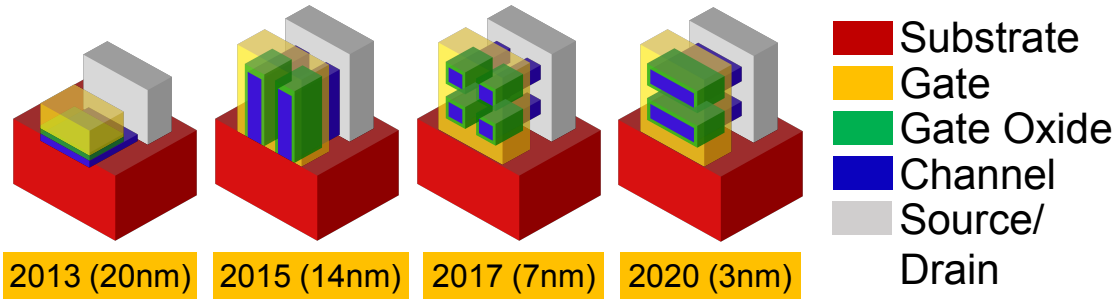

Fig. 1.3. Evolution of the transistor structure as node size becomes smaller.

empirical observation that Gordon Moore articulated in 1965 [1]. In the paper, he predicted the number of transistors per chip will double every 1.5 to 2 years. This doubling of transistor integration (and the corresponding decrease in cost) has allowed the semiconductor industry to flourish over the years and enabled the applications we see today.

Since the first commercial transistor was sold by Western electric, many new transistor structures have been introduced over the years (see Fig. 1.3) to solve issues associated with scaling down the transistor envisioned by Moore's law. Until 2013, planar MOSFET had been the workhorse of the semiconductor industry. The planar structure, however, could not handle high source-to-drain leakage current when node-sizes smaller than 14nm. By changing the channel from 1D to 3D (for example FinFET, NanowireFET, and NanosheetFET) [2, 3], engineers regained the electrostatic control of the channel, and suppressed the leakage current. Nowadays, most manufacturers use 3D FinFETs as the standard transistor topology for advanced, sub-20nm technology nodes [4]. In a few years, nanosheetFET is expected to replace FinFET for even smaller node size, i.e., 3nm.

1.1.2 The shifting focus on integrated systems in the Post-Moore's law era

Moore's law is coming to an end due to both technical and economic reasons. As the minimum feature size reaches a few nano-meters, it is extremely challenging to keep scaling down transistors due to: off-state tunneling between the source and drain, as well as increasing power density and self-heating issues [5]. Moreover, fabrication processes with atomic-scale control are extremely expensive and difficult. Apart from the transistors, interconnect scaling has become another bottleneck for the continuous scaling down of integrated circuits [6]. Increasing interconnect resistances and capacitance have increased the overall interconnect delay and degraded the performance of ICs.

The semiconductor industry, therefore, has augmented its focus on transistor and interconnect scaling to include system level considerations. One finds that the solution of these system-level bottlenecks can continue to improve performance and broaden the application base as shown in Fig. 1.4. Among many technologies to enhance the functionality of the system, system-in-package (SiP) solution such as 2.5D or 3D integration is the most important strategy to achieve a higher value system [7]. In this thesis, several important reliability issues of each branch are investigated by phenomenological studies. In the next section, the most important reliability issue of each branch is studied.

1.2 Moore's law era reliability issues

As mentioned in Sec. 1.1.1, the evolution of transistor topology from planar to confined geometry devices (i.e., FinFET, Nanowire FET, Nanosheet FET) have met the desired performance specification of sub-20nm ICs, but only at the expense of increased power density and thermal resistance (R_{TH}). As the transistors are scaled, the amount of dynamic power dissipated per transistor (P) has reduced [8], however, the self-heating effect (SHE) ($\Delta T = P \times R_{\mathrm{TH}}$) has not [5]. As shown in Fig. 1.5b,

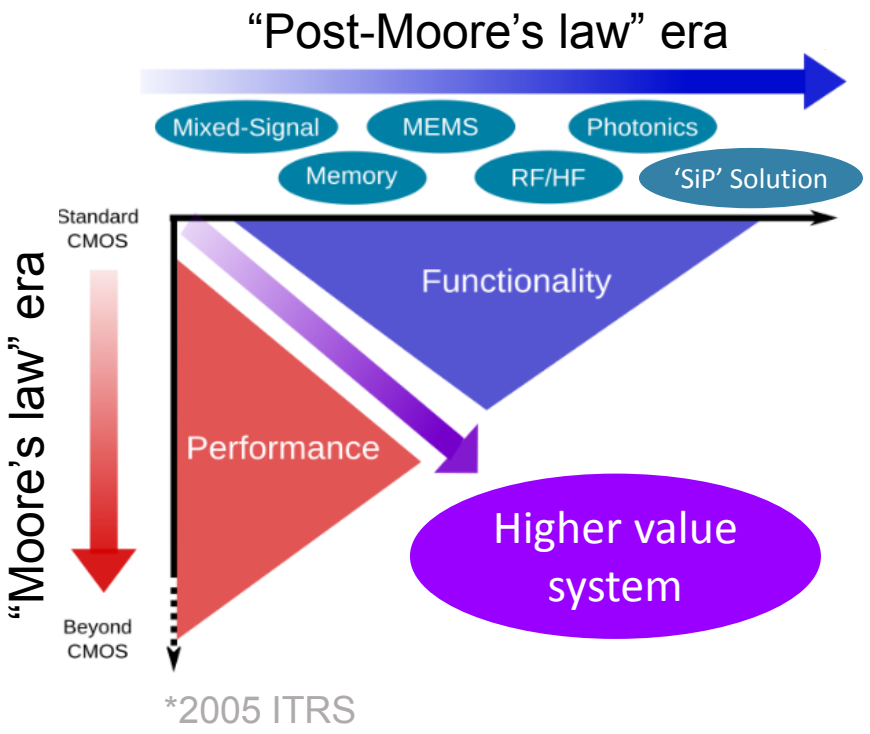

Fig. 1.4. A concept chart that shows integration strategies for Moore's law and post-Moore's law era.

when the channel becomes 3D structure, heat can not dissipate easily so that thermal resistance increases significantly. Luckily, the power density has been saturated since 2004 (as shown in Fig. 1.5a), but due to high R_{TH}, now SHE has emerged as an important design consideration for the modern transistors and interconnects. Fig. 1.5b shows that R_{TH} of FinFET is higher by two orders than that of planar device [9]. This increase in R_{TH} increases the steady-state self-heating of the transistors. In addition, thermal capacitance (C_{TH}), indicated by the blue symbols in Fig. 1.5c [10], is decreasing as channel volume gets smaller. A combination of these two parameters makes transient SHE an important issue as well (see Fig. 1.5d) because the smaller time constant (τ_{c}) allows the transistor channel to reach the peak temperature more quickly.

Self-heating degrades the performance and reliability of transistors and interconnects. As temperature increases, the resistance of the metal interconnects increases significantly, hence RC delay will increase [15]. It will lower electronic speed. For example, there is 5% speed reduction with 10°C temperature increase. Another distinctive effect on Back-End-Of-Line (BEOL) is electromigration at an inter-metal line which is an interconnect. Temperature and diffusion coefficient are related by the Arrhenius relationship (i.e., exponential relationship) so that even small temperature

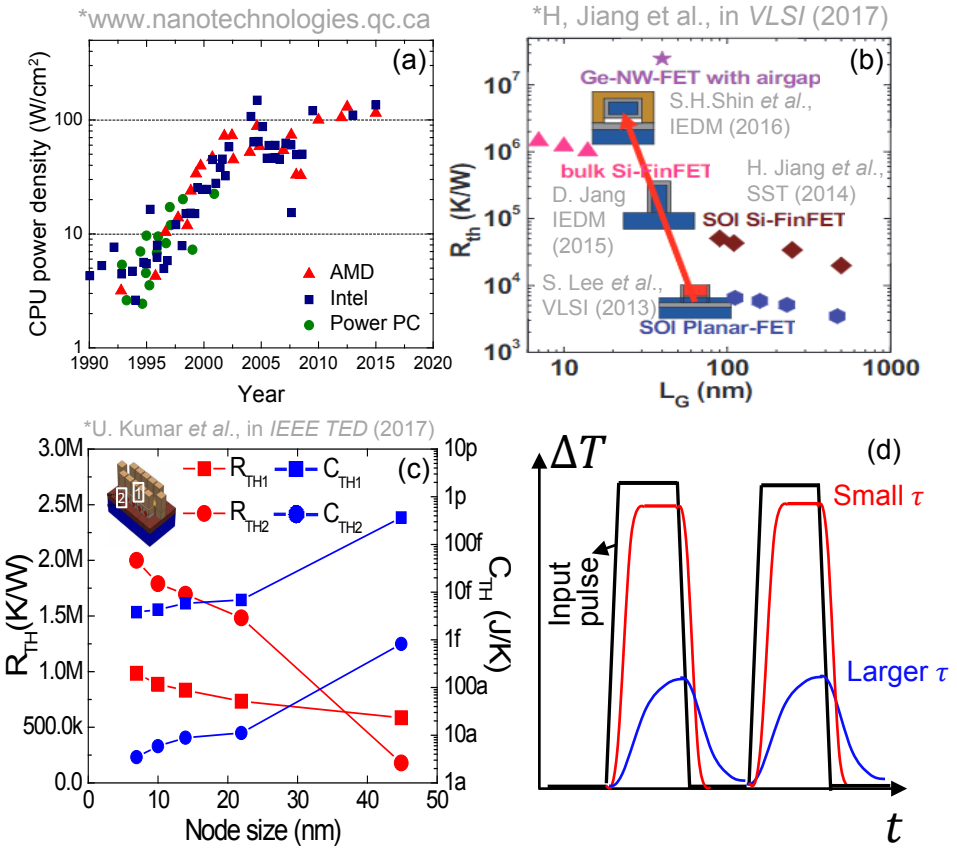

Fig. 1.5. (a) Power density in CPU over the years [8], (b) R_{TH} comparison among different types of transistor [9], (c) Correlation between R_{TH}, C_{TH}, and node size [10], (d) Simple schematic shows detrimental effect of smaller τ_{c}.

increase may increase the diffusivity significantly [16]. For example, 20°C difference doubles the rate of electromigration.

The transistors are vulnerable to self-heating as well. One needs to carefully investigate the self-heating induced acceleration of various transistor degradation modes, such as Negative Bias Temperature Instability (NBTI), Hot Carrier Injection (HCI), and Time Dependence Dielectric Breakdown (TDDB). The details of each degradation mode and the review of the recent models are further described in Sec. 3.6. The NBTI in PMOS takes place when the gate is biased negative bias with respect to the source and drain electrodes. This negative gate bias reduces the energy barrier for Si-H bond dissociation at the Si-SiO_2 interface. Once these bonds capture holes and the weakened bonds eventually dissociate, the corresponding shift in the threshold voltage reduces the saturation current. Based on the expression for temperature-dependent dissociation rate of interface bonds, we can study the temperature impact on NBTI. In the case of NBTI, traps generation rate (N_{IT}) has a strong function

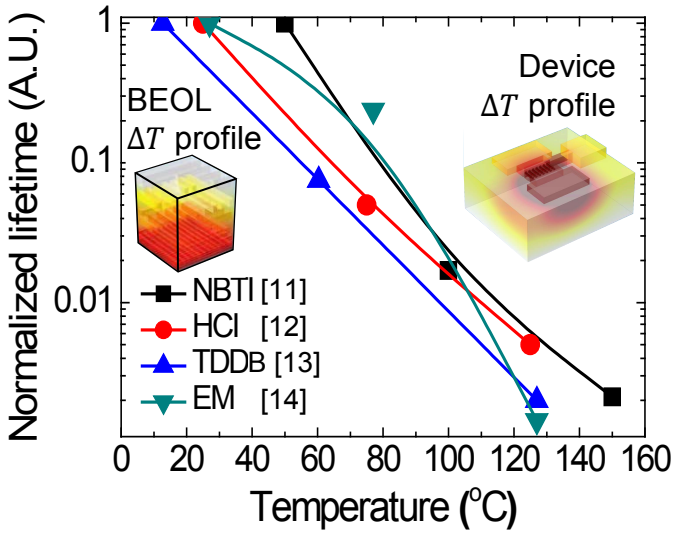

Fig. 1.6. Lifetime ($\Delta V_{\mathrm{TH}} \sim 0.1V$) associated with various degradation modes decreases dramatically with heating [11–14]. Thus, one must calculate ΔT to determine the lifetime of a self-heated IC.

of temperature $N_{\mathrm{IT}} \propto \left(\frac{k_{\mathrm{F}} N_0}{k_{\mathrm{R}}}\right)^m \cdot (D_{\mathrm{H}} t)^n$, where k_{F}, k_{R}, and D_{H} (e.g., hydrogen and silicon forward dissociation rate, reverse dissociation rate, diffusion coefficient) are all temperature dependence by the Arrhenius relationship. If the devices operate for a long time, several tens of degrees of wrong temperature expectation will calculate incorrect threshold voltage shift by orders of different generated traps number.

Unlike NBTI, HCI appears predominantly in NMOS transistors due to the higher mobility of electrons than that of holes in PMOS. HCI occurs when the drain voltage is applied while the source is grounded. This bias condition let electrons (i.e., charge carrier for NMOS) gain high enough energy that can initiate impact ionization. HCI can appear at any gate voltage, however, it is known that the degradation is maximum when the drain bias is half of the gate bias for the long channel devices. The electrons with high energy are injected into the gate oxide, and results in the interface traps. The conventional long channel devices are known to show less degradation at higher temperature since impact ionization can be suppressed at a higher temperature. However, as device size becomes several nanometers length, devices are affected by surroundings such as phonon scattering. Sign and value of activation changes opposite to that of a conventional device for modern ICs. Similar with NBTI, HCI also shows Arrhenius relationship with temperature, $N_{\mathrm{IT}} \propto A \cdot e^{\frac{-E_{\mathrm{A}}}{kT}} \cdot t^n$.

In the case of TDDB, temperature dependence has not been clearly investigated yet due to absent of microscopic model for the defect generation [17]. Generally, TDDB is known to be following defect generation process. Mathematically, TDDB can be described by $T_{\mathrm{BD}} = k \cdot \frac{N_{\mathrm{BD}}^{1/m}}{R_{\mathrm{G}}} \cdot e^{\frac{-E_{\mathrm{A}}}{kT}}$, where N_{BD} is the critical trap density, R_{G} is the rate at which traps are created, and k is a constant, and the exponential term represent the Arrhenius type dependence on temperature [18]. E_{A} has to be found empirically, however, non-Arrhenius dependence has also been reported so far [19,20]. In this thesis, SHE impact on TDDB is not covered, since temperature dependence of TDDB has to be explored in further details. Only NBTI, and HCI are studied in this thesis. As shown in Fig. 1.6, the intrinsic lifetime of a typical IC transistor may reduce 100-fold due to self-heating [11–14]. Therefore, an accurate SHE model is

essential for predictive, reliability-aware ICs design. In the next section, the reliability issues within the packaging level are studied.

1.3 New reliability challenges in the Post Moore's law era

As the pace of transistor scaling has reduced, further improvements in power and performance can be realized from advanced packaging technologies such as 2.5D or 3D integration. However, as we stack more dies, the complexity of an IC, the number of devices per chip, the power density all give rise to severe thermal issues again in system level with FEOL and BEOL SHE [21]. For the server application, one may argue that the thermal issue can be solved by the integration of an effective cooling strategy such as heat sinks, water cooling, and heat pipes [22, 23]. However, for mobile devices, the cooling strategies cannot be applied easily. The severe thermal issues subsequently impact on mechanical stress as the substrate thickness becomes less than 100 μm. Due to the difference of coefficient of thermal expansion (CTE) between different materials, ICs can undergo multiple mechanical stresses such as warpage, copper pumping, and cracks can result in a significant performance and reliability degradation especially at the interconnecting structure, such as controlled collapse chip connection (C4) bumps, and ball grid array (BGA) bumps, see Fig. 1.7 [24]. Recently, the reliability issues of these solder bumps becomes more significant because of the miniaturization of ICs and the high performance requirement. Increasing current density results in electromigration issues due to current crowding, and also excessive intermetallic compound (IMC) growth can degrade the mechanical reliability as well by changing the stress and strain fields around the interface significantly.

As the thermal issue becomes nontrivial, species transport such as moisture or charge transport within an encapsulation can give rise to another degradation mechanism since the diffusivity of species exhibits Arrhenius relationship with temperature as shown in Fig. 1.7. A poor prediction of species transport can result in the protection failure from environmental factors such as moisture, ions, and atmospheric

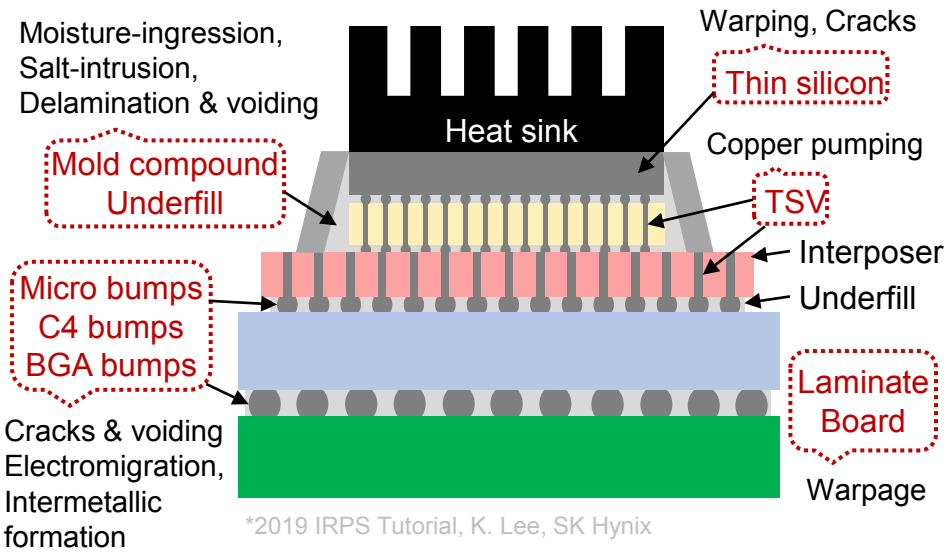

Fig. 1.7. Reliability challenges in 2.5D/3D packaging

contaminants. For example, moisture ingress can lead to corrosion, delamination, hygroswelling as shown in Fig. 1.8 [25,26]. Also, for high voltage IC (HV-IC) applications, the moisture ingress can cause the accelerated charge transport that can distort the electric field within the encapsulation, and initiate breakdown phenomenon. In conclusion, the predictive modeling framework of species transport and temperature distribution within an IC is necessary, and yet, there has been no predictive model proposed due to the challenges described in the following section.

1.4 The reliability modeling challenges for modern integrated circuits

1.4.1 The ubiquity of heterogeneous system

In the 1950s, only epoxy resin was used for IC packaging material [27]. Several decades later, inorganic fillers, such as fused silica or organic clay was added to help tailor/co-optimize the mechanical toughness, thermal conductivity, and moisture diffusivity within polymer mold compounds (MCs) used to package microelectronic integrated circuits. An optimally designed MC is particularly important for high

power applications in smart-grid and electric automobiles that operate in extreme environments. Despite the long history and wide-spread use, the optimization of filler-infused composites is generally empirical and therefore time-consuming due to the heterogeneous system that makes the transport modeling non-trivial.

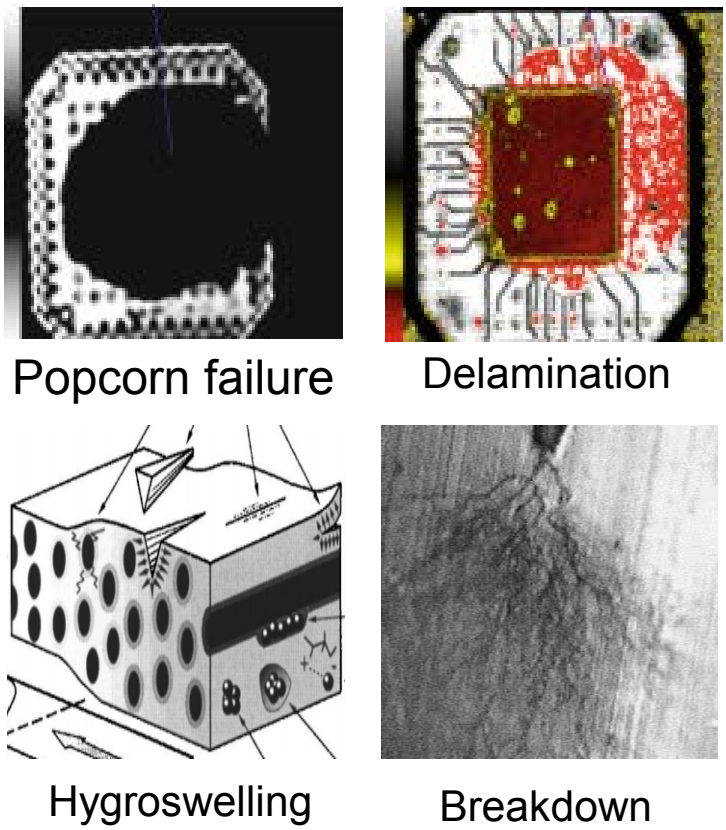

Fig. 1.8. Examples of detrimental ageing processes that can caused by moisture ingress. Popcorn failure occurs due to the high internal pressures caused by sudden evaporation of moisture during high temperature processes. This phenomenon can cause cracks or delamination between encapsulant and board. Also, moisture can result in the encapsulant expansion (i.e., hygroswelling) that can exert stress on the material. Lastly, moisture can initiate breakdown by dielectric heating and activation energy reduction.

1.4.2 The challenge of Multi-scale modeling

Of all the most, it is crucial to define the accurate thermal parameters (R_{TH}, and C_{TH}), in order to predict the precise temperature distribution within ICs. Different approximations of the original systems have led to slightly different modeling frameworks to define thermal parameters and predict SHE within ICs. However, most groups have focused on isolated components within the hierarchy (i.e., a single transistor, specific circuit configuration, or package type) as shown in Fig. 1.9 so that this fragmented approach makes it difficult to verify the implications of SHE on performance and reliability of ICs. In the same words, SHE cannot be accurately predicted unless thermal coupling with FEOL, BEOL, and printed-circuit-board (PCB) is taken into account. Indeed, the hierarchical integration of BEOL and PCB Joule heating, FEOL self-heating, and the coupling of three factors should be considered for accurate prediction of self-heating in modern ICs.

Finite element method (FEM) simulation can be used to describe the self-heating effects accurately, however, discretization of equations are not trivial when the physical phenomena involve length and time-scales that span many orders of magnitude.

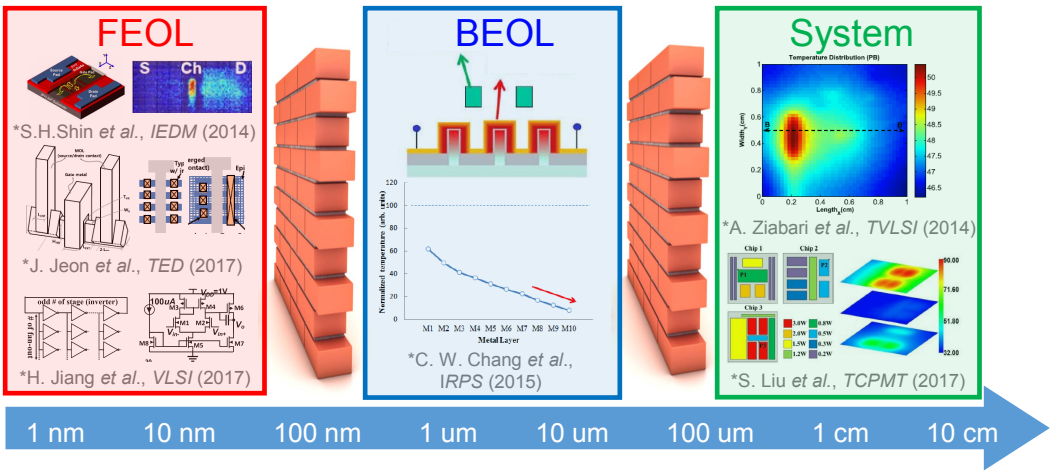

Fig. 1.9. A schematic describes that many researches have been done without considering the coupling between different tiers (FEOL, BEOL, and system level)

An individual transistor can be described by ∼nm range, whereas, packaging level can be described by ∼100um to ∼mm range. Thus, a single mesh model would not be able to cover all length scales due to the considerable amount of computation loads. In addition, multiple time scales is another challenging issue. Temperature rise within an interconnect can be described $\sim \mu m$ range, whereas, some reliability issues such as electromigration, moisture ingression, corrosion can be described ∼s to even years. Similar to the multi-length scales issue, FEM simulations cannot span over a full range of time scales. In this case, the development of a physics-based compact model can be developed which is not a simple task.

1.4.3 The challenge of Multi-physics modeling

Another challenging issue other than the multi-scale issue is the multi-physics issue. As the system becomes more integrated and complicated, many reliability phenomena get affected by various multiple physics: electrical, thermal, and diffusion simultaneously. For example, ions that transport between high voltage electrodes can be affected by the voltage applied to the electrode (i.e., electrical), the temperature of the system (i.e., thermal) and the moisture concentration (i.e., diffusion) within the encapsulant. The modeling interactions between two physics, or even three physics is extremely difficult. If this difficulty needs to be modeled on top of the multi-scale issue as well, the modeling has to be done in a compact way based on a careful and deep understanding of the relevant physical phenomena.

1.5 Outline of the thesis

The goal of this thesis is to develop a physics-based methodology and predictive modeling framework that allows the modeling and simulation of the reliability of modern ICs so that the transistors, interconnects, and packaging material can be co-optimized. Among many reliability issues, the thesis investigates three main topics: (i) generalize the effective medium theories (EMT) and develop a random network

(RN) model to deal with different heterogeneous systems discussed in chapter 2, and 6; (ii) develop thermal compact models to describe self-heating in transistors and interconnects (the results are summarized in chapters 3, and 4); and finally (iii) in Chapters 5 and 6, propose optimized filler configuration that can minimize the impact from moisture-assisted charge transport within encapsulation material. The detailed outline of each chapter is as follows.

In chapter 2, the methodologies to define macroscopic effective physical parameters of the various heterogeneous system is described. The most natural and engineered systems involve a variety of material and therefore are heterogeneous by definition. In order to develop a modeling framework in a heterogeneous system, we need to study how to replace a composite system with an effective system composed of one effective material. First, conventional EMT models are studied and then the methodologies in which how different situations (e.g., discontinuity at the interface between different materials, different number of materials, and anisotropic filler configuration) can be taken into consideration appropriately. When the material properties contrast is very large (i.e., more than three orders of magnitude), the composite system must be described by the percolation theory. In this thesis, conventional RN-model is also generalized to describe the system with highly conducting interfacial region.

In chapter 3, the modeling framework to extract thermal parameters from transistor level to system level is suggested. In this chapter, we also demonstrate the importance of multi-time constant thermal circuits to predict the spatiotemporal SHE in modern sub-20 nm transistors. Based on the refined Berkeley Short-channel IGFET Model Common Multi-Gate (BSIM-CMG) model, we examine SHE in typical digital circuits (e.g., ring oscillator) and analog circuits (e.g., two-stage operational amplifier) by Verilog-A based HSPICE simulation. Similarly, I develop a physics-based thermal compact model for packaged ICs using an effective media approximation for the BEOL interconnects and ICs packaging. I integrate these components to investigate SHE behavior due to self-heated transistors, examine ICs reliability degradation due

to SHE, and explain why one must adopt various (biomimetic) strategies to improve the lifetime of self-heated ICs.

In chapter 4, we introduce a closed-form analytical transient (cfa)-Joule heating model within an interconnect is introduced. In addition to self-heated transistor impact on temperature distribution in IC (chapter 3), additional temperature rise due to Joule heating within an interconnect (ΔT_{Int}) must be superposed. Based on the proposed cfa-Joule heating model, I develop a SPICE-compatible compact model to predict the temperature distribution for any given circuits/systems. The model validation by experiments, and FEM simulations are also discussed. After the validation, various model applications to compare ΔT_{Int} of different interconnect materials (e.g., Cu, Co, and Ru), and the effectiveness of various cooling strategies (e.g., more vias, and larger wires) are discussed. Finally, the reliability of interconnects under various operating conditions is predicted.

In chapter 5, a fundamental understanding of moisture transport within molding compounds is studied and the generalized effective medium and solubility ($GEMS$) Langmuir model are proposed to quantify water uptake as a function of filler configuration and relative humidity. Based on the $GEMS$ Langmuir model, the investigation of the dominant impact of reacted-water (Y) on electrical conductivity (σ) through numerical simulations, mass-uptake, and DC conductivity measurements data is also done. In addition, filler configuration impact on $E_{\text{MC}}^{\text{Crit}}$, which is another crucial performance parameter of HV-ICs packaging material is investigated by the electric field distribution FEM simulation and observe how moisture ingress reduces $E_{\text{MC}}^{\text{Crit}}$. Finally, optimization of the filler configuration to lower the dissipation factor, and enhance $E_{\text{MC}}^{\text{Crit}}$ is described.

In chapter 6, a compact model of moisture coupled charges transport within a packaging material is developed. Charge accumulation within MC develops space charge packets and it can cause detrimental aging processes of an IC. Based on a developed compact model, the origin of homo-, heterocharge is discussed, and clarify moisture impact on critical inputs (e.g., mobility, trapping coefficient) of the space

charge behavior. When MC is exposed to a humid environment, reasonable D_{eff} of charges definition is important for charge transport modeling. In this chapter, revised random network (RRN)-model is also proposed to predict D_{eff} of charge. Finally, the filler configuration conditions to lower charges D_{eff} for less heterocharge accumulation is discussed.

In chapter 7, the key conclusions of the thesis and the list of future works are described.

1.6 List of associated publications

Following is the list of publications based on the work presented in this thesis.

Chapter 3

W. Ahn, H. Jiang, S.H. Shin, and M. A. Alam,"A Novel Synthesis of Rents Rule and Effective-Media Theory Predicts FEOL and BEOL Reliability of Self-Heated ICs," in *IEEE International Electron Devices Meeting (IEDM)*, 2016.

*__W. Ahn__, *C. Jiang, J. Xu, and M. A. Alam, "A New Framework of Physics-Based Compact Model Predicts Reliability of Self-Heated Modern ICs: FinFET, NWFET, NSHFET Comparison," in *IEEE International Electron Device Meeting (IEDM),* 2017, (*Equal Contribution).

W. Ahn, H. Zhang, T. Shen, C. Christiansen, P. Justison, S.H. Shin, and M. A. Alam, "A Predictive Model for IC Self-Heating Based on Effective Medium and Image Charge Theories and Its Implications for Interconnect and Transistor Reliability," in *IEEE Transactions on Electronic Devices*, 2017.

W. Ahn, S.H. Shin, C. Jiang, H. Jiang, M. A. Wahab, and M. A. Alam, "[Invited] Integrated modeling of self-heating of confined geometry transistors and its implications for the reliability of sub-20 nm modern ICs," in *Microelectronics Reliability*, 2018.

*__W. Ahn__, *B. Mahajan, *Y.-P. Chen, and M. A. Alam, "Design and Optimization of -Ga2O3 on (h-BN layered) Sapphire for High Efficiency Power Transistors: A Device- Circuit-Package Perspective," in *IEEE International Electron Device Meeting (IEDM)*, 2018, (*Equal Contribution).

S.H. Shin, H. Jiang, **W. Ahn**, H. Wu, W. Chung, D.Y. Peide, M.A. Alam, "Performance potential of Ge CMOS technology from a material-device-circuit perspective," in *IEEE Transactions on Electronic Devices*, 2018.

Chapter 4

H. Tian, **W. Ahn**, K. Maize, M. Si, P. Ye, M. A. Alam, A. Shakouri, P. Bermel, "Thermoreflectance imaging of electromigration evolution in asymmetric aluminum constrictions," in *Journal of Applied Physics*, 2018.

W. Ahn, Y.-P. Chen, M. A. Alam, "An Analytical Transient Joule Heating Model for an Interconnect in a Modern IC: Comparison of Material and Cooling Strategies," in *IEEE International Reliability Physics Symposium (IRPS)*, 2019.

W. Ahn, H. Zhang, T. Shen, P. Justison, M. A. Alam, "Derivation of Closed-form Analytical Joule Heating Model and Experimental Validations," in *IEEE Electron Device Letter*, 2019, (Under review).

Chapter 5

W. Ahn, S.H. Shin, R. Asadpour, D. Varghese, L. Nguyen, S. Krishnan, M. A. Alam, "Optimum filler geometry for suppression of moisture diffusion in molding compounds," in *IEEE International Reliability Physics Symposium (IRPS)*, 2016.

I. Imperiale, S. Reggiani, G. Pavarese, E. Gnani, A. Gnudi, G. Baccarani, **W. Ahn**, M. A. Alam, D. Varghese, A. Hernandez-Luna, L. Nguyen, S. Krishnan, "Role of the

Insulating Fillers in the Encapsulation Material on the Lateral Charge Spreading in HV-ICs," in *IEEE Transactions on Electronic Devices*, 2017.

W. Ahn, D. Cornigli, D. Varghese, L. Nguyen, S. Krishnan, S. Reggiani, M. A. Alam, "Effects of Filler Configuration and Moisture on Dissipation Factor and Critical Electric Field of Epoxy Composites for HV-ICs Encapsulation," in *Composites Science and Technology*, 2019, (Under review).

Chapter 6

W. Ahn, D. Cornigli, D. Varghese, S. Krishnan, S. Reggiani, and M. A. Alam, "Revisited the origin of space charge packets based on a compact analytical model in a highly insulating composite under humid environment," in *Composites Science and Technology*, 2019 (in preparation).

W. Ahn, D. Cornigli, H. Liu, D. Varghese, S. Krishnan, S. Reggiani, G. Subbarayan, and M. A. Alam, "Estimation of Effective Diffusivity of Ions within Molding Compounds Under Humid Environment by Revised Random Network Model," in *Composites Science and Technology*, 2019 (in preparation)

2. ANISOTROPIC AND MULTI-COMPONENT EFFECTIVE MATERIAL PROPERTY

2.1 Background

Natural or engineered materials are often composed of geometrically-complex arrangements of several phases. As explained in the Introduction, solving transport problems in these complex structures is nontrivial. These transport problems include: Transport of heat flux from self-heated transistors through the complicated stack of interconnects, moisture-assisted charge transport through a mold compound composed of epoxy and silica fillers; stress propagation and delamination of multi-layer

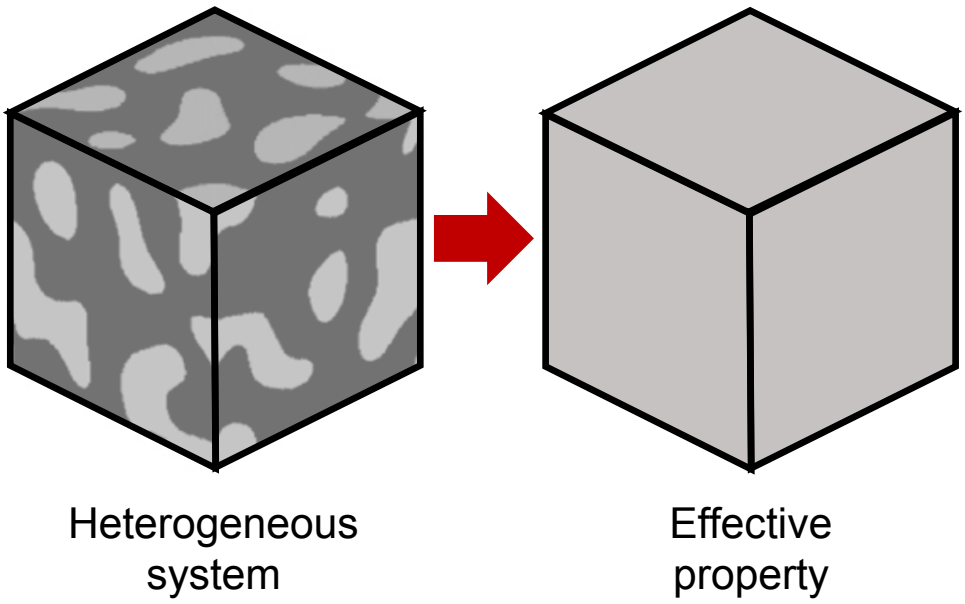

Fig. 2.1. EMT models can calculate the effective property of a heterogeneous system and the output value can be used in a various modeling frameworks

Table 2.1.
Steady-state of different physics are mathematically analogous. Average flux = Effective property × Average field.

Average flux	**Effective property**	**Average field**
Electric displacement	Dielectric constant	Electric field
Heat flux	Thermal conductivity	Temperature gradient
Mass flux	Diffusivity	Concentration gradient

thin-film stacks, and so on. The solution of the transport problem would be simplified if the multi-phase, inhomogeneous material could be replaced by an "equivalent" homogeneous material that nonetheless retains the essential material and geometrical information of the original composite, see Fig. 2.1. Depending on the specific composite system and the transport problem of interest, over the years the scientists have proposed a variety of these effective medium theory (EMT) models. One advantage of an EMT model is that, once we obtain the effective property for a particular transport problem, it can be used to solve other mathematically analogous transport problems [28]. For example, once we can determine the effective thermal conductivity of a certain structure, Table 2.1 shows that we can also calculate the effective dielectric constant or effective diffusivity by using the same formula with appropriate material properties. In this chapter, we will first review the classical EMT models (Sec. 2.2). We will in Sec. 2.3 that the classical models do not apply and therefore must be generalized: (a) if the parameter contrast of components of the composite is large (Sec. 2.3.1), (b) if the material properties are highly anisotropic (Sec. 2.3.2), (c) if the material system involves more than two components (Sec. 2.3.3), and/or (d) if the system contains a variety of systems of various geometric shapes and sizes (Sec. 2.3.4).

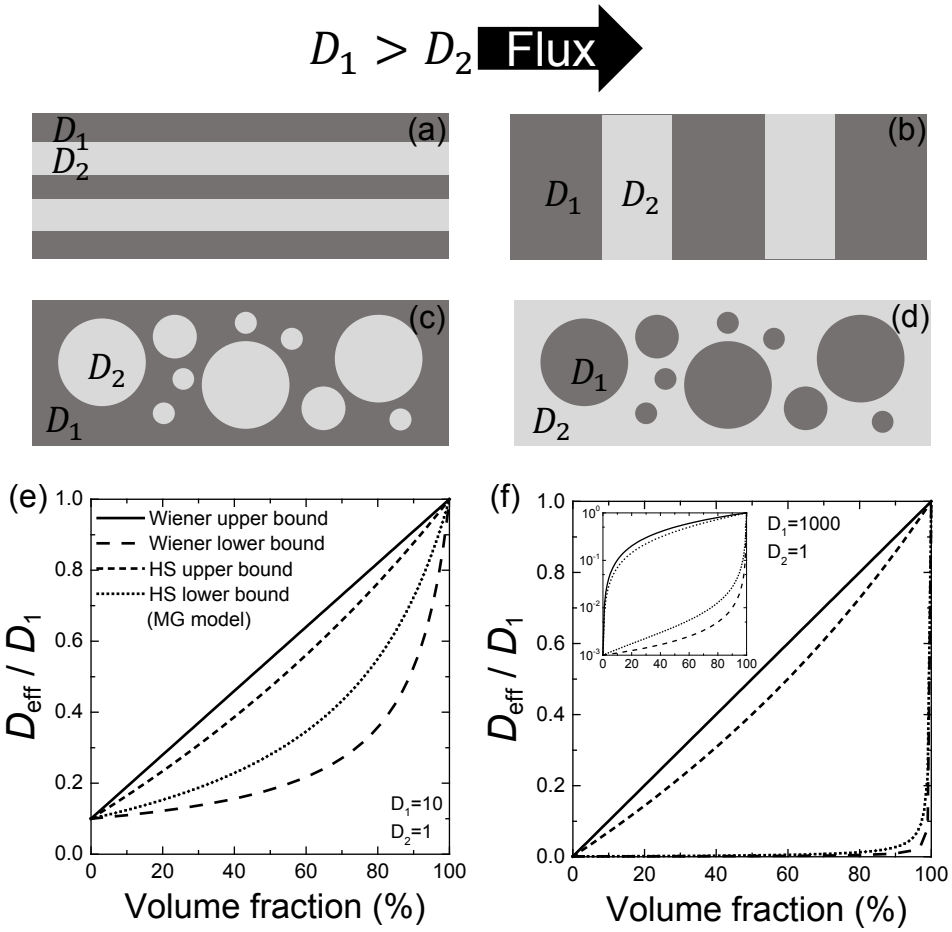

Fig. 2.2. Schematics of some simple structure of composites that can be estimated accurately (a) parallel placement; (b) series placement; (c) conducting phase covering insulating fillers; and (d) insulating phase covering conductive fillers. Wiener and Hashin-Shtrikman bounds comparison when (e) D_1/D_2=10, and (f) D_1/D_2=1000.

2.2 Classical EMT model

2.2.1 Series-Parallel theoretical bounds

Weiner [29] and Hashin-Shtrikman [30] suggest two simple, intuitive ways to estimate the upper and lower bounds of the effective property of a two-phase system, as shown in Fig. 2.2. The validity of the approaches presumes that the system size is much larger than the length scale of inhomogeneities. First, the most extreme two

cases can be considered: (i) one phase connects to the opposite side at all volume fraction as shown in Fig. 2.2a, and (ii) one phase does not connect to the opposite side at all volume fraction as shown in Fig. 2.2b. These two cases can be described by the linear average shown by Eq. 2.1. For example, when two different slabs are arranged in parallel as shown in Fig. 2.2a, we can retain the relative volume-fraction of the original composite based on Eq. 2.1a. The "series-bound" can be used when high-conductivity phased is fully embedded in the low-conductivity phase so that if high-conductivity phase does not connect two sides. In this case, the volume-fraction can be retained based on Eq. 2.1b, and the slabs are now arranged in series. If both-phases are percolating, as often is the case for 3D composites, the series-parallel bounds can be viewed as lower and upper bounds of the transport problem. Equation 2.1 summarizes the formula for the Wiener bounds of a two-phase composite.

$$D_{\text{eff}} = \phi_{\text{f}} \cdot D_1 + (1 - \phi_{\text{f}}) \cdot D_2 \tag{2.1a}$$

$$D_{\text{eff}} = \frac{1}{\phi_{\text{f}}/D_1 + (1 - \phi_{\text{f}})/D_2} \tag{2.1b}$$

where ϕ_{f} is the volume fraction of phase 1.

For extreme parameter contrast in an otherwise isotropic composite (insulating phase embedded into a conducting phase or vice versa), Hashin-Shtrikman (HS) model [30] offers a slightly general formulation. When the composite material is composed of one conductive phase coating the other insulating phase (in Fig. 2.2c, Eq. 2.2a, i.e., upper bound) or the opposite case (in Fig. 2.2d, Eq.2.2b, i.e., lower bound), the effective property can be calculated based on HS model, see Eq. 2.2. The equations are derived by Hashin and Shtrikman using variational principles [30] and HS bounds exhibits tighter bound than that of Wiener bounds as it requires isotropy.

$$D_{\text{eff}} = \frac{1 - \phi_{\text{f}}}{1/(D_2 - D_1) + \phi_{\text{f}}/3D_1} + D_1 \tag{2.2a}$$

$$D_{\text{eff}} = \frac{\phi_{\text{f}}}{1/(D_1 - D_2) + (1 - \phi_{\text{f}})/3D_2} + D_2 \tag{2.2b}$$

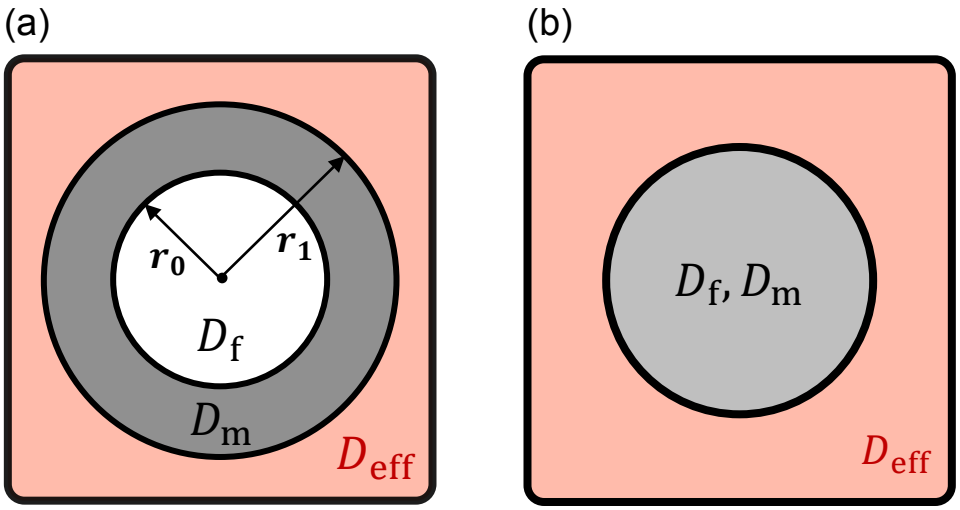

Fig. 2.3. (a) Simple schematic of Maxwell-Garnett (MG) model where phases are not interchangeable (b) Bruggeman model; phases are interchangeable

Note that Eq. 2.2b is same as Maxwell-Garnett model [31] another widely known EMT model for the same geometric arrangement shown in the fourth schematic in Fig. 2.2d.

As shown in Fig. 2.2e, HS bounds are always narrower than those of the Wiener bounds as HS bounds assume isotropy of the inclusion. The bounds can be further narrowed to the percolation limit by including higher-order terms that account for geometrical correlation [32,33]. However, these additional terms are difficult to calculate and not necessarily unique. Moreover, when the contrast ratio (D_1/D_2) between different phase becomes larger, upper bound and lower bound becomes far apart and do not provide useful information as you can see in Fig. 2.2f. As a result, EMT model which is introduced in the next section has been also widely adopted to get the effective property.

2.2.2 Maxwell-Garnett model describes low-density inclusions in a sub-percolating system

Maxwell-Garnett (MG) model is the first analytical model to calculate effective transport properties of composite materials [31]. Originally developed to estimate effective dielectric constant (ε_{eff}), the approach calculates the filler polarization induced by the external field, and presumes (i) dipole of one quasi-spherical medium does not affect its neighbors and (ii) $V_{\text{m}} = V_{\text{f}}$ at the interface, so that the field lines are continuous from one medium to the other. Because of the assumption in the model derivation, MG model works especially well when the filler volume fraction (ϕ_{f}) is low. By mathematical analogy, the ε_{eff} can translate into equivalent results for the thermal conductivity, magnetic permeability, or diffusion coefficient. With the following steady state equation (Eq. 3a) converted to azimuthally symmetric solution of Laplace equation for each region (e.g., A, B, and effective region) and four boundary conditions (Eq. 3b-e), MG theory defines the relationship between effective physical constant (ε_{eff}), within mold (ε_{m}), and within filler (ε_{f}) as shown in Eq. 2.4 [31].

$$\varepsilon \nabla^2 V = 0 \tag{2.3a}$$

$$V_{\text{f}}(r_0, \theta, \varphi) = V_{\text{m}}(r_0, \theta, \varphi) \tag{2.3b}$$

$$\varepsilon_{\text{f}} \nabla V_{\text{f}} = \varepsilon_{\text{m}} \nabla V_{\text{m}} (r = r_0) \tag{2.3c}$$

$$V_{\text{m}}(r_1, \theta, \varphi) = V_{\text{eff}}(r_1, \theta, \varphi) \tag{2.3d}$$

$$\varepsilon_{\text{m}} \nabla V_{\text{m}} = \varepsilon_{\text{eff}} \nabla V_{\text{eff}} (r = r_1) \tag{2.3e}$$

In an isotropic, and infinite system, ε_{eff} can be written as:

$$\varepsilon_{\text{eff}} = \varepsilon_{\text{m}} \left[1 + \frac{3(\varepsilon_{\text{f}} - \varepsilon_{\text{m}})\phi_{\text{f}}}{\varepsilon_{\text{f}} + 2\varepsilon_{\text{m}} - (\varepsilon_{\text{f}} - \varepsilon_{\text{m}})\phi_{\text{f}}} \right] \tag{2.4}$$

2.2.3 Bruggeman model considers the background and the inclusions symmetrically

In contrast to MG model, Bruggeman model focuses on composites with high concentration of fillers, namely, aggregate structure [34]. The unit cell in Bruggeman

model comprises two mediums on an equal basis so that none of the material encapsulates the other, see Fig. 2.3b. The assumptions for Bruggeman model is as follows: (i) Average internal field in each particle is given by isolated sphere relation, and; (ii) Particles consisting of material A and B are both located in effective dielectric environment. Thus, each physical parameter (e.g., ε_{f}, and ε_{m}) is interchangeable, in Eq. 5. Bruggeman model gives a better estimate for $\phi_{\mathrm{f}} \to 1$ compared to the MG model.

$$\phi_{\mathrm{f}} \frac{\varepsilon_{\mathrm{f}} - \varepsilon_{\mathrm{eff}}}{\varepsilon_{\mathrm{f}} + 2\varepsilon_{\mathrm{eff}}} + (1 - \phi_{\mathrm{f}}) \frac{\varepsilon_{\mathrm{m}} - \varepsilon_{\mathrm{eff}}}{\varepsilon_{\mathrm{m}} + 2\varepsilon_{\mathrm{eff}}} = 0 \tag{2.5}$$

2.2.4 Discussion: Bruggeman vs. MG Models

If the filler and the background parameters are comparable, the EMT models predict comparable effective properties. Given the experimental uncertainties, either model can be used to interpret the experimental data, see Fig. 2.4(inset). The model selection becomes more important with the increased contrast of the parameters. Since the two EMT models focus on low vs. high-density limits, it is not easy to decide the appropriate model to use close the percolation threshold.

Numerical studies show that MG model offers a good estimate of the effective properties *until* the inclusions begin to touch each other, close to but below the percolation limit. Once this density is an approach, the analytical model deviates rapidly from the numerical results. Indeed, extensive Monte Carlo simulations have been reported for various geometry configurations that validates MG model prediction for $\phi_{\mathrm{f}} < 0.3$.

In general, the Bruggeman model predicts $\varepsilon_{\mathrm{eff}}$ higher than that of MG model in the case when ε_{f} is smaller than that of ε_{m}, see Fig. 2.4. Numerical results show that Bruggeman model compares well with the numerical result when the inclusion density exceeds the percolation threshold. The filler fraction when cut off happens acts like

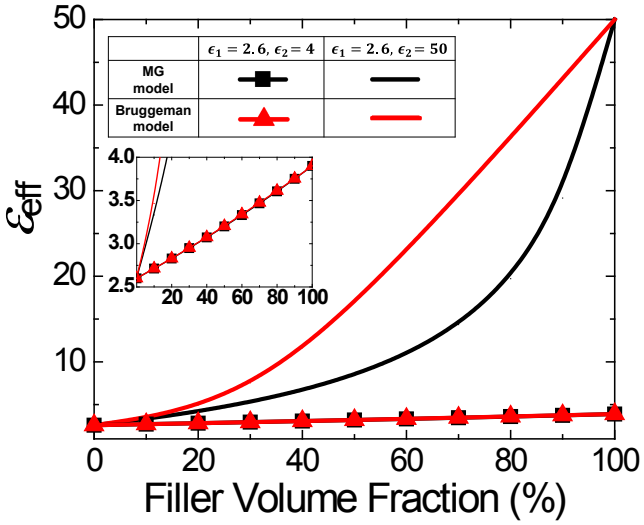

Fig. 2.4. EMT model comparison between MG model and Bruggeman model when each phase dielectric constant shows big difference (inset) expanded view of the comparison when each dielectric constant is similar: Miniscule difference between two different model.

a percolation threshold, namely, effective physical parameter increases rapidly when the inclusion creates a continuum phase within the background material.

The issue of two models is that they have been derived by neglecting interactions among the fillers. The interaction can be important when the distance between neighboring particles becomes very close, or the contrast ratio at each phase becomes large. In these cases, one may adopt percolation theory for the calculation.

Although MG and Bruggeman models are derived are based on simplified physics with spherical inclusions, the models are simple and quick to use. If the limitations of the models are understood and if the models are appropriately generalized (and experimentally calibrated) for specific applications, the techniques can offer a powerful methodology to solve a variety of problems. In the following section, we will discuss these generalizations of the effective media theory so that we can solve a variety of transport problem of great practical interest (e.g self-heating in modern ICs, moisture diffusion in mold compounds, etc.)

2.3 Physics-inspired generalization of the classical EMT models

2.3.1 Infinite-contrast composites violet interface-continuity assumption of the classical EMT models

Sometimes a MG model fails to explain the experimental data even for low-density subpercolating systems. On closer examination, one finds that for extremely high or infinite-contrast systems ($D_{\mathrm{m}} >> D_{\mathrm{f}}$), the interface concentration may actually be discontinuous (i.e., filler is essentially impermeable to moisture), making MG theory poorly suited to the problem of moisture diffusion. This explains why classical MG model significantly underestimate D_{eff}.

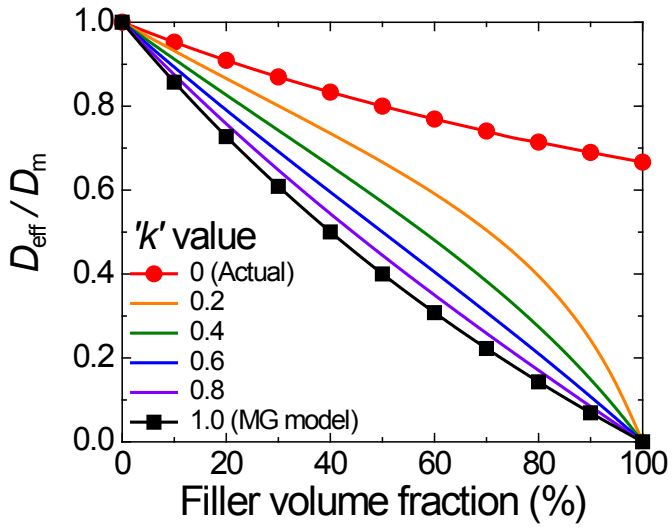

Fig. 2.5. Analytical curves for various partition coefficient (k) of modified MG model. The model becomes conventional MG model when k is equal to 1.

To generalize the MG model for high-contrast systems, recall that unlike thermal or electrostatic analysis, the concentration of the diffusing particles (e.g., moisture) can be discontinuous at the interface even at steady state. This discontinuity can be incorporated with the MG framework through an additional factor, namely the

partition coefficient (k), given by the ratio of the concentration in one phase to the concentration in a second phase at equilibrium state. The concept has been generally adopted in chemical and pharmaceutical sciences where both phases are solvents with different hydrophilicity so that k information has been frequently studied to estimates how hydrophilic a chemical is, or the redistribution of drugs in the body. In our case, k can be defined as $w_{\mathrm{f}}/w_{\mathrm{m}}$, where w_{f}, and w_{m} are water concentration within filler, and mold, respectively, as shown in Eq. 2.6b.

With the modified boundary conditions, D_{eff} can be determined by using Eq. 2.7 [35]. If water molecules cannot go through fillers, we can set both k and D_{f} as zero.

$$D\nabla^2 w = 0 \tag{2.6a}$$

$$w_{\mathrm{f}}\left(r_0, \theta, \varphi\right) = k \cdot w_{\mathrm{m}}\left(r_0, \theta, \varphi\right) \tag{2.6b}$$

$$D_{\mathrm{f}}\nabla w_{\mathrm{f}} = D_{\mathrm{m}}\nabla w_{\mathrm{m}} \tag{2.6c}$$

$$w_{\mathrm{m}}\left(r_1, \theta, \varphi\right) = k_1 \cdot w_{\mathrm{eff}}\left(r_1, \theta, \varphi\right) \tag{2.6d}$$

$$D_{\mathrm{m}}\nabla n_{\mathrm{mold}} = D_{\mathrm{eff}}\nabla w_{\mathrm{eff}} \tag{2.6e}$$

In an infinite system, D_{eff} can be shown as:

$$D_{\mathrm{eff}} = \frac{D_{\mathrm{m}}}{1 - \phi_{\mathrm{f}} + k \cdot \phi_{\mathrm{f}}}\left[1 + \frac{3\left(k \cdot D_{\mathrm{f}} - D_{\mathrm{m}}\right)\phi_{\mathrm{f}}}{2D_{\mathrm{m}} + k \cdot D_{\mathrm{f}} - \left(k \cdot D_{\mathrm{f}} - D_{\mathrm{m}}\right)\phi_{\mathrm{f}}}\right] \tag{2.7}$$

The formula is also applicable for the system where arbitrary k value taking place at the interface (e.i., chemical science, pharmacology). From Eq. 2.7, we can also estimate effective physical parameter function of inclusion fraction for any k, see Fig. 2.5. This partition coefficient attribute to different transit probability from the inclusion phase to the matrix and from the matrix to inclusion. Considering diverse potential energy (e.i., different solubility) for each phase, knowing the exact energy difference at the interface is essential for correct k value calculation. Once we have a precise k value and inclusion fraction information, we can describe the diffusion process of any two phase composites material.

Validation by FEM simulation

Numerical studies using FEM simulation tool (e.g., Comsol multi-physics), is performed to validate the modified MG model. At the interface between two different phases, we set concentration discontinuity and performed simulation multiple times for different k value for the validation. The dimension is chosen 2D due to limited computation load of the simulation tool. Our new calculation approach involves the following steps: (i) the geometry of the mold compounds is specified; (ii) the diffusion equation is discretized and solved using a 3D commercial simulator, COMSOL; and (iii) based on Fick's law (e.g., $D_{\text{eff}} = J/\langle \nabla w \rangle$), D_{eff} is calculated as the ratio of fixed flux at the top plane to average concentration gradient within the unit cell. The boundary conditions are as follows; constant flux at the top plane ($1\text{mol/mm}^2 - \text{s}$), zero concentration at the bottom plane (Dirichlet), zero flux at four side planes.

D_{eff} is calculated for various filler configurations, see Fig. 2.6b. The general figure of fillers is a circle with different configuration and to investigate the impact of the cut-off at a higher ϕ_{f}, square filler case is also performed. In the same configuration, two different cases which are high ϕ_{f} (e.g., diffusion path is cut-off, solid symbol) and low ϕ_{f} (e.g., open symbol) are compared.

Remarkably, as the cylinders begin to touch at critical volume fraction ($\phi_c \ll 1$), D_{eff} begins to drop dramatically, as the paths are completely cut-off (e.g., solid circle, and hexagon). Inclusions with circular cross-section may be the most effective, as they reduce the $D_{\text{eff}} \to 0$ only at $\phi_c = \pi/4 (\sim 78.5\%)$, see Fig. 2.6a. The actual geometry of aligned rod-like filler geometry is also realistically attainable [36, 37]. A randomly filled rod-shaped inclusion would reduce D_{eff} at even lower ϕ_{c}. Thus, aligned rod-like fillers can be an optimum geometric condition for efficient moisture blockage even by lower filler volume fraction. However, square filler even at high ϕ_{f}, D_{eff} value does not deviated from the model since fillers are not touching each other. Similarly, all open symbol cases do not deviated from the modified MG model.

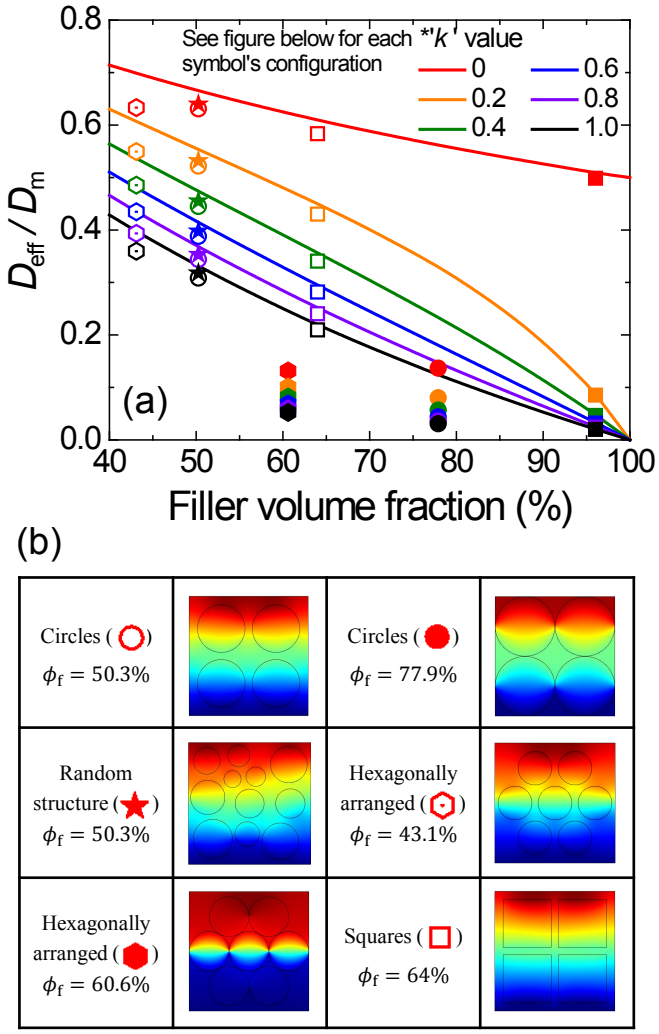

Fig. 2.6. (a) Comparison between analytical modified MG model and numerical simulation results for various k values of various fillers configuration. (b) ϕ_f, symbols, and simulated structures

Also, the ratio of D_{eff} value between arbitrary different two k value in the case of numerical studies and that of the analytical model shows exact match. The D_{eff} value itself shows a slightly lower value than that of the analytical model, however, the difference is not considerable. Moreover, once the ϕ_f is same, D_{eff} shows almost same value (e.g., open circle, and star). Thus, once we know exact k, and ϕ_f for the

composite material, we can predict D_{eff} value if the diffusion path of the system is not cut-off.

2.3.2 Many composites involve more than two-phases: Belova vs. Iterated MG-model

Reliability issue from charge spreading of MCs is determined by ions transport associated with the interface where the diffusivity is the highest due to a loosely bonded region between filler and mold and this is validated by glass transition temperature (T_{g}) measurement of MCs [38]. Increased conductivity at bound region also can be explained by measuring the conductivity of two different material showing different T_{g} [39]. In this case, we have to consider ternary regions for the effective property estimation. If the difference between diffusivity within the interfacial region and mold is within an order magnitude, we can consider two approaches explained below. However, if the difference becomes more than several orders of magnitude, we need to consider the percolation concept which will be shown in section 2.4.

When the difference is within an order of magnitude, the first method is so-called Belova's model, using the same derivation method that we applied in section 2.2.2 can be extended in the presence of bound region between two phases as shown in Fig. 2.7a [40]. Thus, we need to solve the solution of Laplace equation (Eq. 2.6a) with eight boundary conditions (e.g., two equations at four interfaces: region filler/interface, the interface of filler/effective region, region mold/ interface, and interface of mold/effective region) for the derivation.

The second approach is called explicit approach that uses MG model twice. First, we can combine D_{f} and D_{int} to get D_{if} as shown in Eq. 2.10 with the consideration of k at the interface. Once we obtain D_{if}, we can view D_{if} as the effective host material with respect to mold phase. The details of these two models are shown in [40]. As described in [40], Belova model performs best where $D_{\text{f}} \cdot k_{\text{bf}} \approx D_{\text{m}} \cdot k_{\text{mb}}$ (where,

$k_{bf} = w_f/w_{int}$, and $k_{mb} = w_m/w_{int}$ at equilibrium) which is not the case for general MCs ($D_m \gg D_f$, and $k_{mb} \gg k_{bf}$).

Therefore, we apply the second approach, so called, explicit approach which works better for the condition as follows: $D_f \cdot k_{bf} \neq D_m \cdot k_{mb}$ (due to the impermeableness of water into the fillers). When the filler volume fraction (ϕ_f) is larger than that of mold (ϕ_m) fraction, the final D_{eff} can be shown as:

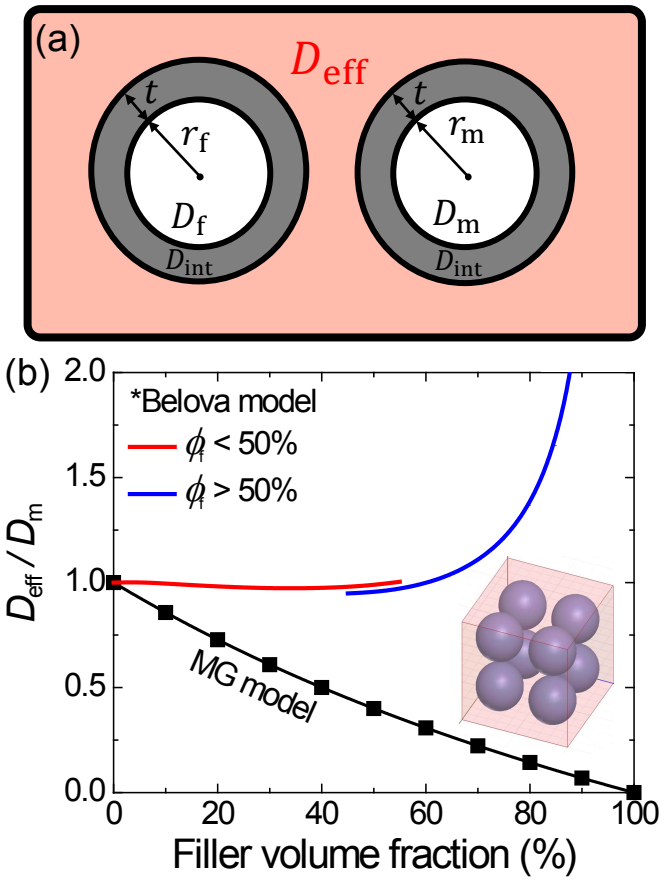

Fig. 2.7. (a) Simple schematic of ternary regions of EMT model (b) Analytical curve of Belova model (explicit approach). Both curves (e.g., when ϕ_f¡50% and ϕ_f¿50%) are shown. Unlike MG model, D_{eff} increases as ϕ_f increases. (inset) 3D Unit cell schematic for the calculation.

Table 2.2.
Assumed input parameters value for Belova model. Diffusivity is normalized to mold region.

Parameter	Value	Parameter	Value
D_{f}	0.0001	D_{m}	1
D_{bnd}	10	k_{bf}	0.0001
k_{mb}	1	ϕ_{f}	x
ϕ_{m}	$1-x-\phi_{\mathrm{bnd}}$	ϕ_{bnd}	$\frac{4\pi}{3}\left[\left(\left(\frac{4\pi}{3}\right)^{1/3}+t\right)^{3}-\frac{3x}{4\pi}\right]$

$$D_{\mathrm{eff}}=\frac{k'D_{\mathrm{if}}\left[1-2\phi_{\mathrm{bnd}}\left(\frac{D_{\mathrm{if}}}{k_{\mathrm{mb}}}-D_{\mathrm{m}}\right)/\left(2\frac{D_{\mathrm{if}}}{k_{\mathrm{mb}}}+D_{\mathrm{m}}\right)\right]}{1+\phi_{\mathrm{bnd}}\left(\frac{D_{\mathrm{if}}}{k_{\mathrm{mb}}}-D_{\mathrm{m}}\right)/\left(2\frac{D_{\mathrm{mb}}}{k_{\mathrm{mb}}}+D_{\mathrm{m}}\right)} \tag{2.8}$$

where k', D_{if} can be shown as:

$$k'=\left(\phi_{\mathrm{bnd}}+k_{\mathrm{bb}}\phi_{\mathrm{f}}+k_{\mathrm{mb}}\phi_{\mathrm{m}}\right)^{-1} \tag{2.9}$$

$$D_{\mathrm{if}}=\frac{D_{\mathrm{int}}\left[1-2\phi_{\mathrm{f}}\left(\frac{D_{\mathrm{bnd}}}{k_{\mathrm{bf}}}-D_{\mathrm{f}}\right)/\left(1-\phi_{\mathrm{m}}\right)\left(2\frac{D_{\mathrm{bnd}}}{k_{\mathrm{bf}}}+D_{\mathrm{f}}\right)\right]}{1+\phi_{\mathrm{f}}\left(\frac{D_{\mathrm{bfd}}}{k_{\mathrm{bf}}}-D_{\mathrm{f}}\right)/\left(1-\phi_{\mathrm{m}}\right)\left(2\frac{D_{\mathrm{bnd}}}{k_{\mathrm{bf}}}+D_{\mathrm{f}}\right)} \tag{2.10}$$

Here, we assume the fillers are randomly and uniformly distributed within the mold so that use the concept of a unit cell to represent the whole system. The unit cell is a cube with one spherical filler at the center covered with the interfacial region, see Fig. 2.7b(inset). For analytical calculation, we normalized diffusivity in mold region as one, and other parameters information is shown in the Table 1. Based on our assumptions and Eq. 2.6, analytical correlation between D_{eff} and ϕ_{f} is shown in the Fig. 2.7b. Unlike conventional MG theory, D_{eff} shows slight decrease at low ϕ_{f}, however, it increases after $\sim$ 35%. This result shows that highly conductive path determines the conductivity of the system after a certain ϕ_{f}, so that careful optimization of filler content in MCs would be necessary.

Validation by FEM simulation

Similarly, this ternary region EMT model is also validated by FEM simulation as shown in Fig. 2.8. The set up of FEM simulation is same as that of the previous section. In order to investigate highly diffusive interfacial region (e.g., between filler and mold) effect on D_{eff}, we divided the system into three regions (e.g., filler, bound, and mold), see Fig. 6(b). Also, we applied concentration discontinuity at two interfaces which are at between filler and bound, and between bound and mold. As you can see in Fig. 8(inset), cube-shaped unit cell with one sphere included is built and for the reasonable comparison with the analytical model, we applied same physical parameters with that of the analytical model, see Table 1. The size of the filler is gradually increased to see the correlation between ϕ_{f} and D_{eff}. Due to the computation load, up to 40% of ϕ_{f} is investigated.

Between two approaches in Belova model, explicit approach shows better estimation due to considerable difference between k_{mb} ,and k_{bf} value. In order to see a more detailed comparison, we expand the y-axis scale, see Fig. 8(inset). At lower fraction,

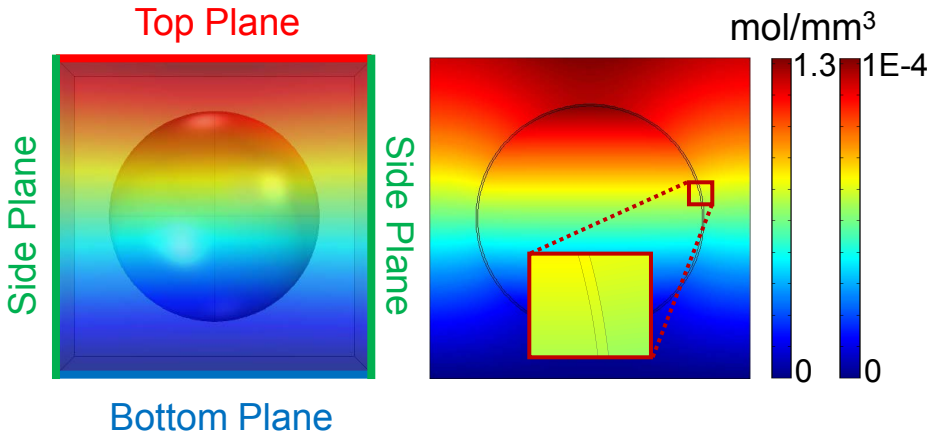

Fig. 2.8. (a) Boundary condition of simulated structure (b) Cross section of simulated structure for Belova model validation. Concentration profile is shown by two legend (Left legend: within mold and bound region. Right legend: filler)

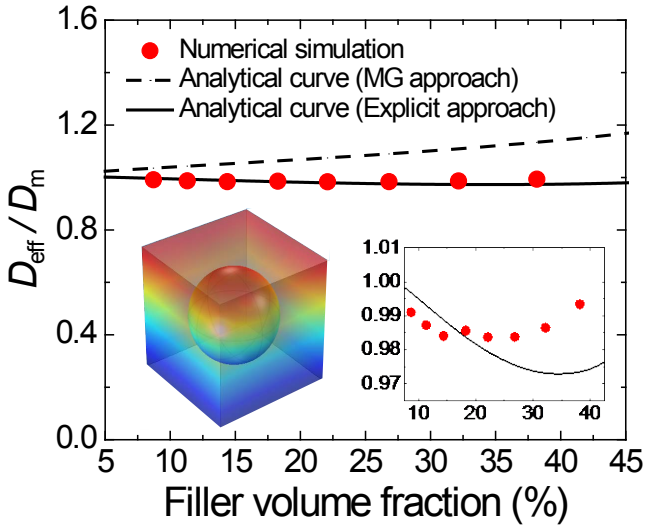

Fig. 2.9. Comparison between analytical curve and numerical simulation of Belova model. (inset) expanded view of analytical curve and numerical study comparison (explicit approach)

numerical results also show decreasing correlation, however, it turns up earlier (at 25%) than that of the analytical model (at 35%). Further study is necessary to figure out different minimum point, however, in general, numerical simulation results are in a good agreement with results from the explicit approach of Belova model. Therefore if we know exact geometric information of MCs, we will be able to predict approximate D_{eff} to investigate reliability characteristics of packaging material.

Table 2.3.
Filler geometric information of samples for experiments.

Material Label	Filler wt (%)	ϕ_{f} (%)	Mean filler size (μm)
MC0	∼70	∼60	∼20
MC1	∼90	∼84	∼25
MC2	∼90	∼84	∼20

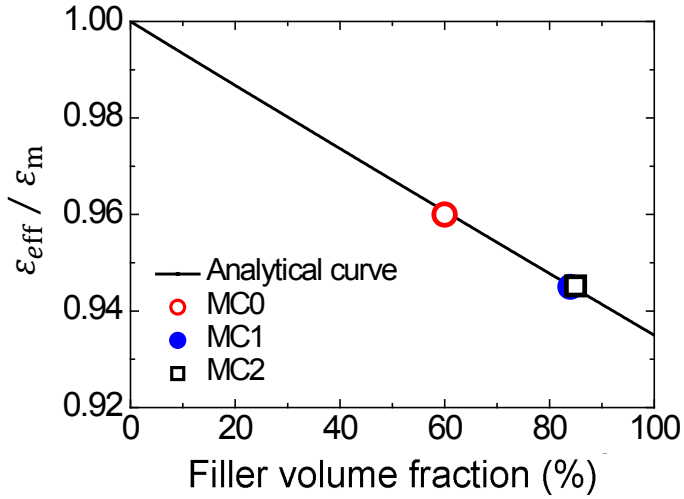

Fig. 2.10. Comparison between experimental data and analytical model (estimated effective dielectric constant value by MG model) [41].

Validation by dielectric constant measurement

Three types of Epoxy Molding Compounds (EMC) are prepared for the experimental study, see Table 2.2. The relative permittivity of each sample is measured to validate MG model [41]. In order to prove volume dependence of the model, samples with the same amount of filler but different filler size distribution is compared (e.g., MC1 and MC2). Also, MC0 which contains smaller filler than that of MC1 and MC2 is compared. Contrary to the concentration profile system, the electrical system does not need to take account of boundary discontinuity at the interface. Thus, conventional MG model or Bruggeman model would be able to predict exact effective dielectric constant (ε_f) for any given sample. As you can see in Fig. 9, MC1 and MC2 exhibits same ε_f even with different size distribution proving that analytical EMT model has the major volumetric function to describe effective physical parameter. Also, measured relative values between different filler fraction are matching agreeably with that of the analytical model showing EMT model validity.

Validation by charge conductivity and moisture diffusivity measurement

Unlike ε_f calculation, D_f need to take account of concentration discontinuity at the interface so that the auxiliary analytical models for different cases were investigated in section 2 and in this section, we validate the models by measuring moisture diffusivity and conductivity of EMCs samples.

Experimental results also show increasing conductivity as more fillers are filled in due to the highly conductive interface region, see Fig. 10. In order to certify an increasing correlation, we compared measured conductivity with numerical simulation results. All results are normalized with conductivity at mold and numerical simulation is done in 2D due to the computational limit. It is obvious that more and more filler

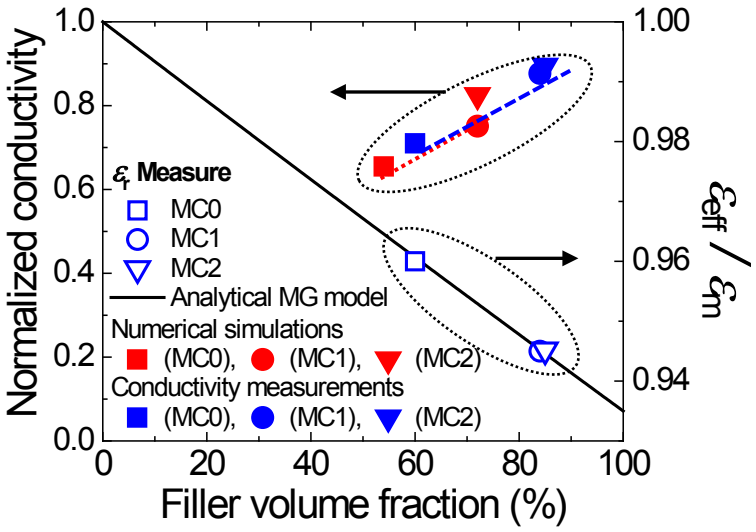

Fig. 2.11. Numerical simulation results of the D_{eff} calculated on various MC structures (Red symbols), Measured electrical conductivity data (Blue symbols) shows a good match [41]. This correlation can be described by modified MaxwellGarnett model extended to the presence of an interfacial layer with high diffusion coefficient. However, dielectric constant measurement data shows same correlation with conventional MG model.

introduction causes the increase of conductivity (e.g., diffusivity) and the measured increasing correlation fits well with numerical studies.

Moisture diffusivity is also investigated for different case by performing humidity absorption test. We measured weight gain for the first 22 hours where moisture is spreading under Fickian diffusion theory. As you can see in Fig. 10, samples with more filler block moisture effectively due to the less available region for moisture to

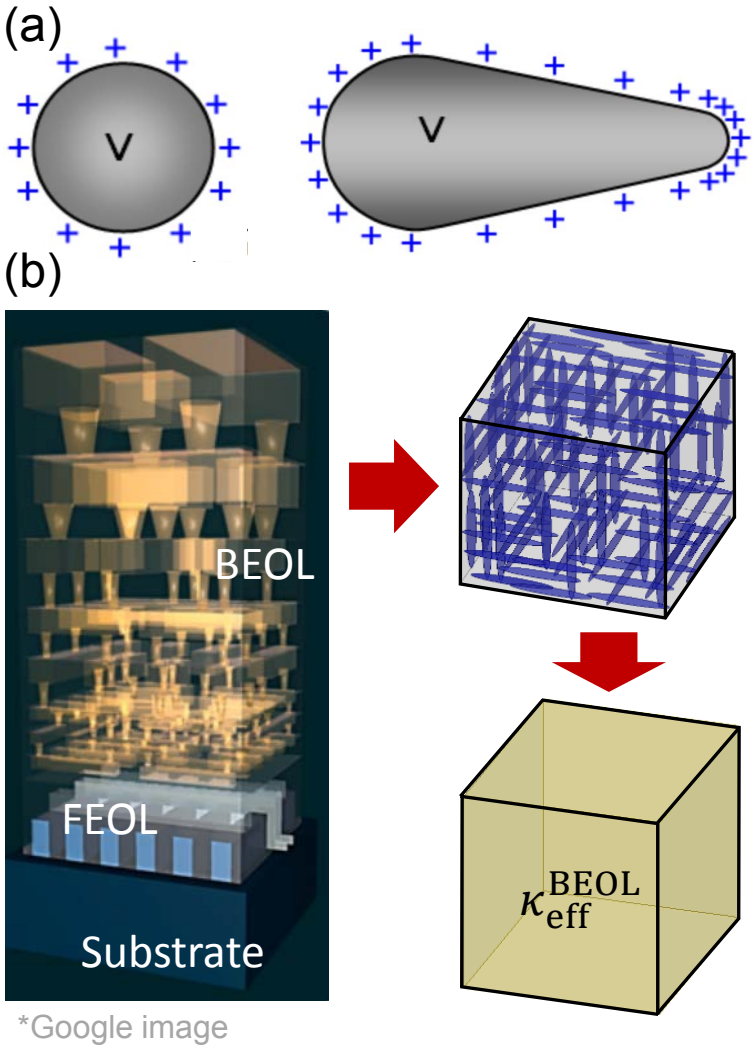

Fig. 2.12. (a) Charge distribution comparison between isotropic and anisotropic inclusion. (b) Modeling framework to estimate effective thermal conductivity of BEOL.

travel. Notably, the fact that measured MC1 and MC2 diffusivity exhibit similar also explains volumetric dependence of EMT model for composite material. In the case of high filler fraction, considerable downward deviation from the analytical curve may attribute to substantial filler fraction so that the beginning of cut off event may be the reason for the lesser diffusivity.

2.3.3 Many composites are have anistropic fillers not described by the classical EMT models

In the previous two sections (2.3.1, and 2.3.2) assume that isotropic fillers (i.e., spherical fillers), just like the fillers we use in the actual MCs. As filler gets more elongated, interface free-charge increases at the high curvature points as shown in Fig. 2.12a. Considering $\mathbf{D} = \varepsilon \cdot \mathbf{E} + \mathbf{P}$, where $\mathbf{D}$, $\mathbf{E}$, and $\mathbf{P}$ is electric displacement, electric field, and polarization charge density, $\mathbf{P}$ has to be defined function of the inclusion geometry and orientation with respect to $\mathbf{E}$. For anisotropic fillers packing, C. W. Nan derived a model [42] by defining depolarization factor which includes both geometric and orientation impact on the effective property.

In this thesis, BEOL is modeled by this Nan's model considering all the interconnects can be viewed as anisotropic fillers as shown in Fig. 2.12b. First, the fillers geometric information for each metal layer is defined based on Rent's rule, and the effective property of each layer is obtained based on Nan's model. Finally, every layer is linearly superposed to represent the macroscopic effective property of a whole BEOL system. More details will be shown in chapter 3.4. In chapter 3.4, the proposed methodology is also validated by FEM simulations and experiments. I believe this methodology can be also applied to any stacked layers with anisotropic fillers for different physics transport issue.

2.4 When the EMT model fails close to the jamming threshold, the percolation models offers an improved alternative

As mentioned in the previous section, the EMT models assume that the inclusions are well-separated and filler-filler interaction can be neglected. Moreover, one assumes that the fillers have the same (or similar) radii. Therefore, when the interaction becomes important (i.e. filler fraction becomes high, physical property contrast between each phase becomes larger, or fillers have very different radii), a more realistic model needs to be adopted to describe the macroscopic property of the system [43].

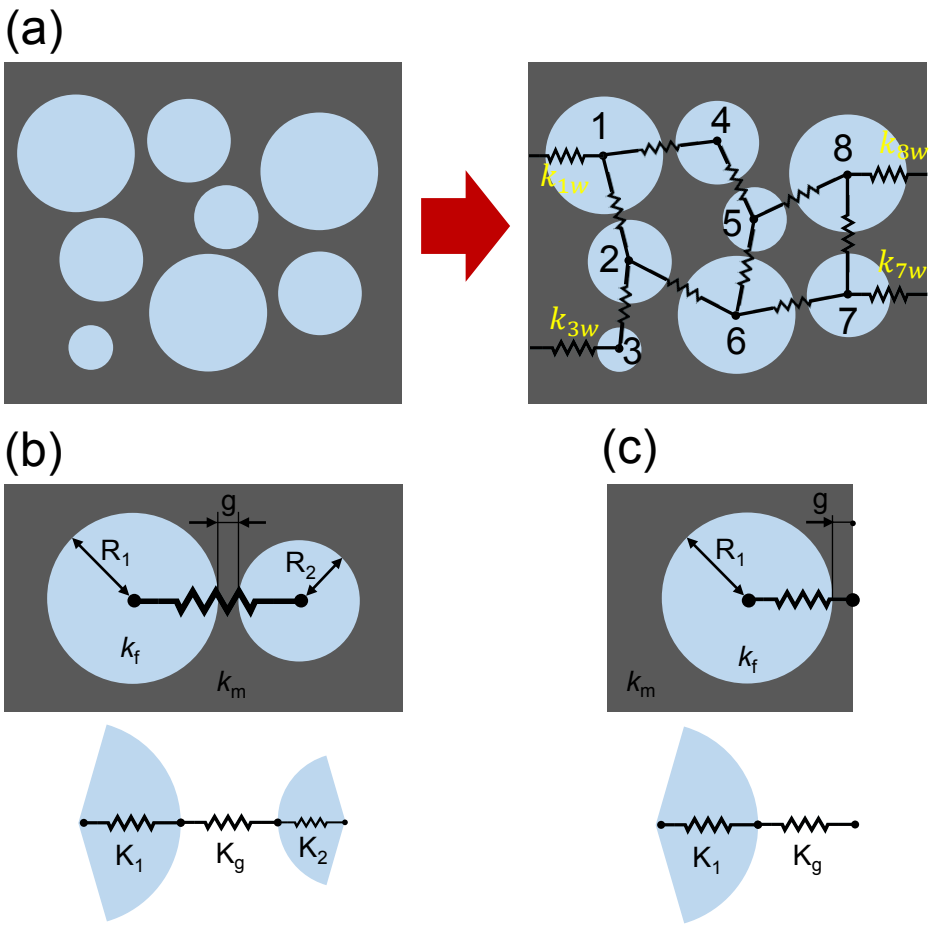

Fig. 2.13. (a) Strong interaction system can be described by random network model. Conductivity connection scheme in the case of (b) neighboring two spheres, and (c) between a sphere and a wall.

In this thesis, we have adopted a generalized random network (RN) model [44–46] to describe the composite system that exhibits strong interaction between neighboring fillers as shown in Fig. 2.13a.

The basic idea of RN-model is to connect neighboring spheres with the conductivity value defined. Conductivity calculation can be divided into two cases: between neighboring two spheres as shown in Fig. 2.13b, and between the sphere and the wall as shown in Fig. 2.13c. Between two spheres, the conductivity analytical formula can be shown as Eq. 2.11 [47].

$$\frac{1}{K_{12}} = \frac{1}{K_1} + \frac{1}{K_{\mathrm{g}}} + \frac{1}{K_2} \tag{2.11}$$

where K_{i}, and K_{g} are intra-particle conductance, and gap conductance, respectively. The formula for intra-particle conductance, and gap conductance are shown below.

$$K_{\mathrm{i}} = k_{\mathrm{p}} \frac{\pi R_{12}^2}{R_{\mathrm{i}}} (\mathrm{i} = 1, 2) \tag{2.12a}$$

$$K_{\mathrm{g}} = \pi k_{\mathrm{m}} a_{12} \log\left(1 + \frac{R_{12}^2}{a_{12} g}\right) \tag{2.12b}$$

where a_{12} is the mean radius of two neighboring spheres, i.e., $2R_1R_2/\left(R_1 + R_2\right)$. Here, R_{12} is $0.5 \times a_{12}$. Between a sphere and the wall, Eq. 2.11 should be revised where R_2 approaches infinity so that the revised conductivity formula is as shown below.

$$\frac{1}{K_{1\mathrm{w}}} = \frac{1}{K_1} + \frac{1}{K_{\mathrm{g}}} \tag{2.13}$$

In this case only K_{g} term needs to be revised.

$$K_{\mathrm{gap}} = 2\pi k_m R_1 \log\left(1 + \frac{R_{12}^2}{2R_1 g}\right) \tag{2.14}$$

Once we define all the conductivity between each sphere, we can obtain effective conductivity of the system based on a widely know FEM approach, direct stiffness method. The detailed algorithm of this method will be further discussed in chapter 6. This conventional RN-model is revised to describe ions transport within MC exposed to a humid environment.

2.5 Conclusions

In this chapter, we have explained the importance and limitations of EMT models to describe transport in complex composite systems. We have explained the appropriate generalization of the EMT models for high-contrast, multi-component, anisotropic systems. For a composite with the inclusion of varies shapes and sizes and packed to the jamming limit or percolation threshold, the EMT model must be replaced by a computationally-efficient random-network model. An important limitation of all these approaches (including the percolation theory) is that it focuses either on drift or diffusive transport. When both are present, a generalized nonlinear percolation model must be used [48]. For example, when water diffusion can cause ions' local diffusivity changes, we need to clarify their correlation between each other, and develop the modeling framework to describe the macroscopic transport characteristic of the ions to predict the reliability.

In the following chapters, the generalized EMT theory and random-network theory will be used to solve a variety of transport problems. In chapter 3 and 4, in order to estimate the effective thermal conductivity of BEOL, modified EMT model due to the anisotropic fillers is used which is shown in section 2.3.3. In chapter 5, effective diffusivity of water molecules function of filler volumetric fraction can be described by the model introduced in section 2.3.1. However, for more general volumetric fraction case, another EMT model is introduced in section 5.2.3. Lastly, for the percolative system, we can adopt the methodology shown in section 2.4, and the more details about effective property calculation based on the direct stiffness method are explained in chapter 6. These EMT models reduce the time and effort when we develop the modeling framework for composite material. Also, EMT models will provide a deep and fundamental new insight regarding the physics of any given composite material. The model can be useful to the initial optimization of a composite system that can lead to the fundamental reconsideration of the design for better performance and reliability.

3. FEOL SELF-HEATING DUE TO TRANSISTORS: THERMAL COMPACT MODEL OF A PACKAGED IC

3.1 Introduction

Transistors and ICs have been scaled down continuously under Moores law to achieve better performance at a lower cost [1, 49]. Scaling of transistors decreases both power dissipation and the intrinsic switching time so that a densely-packed, high-speed circuit can operate with modest self-heating. However, short channel effect (SCE) arising from ineffective gate control makes sustained scaling difficult [50, 51]. The deterioration of the subthreshold swing (SS) increases off-state leakage current (e.g., threshold voltage (V_{TH}) roll-off), with the corresponding increase in the static power dissipation. In order to resolve SCE, the configuration of the transistors has been modified to obtain a good electrostatic control of its channel. Multi-gate (MG) transistor, such as FinFET, gate-all-round (GAA) nanowires (NW) FET, [4, 52], and Floating body structures, such as extremely-thin-silicon-on-insulator (SOI)-FinFET [53] have been introduced and the structures have successfully minimized the SCE.

The introduction of confined geometry, multi-gate transistors has allowed scaling to continue below 20nm-node. Unfortunately, leakage current and V_{TH} have not scaled, therefore there has been a net increase in power density as ICs have become smaller. Thus, temperature rise (ΔT) which is the multiplication between power (P), and thermal resistance (R_{TH}) has become one of the important performance limiters, restricting practical processor frequency (f) to around 4GHz [54]. Self-heating effect (SHE) can have a detrimental effect not only on the performance but also on the reliability, such as Negative Bias Temperature Instability (NBTI), and Hot Carrier Injection (HCI) of a transistor. Let us consider an Arrhenius relationship for diffusion coefficient in solids (D), see Eq. 3.1.

$$D = D_0 e^{\frac{-\Delta H}{kT}} \tag{3.1}$$

where D_0, ΔH, k, and T are the maximum diffusivity at the reference temperature, activation energy, Boltzmann constant, and absolute temperature, respectively. For example, with ΔH=$1eV$, a $30°C$ rise in temperature decreases the diffusivity hundred-fold. Indeed, bond dissociation rates for NBTI and HCI, or diffusivity of Cu atoms that dictate electromigration (EM) cannot be modeled unless transistor SHE is quantified. As the channel length becomes smaller (e.g., sub-20nm), and the channel configuration becomes more confined, SHE increases due to the following reasons. Confined geometry transistors ensure excellent electrostatics, only at the expense of increased R_{TH} very close to the heat source. Furthermore, new high-mobility channels (i.e., SiGe, Ge) [55, 56] and high-K gate dielectrics (i.e., HfO_2) [57] have been developed to increase on-current at lower voltage and to reduce gate leakage, respectively. Unfortunately, high mobility and high-K materials have lower thermal conductivities, which further increase channel R_{TH}. In other words, confined geometry transistors shift the burden of transistor design from electrostatic control to the management/control of thermal effects.

Another crucial issue is the decreasing time constant (τ_{c}) for self-heating. As the channel volume becomes smaller, thermal capacitance (e.g., $C_{\mathrm{TH}} = \rho \cdot c_{\mathrm{P}} \cdot V$, where ρ, c_{P}, and V are the density of the material, specific heat, and volume, respectively) becomes extremely small as well. Consequently, the channel heats up much faster (with the time constant ($\tau_{\mathrm{c}} = R_{\mathrm{TH}} \cdot C_{\mathrm{TH}}$) than it used to for long channel planar transistors. When the slew rate is low, the effect of the small τ_{c} would be negligible, however, when the slew rate is high, the channel may heat up quickly to its steady-state temperature at sub-ns timescale. This thermal time-constant issue must be accounted for sub-20nm high-speed ICs. One group have already introduced the multi τ_{c} concept for 14nm node FinFETs [10]. Indeed, the importance of thermal-aware transistor and circuit designs have been highlighted by many groups to address issues regarding performances, variability, and reliability of confined geometry transistors.

In order to predict the reliability of a fully packaged IC, one must simultaneously consider hierarchical heat dissipation through the transistor channel and contacts, Back End Of Line (BEOL) interconnects, and the package. Many groups have developed tier-specific thermal models, which can neither predict the channel temperature rise (ΔT_{C}) accurately nor suggest innovative strategies to reduce ΔT_{C} by identifying /removing thermal bottlenecks in the hierarchy. Experimental observations from each level may actually mislead and not correlate at all to the actual performance and lifetime of the ICs. For example, the floating-body transistor under DC operation may show severe self-heating. However, the self-heating extracted from the circuit simulation shows that self-heating is negligibly small (below $5°C$), as reported in [58, 59]. When considering the effect of BEOL, the coupled SHE behavior may get worse or better depending on the additionally available heat dissipation paths or Joule heating in BEOL [60]. In short, fragmented focus on isolated components leads to confusing conclusions.

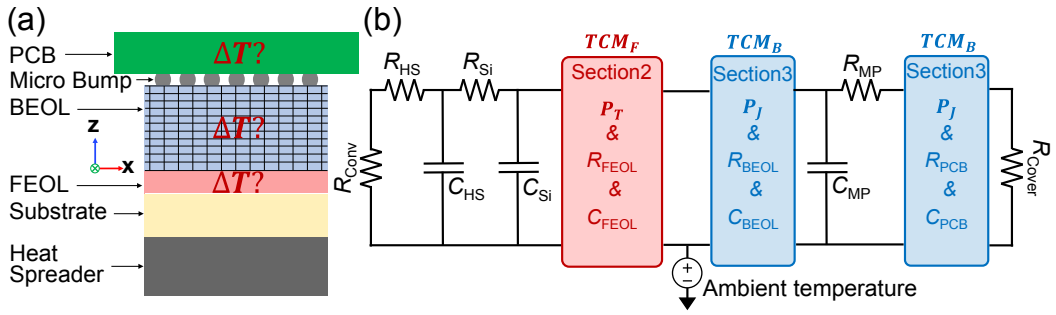

Fig. 3.1. (a) Simple cross sectional schematic of packaged ICs. ΔT information at FEOL, BEOL, and PCB are important for reliability prediction. (b) Thermal network for the new compact model presented in this paper. Specific network configuration for TCM_F, and TCM_B is shown in section 3.2, section 3.4, respectively.

In this chapter, I develop a new physics-based compact model to predict ΔT_{C} for any given device geometry and arbitrary system configuration, see Fig. 3.1. In section 3.2, I refine thermal compact model for font-end-of-line (FEOL) (TCM_F) and all the thermal parameters are extracted by transient 3D FEM simulations. In section

3.3, I investigate the ΔT_{C} in the digital and analog circuits with the revised TCM_F by HSPICE circuit simulations. In section 3.4, I develop thermal compact model for back-end-of-line (BEOL) (TCM_B) in order to investigate self-heated transistors impact on the temperature distribution within BEOL, and system as well. we applied an EMT model to define thermal parameters. Moreover, the model for thermal coupling effects between transistors and BEOL ($\Delta T_{\mathrm{T}\rightarrow\mathrm{B}}$) is developed based on image charge theory. In section 3.5, I discuss how NBTI, HCI, and EM affected by SHE and in section 3.6, I suggest several innovative solutions for each tier to increase the lifetime of ICs.

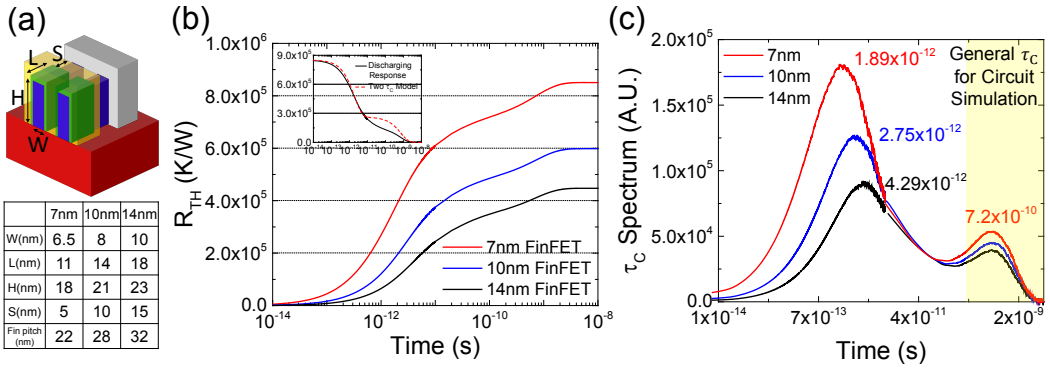

	7nm	10nm	14nm
W(nm)	6.5	8	10
L(nm)	11	14	18
H(nm)	18	21	23
S(nm)	5	10	15
Fin pitch (nm)	22	28	32

Fig. 3.2. (a) 3-D simple schematic of FinFET. Device parameters are obtained from high-performance bulk FinFETs model [61]. (b) Simulated heat source transient response by 3-D COMSOL FEM . (Inset) Discharging transient response which is symmetry to the charging response. 7nm FinFET shows the highest R_{TH}. (c) Differentiated transient responses to extract τ_{c}. 7nm shows the smallest 1st τ_{c} due to its smallest channel size. The τ_{c} spectrum can be obtained as follows: (i) Transfer the response function to the logarithmic time variable. and (ii) Differentiate numerically.

3.2 Revised FEOL thermal compact model

BSIM-CMG simulation [62] has been widely adopted to investigate circuit performance of modern FETs [59, 63]. Unfortunately, previous studies have been based

on a single-τ_c thermal network, which cannot describe the SH in sub-10nm technologies correctly [59], see Figs. 3.2-3.3. In addition, the thermal network used in BSIM-CMG model presumes that heat dissipation occurs either through the BEOL or through the FEOL, although in practice, they must be considered on equal footing. Naturally, therefore the existing BSIM-CMGS model cannot predict the IC-specific, frequency-dependent SHE of sub-10nm transistors correctly.

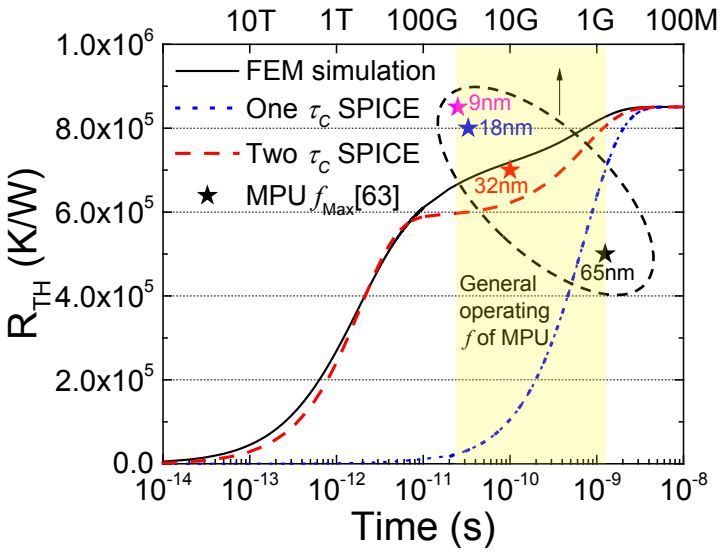

Fig. 3.3. SPICE simulation comparison between one τ_c model, two τ_c model, and transient FEM simulation. As node size becomes smaller than 32nm, one τ_c model would underestimates SHE for high f regime [64]. (inset) Each model thermal network for 7nm FinFETs.

Transient 3D FEM simulations are done to extract R_{TH}, and C_{TH} for any given device geometry by solving the Fourier equation for heat transport. One may argue solving Boltzmann transport equation, or molecular dynamic simulation can be essential in understanding nano-scale heat transport. In this work, however, we performed the simulations based on Fourier equation with size-dependent thermal conductivity for the efficient computation without sacrificing the accuracy [65]. Simulated device parameters are obtained from the PTM high-performance FinFET model [61], see Fig. 2a. For the high fidelity modeling, thermal conductivity is applied from pre-

vious work [66]. For the volumetric heat capacity, we applied bulk property since the nano-scale property is predicted not to change significantly [67]. Figure 3.2b clearly exhibits multi τ_c response associated with the complex transistor geometry (e.g., channel, and confined substrate with isolation oxide). The τ_cs are extracted by differentiating the response function as shown in the Fig. 3.2c. A two-τ_c model provides a satisfactory balance between accuracy and computational efficiency; the third τ_c was not included because it contributes little to self-heating. The SPICE simulation in Fig. 3.3 proves that two-τ_c model describes actual response function better than single-τ_c model, especially for the high f regime ($> 1GHZ$). As heat

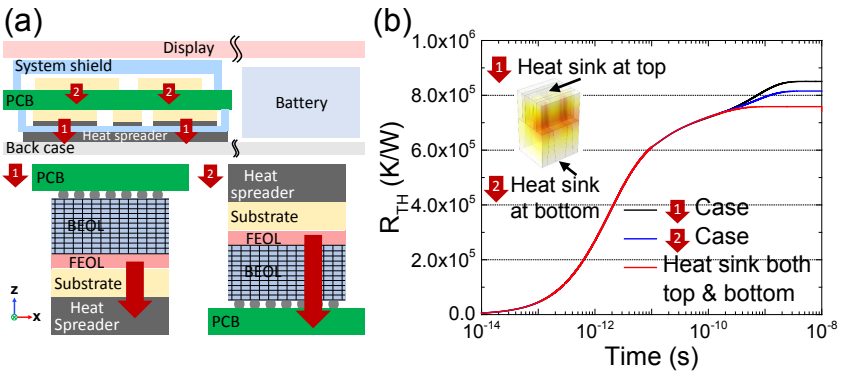

Fig. 3.4. (a) Simple cross sectional schematic of cellphone. Depending on the electronics location, the main heat flux direction can be either through substrate (e.g., #1 case) or through interconnects (e.g., #2 case). (b) Transient simulation for different heat sink locations. Deviation occurs at low f regime meaning 2^{nd} τ_c should be based on different thermal parameters for each case. (inset) Simulated FEM geometry and the location of each heat sink.

can flow through BEOL or substrate, thus we must consider these heat dissipation paths simultaneously, see Fig. 3.4. Depending on the heat sink location, transient response differs significantly at low f, see Fig. 3.4b. However, the responses converge at the high f, indicating that the same R_{TH} dictates SHE regardless of the heat sink location. Our FEM simulation suggests the TCM_F shown in Fig. 3.5a. Extracted parameters for different nodes are summarized in the Fig. 3.5b. For the 7nm node,

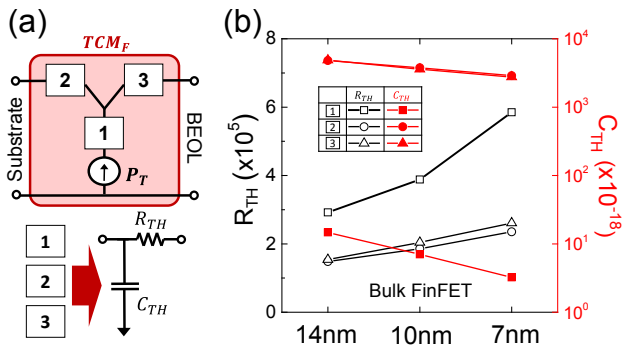

Fig. 3.5. (a) The refined thermal network for FEOL part in Fig. 3.1b. Each # of box has one pair of R_{TH}, and C_{TH}. (b) Extracted thermal parameters for different node sizes. As node size becomes smaller, more confined structure result in smaller C_{TH} and larger R_{TH} for #1 box which is thermal parameters for the channel.

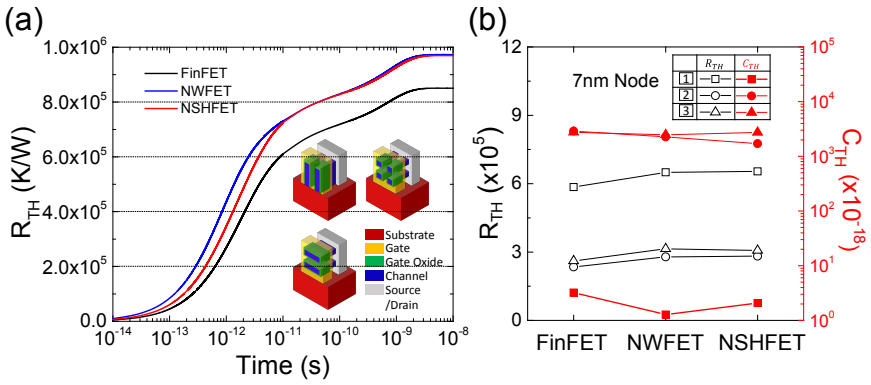

Fig. 3.6. (a) Simulated heat source transient response for different device structures (e.g., FinFET, NWFET, and NSHFET). All devices have same channel width. (inset) Simple 3-D schematic of each device. At the high f, curves are not same due to different channel structure. (b) Extracted thermal parameters for different transistors. For #1 box, NWFET shows the smallest C_{TH} but highest R_{TH} due to the smallest channel volume.

we also extracted R_{TH}, and C_{TH} for FinFET, NWFET, and NSHFET based on the transient responses shown in Fig. 3.6.

3.3 Self-heating in circuits

For static operation, the product of current and drain voltage of a transistor would give us the power dissipated, however, in an actual circuit operation, we need to consider the specific circuit configuration and the sum up the power dissipated in all the transistors. For the circuit simulation, the MG-FET Berkeley Short-channel IGFET Model (BSIM) model which is a physics-based transistor SPICE model is augmented by a thermal circuit – composed of a parallel combination of its R_{TH} and C_{TH} – driven by the power dissipation ($P(t)$) in the transistor. Given the circuit netlists with the specific device technology parameters, we can perform the circuit simulation by HSPICE as shown in Fig. 3.7. Figure 3.8 shows that NWFET has the best electrostatic integrity among the three devices, which reduces the leakage power dissipation in subthreshold regime. Here, we use a 14nm SOI FinFET technology PTM online model [61]. Based on the device parameters (channel length: L_G, fin height: H_{FIN}, fin width: W_{FIN}, fin number: N_{FIN}, fin pitch: F_{pitch}), and extracted thermal parameters by TCM_{F} shown in Sec. 3.2, we can calculate the electro-thermal response of any circuit self-consistently.

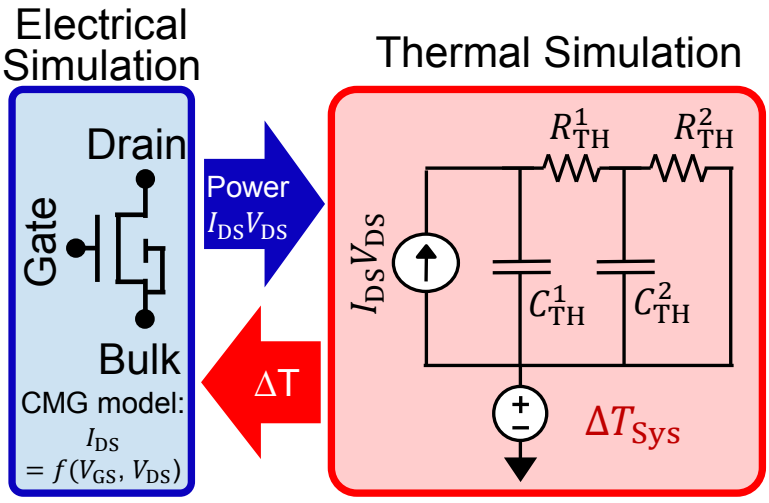

Fig. 3.7. Circuit simulation strategy using modified BSIM-CMG model.

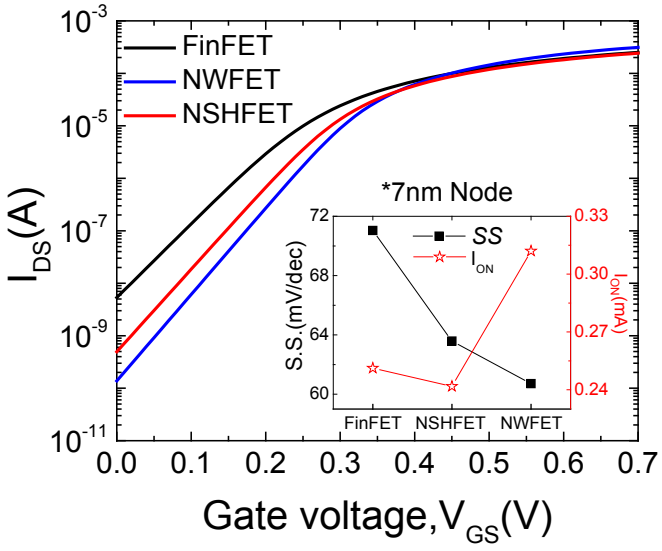

Fig. 3.8. Transfer characteristics of different configurations. (inset) Comparis-on of SS and I_{on} (at V_{DS}=0.7V) for different devices.

3.3.1 Self-heating in digital circuits

For a transistor in a digital circuit, heat is generated only during the switching events (provided the leakage power is negligible). Therefore, we can get the cyclo-stationary solution of the thermal equivalent circuit in the response of pulse power input. The maximum temperature rise at the channel for a certain circuit configuration ($\Delta T_{\text{Cir}}^{\max}$) related to the average temperature rise ($\Delta T_{\text{Cir}}^{\text{avg}}$) shows as follow:

$$\Delta T_{\text{Cir}}^{\max} - \Delta T_{\text{Cir}}^{\text{avg}} = H(f, \xi, \tau) \times (P_{\max} - P_{\text{avg}}(f)) \tag{3.2}$$

$$\Delta T_{\text{Cir}}^{\text{avg}} \equiv \sum_{i=1}^{2} R_{\text{THi}i} \times P_{\text{avg}} \tag{3.3}$$

$$H = R_{\text{TH}} \times \left(\frac{1 - e^{-\frac{\zeta}{f\tau}}}{1 - e^{-\frac{1}{f\tau}}} \right) \times \left(1 - e^{-\frac{(1-\zeta)}{f\tau}} \right) \tag{3.4}$$

$$H = \sum_{i=1}^{2} R_{\text{THi}} \times \left(\frac{1 - e^{-\frac{\zeta}{f\tau_i}}}{1 - e^{-\frac{1}{f\tau_i}}} \right) \times \left(1 - e^{-\frac{(1-\zeta)}{f\tau_i}} \right) \tag{3.5}$$

$$\tau \equiv R_{\text{TH}} \times C_{\text{TH}} \tag{3.6}$$

Here, $H(f, \xi, \tau)$ can be understood as a differential thermal resistance, defined by the signal frequency (f), power duty cycle $\xi \equiv P_{\text{avg}}/P_{\text{max}}$, and thermal time constant (τ). P_{max}, P_{avg} are the peak power and average power in single transistor within a given circuit, respectively. Fig. 3.9 shows the analytical form of H(f) for one-τ_{c} model of various nodes, and device types. In Fig. 3.10, we can find out that NWFET experiences the most serious SHE, even though it has best short-channel performance. As shown in Fig. 3.9, and 3.10, we can use this analytical model to predict the self-heating in a digital circuit and explain the disappearance of excess self-heating ($\Delta T_{\text{Cir}}^{\text{max}}$-$\Delta T_{\text{Cir}}^{\text{avg}}$) in high-frequency digital circuits as well. The analytical model for H(f) (i.e., Eq. 3.5) agrees well with the simulated data, as shown in Fig. 3.11. At typical operating frequencies (few GHz), traditional single-τ_{c} model dramatically underestimates H(f) compared with two-τ_{c} model at high f, so that two-τ_{c} model must be adopted to predict reasonable SHE behavior of sub-10nm devices. Also, BEOL has to be considered for those systems where heat dissipates through the interconnects. SHE behavior of a single transistor varies considerably as we take into account both two-τ_{c} model, and BEOL as shown in Fig. 3.11 (inset). Therefore, FEOL compact model has to be carefully constructed in order to obtain reasonable HSPICE simulation results.

Let us consider a ring oscillator (RO) with a variable number of inverter stages (N_{inv}) loaded by a fixed capacitor (C_{Load}) to represent the fan-out. The oscillation frequency is defined as $f = I_{\text{D}}/\left(C_{\text{Load}} \times V_{\text{DD}} \times N_{\text{inv}} \times 2\right)$, where I_D, and V_{DD} are drain current, and drain voltage, respectively, which means that oscillation frequency decreases with the increasing number of inverter stages. The simulation (symbol) results in Fig. 3.12 shows that the $\Delta T_{\text{Cir}}^{\text{max}}$ increases linearly with oscillation frequency (log x-axis). We can explain this linear increase by comparing each component quantitatively in Eq. 3.2. First, H normalized to R_{TH} (HR_{TH}) is very small and decreases with frequency. Meanwhile, (P_{max}-P_{avg}) reduces with frequency. Thus, the dynamic self-heating ($\Delta T_{\text{Cir}}^{\text{max}}$-$\Delta T_{\text{Cir}}^{\text{avg}}$) is suppressed and $\Delta T_{\text{Cir}}^{\text{max}}$ simply follows $\Delta T_{\text{Cir}}^{\text{avg}}$. Since the $\Delta T_{\text{Cir}}^{\text{avg}}$ is proportional to P_{avg} (e.g.,$\sim C_{\text{Load}} \times V_{DD}^2 \times f/2$), which increases linearly

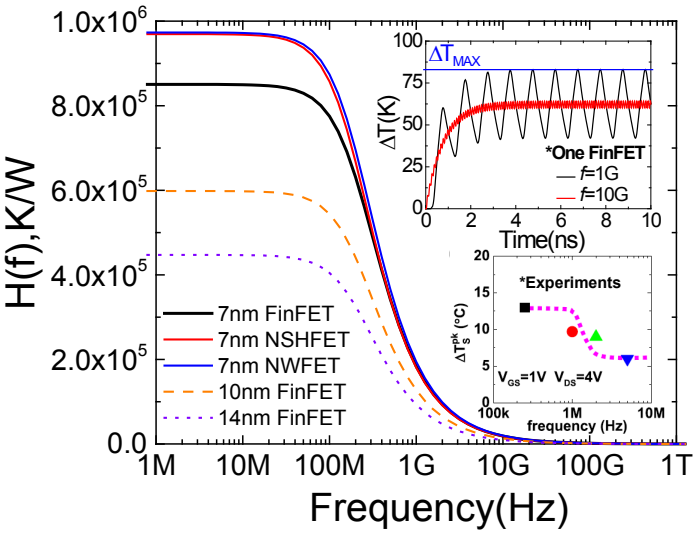

Fig. 3.9. Differential R_{TH} of different transistor types and node sizes for one single transistor. (inset1) ΔT varies with time of one single FinFET for different frequencies. (inset2) Measured electrode surface ΔT function of frequency also shows same trend [59].

with frequency, $\Delta T_{\text{Cir}}^{\text{max}}$ increases linearly with oscillation frequency. If we consider two-τ_c model for the FEOL, $\Delta T_{\text{Cir}}^{\text{avg}}$ increases slightly, however, $\Delta T_{\text{Cir}}^{\text{max}}$ exhibits much higher value than that of one-τ_c model. Considering extremely short τ_c within the channel region, these results are reasonable. Therefore, in the case of sub-20nm ICs, the newly proposed two-τ_c model must be applied to analyze self-heating properly for various confined geometry transistors.

3.3.2 Self-heating in analog circuits

Besides the discussion of self-heating in digital circuits (RO), we also investigated the self-heating in two-stage operational amplifier (2-stage op amp), which is one of the main blocks in a wide range of analog and mixed-signal systems. Considering the lower operating frequency (e.g., lower slew rate) than that of digital circuits and larger device node size, one τ_c for FEOL compact model would suffice for the analysis.

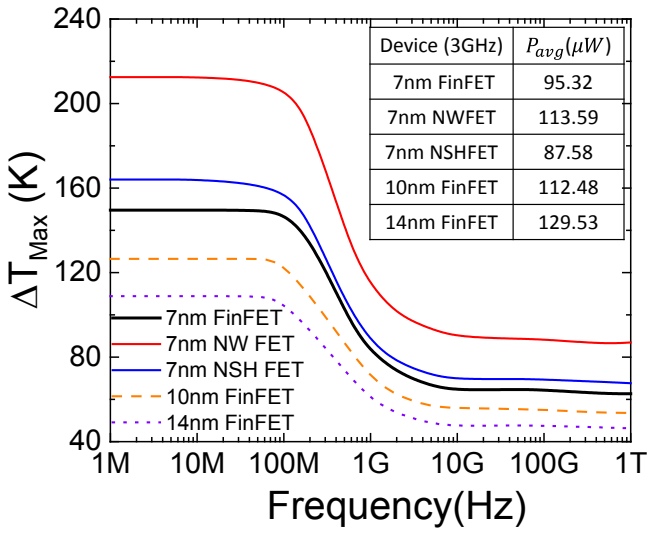

Fig. 3.10. Peak temperature rise (ΔT_{MAX}) varies with frequency for different devices and node sizes. The inset table shows the dissipated P_{avg} at 3GHz for a single transistor.

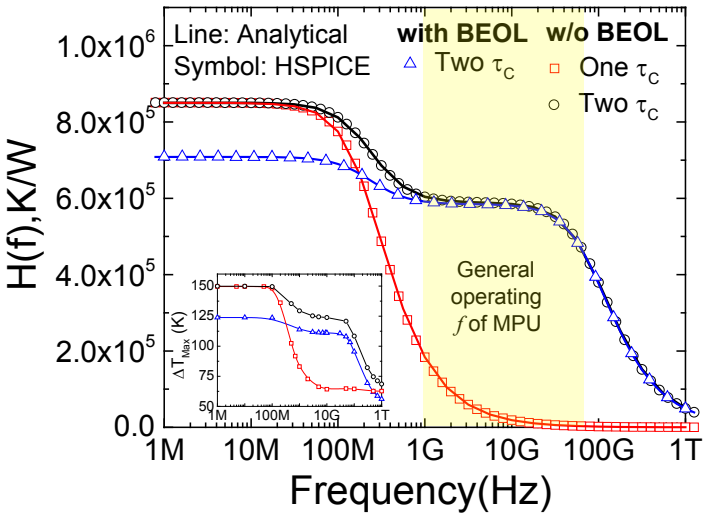

Fig. 3.11. Differential R_{TH} of a 7 nm FinFET using different thermal models. (inset) The ΔT_{MAX}varies with frequency of a single FinFET using different thermal models.

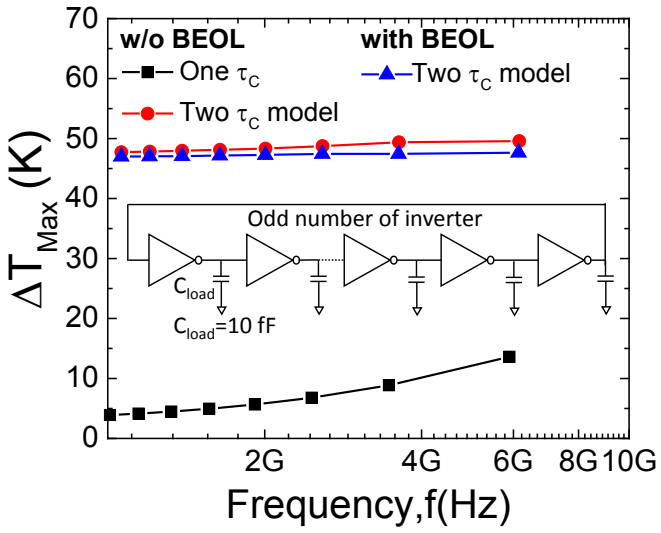

Fig. 3.12. ΔT_{MAX} varies with frequency for the FinFET oscillators using different thermal models. (inset) The schematic of an oscillator made of odd numbers of inverters.

Fig. 3.13a shows the diagram of 2-stage op amp. Because the current mirror (M3 and M4, M8 and M5) is sensitive to short channel effect, we use L_G=1.6,L_{min}=30nm in this circuits design. To achieve high gain, we use N_{Fin}=20 for the differential transconductance stage and N_{Fin}=100 for the high gain stage. The load capacitor (C_L) is 1pF and the compensator capacitor (C_c) is 0.4pF. This circuit is simulated by HSPICE with SHE consideration. The simulation results show that the DC gain (A_{V0}) is 48 dB; unity gain frequency (f_T) is 219 MHz; and the phase margin is 54°.

Given the $V_{\text{in}+} = 0.4 + 5 \times 10^{-4} \sin(120\pi t) V$, we illustrate the self-heating temperature of each transistor in Fig. 3.13b. The total power dissipation in this operating condition is 210.4μW. From these results, we see that the self-heating is negligible (below 4°C.) One reason is that the bias points chosen for an amplifier are typically in saturation region for each transistor. But the V_{GS} typically set to values in the range of 50mV-300mV above V_{TH} to get a high gain [68] leading to a quite low power dissipation in each transistor. Another reason is the adoption of large N_{Fin} devices which have a good thermal cross-section to dissipate heat resulting in small R_{TH}.

Therefore, the self-heating in 2-stage op amp is insignificant. An HSPICE simulation provides many insights regarding self-heating. Indeed, it allows us/one to calculate $\Delta T_{\mathrm{Cir}}^{\mathrm{max}}$ and $\Delta T_{\mathrm{Cir}}^{\mathrm{avg}}$ for any analog or digital circuits. Moreover, the power dissipated (e.g., P_{avg}) can be used as an input for SHE estimation due to thermal coupling from transistors to BEOL ($\Delta T_{\mathrm{T}\rightarrow\mathrm{B}}$) as described in Sec. 4.2.

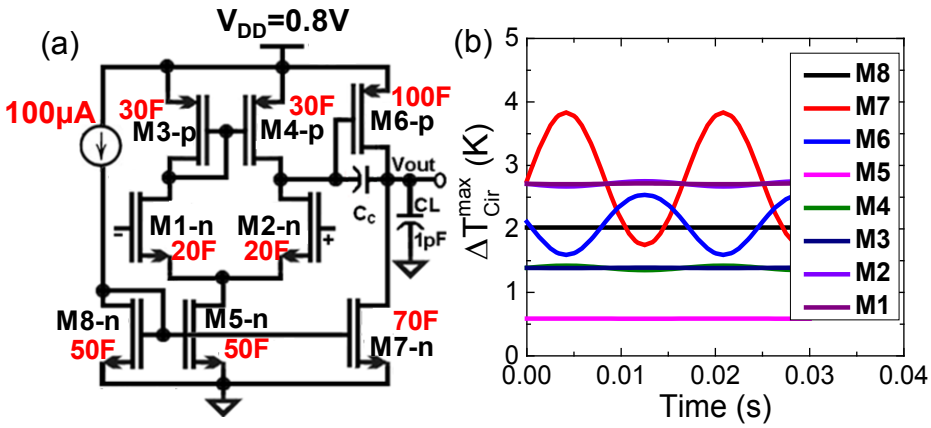

Fig. 3.13. (a) The schematic of two-stage operational amplifier. (b) The self-heating temperature in each transistor.

3.4 BEOL & System modeling methodology

As the final step, we must calculate the thermal resistance and self-heating of BEOL interconnects, and couple them to the self-heating of FEOL transistors to determine ΔT_{C} of a packaged device. Since SHE is determined by the configuration of the surrounding system, assigning correct R_{TH}, and C_{TH} values for BEOL is an important step in the overall self-heating modeling of an integrated circuit.

3.4.1 BEOL modeling method

Spatially-resolved precise prediction of local temperature, $T(x, y, z)$, is essential to evaluate Arrhenius-activated interconnect (e.g., electromigration) and transistor

reliability (e.g., NBTI, HCI, TDDB, etc). 3D Finite Element modeling (FEM) do provide excellent results, but the calculation is too time-consuming for a structure that involves 8 to 10 layers of percolating interconnects, especially for fast turn-around reliability modeling. Here, an analytical model that can quickly/accurately determine $T(x, y, z)$ will reduce the design time of self-heated modern IC.

Given these limitations, we can approach the issue by developing faster alternatives, such as thermal compact models (TCMs) composed of lumped RC networks as shown in Fig. 3.1b. The results do provide a reasonable estimate, provided that the heat-flow is essentially one-dimensional. It is well known, however, that the 1-D heat transfer models are not sufficiently accurate for the regions close to the sources of self-heating, where the direction of the heat flux is not parallel to the z-axis. Moreover, BEOL thermal resistance (R_{BEOL}) and capacitances (C_{BEOL}) are poorly specified because they depend on the complex, and IC-specific interconnects layout. Obviously, one may calculate R_{BEOL} accurately by solving the 3-D heat diffusion equation with distributed power-sources and relevant boundary conditions by FEM simulation, but returning to FEM to calculate TCM parameters defeats the original purpose (i.e., computational efficiency) of the TCM model.

Therefore, several groups have calculated R_{BEOL} by using methods that are more efficient than FEM, but still capture the essential details of the geometry. Various versions of Hotspot [69, 70] predict R_{BEOL} based on Rents rule and distributed thermal resistance and capacitance network. With reasonably detailed information about geometry and material parameters, the predicted temperature distribution and macroscopic heat fluxes compare well with experiments. However, the accuracy of the temperature profiles very close to the heat sources (required for reliability modeling) is not known. The two-step pseudo-isothermal plane model [71] is derived from thermal network composed of metal wire and via to estimates R_{BEOL}. The model is simpler than FEM or Hotspot but lacks flexibility regarding via placement. In this paper, we wish to demonstrate that a new model, based on generalized effective medium theory (EMT) of the BEOL, combines the precision of the FEM model, with

the computational efficiency of the TCM model. Indeed, we find that an even simpler single-parameter-EMT, based only on the image charge theory, often provides $T(x, y, z)$ that compares remarkably well with the experiments and could be sufficient for early-stage reliability prediction at the IC design stage.

This subsection is organized as follows. In Sec. 3.4.1.1, we develop an explicit EMT model to capture thermal anisotropy of BEOL by applying multiple-scattering approach and validate the model by both numerical studies and experiments. In Sec. 3.4.1.2, we show that a simpler EMT model based on the image charge theory predict localized temperature around the heat source, and justify the analytical scheme by numerical simulation and measured temperature profile obtained from industry. Our models suggest new opportunities for the optimization and reliability prediction for emerging microelectronic devices.

3.4.1.1 Effective media theory for BEOL region

An EMT model describes the effective macroscopic properties of a complex, composite material based on a few material parameters and a simple formula. There are many variants of EMT, but the most widely used models are Maxwell-Garnett (MG) and Bruggeman (BG) [31,34]. Given the material properties and relative volume fractions ($\emptyset_i$), the MG and BG models estimate effective properties of a multi-component composite based on mean field theory for (nearly) spherical inclusions embedded in an infinite medium. Isotropic and anisotropic EMT models have long been used in many fields to describe the effective properties of a composite system [72, 73].

The BEOL, however, is a highly anisotropic medium with wires of various lengths percolating through the thermally insulating inter-level dielectrics, one must generalize the classical EMT models to describe this asymmetric system. In this section, I develop an explicit multi-layer EMT model to describe the thermal properties of the BEOL layers. Once we validate the new EMT model for the composite system (i.e., BEOL), we will be able to calculate the TCM parameters (see Fig. 3.1), and

optimize the thermal design of the overall system. To the best of our knowledge, this is the first use of a generalized anisotropic EMT model to describe thermal transport in integrated circuits.

κ_{eff} Calculation by analytical method

The BEOL consists of alternating layers of interconnects and vias. The high-conductivity interconnects help spread heat in the $x-y$ plane, while the vias act as thermal release-points to help diffuse heat in the z-direction as shown in Fig. 3.14(a). Therefore, we must calculate the thermal conductivities of these two regions (interconnect layer vs. via layers) separately, as follows.

(1) Thermal conductivity of the interconnect layers. As mentioned in the Introduction, MG/BG EMT theories cannot describe the interconnect layers, because they assume that the fillers are spherical and have similar radii. Indeed, interconnects in the BEOL consists of metallic lines of various lengths oriented along the $x-y$ plane as shown in Fig. 3.14b. In principle, we can approximate each interconnects segment as an elongated ellipsoid and uses Nans multiple scattering approach (without interface layer) [42] to calculates κ_{eff}, namely,

$$\kappa_{\text{eff}}^{\text{int}} = \kappa_i \frac{1+\emptyset\left[\beta_{xy}\left(1-L_{11}\right)\left(1-f(\theta)\right)+\beta_z\left(1-L_{33}\right)f(\theta)\right]}{1-\emptyset\left[\beta_{xy}L_{11}(1-f(\theta))+\beta_z L_{33}f(\theta)\right]} \tag{3.7}$$

$$f(\theta) = \left\langle \cos^2\theta \right\rangle = \frac{\int \rho(\theta)\cos^2\theta\sin\theta d\theta}{\int \rho(\theta)\sin\theta d\theta} \tag{3.8}$$

$$\beta_{xy} = \frac{\kappa_{\text{m}}-\kappa_{\text{i}}}{\kappa_{\text{i}}+L_{11}\left(\kappa_{\text{m}}-\kappa_{\text{i}}\right)}, \quad \beta_z = \frac{\kappa_{\text{m}}-\kappa_{\text{i}}}{\kappa_{\text{i}}+L_{33}\left(\kappa_{\text{m}}-\kappa_{\text{i}}\right)} \tag{3.9}$$

where κ_{m}, and κ_{i} are the thermal conductivities of the metallic inclusion (e.g., interconnect) and inter-level dielectric, respectively; $\emptyset$ is the volume fraction of the metal; θ is the angle between z-axis and the local axis of the inclusion; $\rho(\theta)$ describes the probability distribution of inclusion orientation; L_{ii} are polarization factor which depends on the shape and the average aspect ratio (a_{r}) of the wire:

$$L_{11} = L_{22} = \frac{a_{\text{r}}^2}{2\left(a_{\text{r}}^2-1\right)} - \frac{a_{\text{r}}}{2\left(a_{\text{r}}^2-1\right)^{3/2}}\cosh^{-1}a_{\text{r}} \tag{3.10}$$

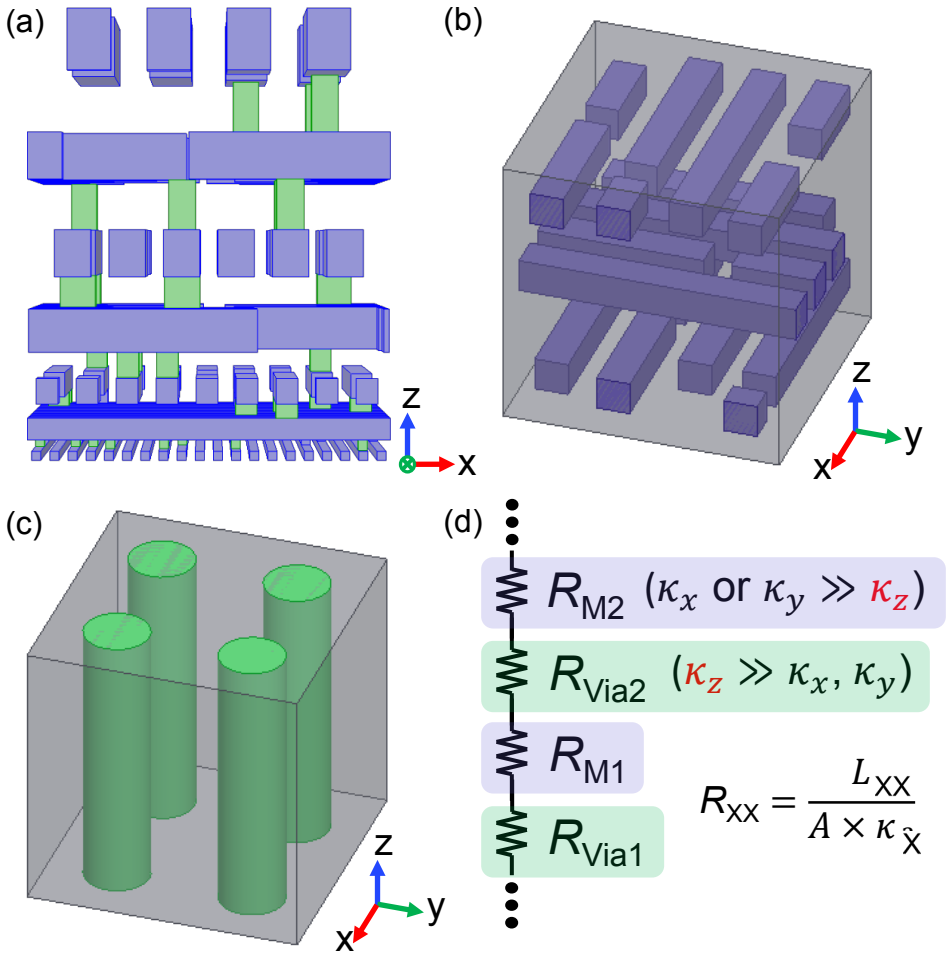

Fig. 3.14. (a) An illustrative example of BEOL configuration. Blue wires are metal interconnects, while green wires (via) connect neighboring layers. (b) The κ_{eff} of the interconnect lines are described by Nan model, and (c) κ_{eff} of the via layers (green) are described by Hart equation. (d) The ($\kappa_{\text{eff}}^{\text{BEOL}}$) for the entire system is calculated by summing over the κ_{eff} of various layers.

$$L_{33} = 1 - 2L_{11} \tag{3.11}$$

Here, $a_r \equiv a_3$(length of the wire)/a_1(height of the wire). Fig. 3.14b shows that interconnect lines are always oriented perpendicular to z-axis (i.e.,f(θ)=0), so that Eq.3.7 is simplified to:

$$\kappa_{\text{eff}}^{\text{int}} = \kappa_{\text{i}} \cdot \frac{1 + \emptyset\left[\beta_{xy}\left(1 - L_{11}\right)\right]}{1 - \emptyset\left(\beta_{xy} L_{11}\right)} \tag{3.12}$$

In order to calculate L_{11}, we must determine the average a_{r} from wire length distribution (a_3) at each metal level because each layer consists of wires of different lengths. This information can be obtained either from IC interconnect layout or from Rents rule based on input and output terminal numbers, total gate number, fan-out, etc. [74]. As a result, the effective length of anisotropic fillers will be varied for different interconnect level. With given filler geometry information (e.g., $\emptyset$, a_{r}, κ_{i}, and κ_{m}), we can calculate $\kappa_{\mathrm{eff}}^{\mathrm{int}}$ as a function of interconnect volume fraction. For high-fidelity modeling, we should not use bulk thermal conductivity for κ_{i}, and κ_{m}. Rather, these values must be determined carefully by considering cross-sectional area and various scattering mechanisms at the surface and within the wire [75].

(2) Thermal conductivity of the via layer. Unlike the interconnects region, vias are oriented in the z-direction as shown in Fig. 3.14c. With $\theta = 0\,(\langle\cos^2\theta\rangle = 1)$, Eq. 3.7 reduces to Hart equation [76], as follows

$$\kappa_{\mathrm{eff}}^{\mathrm{via}} = \kappa_{\mathrm{m}} \cdot \emptyset_{\mathrm{via}} + \kappa_{\mathrm{i}} \cdot (1 - \emptyset_{\mathrm{via}}) \tag{3.13}$$

where κ_{m}, and κ_{i} is thermal conductivity of via, and inter dielectric, respectively, and $\emptyset_{\mathrm{via}}$ is the volumetric fraction of the vias in the layer with vias.

(3) Combined Thermal conductivity. Based on Nan model for interconnect-layer and Hart equation for the via-layer, we can calculate κ_{eff}, and thermal resistance ($(R_{\mathrm{TH}} = L/\,(A \cdot \kappa_{\mathrm{eff}}))$) for every layer within the backend with the geometric information (e.g., thickness, κ_{m}, and κ_{i}). By summing up R_{TH} in series, we can obtain a single κ_{eff} of the total system ($\kappa_{\mathrm{eff}}^{\mathrm{BEOL}}$) as shown in Fig. 3.14d. If we assume uniform area for all the layers in BEOL, $\kappa_{\mathrm{eff}}^{\mathrm{BEOL}}$ can be obtained by Eq. 3.14.

$$\kappa_{\mathrm{eff}}^{\mathrm{BEOL}} = \left[\sum_{n=1}^{M}\left(\frac{L_{\mathrm{n}}^{\mathrm{via}}}{\kappa_{\mathrm{effn}}^{\mathrm{via}}} + \frac{L_{\mathrm{n}}^{\mathrm{int}}}{\kappa_{\mathrm{effn}}^{\mathrm{int}}}\right)\right]^{-1} \times L_{\mathrm{total}} \tag{3.14}$$

where M is the total number of interconnect layers, L_{total} is total thickness of the BEOL. $L_{\mathrm{n}}^{\mathrm{via}}$, and $L_{\mathrm{n}}^{\mathrm{int}}$ are height of via, and height of interconnect for each particular level n, respectively. Similarly, $\kappa_{\mathrm{effn}}^{\mathrm{via}}$ and $\kappa_{\mathrm{effn}}^{\mathrm{int}}$ are calculated κ_{eff} by Hart eq. and Nan model for each particular interconnect layer n, respectively. In the following section,

we will refer to this model as generalized multi-layer EMT (or, *gml*-EMT). The parameters of *gml*-EMT are easily obtained from routinely-available BEOL design information, therefore $\kappa_{\text{eff}}^{\text{BEOL}}$ in Eq. 3.14 is obtained without complex simulation or time-consuming experiment. Let us validate the *gml*-EMT model by numerical simulation and experimental data.

Effective Thermal Conductivity by FEM Simulation

To calculate $\kappa_{\text{eff}}^{\text{BEOL}}$ by FEM simulation, we use the following algorithm. (i) For given via and interconnect volume fractions, a BEOL configuration is synthesized by randomly distributing interconnects and vias within the BEOL; (ii) relevant material properties are assigned to respective regions; ; (iii) heat diffusion equation is solved using a 3D commercial simulator, COMSOL. The boundary conditions are: thermally insulated side-edges, a constant heat flux source at the bottom plane, the temperature at the top plane set to 0K; and finally (iv) $\kappa_{\text{eff}}^{\text{BEOL}}$ is calculated by taking ratio of volume averaged heat flux and spatially averaged thermal gradient, see Eq. 3.15.

$$\kappa_{\text{eff}}^{\text{BEOL}} \left[\frac{W}{K \cdot m}\right] = \frac{\iiint J_{\text{Heat}} dV [W \cdot m]}{\iiint \nabla T dV \, [m^2 \cdot K]} \tag{3.15}$$

For each volume fraction, 10 different random configurations of interconnects/vias are simulated. The a_{r} value for each interconnect layer was chosen to be consistent with typical wire length distribution of modern ICs.

Numerical Validation of the *gml*-EMT model

As an illustrative validation, let us fix $\emptyset_{\text{via}}$ to 2.3% and calculate $\kappa_{\text{eff}}^{\text{FEM}}$ by FEM simulation, for $\emptyset_{\text{m}}$ ranging 14.1 to 32% as shown in Fig. 3.15a. Fig. 3.15c shows that increasing $\emptyset_{\text{m}}$ improves $\kappa_{\text{eff}}^{\text{FEM}}$, as expected. We find the *gml*-EMT model (Eq. 3.14) anticipates the FEM results very well. Even for unrealistically high $\emptyset_m \sim 32\%$, the results differ by less than 15%, as shown in Fig. 3.15b. Note that MG-theories underestimate κ_{eff} by a factor of two, and would, therefore, predict unrealistically high

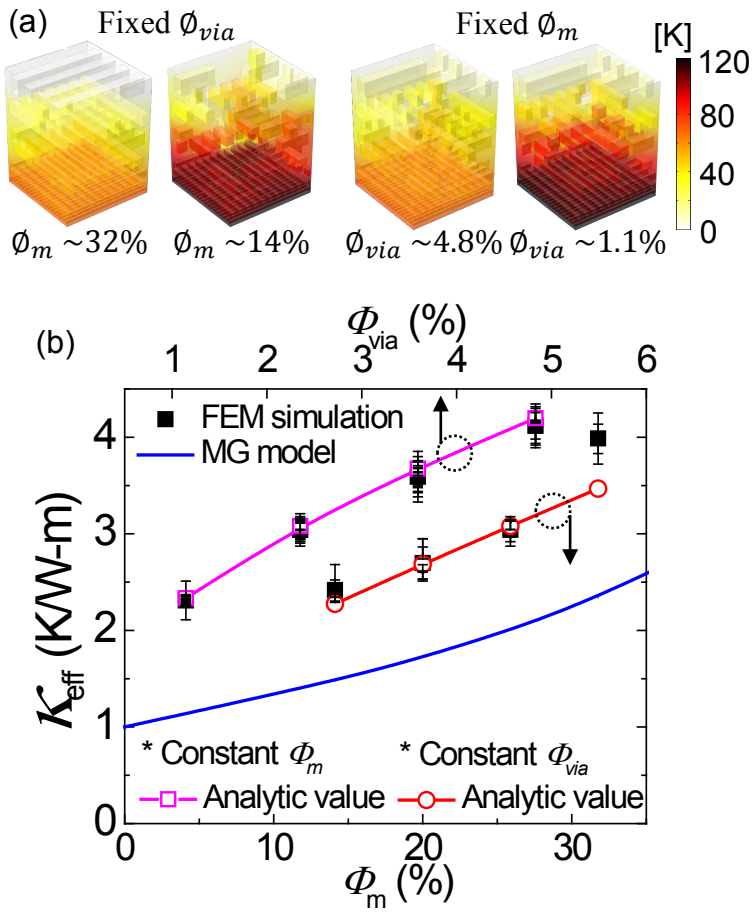

Fig. 3.15. (a) $T(x, y, z)$ profile by COMSOL simulation when $\emptyset_{\text{via}}$ is fixed, $\emptyset_{\text{m}}$ is (Left) 32% (Right) 14% (b) $T(x, y, z)$ profile by COMSOL when $\emptyset_{\text{m}}$ is fixed, $\emptyset_{\text{via}}$ is (Left) 4.832% (Right) 1.145% (c) Comparison between numerical simulation and explicit EMT model for $\kappa_{\text{eff}}^{\text{BEOL}}$ estimation. FEM simulation matches well with the *gml*-EMT model for all cases. The traditional MG-EMT model fails to reproduce the complex via/interconnect dependent conductivity.

BEOL temperature and pessimistic reliability. $\kappa_{\text{eff}}^{\text{BEOL}}$ increases with $\emptyset_{\text{m}}$, therefore larger $\emptyset_{\text{m}}$ helps reduce the temperature of the ICs.

For a second illustrative validation, let us fix $\emptyset_{\text{m}}$=23.5%, and change $\emptyset_{\text{via}}$ from 1 to 5%. Figure 3.15a shows temperature profile comparison between 1.1%, and 4.8% $\emptyset_{\text{via}}$ cases since vias act as thermal release points, $\kappa_{\text{eff}}^{\text{FEM}}$ increases rapidly even for a small increase in $\emptyset_{\text{via}}$, for example, a 4% increase in $\emptyset_{\text{via}}$ increases $\kappa_{\text{eff}}^{\text{BEOL}}$ by a

factor of 2 as shown in Fig. 3.15b. Since the *gml*-EMT model captures $\kappa_{\text{eff}}^{\text{BEOL}}$ the dependencies on $\emptyset_{\text{m}}$ and $\emptyset_{\text{via}}$ very well, in the next section we will compare the results to the experimental data.

Validation by experiments

(1) I_{rms} **measurements.** The *gml*-EMT model is validated by experimental I_{rms} measurements. The measured sample is composed of several types of inter-level dielectric (e.g., κ_{i}=1 A.U.) and copper interconnect lines, assembled on top of a Si substrate. The substrate is grounded electrically and thermally. Obviously, overall thermal resistance R_{TH} is dictated by the distance of the interconnect line from the bottom of the substrate. The measurement and simulation of I_{rms} involve the following steps: (i) Fix the substrate temperature and increase I_{rms} until the test line temperature (ΔT_{test}) increases by $5°C$. ΔT_{test} is determined by measuring the resistance increase of a test line, see Eq. 9.

$$R = R_0 \left[1 + \alpha \left(T - T_0\right)\right] \tag{3.16}$$

where T_0, R_0, and α are reference temperature, reference resistance, and temperature coefficient of resistance, respectively. For the same size (e.g., height, and width) test lines, I_{rms} is reduced as the test-line recedes further from the heat-sink as shown in Fig. 3.16a, because the increasing R_{TH} requires smaller $P = I_{\text{rms}}^2 R$ to increase the temperature ΔT by the same amount. (ii) Next, we calculate $\kappa_{\text{eff}}^{\text{BEOL}}$ based on *gml*-EMT model. Once the thermal resistance is known, we can extract I_{rms} (e.g., open symbols in the Fig. 4) when the temperature rise is $5°C$. The measured and extracted I_{rms} are in excellent agreement (within 5%) for two completely different BEOL stack configurations as shown in Fig. 3.16a, and 3.16b, suggesting the validity of the *gml*-EMT approach.

(2) κ_{eff} **extraction.** From the I_{rms} measurements, we calibrated κ_{eff} of each layer of a BEOL samples involving few interconnect layers (crosslinked by via). The extraction proceeds as follows: (i) First, based on the measured I_{rms} which results in

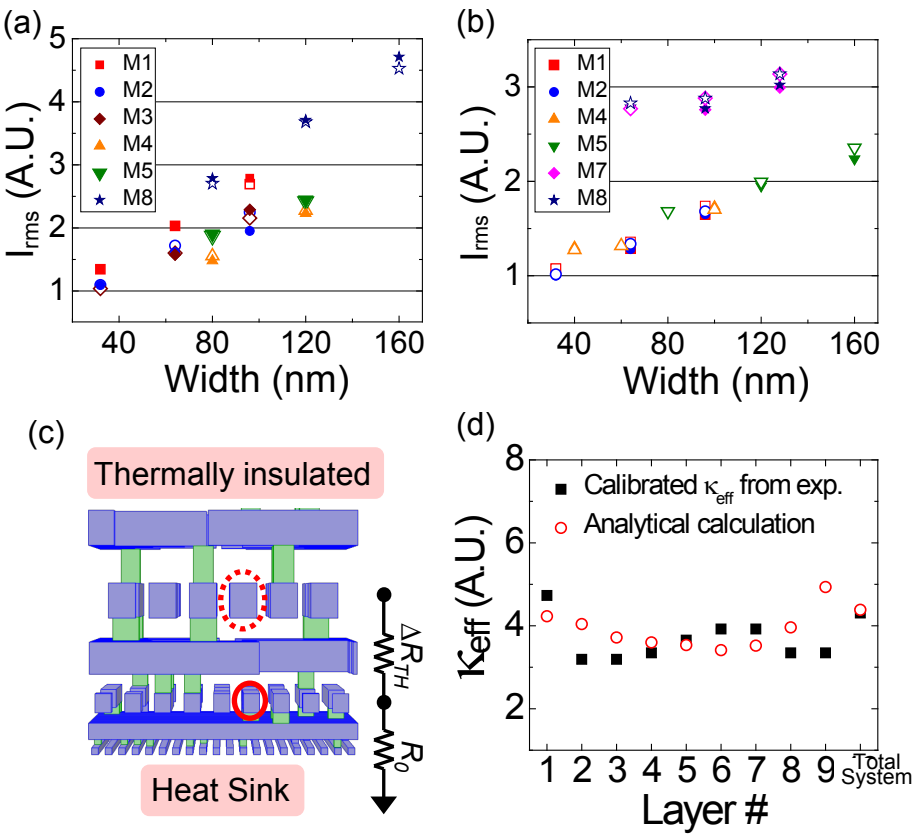

Fig. 3.16. (Solid symbol) Measured I_{rms} for the test lines, (Open symbol) calculated I_{rms} based on $\kappa_{\text{eff}}^{\text{BEOL}}$ predicted by explicit EMT model (a) 1st sample (b) 2nd sample. (c) Simple schematic of the experimental set up to extract κ_{eff} between two targeted test lines. (d) Comparison between calculated κ_{eff} by *gml*-EMT model and experimentally measured value.

ΔT_{test} $5°C$, we calculate the power dissipated, $P = I^2 R_{\text{test}}$; (ii) next we calculate the resistances (R_{i}) of various i-th neighboring line with as small a current as possible, so that the self-heating of these sensor lines can be neglected. The corresponding T_{i} is obtained by Eq. 9. Extract $\Delta R_{\text{TH,i}}$ ($T_{\text{test}} - T_{\text{i}} = P \cdot \Delta R_{\text{TH,i}}$); (iii) Finally, we extract κ_{eff} between two test lines ($\kappa_{\text{eff}} = L/(A \cdot \Delta R_{\text{TH}})$). For this sample, we find $\kappa_{\text{eff}}^{\text{expt}}$ is 4.31W/K-m and calculated $\kappa_{\text{eff}}^{\text{BEOL}}$ by explicit EMT model is 4.38W/K-m (1.786% error) as shown in Fig. 3.16b.

Although the *gml*-EMT prediction compares remarkably well with the experimental results, it is important to understand the assumptions clearly so that the model can be refined further. First, an EMT model does not capture highly localized anisotropic structure (i.e., Through Silicon Via, TSV), so that thermal conductivity may deviate significantly from κ_{eff} for structures containing these localized structures [77,78]. This issue can be dealt by specifying highly asymmetry region separately before estimation. If our targeted transistor or BEOL is within a highly anisotropic region, we can apply EMT model distinctly for that specific region and then integrate the respective regions using a network model for thermal conductivities. Second, sensors located at different points of the same structure may register slightly different temperatures, and therefore the experimental results for κ_{eff} may differ somewhat as well. In other words, due to the anisotropic structure of BEOL, the extracted κ_{eff} cannot be exactly the same for different sensing location. For the reasonable macroscopic κ_{eff} for the modeling, this issue is resolved by placing multiple sensors at different locations and then averaging over the extracted κ_{eff}. Although small deviation exists between experiments and our model, explicit EMT model would be still a good approach to predict macroscopic scale $\kappa_{\text{eff}}^{\text{BEOL}}$ for total system level thermal design of ICs.

It is important to realize that *gml*-EMT provides layer-by-layer κ_{eff} and R_{TH}, as shown in Fig. 3.14d. Once the aspect ratio (a_{r}) and interconnect cross-section of the lines are specified, one can determine the $T(x, y, z)$ throughout the system, as demonstrated by the results in Fig. 3.15 and 3.16. Often, however, the κ_{eff} does not vary significantly from layer-to-layer. In that case, it is unnecessary to spatially resolve the thermal conductivities. Instead, a single κ_{eff}, coupled with the image charge theory, produces comparable results and may often be preferred for initial reliability estimates. In other words, image charge model can be viewed as a single-parameter approximation of the *gml*-EMT model that gives excellent estimates as discussed in the following section.

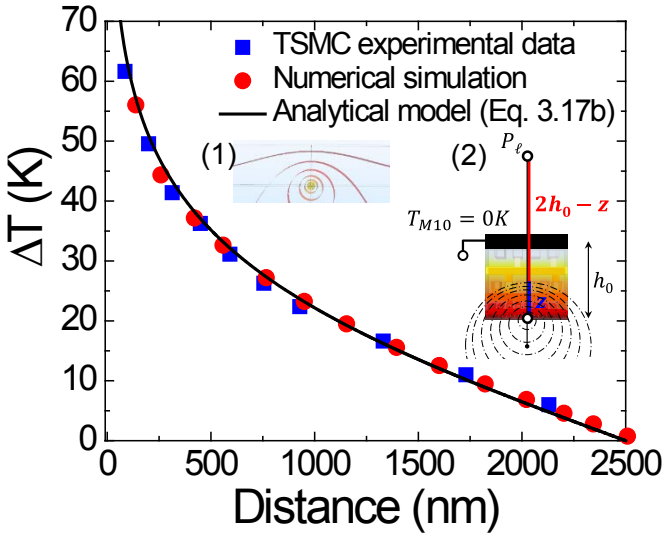

Fig. 3.17. A comparison among experimental data, the analytical model, and FEM simulation. (inset1) Equipotential temperature surface can be predicted by FEM simulation. (inset2) Equipotential temperature surface can be predicted by image charge theory.

3.4.1.2 Localized temperature calculation

Let us assume that a row of self-heated transistors (cross-sectional area, a) serves as a power source (P_{T}, W/m) for the BEOL interconnect stack of thickness, H. The BEOL stack is thermally grounded at the top-interface. The thermal flux lines from the heat-source will terminate at the thermal ground vertically, so that the equi-temperature profiles can be calculated in analogy to a line charge suspended over a conducting plane as shown in Fig. 3.17, insets 1 and 2. In other words, temperature intensity, as a function of z, is given by:

$$\Delta T^{\mathrm{1D}}_{\mathrm{T\to B}}(z) = \frac{-P^{\mathrm{point}}_{\mathrm{avg}}}{4\pi\kappa^{\mathrm{BEOL}}_{\mathrm{eff}}}\left(\frac{1}{\sqrt{(z-2H)^2}} - \frac{1}{\sqrt{z^2}}\right) \tag{3.17a}$$

$$\Delta T^{\mathrm{2D}}_{\mathrm{T\to B}}(z) = \frac{-P^{\mathrm{\ line}}_{\mathrm{avg}}}{2\pi\kappa^{\mathrm{BEOL}}_{\mathrm{eff}}}\ln\left(\frac{Z}{2H-z}\right) \tag{3.17b}$$

Given the thickness of the BEOL layer (H), $P^{\mathrm{\ point}}_{\mathrm{avg}}$ (i.e., 1D heat source), or $P^{\mathrm{\ point}}_{\mathrm{avg}}$ (i.e., 2D heat source, series of transistors) and calculated $\kappa^{\mathrm{BEOL}}_{\mathrm{eff}}$ from a single-parameter

gml-EMT model, the temperatures of various metal lines are fully specified as shown in Fig. 3.17. The temperature drops non-linearly close to the heat source. Remarkably, this simple formula contains the full complexity of the BEOL interconnect structure!

Numerical Validation by FEM modeling

To validate Eq. 3.17 numerically, we once again use a cube containing interconnects with the same average a_{r} and $\emptyset_{\mathrm{m}}$ (as in Fig. 3.14), but now heat the cube from the bottom with a line heat source (e.g., P_{T}=1000W/m). Given the same boundary condition, the analytical results and the FEM simulations agree very well. Finally, the analytical and numerical results are confirmed by comparing against with experimental data, based on identical test structures [79]. Interestingly, the comparison also allows an empirical estimate of $\kappa_{\mathrm{eff}}^{\mathrm{BEOL}}$ through Eq. 3.18, necessary for all subsequent performance and reliability calculations.

3.4.2 Thermal coupling of FEOL and BEOL compact models

Once we know the geometric size, thermal conductivity, boundary conditions (e.g., Fig. 3.18a), and power-dissipated in each interconnect layer, we can construct a thermal network (TCM_{B}) as shown in Fig. 3.1b. In particular, the BEOL region can be modeled by *gml*-EMT described in Sec. 3.4.1. If the lateral dimension of an IC is significantly larger than its thickness (e.g., $L_{\mathrm{Chip}} > t_{\mathrm{Chip}}$), we may use 1-D heat transfer model to calculate the thermal performance of the system [80, 81]. Figure 3.18cc shows an example of location-specific temperature rise in the system level (ΔT_{Sys}) (i.e., T_{HS}, T_{FEOL}, $T_{\mathrm{PCB}}^{\mathrm{Bot}}$, $T_{\mathrm{PCB}}^{\mathrm{Mid}}$, and $T_{\mathrm{PCB}}^{\mathrm{Top}}$ as shown in Fig. 3.18c) transient response calculated by SPICE simulation. Once the ambient temperature (T_{amb}) is specified, $\Delta T = T_{\mathrm{amb}} + \Delta T_{\mathrm{Sys}}$ can be predicted for any location within an ICs.

The Flowchart in Fig. 3.19a summarizes our approach to calculate SHE of an IC. Indeed, ΔT_{C} can now be predicted by coupling the three models, only at a fraction

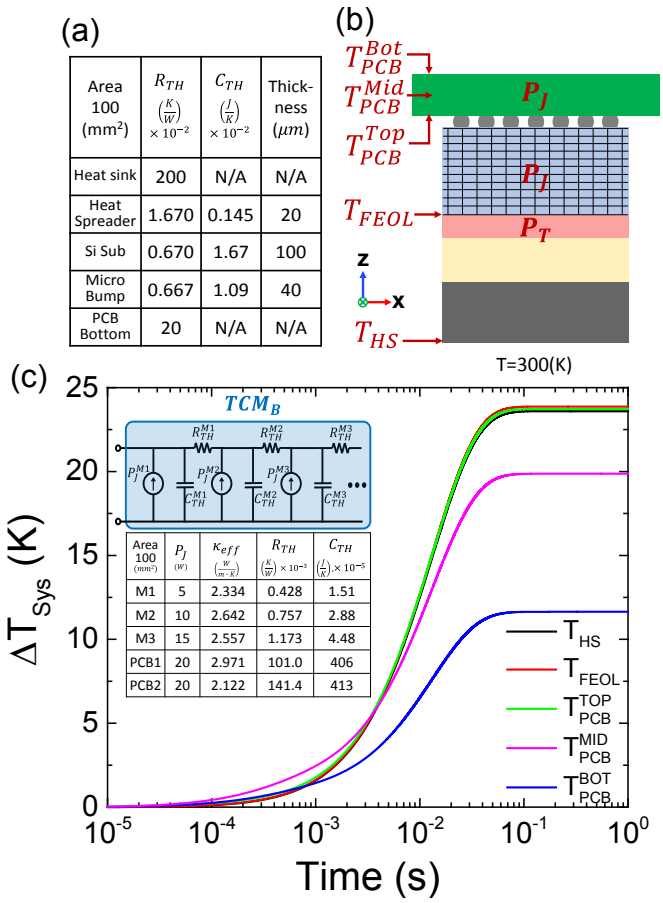

Area 100 (mm²)	R_{TH} $\left(\frac{K}{W}\right)$ $\times 10^{-2}$	C_{TH} $\left(\frac{J}{K}\right)$ $\times 10^{-2}$	Thick-ness (μm)
Heat sink	200	N/A	N/A
Heat Spreader	1.670	0.145	20
Si Sub	0.670	1.67	100
Micro Bump	0.667	1.09	40
PCB Bottom	20	N/A	N/A

Area 100 (mm²)	P_J (W)	κ_{eff} $\left(\frac{W}{m \cdot K}\right)$	R_{TH} $\left(\frac{K}{W}\right) \times 10^{-3}$	C_{TH} $\left(\frac{J}{K}\right) \times 10^{-5}$
M1	5	2.334	0.428	1.51
M2	10	2.642	0.757	2.88
M3	15	2.557	1.173	4.48
PCB1	20	2.971	101.0	406
PCB2	20	2.122	141.4	413

Fig. 3.18. (a) A summary of heat sink and other system thermal parameters. (b) A simple cross sectional schematic of packaged ICs and definition of various location-specific temperature are shown. (c) Simulated transient response due to BEOL, and PCB Joule heating. (inset) The integrated thermal network for BEOL and PCB.

of the computational cost associated with FEM simulations for thermal parameters extraction. With same system configuration and the amount of power dissipation, ΔT distribution within an IC is compared between FinFET and planar MOSFET, see Fig. 3.19b. Based on our model above, it is easy to see that confined geometry transistors would suffer from significant SHE. In the following section, we investigate several strategies for suppressing SHE.

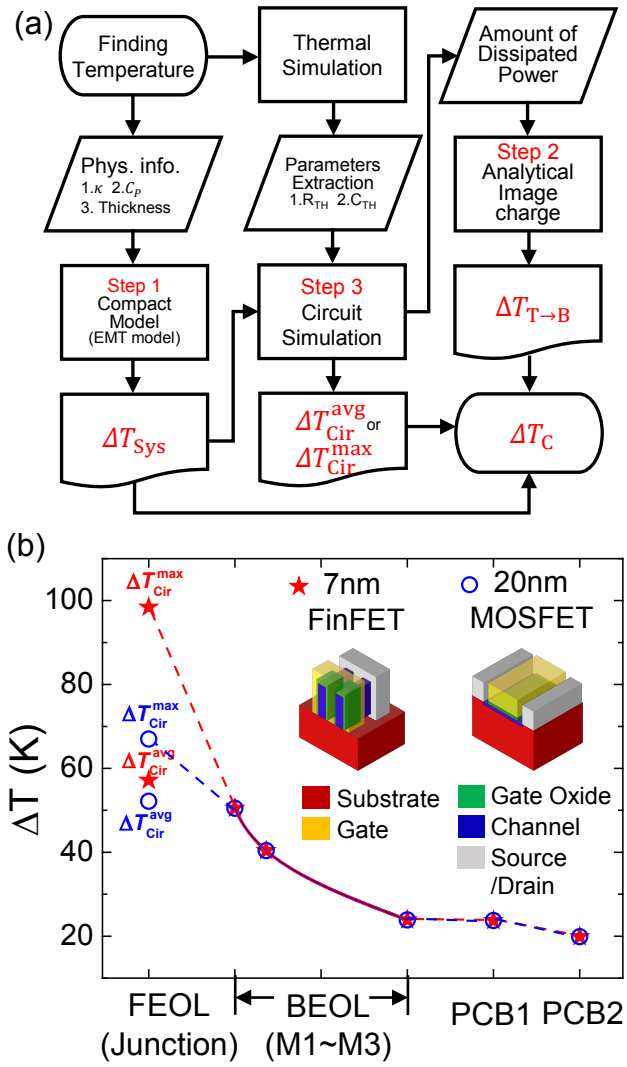

Fig. 3.19. (a) The flow chart describes how compact model for various layers are developed and integrated to determine the channel temperature T_{C} of an IC. T_{C} determines the IC lifetime. (b) $T(x, y, z)$ comparison between 7nm FinFET and 20nm MOSFET when P_{avg} is assumed to be same. 20nm MOSFET shows less $\Delta T_{\mathrm{Cir}}^{\mathrm{avg}}$ than that of 7nm FinFET due to smaller R_{TH}, and similar $\Delta T_{\mathrm{Cir}}^{\mathrm{max}}$ to $\Delta T_{\mathrm{Cir}}^{\mathrm{avg}}$ at 3GHz frequency due to longer τ_{c}.

3.5 Thermal-aware design strategies

3.5.1 BEOL strategies to reduce SHE

For the BEOL, increasing vias volumetric fraction can be a good strategy for SHE mitigation. Fig. 3.15b shows that even a small increase in via volume fraction

increases $\kappa_{\text{eff}}^{\text{BEOL}}$ considerably. The effects of more via volumetric fraction ($\emptyset_{\text{via}}$) on SHE are compared in Fig. 20b. If we increase $\emptyset_{\text{via}}$ from 3% (e.g., 100%) to 9% (e.g., 300%), so as $\kappa_{\text{eff}}^{\text{BEOL}}$ increases, $\Delta T_{\text{T}\rightarrow\text{B}}$ in the vicinity of self-heated transistor reduces by $10°C$, see Eq. 3.18. Even if temperature reduction may be modest, it will enhance the electromigration lifetime of the M1 level dramatically!

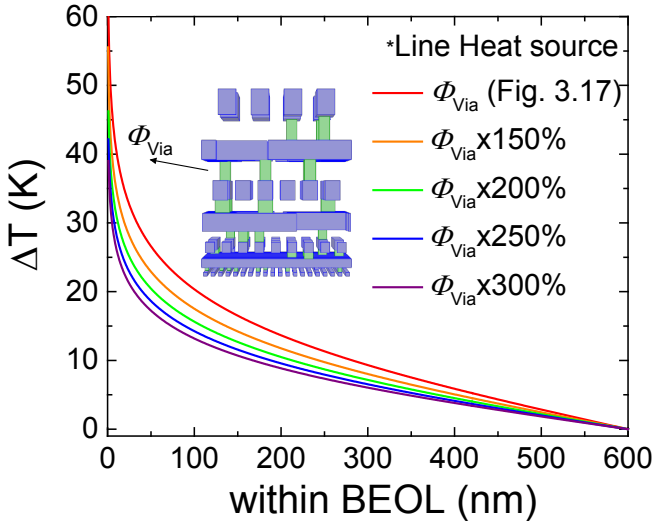

Fig. 3.20. Dummy vias volume impact on $\Delta T_{\text{T}\rightarrow\text{B}}$ distribution within BEOL. (inset) Illustrative example of BEOL, green regions are vias.

3.5.2 PCB strategies to reduce SHE

Researchers at Qualcomm has recently suggested the use of a PCB-embedded heat spreader layer (i.e. an electrically passive Cu plate) to suppress SHE of an IC [82]. Figure 3.21b (inset) shows that the Cu plate must be sufficiently thick to have any noticeable impact on IC temperature. We can use the analytical model described in [83] to investigate the relationship between Cu plate thickness and spreading area at the ICs interface as shown in Fig. 3.21a. The boundary condition for heat dissipation depends on the application (i.e., convection for mobile application, fixed temperature

for forced cooling in desktop applications, etc). In this work, spreading area of heat flux within Cu plate is calculated when the boundary condition at bottom of the plate is assumed to be natural convection (e.g., h=10W/ (m^2K), where h is heat transfer coefficient). If the heat source (e.g., IC) cross-sectional area is $100mm^2$, a 10μm thick Cu plate makes heat dissipation area at the bottom of Cu plate $1285mm^2$ so that convective R_{TH} (e.g., $1/(h \cdot A)$) at the plate bottom surface will be reduced by 10% due to a factor of 10 increase in A. Figure 3.21b shows that even with this small change in convective boundary condition, the thermal transient with Cu plate reduces dramatically (almost by 60%) than that of Fig. 3.18c, highlighting the necessity and importance of thermal management for modern high-performance ICs.

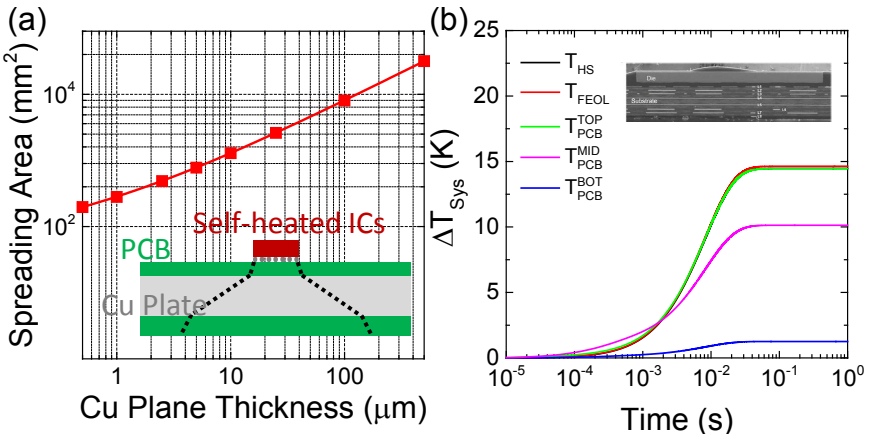

Fig. 3.21. (a) Calculated spreading area depending on Cu plate thickness based on spreading R_{TH} theory [43] (b) Transient response when 10μm Cu plate is inserted. (inset) Cross-sectional view of the PCB with Cu plate [42].

3.6 Implication for IC reliability

Based on the compact model introduced here, we can predict temperature distribution for any given ICs. Even a small increase in ΔT_{C} reduces IC reliability significantly because the degradation processes are often characterized by Arrhenius

activation. Below, we study the temperature and the lifetime relationship for each degradation mode.

3.6.1 Transistors reliability: NBTI & HCI

As the device dimensions scale below 20nm, SHE behavior differs considerably compared to conventional planar devices, so that degradation parameters for various FEOL degradation modes (i.e., NBTI, and HCI) must be carefully investigated.

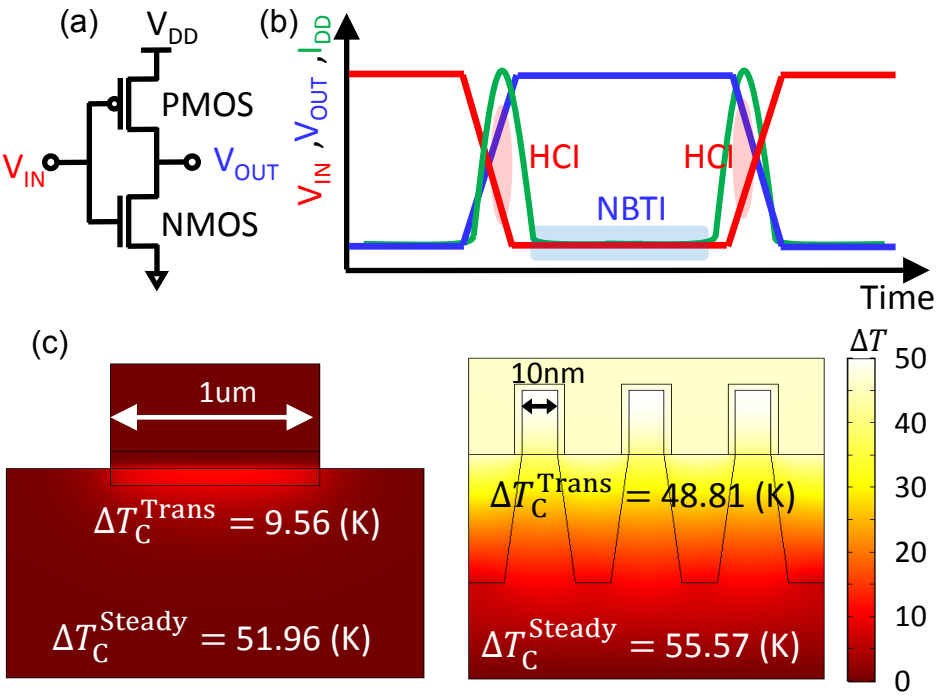

Fig. 3.22. (a) Simple schematic of inverter circuit configuration. (b) Schematic of Input, output signal, and I_{DD}. (c) Simulated transient temperature distribution of conventional planar device channel ($\Delta T_C^{\text{Trans}}$) at $1ns$ after when the pulse (e.g., slew rate: 1G) is on, and FinFET case shown in the right-hand side.

NBTI

NBTI is an important degradation mechanism for transistors. Its physical mechanisms and a proper model development have been an intense undergoing debate [84, 85]. One group describes NBTI by an uncorrelated contribution of Si/SiO_2 interface traps (ΔN_{IT}), holes trapping in pre-existing bulk defects (ΔN_{HT}), and creation of bulk defects within the gate oxide (ΔN_{OT}) [84, 86]. The other group describes ΔN_{IT} by hydrogen release model, and ΔN_{HT} by non-radiative multi-phonon model [87, 88]. The primary contribution of NBTI for ultra-scaled modern devices is known to be due to ΔN_{IT} [89–91]. All models exhibit strong dependence of ΔN_{IT} generation rates on temperature and electric field. Thus, NBTI models rely on a careful specification of temperature and electric field at various locations within an IC.

In conventional planar devices, SHE was not a serious concern for NBTI. After all, a transistor experiences the most severe NBTI degradation when the input pulse is flat as shown in Fig. 3.22a, and 3.22b. On the other hand, the channel heats up only during switching events when current flows from V_{DD} to ground. Conventional devices do not heat up considerably even during switching, therefore $\Delta T_{\mathrm{C}}^{\mathrm{Trans}}$ is not significant enough to affect NBTI as shown in Fig. 3.23c. In contrast, Fig. 3.22c shows that FinFETs heats up to steady-state temperature ($\Delta T_{\mathrm{C}}^{\mathrm{Steady}}$) within a $1ns$ [64]. Moreover, modern transistors turn on and off more frequently than the older devices. Thus, final ΔT_{C} of modern ICs is much higher than that of conventional transistors. Phenomenologically, NBTI can be specified in the form $\Delta V_{\mathrm{TH}} \sim A \cdot \exp\left(-E_{\mathrm{A}}/\left(k \cdot T_{\mathrm{C}}\right)\right) \times t^{n}$, where T_{C} is the summation of $\Delta T_{\mathrm{Cir}}^{\mathrm{avg}}$, $\Delta T_{\mathrm{T}\rightarrow\mathrm{B}}$, and ΔT_{Sys}, if ΔT_{amb} is assumed to be zero, and T_{Sys} and n are technology-specified degradation parameters can be obtained from experiments. In the case of NBTI, $\Delta T_{\mathrm{Cir}}^{\mathrm{avg}}$ has to be taken into account considering the maximum degradation is when the input signal is flat. Moreover, E_{A} and n are the technology-specific degradation parameters which can be obtained from experiments or TCAD simulations [92]. Once all the parameters are extracted, we can examine the SHE impact on NBTI by putting T_{C} predicted by

our compact model. Fig. 3.23a shows that NBTI lifetime can degrade significantly unless one adopts FEOL and BEOL design strategies that reduce SHE.

HCI

Another important reliability issue for a transistor is HCI degradation, presumably caused by hot electrons breaking Si-H and Si-O bonds close to the interface [93]. Unlike NBTI, HCI shows maximum degradation at the transition phase, when I_{DD} is maximum as shown in Fig. 3.22a, and 3.22b. For longer channel planar transistors fabricated in the 1990s, NBTI and HCI differed in the sign of activation energy (E_{A}): While NBTI increased with temperature (positive activation), counterintuitively, HCI decreased with higher temperature (negative activation) [94, 95]. The negative HCI activation energy was correlated to impact-ionization of hot electrons, which decreases with temperature. As the channel length reduced, HCI activation energy also became positive. At reduced voltage, electron injection was dominated by electron-electron scattering and the positive activation energy of the bond-dissociation dominated the process [96–99]. As the channel length has reduced and confined geometry transistors have been adopted to suppress short channel effects, the combination of positive activation energy and significant SHE have resulted in HCI being an important degradation mode for modern transistors [58, 99]. As shown in Fig. 3.22c, the channel temperature of FinFET reaches its maximum value only within a few picoseconds, thus SHE can increase HCI degradation considerably. Several recent papers describe the bias dependence on HCI behavior [96, 98]. In this work, we only focused on the temperature impact for the simplicity.

In our previous work without considering bias dependence, a physics-based compact model of HCI for multi-fin SOI FinFETs was developed and a universal HCI degradation model was proposed based on the bond-dispersion model [99–101]. Similar with NBTI, HCI can also be described in the form $\Delta V_{\mathrm{TH}} \sim A{\cdot}\exp\left(-E_{\mathrm{A}}/\left(k \cdot T_{\mathrm{C}}\right)\right)\times t^{n}$. The only difference is T_{C} where the summation of $\Delta T_{\mathrm{Cir}}^{\mathrm{avg}}$, $\Delta T_{\mathrm{T}\rightarrow\mathrm{B}}$, and ΔT_{Sys}. HCI

has to take maximum channel temperature considering maximum degradation rate occurs when I_{DD} is maximum. Any technique that reduces SHE would improve HCI lifetime as well.

For an illustrative example regarding the importance of self-heating management techniques, consider the self-heating of a 5-stage ring oscillator operating at 3.73GHz composed of 7nm FinFETs. We compare its performance with and without T-AD (e.g., dummy vias in the BEOL, and reasonably thick Cu plane). Our model shows that ΔT_{C} with $\Delta T_{\mathrm{Cir}}^{\mathrm{max}}$ is reduced from 98.43 to 79.83$^{\circ}C$, and with $\Delta T_{\mathrm{Cir}}^{\mathrm{avg}}$ is reduced from 57.17 to 38.57$^{\circ}C$ by applying T-AD. We expect further ΔT_{C} drops by applying FEOL strategies as introduced in Sec. 3.5. By applying T-AD, lifetime increases 4.1 times for NBTI, and 2.2 times for HCI as shown in Fig. 3.23a, and 3.23b.

3.6.2 BEOL reliability

Traditionally, Blacks equation [102] has been used to predict EM mean time to failure (MTTF) under direct current (DC) stress. More recently, Blacks equation has been revised to account for more general stress condition (e.g., pulsed current source) and this generalized Blacks equation is widely used [103–105] to describe EM lifetime in modern interconnects. For simplicity, in this paper, we have used this classical model to describe temperature dependence of BEOL reliability. Considering both traditional and generalized model assume Arrhenius relationship between atoms diffusivity and temperature, we anticipate that the results may not significantly different even if more modern formulation of EM reliability were used [106–108]. In this work, we applied conventional Blacks equation (TTF $= A \times J^{-n} \exp\left(E_{\mathrm{A}}/k_{\mathrm{B}}T_{\mathrm{m}}\right)$), with A $= 1.47 \times 10^{7} A \cdot s/m^{2}$ [109], $E_{\mathrm{A}}= 0.85eV$ (e.g., copper) [110], and $n = 1$ (e.g., void growth) [111], and $T(x, y, z)$ for the specific metal levels) to compare a DC interconnect line MTTF to appreciate how much temperature can impact on its lifetime. The line-specific current densities are obtained from the ITRS document [112].

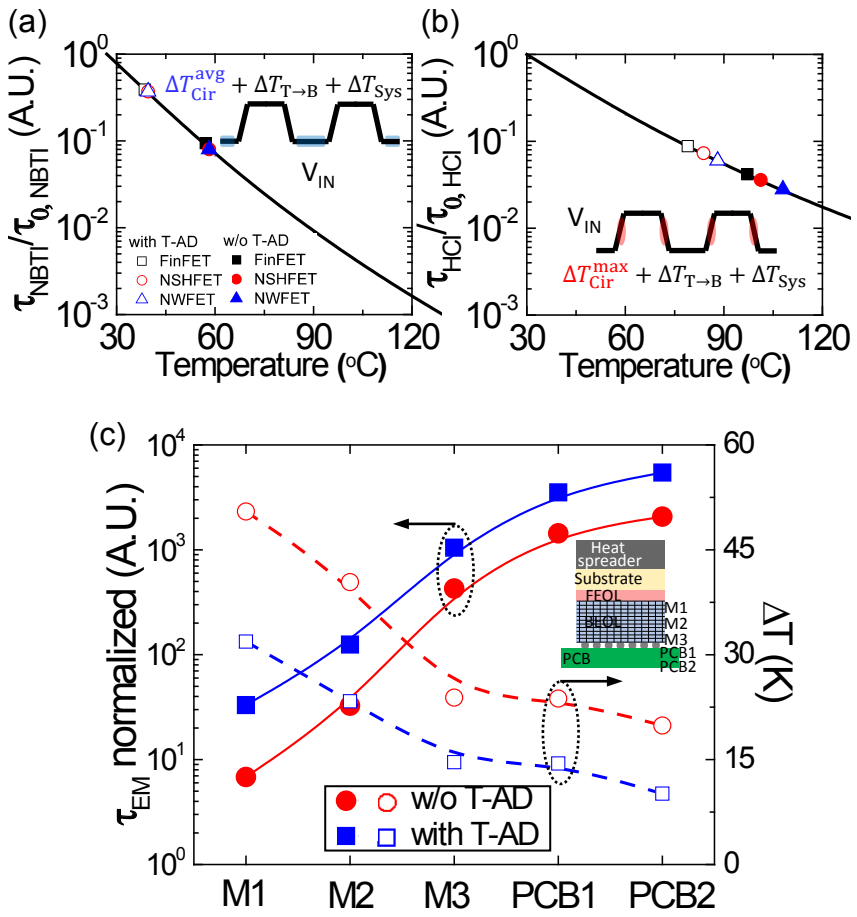

Fig. 3.23. A comparison of (a) NBTI (e.g., based on $\Delta T_{\mathrm{Cir}}^{\mathrm{avg}}$), and (b) HCI (e.g., based on $\Delta T_{\mathrm{Cir}}^{\mathrm{max}}$) lifetime among different device type. (Inset) Shaded regions are when each degradation is maximum (c) Average EM lifetime comparison based on the temperature distribution obtained by the compact model introduced here.

Comparison of the ΔT distribution (e.g., dotted line) due to T-AD within ICs is shown in Fig. 3.23c. Based on predicted ΔT, we can predict the EM lifetime (e.g., solid line) at each level. Among all the layers, M1 layer is expected to be the least reliable due to the self-heated transistors so that additional attention should be required. Considering typical advanced technologies to improve EM reliability nowadays (i.e., metal cap, doped seed) exhibits higher E_{A} value ($1.0eV$), so that SHE

would make the lifetime reduction even more [113]. By applying dummy vias and Cu plate, the EM life increases 4.8 times more in the case of a M1 layer, highlighting the importance of T-AD for self-heated ICs.

3.7 Conclusions

SHE has now become an inevitable problem associated with the scaling down of transistors. In this chapter, we have (a) investigated the origin of SHE at each level of transistor, interconnect, and package hierarchy, (b) explained the electro-thermal modelling approach for FEOL, BEOL, and PCB layers, and (c) introduced the methodology to combine compact models of each layer to predict the overall temperature rise in various types of analog and digital circuits. We have also explored the implications of SHE on various degradation modes of a modern transistor (i.e., NBTI, HCI, and EM). We find that as device node size reaches sub-20nm regime, multi-τ_c thermal response makes SHE an important concern even at the high frequencies, especially for digital circuits. In order to suppress SHE, we discussed various strategies that can be used during the frontend and/or backend design of an IC. Finally, we compared temperature distribution to examine the impact of T-AD techniques on the reliability of self-heated ICs. Our study enhances the understanding of SHE behavior at each tier and frames a thermal guideline to predict ΔT_C and reliability of a fully packaged ICs.

4. BEOL SELF-HEATING DUE TO JOULE-HEATING OF THE INTERCONNECTS

4.1 Introduction

Front- and backend self-heating have become an important barrier to the sustained increase in processor speed. Indeed, the severity of backend Joule heating with shrinking BEOL features has emerged as a crucial issue for the ICs reliability [114]. When the BEOL feature size is reduced by k, the interconnect RC delay increases as k^3! Recently, several groups have suggested that the RC delay could be reduced by new materials [115]. For example, airgaps near a wire [116] could reduce C, while carbon nanotubes [117] could reduce R. Besides RC issue, increasing power density have made BEOL thermal management a significant challenge [118]. In this context of fast technology innovation, an accurate and efficient compact thermal model will greatly facilitate the BEOL performance-reliability optimization.

As I have pointed out several times already, temperature is one of the most important parameters for IC optimization. Many degradation modes depend exponentially on local temperature (i.e. Arrhenius activation), therefore even a slight inaccuracy in the peak temperature (ΔT_p) modeling often translates to orders-of-magnitude uncertainly in the predicted lifetime. In chapter 3, a physics-based compact thermal model for the temperature distribution ($T(x, y, z)$) within an ICs due to self-heated transistors was shown. As shown in Fig. 4.1a, a transient thermal response of a self-heated interconnect (ΔT_{Int}) must be superposed onto $\Delta T(x, y, z)$ in order to predict the peak wire temperature (ΔT_p) accurately. Once ΔT_{Int} and ΔT_p are predicted accurately, they can be used as an input to a variety of other BEOL reliability phenomena: time-dependent dielectric breakdown (TDDB) of BEOL dielectric [119], Joule-heating in carbon nanotube integrated BEOL [117] , and electromigration in existing and novel

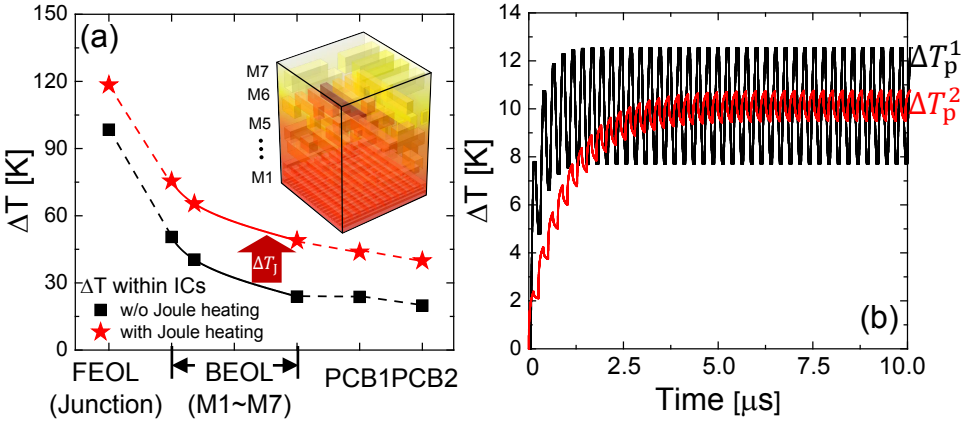

Fig. 4.1. (a) $\Delta T(x, y, z)$ comparison between with and without Joule heating. Estimation of additional ΔT_{Int} at various interconnect levels is critical for BEOL design. (b) Transient Joule heating behavior comparison of different analytic charging models (i.e., with same R_{TH}) in the case of unipolar periodic input power.

interconnects [105]. Given its importance, transient self-heating is sometimes analyzed by a 3D FEM simulation for specialized configurations. Unfortunately, there has been no closed-form analytical (cfa) ΔT_{Int} model that can accurately and efficiently predict the temperature rise of a self-heated interconnect.

The complex geometry of BEOL makes transient thermal modeling difficult. Once we calculate the effective thermal conductivity of the BEOL ($\kappa_{\text{eff}}^{\text{BEOL}}$), we can predict transient thermal response based on a simple RC charging model [120–122]. Unfortunately, this simple RC model does not capture the complexity of actual thermal response due to the two oversimplifications: a single time constant (τ_{C}), and infinite slope of the power input pulse, see Fig. 4.2d, and 4.2e, respectively. Rinaldi proposed a mathematical model for a cuboid heat source in a homogeneous system and showed a good match with numerical simulations [123]. As shown in Fig. 4.2f, considering a substrate impact on a thermal response, Rinaldi model can be generalized to more complex systems involving multiple layers [124], although the charging/discharging formula becomes unacceptably complicated (14 τ_{C}, just for two layers!) and the tem-

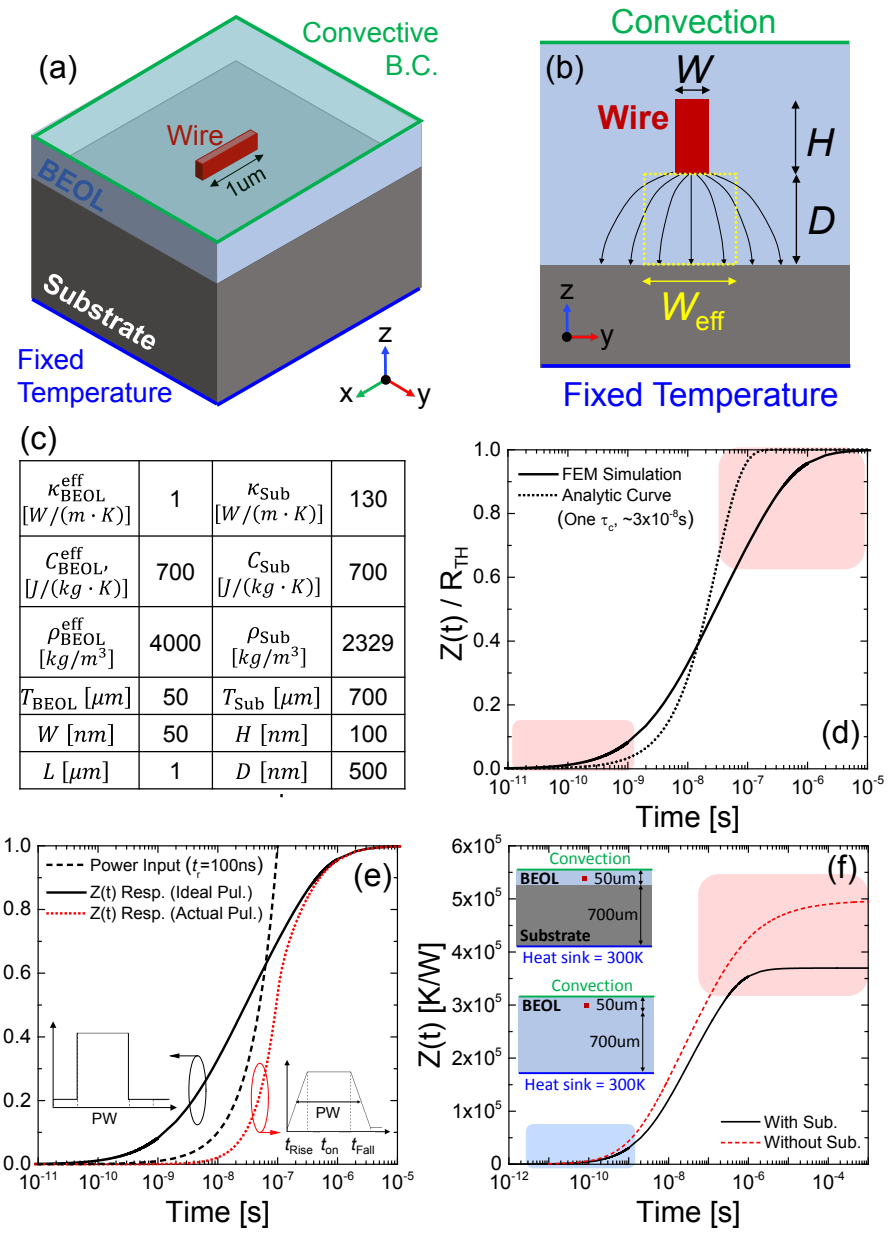

$\kappa_{\mathrm{BEOL}}^{\mathrm{eff}}$ $[W/(m\cdot K)]$	1	κ_{Sub} $[W/(m\cdot K)]$	130
$C_{\mathrm{BEOL}}^{\mathrm{eff}}$, $[J/(kg\cdot K)]$	700	C_{Sub} $[J/(kg\cdot K)]$	700
$\rho_{\mathrm{BEOL}}^{\mathrm{eff}}$ $[kg/m^3]$	4000	ρ_{Sub} $[kg/m^3]$	2329
T_{BEOL} $[\mu m]$	50	T_{Sub} $[\mu m]$	700
W $[nm]$	50	H $[nm]$	100
L $[\mu m]$	1	D $[nm]$	500

Fig. 4.2. (a) 3D schematic of simulated structure for Fig. 4.2d-f. (b) Cross-sectional view of simulated structure. (c) Simulated structure information (d) One-τ_{C} model cannot describe ΔT_{Int} accurately especially for red shaded regions. (e) When power pulse (dashed line) has slower rising time than τ_1, ΔT_{Int} response (red dotted line) must be slower than that of power pulse. (f) Regardless of substrate, ΔT_{Int} starts to rise at the same time as shown in blue shaded region. However, the substrate affects the ΔT_{Int} saturation behavior differently shown in red shaded region.

perature prediction within the heat source is limited. Recently, an accurate transient thermal model of an interconnect based on empirical fitting has been developed [125]. However, its application to general interconnect geometry is challenging due to a demanding data fitting procedure.

This chapter is organized as follows. In section II, we describe the derivation and validate the cfa-Joule heating model. Section III introduces a SPICE-compatible compact model for various circuits based on the cfa-Joule heating model. In section IV, we compare $\Delta T_{\mathrm{Int}}(\mathrm{t})$ for different interconnect metals (e.g., Cu, Co, and Ru) and different cooling strategies. Finally, based on the compact model and the results from Sec. IV, we demonstrate how different metal, and cooling strategies impact the reliability of an interconnect. Our cfa-Joule heating model offers new opportunities for the optimization of BEOL reliability, thereby improve IC performance.

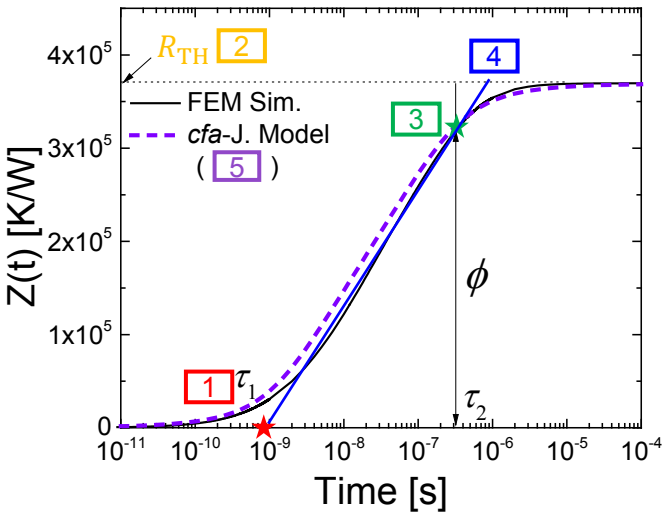

Fig. 4.3. Our cfa-Joule heating model (purple dashed line) shows a good match with actual transient FEM simulation. Simulated structure information is shown in Fig. 4.2b, and 4.2c.

4.2 Analytical model derivation

Extensive FEM simulations (shown in Sec. 4.3) of a variety of interconnects shows that $\Delta T_{\mathrm{Int}}(\mathrm{t})$ is characterized by three parameters: onset-time (τ_1, red star), saturation-time (τ_2, green star), and temperature asymptote defined by thermal resistance (R_{TH}). In this paper, we derive an analytical formula for $\Delta T_{\mathrm{Int}}(\mathrm{t})$ that captures these three through a nontrivial generalization/ integration of three models: (i) generalized multi-layers effective medium theory (*gml*-EMT) model for $\kappa_{\mathrm{eff}}^{\mathrm{BEOL}}$ introduced in chapter 3, (ii) Rinaldi model for τ_1 [123], and (iii) HG model for steady state asymptote [125], and τ_2.

4.2.1 Ternary inputs of the model

First of all, we must determine $\kappa_{\mathrm{eff}}^{\mathrm{BEOL}}$ associated with complex metal-insulator stack surrounding the interconnect of interest. Fortunately, $\kappa_{\mathrm{eff}}^{\mathrm{BEOL}}$ can be calculated by *gml*-EMT model, see chapter 3 for numerical and experimental validation. Next, we calculate thermal diffusivity ($\alpha = \kappa_{\mathrm{eff}}^{\mathrm{BEOL}} / (\rho_{\mathrm{D}} \cdot c_{\mathrm{p}})$), where ρ_{D}, and c_{p} are density, and specific heat of the material, respectively. Now, α can be used to calculate τ_1, τ_2, and R_{TH}, as follows.

Step #1

This onset time (τ_1) in Fig. 4.3 depends on the intrinsic material characteristics (i.e., density, and specific heat) of the interconnect, and the surrounding characterized by $\kappa_{\mathrm{eff}}^{\mathrm{BEOL}}$:

$$\tau_1 = \min\left(\frac{W^2}{4 \cdot \pi \cdot \alpha_{\mathrm{Cu}}}, \frac{H^2}{\pi \cdot \alpha_{\mathrm{Cu}}}\right) \tag{4.1}$$

where W and H are the width and height of the interconnect. The thermal diffusivity $\left(\alpha = \kappa_{\mathrm{eff}}^{\mathrm{BEOL}} / (\rho_{\mathrm{m}} \cdot c_{\mathrm{m}})\right)$ depends on the density (ρ_{m}), and specific heat (c_{m}) of the interconnect metal.

Step #2

Fig. 4.3 shows the steady-state asymptote $\Delta T_{\mathrm{Int}}(t \to \infty)$ can be calculated by the HG model. In this work, interfacial thermal resistance between different metal is neglected so that the value can be regarded as the lower bounds. With R_{TH} specified, the saturation time-constant, τ_2, is given by :

$$\tau_2 = \left[\frac{D}{\kappa_{\mathrm{eff}}^{\mathrm{BEOL}} \cdot L \cdot W_{\mathrm{eff}}}\right] \times \left[c_{\mathrm{eff}}^{\mathrm{BEOL}} \cdot \rho_{\mathrm{eff}}^{\mathrm{BEOL}} \cdot L \cdot W_{\mathrm{eff}} \cdot D\right] \tag{4.2}$$

Table 1 summarizes the physical parameters needed to evaluate Eq.4.2.

Table 4.1.
Physical parameters needed to calculate Eq. 4.2.

D	Distance between interconnect and substrate
L	Interconnect length
W_{eff}	Virtual width shows how much heat can spreads
ρ_{eff}	$\rho_{\mathrm{m}} \cdot \phi_{\mathrm{m}} + \rho_{\mathrm{Ins}} \cdot \phi_{\mathrm{Ins}}$
ρ_{m}	Metal density
ϕ_{m}	Volume fraction of the interconnects in BEOL
ρ_{Ins}	Insulator density
ϕ_{Ins}	Volume fraction of the insulator in BEOL
c_{eff}	Defined by volume averaging scheme similar to ρ_{eff}

Step #3

Once we calculate τ_2, the saturation time (i.e., green star in Fig. 4.3) is located by calculating ϕ. In practice, R_{TH} is determined by the spreading resistance between the interconnect and the substrate. For $D \gg \lambda_{\mathrm{TH}}$ (thermal characteristic length), R_{TH} becomes independent of D [126]. Therefore, when D is very large, actual volume that determines the thermal response would be smaller than that of we defined in c_{TH}

term in Eq. 4.2. In this case, the actual saturation time is faster than τ_2. For smaller D, however, saturation time would be slower than τ_2. Eq. 4.3 empirically relates ϕ to D for a variety of interconnect configurations:

$$\phi = \begin{cases} 0.37 \cdot \log_{10} \frac{D}{\max(W,H)} + 0.72, (D < 20 \max(W,H)) \\ 1.2, (D \geq 20 \max(W,H) \end{cases} \tag{4.3}$$

4.2.2 Integrated time response

Step #4

With τ_1, τ_2, and ϕ specified, Eq. 4.4 connects the two points (i.e., (τ_1,0), and (τ_2,ϕR_{TH})) by a linear relationship in semi-log plot as shown in Fig. 4.3, step #4:

$$f(t) = \frac{\phi \cdot R_{\mathrm{TH}} \cdot \log(t/\tau_1)}{\log(\tau_2/\tau_1)} \tag{4.4}$$

Here, $f(t)$ describes the transition between τ_1, and τ_2.

Step #5

The asymptotic transition for $t < \tau_1$ and $t > \tau_2$ can be described by Eq. 4.5.

$$Z(t) = \frac{f(t) - R_{\mathrm{TH}}/2}{\left[1 + (2f(t)/R_{\mathrm{TH}} - 1)^{2\beta}\right]^{1/2\beta}} + \frac{R_{\mathrm{TH}}}{2} \tag{4.5}$$

ΔT_{Int}can be predicted by multiplying P to $Z(t)$. In Eq. 4.5, $\beta(\sim 2$, based on FEM simulations, Sec. III.A) defines the sharpness of the response.

4.2.3 Transient Joule-heating and cooling under periodic pulses

For unipolar periodic AC pulse, transient self-heating and cooling behaviors are predicted by Eq. 4.5. Specifically, the n $^{\text{th}}$ cycle heating and cooling ΔT_{Int} is shown in Eq. 4.6.

$$T_{\text{n}}^{\text{C}}(t) = Z(t) \cdot P + (R_{\text{TH}} - Z(t)) \cdot \frac{T_{\text{n-1}}^{\text{D}}}{R_{\text{TH}}} \cdot P \tag{4.6a}$$

$$T_{\text{n}}^{\text{D}}(t) = (R_{\text{TH}} - Z(t)) \cdot \frac{T_{\text{n}}^{\text{C}}}{R_{\text{TH}}} \cdot P \tag{4.6b}$$

We find cyclo-stationary peak temperature of an IC under unipolar pulse with the duty cycle (ζ) by summing over the geometric series in Eq. 4.6:

$$\Delta T_{\text{p}} = \frac{Z(\zeta T) R_{\text{TH}}^2 \cdot P}{R_{\text{TH}}(Z(\zeta T) + Z((1-\zeta)T)) - Z(\zeta T) Z((1-\zeta)T)} \tag{4.7}$$

where T is cycle (s). For ζ=0.5, Eq. 4.7 is simplified to Eq. 4.8.

$$\Delta T_{\text{p}}(\zeta = 50\%) = \frac{R_{\text{TH}}^2 \cdot P}{2R_{\text{TH}} - Z(0.5 \cdot T)} \tag{4.8}$$

To summarize, based on the geometrical/physical properties of an interconnect and its dielectric surrounding, Eq. 4.5 and 4.7 can be used to predict its transient thermal responses under a single or periodic pulse trains as shown in Fig. 4.4.

4.3 Model validation

4.3.1 FEM numerical simulation

In order to validate our cfa-Joule heating model for all feasible BEOL configurations, we perform both Finite Element Method (FEM) numerical simulations. FEM simulation results are compared with our analytic model and discussed.

Steady-state simulation

One of the most crucial inputs of our cfa-Joule heating model is steady state thermal resistance (R_{TH}). The first analytical R_{TH} calculation model (HG model)

was proposed by Harmon and Gill based on the conformal mapping scheme [127,128]. Recently, HG model is revised for the narrow-width metals based on FEM analysis [125]. In this work, HG model is revisited again by our FEM simulations for all feasible wire configurations to confirm the practicality of our cfa-Joule heating model. First of all, the reference structure (W, H, L, and D set to 50, 100, 1000, and 200nm, respectively.) is determined as shown in Fig. 4.2a-4.2c. Among many variables, only one variable is modified, and its impact on R_{TH} is investigated.

To extract R_{TH} by FEM simulations, we use the following steps. 1) Four variables are defined: wire length (L), wire width (W), the distance between the bottom of the wire and substrate (D), and $\kappa_{\mathrm{eff}}^{\mathrm{BEOL}}$; 2) material properties are assigned for each region as shown in Fig. 4.2c; 3) heat equation is solved using a 3D commercial simulator, COMSOL. The boundary conditions are shown in Fig. 4.2a; and finally 4) R_{TH} is calculated by applying the power of $1W$ to the wire, and then the maximum temperature is extracted which can be considered as R_{TH} based on the relationship,

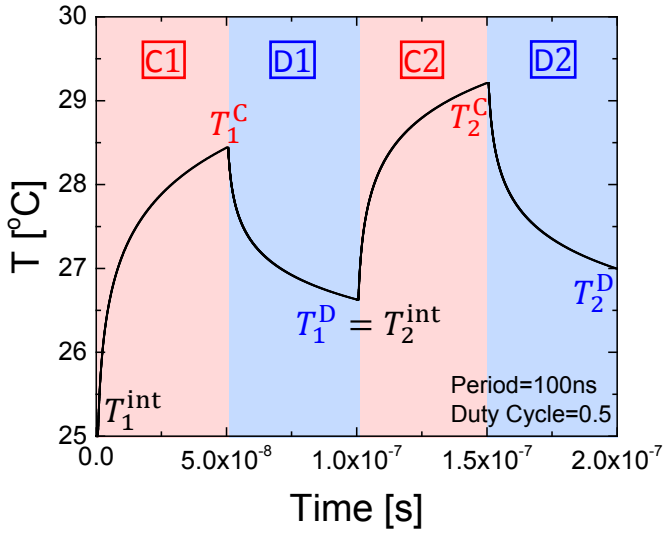

Fig. 4.4. Based on derived Jouleheating analytical formula $Z(t)$, closed-form of cooling, and reheating stages with non-zero initial value analytic formulas can be derived, see inset equations.

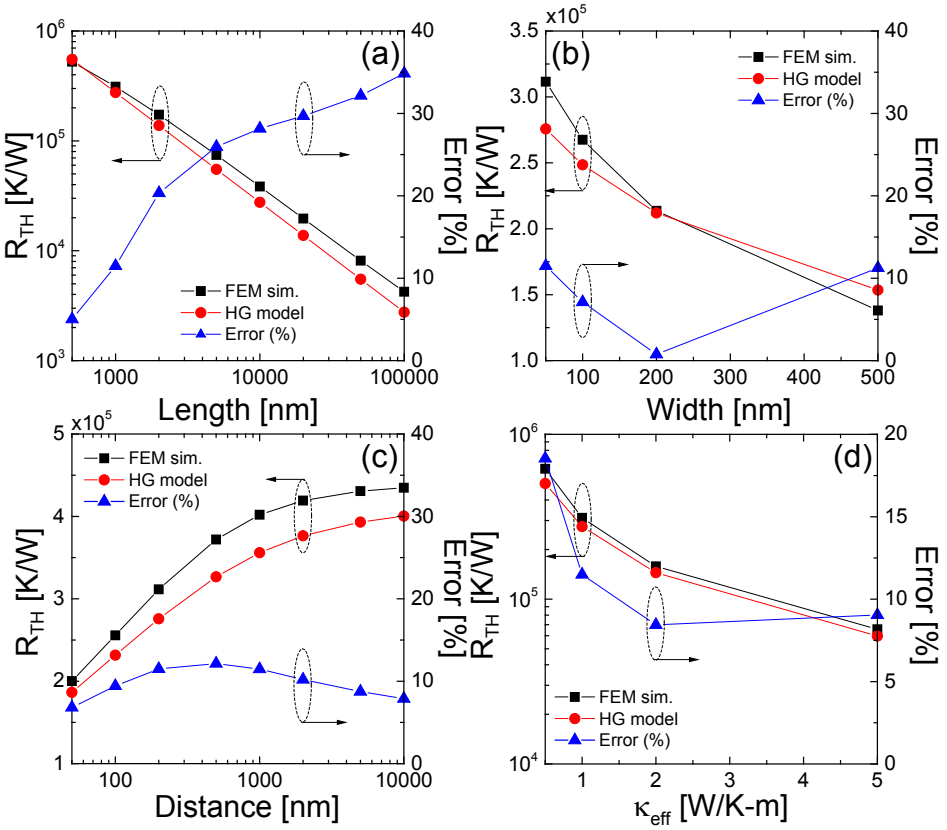

Fig. 4.5. Calculated R_{TH} comparison (%) between FEM simulation and HG model when various parameters; (a) Length, (b) Width (c) Distance, and (d) $\kappa_{\mathrm{eff}}^{\mathrm{BEOL}}$ are varied. The reference structure is defined in Fig. 4.2b, and 4.2c.

$\Delta T = R_{\mathrm{TH}} \times P$. As shown in Fig. 4.5, except when the length becomes longer than $5\mu m$, all cases show the error percentage less than 20%. As a result, we conclude HG model is sufficient to be adopted for the compact model application considering insignificant error percentage.

Transient simulation

Firstly, the empirical relationship between ϕ, D, and interconnect dimenisons (W, H) given by Eq. 4.3 is validated in Fig. 4.6a, and 4.6b. As D becomes larger, R_{TH}

change become less considering spreading resistance concept and this behavior is well captured as shown in Fig. 4.6a, and 4.6b. With Eq. 4.3 validation, the impact of each interconnect parameter on the transient thermal response is further investigated. If

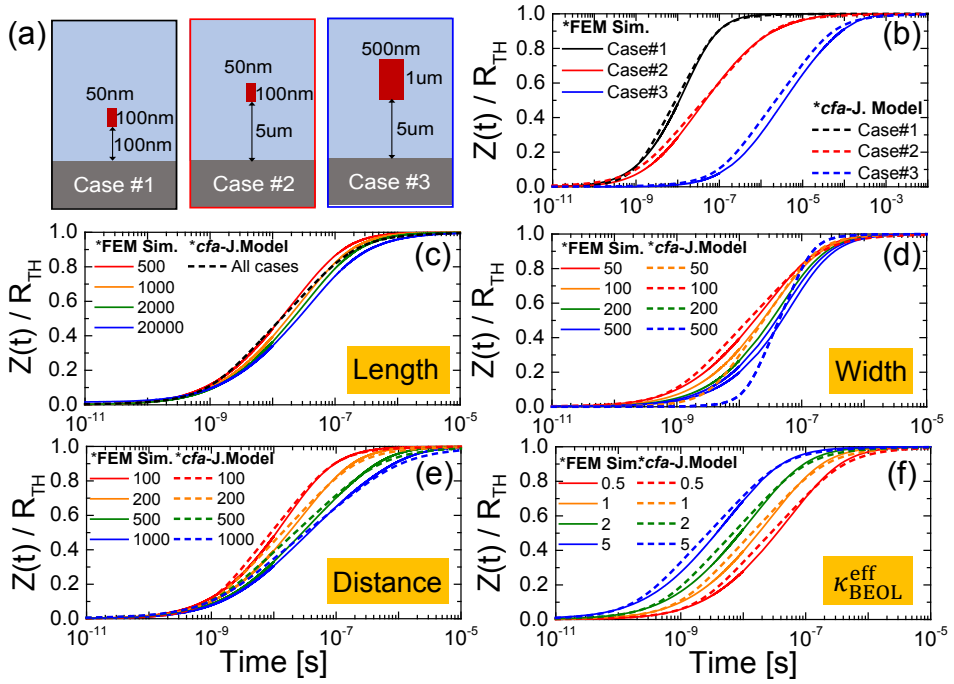

Fig. 4.6. (a) Simple schematics of simulated structure to validate Eq. 4.3. Transient ΔT_{Int}simulated by COMSOL, and compared to our cfa-Joule heating model at the variety of different conditions (Ref. case #1): (b) Different interconnect configurations, (c) Length, (d) Width, (e) Distance, and (f) $\kappa_{\mathrm{eff}}^{\mathrm{BEOL}}$ are varied.

we normalize the transient response by R_{TH} (i.e., $Z(t)/R_{\mathrm{TH}}$), then three parameters (i.e., τ_1, τ_2, and ϕ in Fig. 4.3) determine how ΔT_{Int} increases from 0 to 1. The impact of the variables on the transient ΔT_{Int} can be explained as follows: 1) The Eq. 4.1, and 4.2 are essentially independent of L, therefore wires with different L in Fig. 4.6c show comparable Z(t)/R_{TH}; 2) Similarly, W affects the self-heating onset time τ_1, but not the saturation time τ_2. This is confirmed by FEM simulation in Fig. 4.6d; 3) In contrast, the wire-substrate distance D does not change τ_1, but it does affect τ_2. Moreover, ϕ increases with increasing D. Therefore, ΔT_{Int} begins to

increase at comparable times, but saturates at a different time, as shown in Fig. 4.6e; 4) Finally, $\kappa_{\text{eff}}^{\text{BEOL}}$ affects both τ_1, and τ_2. The larger the $\kappa_{\text{eff}}^{\text{BEOL}}$, the faster the ΔT_{Int} due to increased thermal diffusivity. Fig. 4.6f shows that the our analytical model compares well with transient FEM simulations. Note that ΔT_{Int}can be predicted by multiplying $Z(t)/R_{\text{TH}}$ curve by power, and R_{TH}. In the following section, both R_{TH}, and our cfa-Joule heating model is validated by temperature coefficient of resistance (TCR) experiments.

4.3.2 Experimental data

In this work, HG model [125, 127] is revisited again by our experiments for all feasible interconnect configurations to confirm practicality of our cfa-Joule heating model. We investigate different BEOL level, and also multiple interconnects with different width at each level. Firstly, we fix the substrate temperature and increase I_{rms} until the ΔT_{Int} increases by $5°C$. ΔT_{Int} is determined by measuring the resistance increase of the interconnect based on Eq. 4.9.

$$R = R_0 \left[1 + \alpha \left(T - T_0\right)\right] \tag{4.9}$$

where T_0, R_0, and α are reference temperature, reference resistance, and TCR, respectively.

Steady-state

Fig. 4.7a shows that the steady-state temperature predicted by our model compares well with the data ($\Delta T = 5°\text{C}$) taken from various BEOL levels. The deviations reflect our use of a single $\kappa_{\text{eff}}^{\text{BEOL}}$ for all levels; infact, $\kappa_{\text{eff}}^{\text{BEOL}}$ depends on the local surrounding of a metal level.

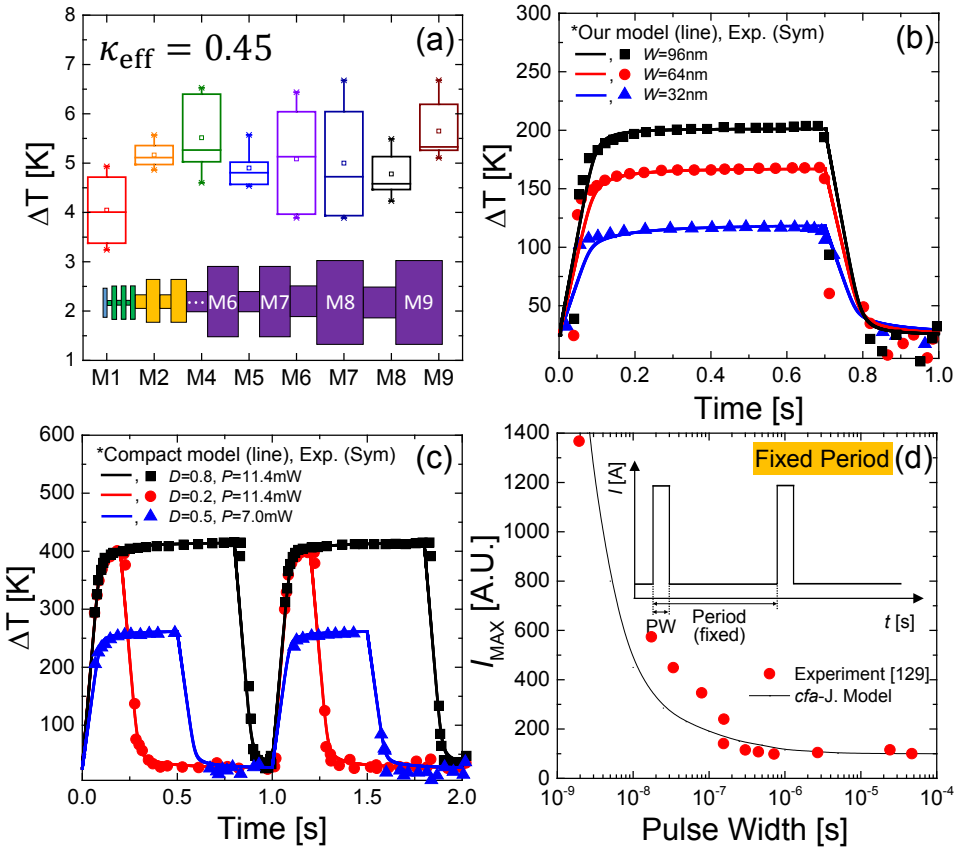

Fig. 4.7. (a) Saturated ΔT_{Int} comparison between HG model and experiments (b) Measured temperature using TCR method (Symbols), and cfa-Joule heating model of $150\mu m$ Cu line. Extracted parameters: c_{eff}, ρ_{eff}, $\kappa_{\text{eff}}^{\text{BEOL}}$ when W=96nm, $\kappa_{\text{eff}}^{\text{BEOL}}$ when W=64nm, and $\kappa_{\text{eff}}^{\text{BEOL}}$ when W=32nm are $650[J/kg-K]$, $4000[kg/m^3]$, $0.59[W/K-m]$, 0.50, and 0.40, respectively. (c) For $5\mu m$ case, only $\kappa_{\text{eff}}^{\text{BEOL}}$ is different to $150\mu m$ case, the value is 1.58. $5\mu m$ case shows larger $\kappa_{\text{eff}}^{\text{BEOL}}$ due to the closer distance between vias for shorter interconnect. (d) I_{Max} prediction for different duty cycle when period is fixed.

Transient response

Next, to validate the transient response, we determine ΔT_{Int}(t) of straight Cu lines with the length of 150, and 5m. Here, the active Cu line is surrounded by passive lines, and ΔT_{Int}(t) is measured using TCR by a waveform generator, and fast current measurement unit. We fix the frequency to 1MHz, and change the duty cycle (ζ) for

different metal width: 32, 64, and 96nm. $\rho_{\text{eff}}^{\text{BEOL}}$, $c_{\text{eff}}^{\text{BEOL}}$, and $\kappa_{\text{eff}}^{\text{BEOL}}$ are calibrated by the thermal response of the 96nm interconnect, and the thermal responses of 32, 64nm cases are predicted. As shown in Fig. 4.7b, the responses predicted by the analytical model compares well with experimental data. The results of 5m line also shows a good match, shown in Fig. 4.7c. As expected, a local variation of $\kappa_{\text{eff}}^{\text{BEOL}}$ is observed for a different wire configuration. Once the $\kappa_{\text{eff}}^{\text{BEOL}}$ is calibrated, we can obtain the accurate analytical Joule heating behavior of any interconnect within an IC. If the calibration step is not feasible, the methodology shown in chapter 3 should be viewed as an excellent approximation of the exact result.

Our model also allows us to predict the maximum current (I_{Max}) of $5°C$ ΔT for different ζ with constant period, see Fig. 4.7d. In high-performance ICs, interconnects should be able to sustain a pulse width smaller than several 10ps or current overshoot that occurs during logic transition. Thus, it is crucial to know how much I_{Max} can be applied to the specific wire. Remarkably, our model reproduces the reported experimental data [129]. As a result, cfa-Joule heating model can be used to define the guideline of BEOL thermal design as well.

4.4 Circuit simulation with the model

In order to investigate ΔT_{Int} of an interconnect constituting a specific circuit, we perform HSPICE circuit simulations based on BSIM-CMG compact model (7nm FinFETs) for the power input pulse shape. Both digital circuit (ring oscillator), and analog circuit (differential operational amplifier) simulations are done for the V_{DD} node, see Fig. 4.8b inset, and 4.8d inset. Surrounding BEOL conditions and wire size is defined based on recent node-technology as shown in Fig. 4.8a, and 4.8c. Once the input pulse schematic is defined, we can predict ΔT_{Int} of a certain wire at any node based on the flowchart shown in Fig. 4.9. Three main inputs are needed: 1) τ_1 from Rinaldi model; 2) R_{TH} between the substrate and heated wire, and τ_2 based on HG model; 3) $\kappa_{\text{eff}}^{\text{BEOL}}$ based on EMT model shown in chapter 3, and $\rho_{\text{eff}}^{\text{BEOL}}$, and

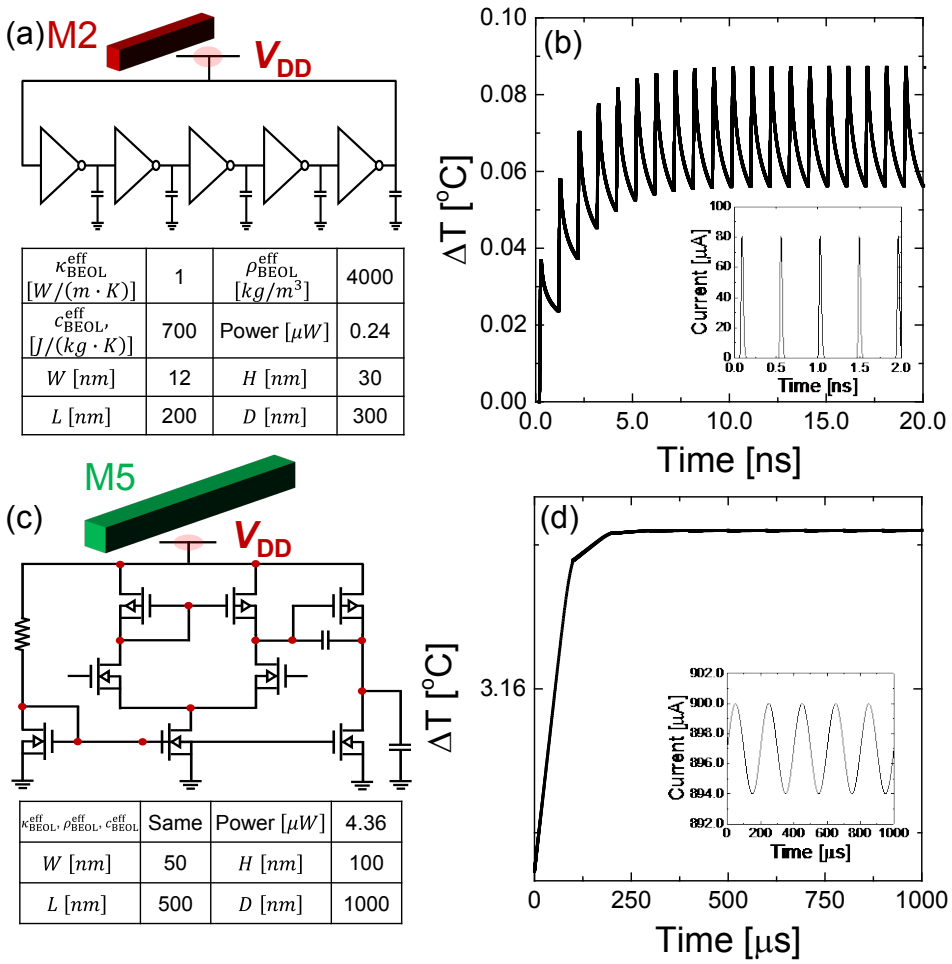

κ_{BEOL}^{eff} $[W/(m\cdot K)]$	1	ρ_{BEOL}^{eff} $[kg/m^3]$	4000
c_{BEOL}^{eff}, $[J/(kg\cdot K)]$	700	Power $[\mu W]$	0.24
W $[nm]$	12	H $[nm]$	30
L $[nm]$	200	D $[nm]$	300

κ_{BEOL}^{eff}, ρ_{BEOL}^{eff}, c_{BEOL}^{eff}	Same	Power $[\mu W]$	4.36
W $[nm]$	50	H $[nm]$	100
L $[nm]$	500	D $[nm]$	1000

Fig. 4.8. (a) The schematic of a 5 stages oscillator. (Table) Surrounding parameters, power value, and wire sizes at V_{DD} node. (b) ΔT_{Int} behavior of a Joule heated wire shown in Fig.10a. (inset) Transient current response (AC with 0.1 duty cycle) at V_{DD} node obtained by HSPICE simulation. (c) The schematic of 2-stage operational amplifier. (Table) Surrounding parameters are same as Fig. 10 case, power value, and wire sizes at V_{DD} node. (d) ΔT_{Int} behavior of the wire shown in Fig.11a. (inset) Transient current response (almost DC) at V_{DD} node obtained by HSPICE simulation.

c_{eff}^{BEOL} based on the volume averaging concept. The flowchart in Fig. 4.9 allows us to calculate ΔT_{Int} at the V_{DD} node for the RO (Fig. 4.8b), and for the op-amp (Fig. 4.8d). The RO power dissipation is small (see Fig. 4.8b, inset), therefore

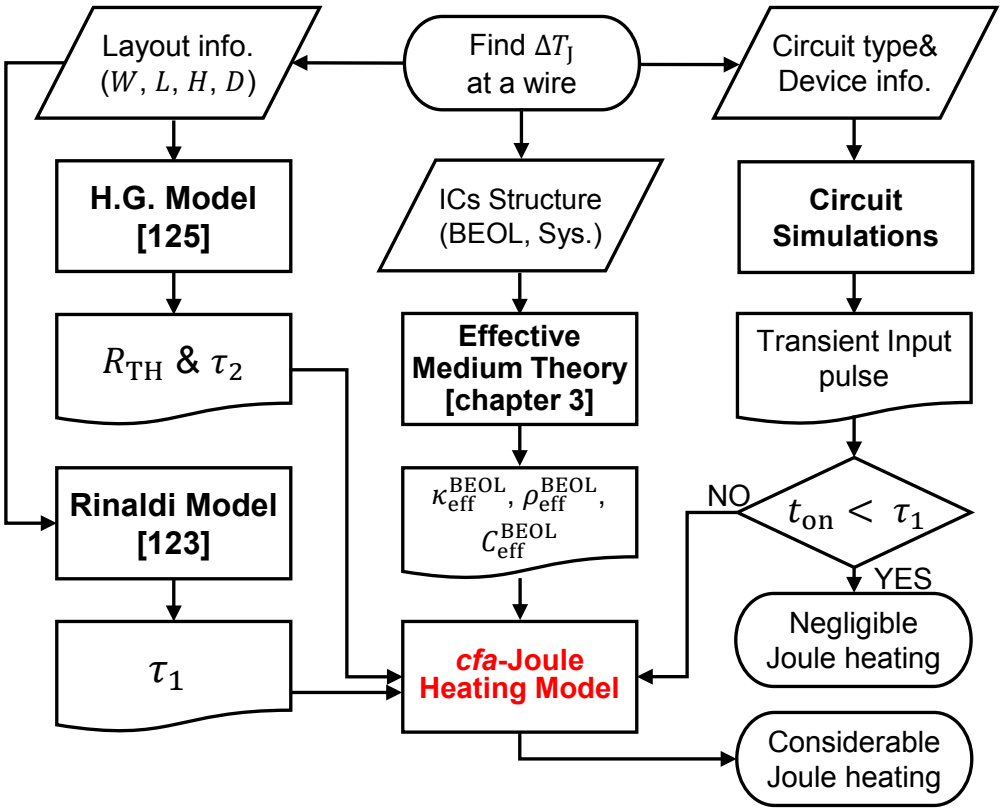

Fig. 4.9. Flow chart of the full compact model based on cfa-Joule heating model presented in this work.

ΔT_{Int} ($0.07°C$) is negligible. On the other hand, ΔT_{Int} ($3.1°C$) for the op-amp is significantly higher because the power input is an order of magnitude higher than the RO. Consequently, power grid line of an analog circuit must be carefully designed to prevent severe Joule heating. In the following section, we will compare ΔT_{Int} of wires made of different metal (Cu, Co, and Ru), the effect of various cooling strategies, and establish the corresponding reliability limits.

(a)		Copper	Cobalt	Ruthenium
ρ_R [$\mu\Omega \cdot cm$]	C.D. ~20nm	6 [130]	21.67 [115]	24.67 [115]
	C.D. ~50nm	3 [130]	10.83 [115]	12.33 [115]
Cross-section Area ratio [A.U.]				
κ [W/m-K]	Bulk	400	100	117
	Nano	~230	~30	~35
ρ_D [kg/m^3]		8960	8900	12200
C_p [J/kg-K]		385	421	238

EMT [Chp. 3], HG model [125], Rinaldi model [123], HSPICE Sim.

(b)	Copper	Cobalt	Ruthenium
κ_{eff}^{BEOL} [W/m-K]	0.98	0.64	0.67
ρ_{eff}^{BEOL} [kg/m^3]	2655.41	2651.35	2848.91
C_{eff}^{BEOL} [J/kg-K]	688.72	696.89	653.15
P (R.O) [μW]	0.27	0.77	0.88
τ_1,τ_2(R.O.) [s]	4.03×10^{-11}, 1.12×10^{-7}	1.05×10^{-10}, 2.60×10^{-7}	7.76×10^{-11}, 1.66×10^{-7}
P (Amp.) [μW]	2.40	8.17	9.30
τ_1,τ_2(Amp.) [s]	7.00×10^{-10}, 9.33×10^{-7}	1.31×10^{-9}, 1.44×10^{-6}	9.69×10^{-10}, 1.39×10^{-6}

Fig. 4.10. (a) Cu, Co, and Ru, physical parameters, and relative wire cross-section area used in this work. (b) Calculated parameters required for analytic ΔT_{Int} prediction based on EMT shown in chapter 3, Rinaldi [123], HG model [125], and HSPICE simulations.

4.5 Compact model application

4.5.1 Various interconnect material comparison

Typical interconnect metal lines are composed of multiple layers: barrier (i.e., tantalum nitride) to prevent metal ion's diffusion into the dielectric, liner (i.e., tantalum) to make better adherence between metal and barrier, and bulk metal which conducts current. For the practical input parameters, we applied a measured resistivity [115, 130]for the critical dimension (CD) of $20nm$ Cu, Co, and Ru metal wires. Relative ρ_{R}, and different cross-section area due to the different barrier thickness for each metal are shown in Fig. 4.10a. The Cobalt and Ruthenium cross-section area is set to be larger than that of Copper as these new materials has been demonstrated that a single film ($1nm$) is sufficient for both liner and barrier where as Copper requires several nm for both liner and barrier. Moreover, applied physical parameters (κ, ρ_{D}, and specific heat (c_{p})) for each metal are also shown in Fig. 4.10a. Based on BEOL system information, EMT model, HSPICE simulation, and cfa-Joule heating model, the required parameters to calculate transient thermal response can be obtained, see Fig. 4.10b. or different metal, RO, and op-amp, $\Delta T(x, y, z)$ by transistors heating at FEOL is obtained by our previously-published EMT-compact model shown in Fig. 4.11a [6, 7]. In practice, additional ΔT_{Int} (t) needs to be superposed to the results shown in Fig. 4.11a. Eventually, the final temperature within the wire will be the addition of the result shown in Fig. 4.11a, and 4.11b. As explained in the previous section, RO shows negligible ΔT_{Int}, and op-amp shows considerable ΔT_{Int}. In the case of DC line at the higher level (e.g., at the op-amp V_{DD} node), Co, and Ru shows higher ΔT_{Int} than that of Cu due to its higher ρ_{R}. However, when the wire CD becomes $20nm$, ΔT_{Int} begins to exhibit comparable due to increased area ratio difference (130%). Therefore, we can realize that the application of Co instead of Cu at a lower level (e.g., M1-M3) can be used without the expense of higher ΔT_{Int}.

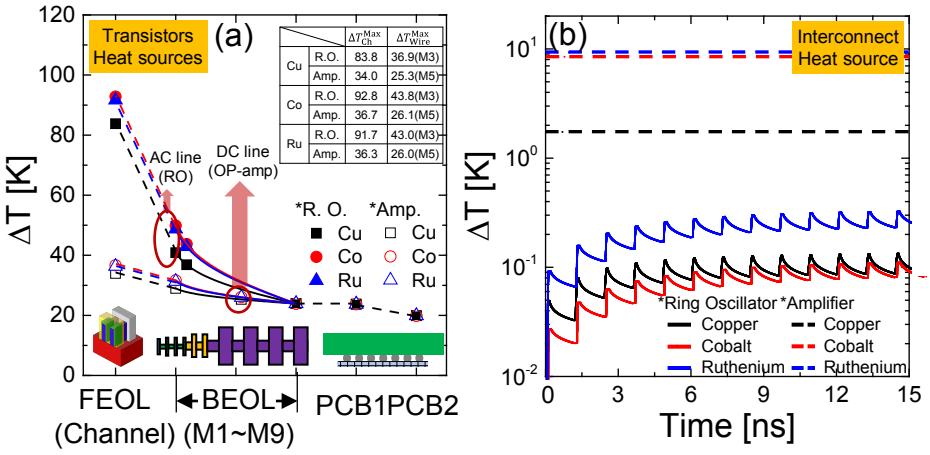

Fig. 4.11. (a) Temperature profile without Joule heating with BEOL of various metals based on the model shown in chapter 3. Additional ΔT_{Int} should be superposed to the current distribution. (b) ΔT_{Int} comparison of the wire at V_{DD} node of RO, and op-amp composed of different metals. In the case of RO, Co shows comparable ΔT_{Int} to that of Cu.

4.5.2 Comparison of cooling strategies

In this work, we compare two cooling strategies, namely, placing more vias in the BEOL and increasing wire size. Increasing both via density and/or doubling the wire cross-section significantly reduce ΔT_{Int} for op-amp DC line. However, Fig. 4.12a shows that increasing the via density counterintuitively increases ΔT_{Int} of RO circuits, primarily due to reduced τ_1. An early onset of the heating transient allows a longer time for the wire to heat up to a higher ΔT_{Int}. On the contrary, increasing wire size suppresses ΔT_{Int} by increasing τ_1. Once τ_1 becomes larger than the pulse width, the heating time would be insufficient to make the wire hot and ΔT_{Int} will be negligibly small. Thus, enlarging wire dimensions is better than inserting vias as long as the BEOL feature size permits. Relative ΔT_{Int} change according to the degree of alternation for both strategies is shown in Fig. 4.12b. We find that even 150%

increase can cause considerable reduction in ΔT_{Int}, and more than 200% changes result in insignificant enhancement.

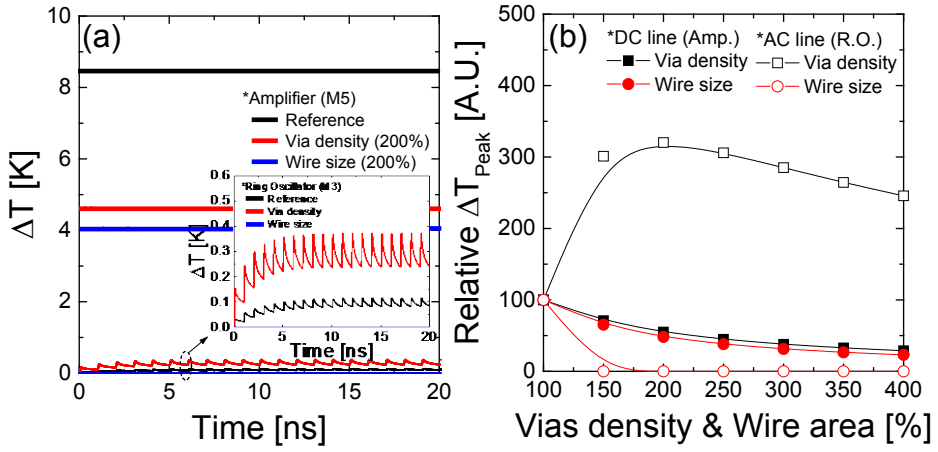

Fig. 4.12. (a) Cooling strategies performance comparison for both RO, and op-amp. Increasing wire size is better than putting more vias. Increasing $\kappa_{\mathrm{eff}}^{\mathrm{BEOL}}$ near RO wires may results in higher ΔT_{Int} by lowering τ_1. (b) Degree of changes impacts on ΔT_{Int} reduction. Even 150% of increase can results in considerable change. Impacts when more than 200% are insignificant.

4.5.3 Reliability comparison

Once we obtain ΔT_{Int}, we can compare τ_{EM} among different metals based on Blacks equation, $A \times J^{-n} \exp\left(E_{\mathrm{A}}/k_{\mathrm{B}}\Delta T_{\mathrm{Int}}\right)$, where A, E_{A}, and n are constant, activation energy, and the exponent depends on a specific degradation [102], respectively. The temperature peaks at every cycle and the activation integral over a cycle is essentially defined by this peak temperature, therefore the peak-temperature defines the mean-time-to-failure. We define τ_0 being the τ_{EM} of Cu at T=300K. E_{A} of Cu, Co, and Ru is defined as 1.6 [110], 2.4 [110], and $1.9eV$ [115], respectively. Also, when A of Cu is defined as 1, Co, and Ru is defined as 6×10^{-6}, and 0.15, respectively [115]. As shown in Fig. 4.13, Co, and Ru exhibit much longer τ_{EM} than that of Cu due to its

larger E_A: longer by 10^6, and 10^3, respectively. In conclusion, as node size becomes smaller, Co can be a good alternate metal to replace Cu at the lower BEOL level (e.g., M1-M3) considering superior reliability, and comparable ΔT_{Int} to Cu.

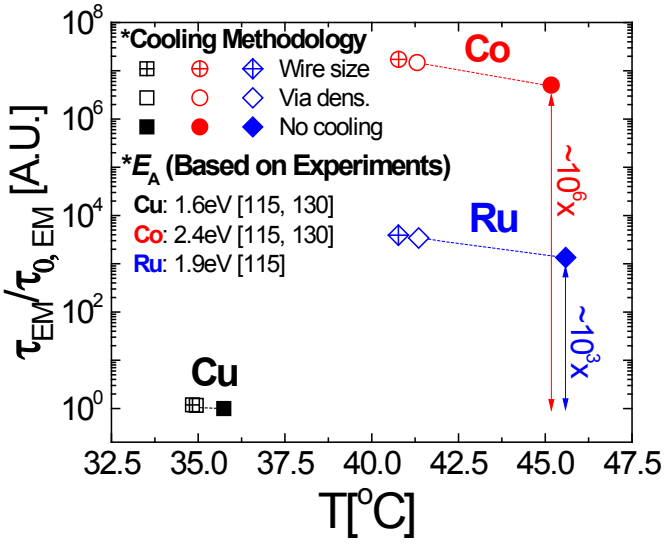

Fig. 4.13. Impact of ΔT_{Int} on BEOL reliability comparisons. τ_{EM} shows strong dependence on activation energy of material. By applying cooling strategies, τ_{EM} can be further increase by 300%.

4.6 Conclusions

A closed-form analytical Joule heating model developed in this paper is based on the nontrivial/innovative integration of Rinaldi, HG, and EMT models. The model demonstrates that among Cu, Co, and Ru wire, Cu has the lowest ΔT_{Int} due to its lowest ρ_R, especially for higher level interconnects (e.g., M8-M10). However, for lower level interconnects (e.g., M1-M3), Co is a good candidate to replace Cu because of its improved EM reliability, comparable steady-state ΔT_{Int} due to its wider cross-sectional area, and slower time constant for the ΔT_{Int} response. Between the two cooling strategies discussed in this paper, we find that increasing the wire size reduces ΔT_{Int} more significantly than increasing via density. Overall, this novel and powerful

cfa-Joule heating model can optimize BEOL efficiently by estimating ΔT_{Int} quickly and precisely for any interconnect level within an IC based on any technology node.

5. CHIP-PACKAGE INTERACTION: THE IMPACT OF MOISTURE INGRESS

5.1 Introduction

The first proposed encapsulation material is pure epoxy as it offers superior chemical resistance and it becomes harden material once it undergoes thermoset (i.e., curing) process. However, after the curing process, pure epoxy becomes a high stiffness material so that a considerable induced stress breaks ICs underneath. Nowadays, a typical encapsulation material, so called molding compounds (MCs) which is consist of inorganic fillers, such as fused silica or organic clay, embedded within an epoxy resin. The MCs are widely used as a protective encapsulant of ICs, due to their mechanical strength, conformal coverage, simple processing, and low-cost [131]. Sometimes, an IC may be exposed to extreme (hot and humid) environments for a long time, particularly for high power applications in robotics, self-driving car, etc. For these systems, moisture from the external environment and a low level of ionic contamination within the MCs often leads to serious reliability challenges. For example, moisture ingress leads to corrosion, delamination, hygroswelling [26,132,133], and charge spreading on the Back End Of Line (BEOL) region (due to significant injection from high voltage bond wires) parasitically shifts the threshold voltage of the transistors [134]. The charge accumulation at the passivation/mold compound interface is known to directly affect the long-term stability of power devices in high-temperature reverse-bias stress tests, requiring a re-design of the top metal/poly-silicon layers on the active regions [135]. Thus for all these applications, the MCs must be carefully optimized to suppress moisture ingress and charge spreading. Specifically, the MC optimization involves tailoring the inorganic filler size, shape, type, and volume fraction (ϕ_{f})

(see Fig. 5.1) to achieve the desired thermal resistance, dielectric isolation, moisture resistance, and breakdown voltage [136].

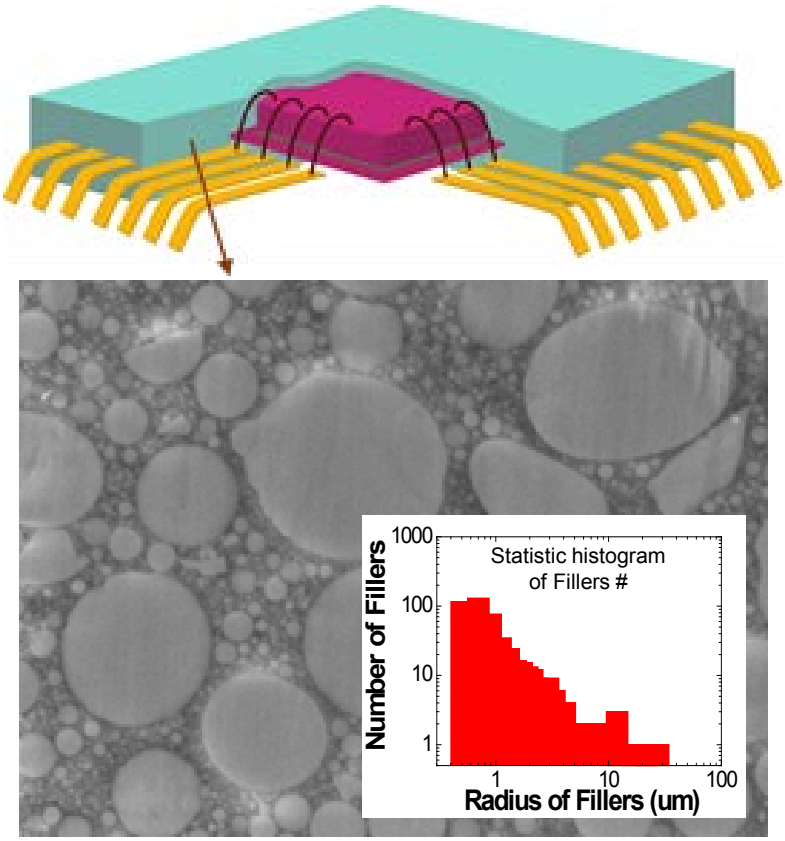

Fig. 5.1. (a) 3D schematic of Quad Flat Packaged device encapsulated with composite material. (b) SEM image of cross-section view of a composite material. (inset) Extracted filler size distribution.

In the 1960s, moisture uptake in bulk polymers was often described by Fickian diffusion models which were originally developed for inorganic materials. More recently, Fickian model has been used to describe water diffusion through mold-compounds, where the effective diffusivity (D_{eff} (ϕ_{f})) depends on the filler volume fraction, ϕ_{f} [35, 137, 138]. By the 1980s, however, a variety of experiments demonstrated that the Fickian model cannot predict the additional mass gain due to the reaction between polymer chains and water molecules [139–141]. Since then, a bulk-Langmuir model has been used to describe reaction-diffusion of water within the

polymer, where water molecules can reside either in the mobile phase (w) or in the bound phase (Y) [142–144]. This distinction is important because ion diffusion depends exclusively on Y concentration. Therefore, a generalization of the Langmuir model that describes the filler-fraction dependent transport in MC is necessary to describe ion-transport in these composite materials. Such a model has neither been developed nor experimentally validated.

This Chapter is as follows. In section 5.2, I develop a general theory of water transport in a composite material as a function of fill-fraction, size-dispersion, and topology of fillers. The result show that the best moisture barrier can be obtained by incorporation of rod-shaped fillers, at $\sim$60% fillers volumetric fraction. In section 5.3, I generalize the Langmuir model for moisture uptake in MCs by explicitly accounting for the filler properties and propose generalize effective medium and solubility ($GEMS$) Langmuir model. In section 5.4, I validate the $GEMS$- Langmuir model theoretically by finite element method (FEM) simulation [145] and empirically by water uptake experiments done by our collaborator for various MCs with different filler configurations. Moreover, I reassess extracted parameters to successfully estimate reacted water (Y) amount of any arbitrary structure of MCs, and show Y plays a dominant role on σ change by experiments. Finally, in section 5.5, I investigate the impact of filler configuration (e.g., fillers amount, fillers size distribution, and adhesion promoter existence) on HV-ICs encapsulant, such as dissipation factor, and dielectric strength. The $GEMS$-Langmuir can be adopted to describe more detailed anomalous water diffusion, suggesting new opportunities for co-optimization and reliability prediction for traditional and emerging MCs.

5.2 Transport parameters definition in a composite material

5.2.1 Analytical model

An optimally designed mold compound is particularly important for high power applications in smart-grid and electric automobiles that operate in extreme environ-

ments. Empirical optimization of mold compounds involve tailoring the size, shape, type, and filler-fraction (ϕ_f) of the inorganic fillers to achieve the desired thermal resistance, dielectric isolation, moisture resistance, and breakdown voltage [136]. Despite the importance in performance and reliability, the traditional approach of empirical design does not allow systematic co-optimization various performance metrics. For example, moisture ingress leads to corrosion, delamination, hygroswelling [26, 132, 133], and yet, the empirical data for effective diffusion coefficient (D_{eff}) as a function of the composite parameters are scattered, and typically uncorrelated to (and much higher than) the theoretical predictions of classical Maxwell-Garnett (MG) model, see Fig. 5.2d [146, 147]. If the MG theory fails to predict the relatively simple polymers with spherical inclusion, one wonders if physics-based modeling can ever be relevant for optimization of composite mold compounds with more complex inclusions.

As discussed in chapter 2, one can correctly predict the value of ε_{eff} in the case of lower ϕ_f by using MG model and using Bruggeman model at higher ϕ_f. Both MG and Bruggeman models depend on a single variable, namely, ϕ_f, regardless the sizes of individual fillers. Both models prediction is confirmed in detail in Fig. 5.3, where we plot the field distributions in three samples that have different filler radii, but with same ϕ_f. Remarkably, both models not only captures $\varepsilon_{\text{eff}}(\phi_f)$ (related to average field, E_0), but also the $E(x, y, z)$ throughout the volume. Since the Poisson equation ($\varepsilon\nabla^2 V = 0$) and the steady-state diffusion equations ($D\nabla^2 n = 0$) are isomorphic ($D \to \varepsilon, n \to V$), it is easy to use MG theory to calculate the D_{eff} simply by changing the variables in Eq. 2.4. This is precisely the recipe followed in deriving the theoretical D_{eff} in the Fig. 5.2d, solid line. If the MG and Bruggeman models are so accurate (see Fig. 5.3), one wonders why theory fails to explain the experimental results in Fig. 5.2.

Unlike thermal or electrostatic analysis, discontinuity of concentration at the interface between filler and mold has to be incorporated. As shown in sec. 2.3.1, this

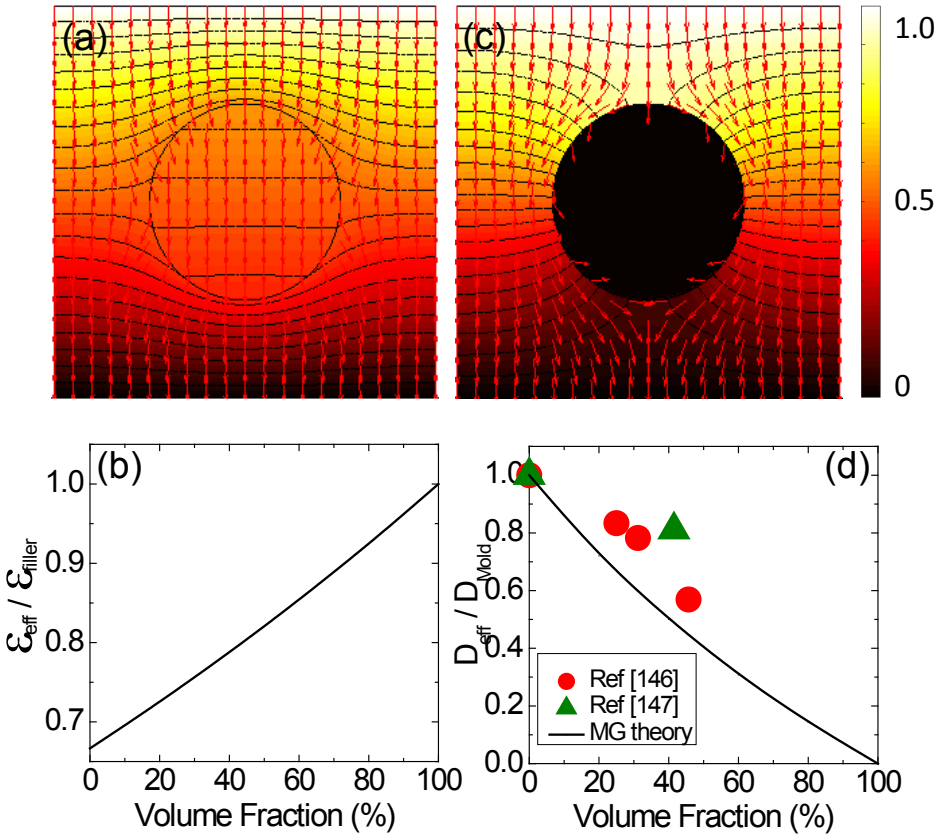

Fig. 5.2. (a) Potential profile and electric field direction (red arrows), (b) Calculated ε_{eff} as a function of filler volume fraction, (c) Concentration profile and flux direction (red arrows), (d) Calculated D_{eff} as a function of filler fraction & experimentally measured D_{eff}.

discontinuity can be considered with the MG framework through an additional factor, 'partition coefficient', see Eq. 5.1.

$$D_{\text{eff}} = \frac{D_{\text{m}}}{1-\phi_{\text{f}}+k\cdot\phi_{\text{f}}}\left[1+\frac{3\left(D_{\text{f}}\cdot k-D_{\text{m}}\right)\cdot\phi_{\text{f}}}{2D_{\text{m}}+k\cdot D_{\text{f}}-\left(k\cdot D_{\text{f}}-D_{\text{m}}\right)\cdot\phi_{\text{f}}}\right] \tag{5.1}$$

By seeting k=1, one can get conventional MG model. Therefore, The correct approach would be to refine effective media theory with modified boundary conditions, and numerically solve the 3D diffusion equation within the mold compound to assess the changes of D_{eff} (ϕ_{f}), and then directly compare theory and experiment.

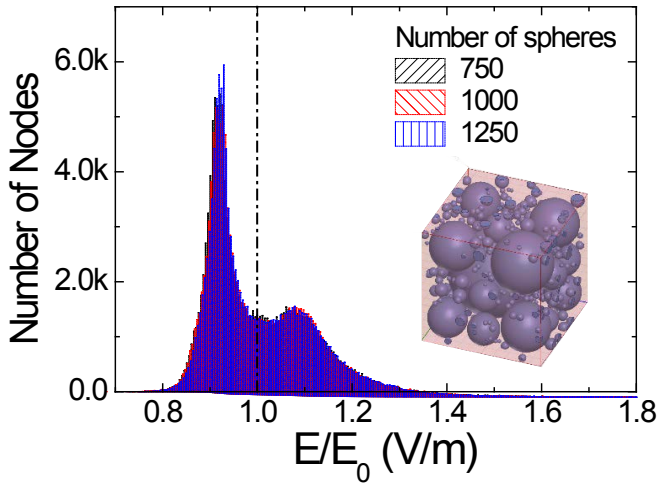

Fig. 5.3. Normalized electric field distribution of mold compounds for different filler numbers but the same volume fraction. The coincidence of the distributions directly support the center tenet of the effective media theory.

5.2.2 Model validation by numerical simulation

FEM simulations

Our new calculation approach involves the following steps: (i) the geometry of the mold compounds is specified; (ii) the diffusion equation is discretized and solved using a 3D commercial simulator, ANSYS; and (iii) since $\langle J \rangle = D_{\text{eff}} \langle dn/dx \rangle$, therefore, D_{eff} is calculated as the ratio of volume averaged flux, $\langle J \rangle = (1/V) \int J dV$ to concentration gradient, $\langle dn/dx \rangle = (1/V) \int (dn/dx) dV$, where V is the volume of the molding compounds, and final D_{eff} value would be the value normalized by the volume of polymer, excluding the impermeable fillers. This normalization step is also consistent with analytical formula. $1 - \phi_{\text{f}} + k \cdot \phi_{\text{f}}$ part will become $1 - \phi_{\text{f}}$ when k=0.

This remarkable conclusion can be illustrated by three examples, as follows. If an idealized mold compound contains spherical fillers of a single diameter arranged in a periodic lattice (a hypothetical case), D_{eff} reduces only by ~21.37% even at

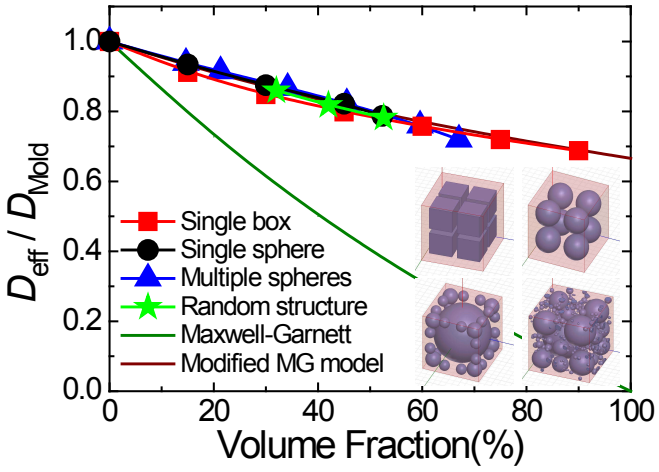

Fig. 5.4. Numerical simulation results of D_{eff} for different geometries and comparison with analytical models: conventional Maxwell Garnett (MG) theory and modified MG model (Ref. [35]).(inset) Simulated structure for simulation: counter clockwise from top right: single sphere per unit cell, single box per unit cell, regularly distributed multiple spheres, random structure.

the maximum packing density of (ϕ_{f}=0.52), see Fig. 5.4, black line. A collection of spheres of several different sizes (periodic array) packs to ϕ_{f} →67%, yet D_{eff} reduces only by ∼28.13% or so (blue line). Even a realistic arrangement (based on extracted sphere size distribution (see inset of Fig. 5.1b), involving random arrangement of spheres (green points) also exactly matching with the dark brown line, consistent with analytical modified MG model. This indicates in 3D, even though spheres are packed and almost touching each other, dipoles on each filler have not been affected by its neighbor, so that the result shows miniscule deviation from modified MG model. If we reshaped sphere into a cube, so that ϕ_{f} →100%, D_{eff} reduces only by 33%. With 3D fillers, not enough densely packed to affect dipoles on each filler and the diffusion channels are never fully closed until the very end, therefore, D_{eff} is not dramatically suppressed. This enhanced diffusion is consistent with the experimental data reported in the literature.

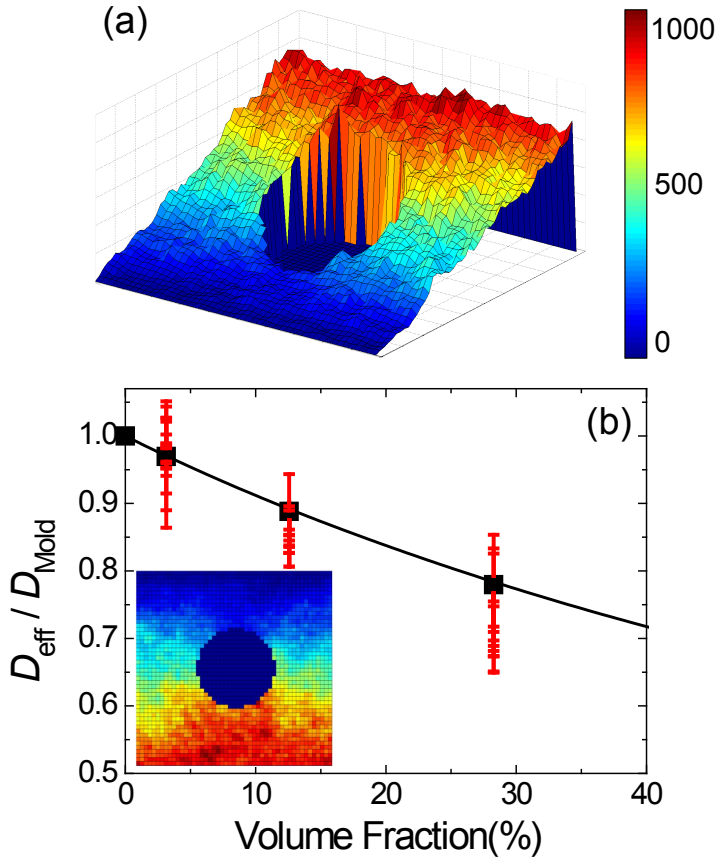

Fig. 5.5. Monte Carlo simulation verification: (a) Steady state profile of 2D Monte Carlo simulation. Input particle number per grid=200, Input location= top row (b) Correlation between D_{eff} and fillers volume fraction at 3.1, 12.6, and 28.3% and comparison with modified MG model.

Monte Carlo simulations

A detailed stochastic Monte Carlo simulation, shown in Fig. 5.5a, supports the continuum model discussed above and validates the theory. 10,000 particles (i.e., water molecules) are released at the top side of square (200 particles at each grid) and explore randomly walking particles. Starting from Einsteins equation, the diffusivity value is extracted from two information which is the time all particles move out and

the number of particles that are reached to the other end: where L is the length of square size, $\mathcal{D}$ is the dimensions, and τ is the diffusion time.

$$D = \frac{L^2}{2\mathcal{D}\tau} \tag{5.2}$$

The procedure is done multiple times for each different filler fraction condition and extracted diffusivity (red bars) shows a similar correlation with that of analytical curve, see Fig. 5.5b. The results also reproduce the asymptotic trends reported by other groups for simpler model system [35, 138].

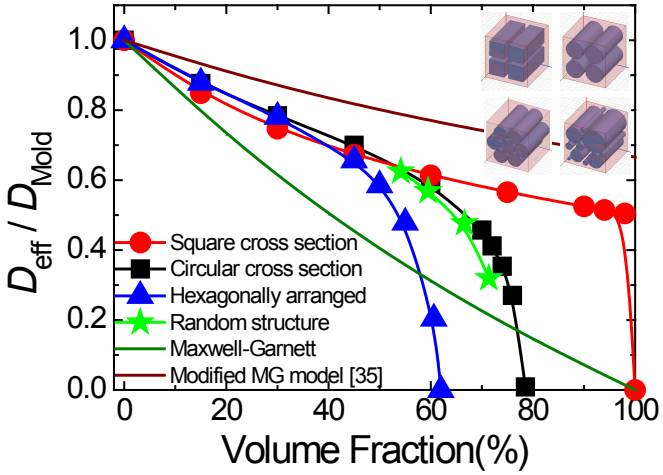

Fig. 5.6. Numerical simulation results of D_{eff} for different geometries. Hexagonally arranged cylindrical fillers exhibits maximum moisture suppression. (inset) Simulated structure for simulations (counter clockwise from top right): circular cross section, square cross section, hexagonally arranged, random structure.

5.2.3 Fillers configuration optimization

Since classical composites (with spherical inclusion) is an ineffective moisture barrier, it is worthwhile to see if the performance can be improved with non-spherical fillers. To calculate D_{eff} associated with elongated inclusion, for example, we consider

rod-like fillers with circular and square cross-sections, arranged either periodically (hexagonal) or randomly (see Fig. 5.6a). The same numerical algorithm discussed in Sec.5.2 was used to calculate D_{eff}. Remarkably, as the cylinders begin to touch at critical volume fraction ($\phi_c \ll 1$), D_{eff} begins to drop dramatically, as the paths to moisture diffusion are completely cut-off. Inclusions with circular cross-section is most effective, as they reduce the $D_{\text{eff}} \to 0$ only at $\phi_c = \pi/4$, see Fig. 5.6b. Actual geometry of aligned rod-like filler geometry is also realistically attainable [36,37]. A randomly filled rod-shaped inclusion would reduce D_{eff} at even lower ϕ_c. Thus, aligned rod-like fillers can be an optimum geometric condition for efficient moisture blockage even by lower filler volume fraction.

It is clear from Fig. 5.7 ($D_m = 1 \times 10^{-12}\text{cm}^2/\text{s}$, and thickness $500\mu m$), that unless D_{eff} must be reduced by $\sim$75% for significant improvement in moisture diffusion time. Under same filler volume fraction condition, the symmetric 3D fillers (black box) would not do; but asymmetric fillers (red box) may help.

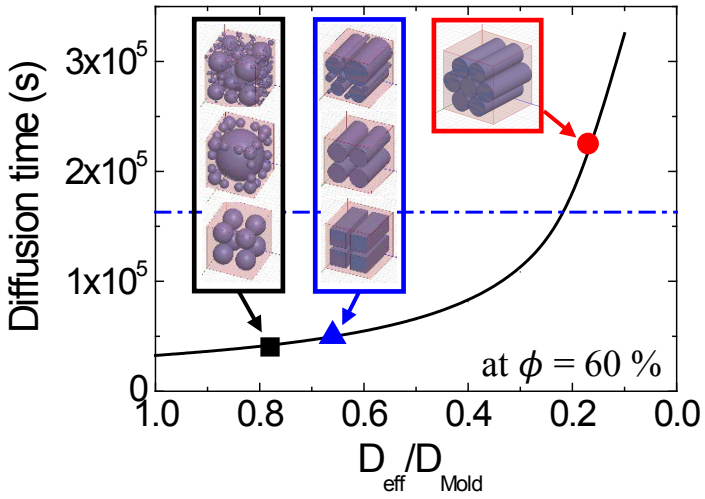

Fig. 5.7. Calculated diffusion time as a function of reduced diffusivity by using PDEtool Matlab, dotted line indicates 5 times longer than that of the case with no filler.

Generalized model for all volumetric fraction

When ϕ_f becomes larger and larger so that fillers are densely packed to affect dipoles on each filler, diffusion channels will be start to close gradually. Although it would be difficult to fully close the diffusion channels by spherical fillers, deviation from modified MG model is not simple to describe as a function of ϕ_f as shown in Fig. 5.4, and 5.6. Considering diffusivity of water in polymer is much larger than that of in silica, we can view this case as a a perfect contrast phase system. In this case, effective properties depend primarily on network connectivity, as in the case of percolation theory [148]. For these systems, McLachlan developed generalized effective medium (GEM) theory by introducing the percolation threshold and scaling exponents into the symmetric EMT equation as shown in Eq. 5.3 [149–151]. Based on this model, the correlation between D_{eff} and ϕ_f for moderate fraction or even lower fraction case (i.e., modified MG model) can be also described as follows.

$$\phi_f \frac{D_f^{\frac{1}{t}} - D_{eff}^{\frac{1}{t}}}{D_f^{\frac{1}{t}} + (p_c^{-1} - 1) D_{eff}^{\frac{1}{t}}} + (1 - \phi_f) \frac{D_m^{\frac{1}{s}} - D_{eff}^{\frac{1}{s}}}{D_m^{\frac{1}{s}} + (p_c^{-1} - 1) D_{eff}^{\frac{1}{s}}} = 0 \tag{5.3}$$

where D_m, D_f, ϕ_f, p_c, s, and t are water diffusivity in the mold, in the fillers, filler volume fraction, void percolation threshold (from mold perspective), and empirical fitting parameters, respectively. Although the model is empirical, its predictions have validated both experimentally and numerically [152, 153]. When water cannot reside within fillers: a typical condition for MCs, we can set D_f to 0. In this special case and for low-to-moderate fill fraction (e.g., $\phi_f = 0 \sim 60\%$), Eq. 5.3 is numerically identical to modified Maxwell-Garnett (MG) model described in section 5.2.1. As ϕ_f approaches to 1-p_c, the curve deviates from modified MG model and eventually, D_{eff} becomes zero after 1-p_c. Especially for the high ϕ_f case, the feasibility of Eq. 5.3 requires well-defined parameters (i.e., s, t, and p_c) for an accurate prediction.

We know that $p_c \sim 60\%$ [154] for a MC randomly (but loosely) packed with single-sized spheres. Indeed, the highest periodic packing density for the mono-size sphere system is given by the Kepler limit: $\pi/3\sqrt{2} \sim 74\%$ [155]. Since the void percolation

threshold (p_c) for mono-sized spheres is ∼3% [156], therefore $\phi_f \ll 1 - p_c$, and thus a MC with mono-size fillers cannot serve as an effective moisture barrier for an IC. For more effective moisture suppression, one can either (a) increase p_c by adding rod-like fillers as we have shown in the previous section or (b) increase ϕ_f by embedding poly-disperse fillers as in Fig. 1b. For the first strategy, it is easy to calculate the maximum packing density (ϕ_f^{Max}), and p_c associated with infinitely long elongated fillers (i.e., circles packing in a square, 2D system). Although the approach can suppress moisture diffusion very effectively, there are practical difficulties in using long aspect-ratio rod-like fillers in a MC. In practice, the second strategy based on poly-disperse fillers is easier to implement. Here, $\phi_f^{Max} = 0.8 \sim 0.85$ as shown in [157, 158]. p_c of poly-disperse fillers is expected to be larger than 3-5% (mono-sized spherical or ellipsoidal particles), its precise value has not been reported. In this work, we assume that the poly-disperse fillers increase p_c to 10%. Also, based on Ref. [35, 137, 138], the exponents s and t are set to 0.3, and 1, respectively. We will use these three values for s, t, and p_c in Eq. 5.3 to calculate moisture D_{eff} in a poly-disperse MC. We will see later that the corresponding suppression of diffusion close to 1-p_c is essential to describe the experimental results correctly.

5.3 Water mass gain analytical models

Once D_{eff} of water can be defined based on Eq. 5.3, we can describe water uptake mass gain curve based on the analytical model shown below. Mass gain curve also can be investigated experimentally, namely, gravimetric curves inform absorption kinetics when water molecules are absorbed by a material. Two main analytical models are widely have used for the studies: Fickian model, and Langmuir model.

5.3.1 Traditional models for water mass gain

Classical Fickian model

Water diffusion as a result of random molecular motions in a polymer can be modeled by Eq. 5.4, derived by combining the Ficks law and continuity equation.

$$\frac{\partial w}{\partial t} = \nabla \cdot (D_{\text{eff}} \nabla w) \tag{5.4}$$

where D_{eff}, and w are diffusivity, and water concentration, respectively. Fickian model assumes the water flux depends on the magnitude of the concentration gradient of water $(-\nabla w)$. Integration of Eq. 5.4 over the thickness (L) yields fractional mass uptake analytic model as shown in Eq. 5.5 [159, 160].

$$\frac{M_{\text{t}}}{M_{\infty}} = 1 - \frac{8}{\pi^2} \sum_{n=0}^{\infty} \frac{1}{(2n+1)^2} e^{\frac{-D_{\text{eff}}(2n+1)^2 \pi^2}{4L^2} t} \tag{5.5}$$

where M_{t} is $(W_{\text{t}} - W_0)/W_0$. W_{t}, and W_0 are the sample weight after time t, and initial sample weight, respectively. Thus, M_{t}, M_{∞} corresponds to the ratio of absorbed water weight to initial weight at time t, and $(W_{\infty} - W_0)/W_0$, respectively. Fickian model anticipates that M_{t} increases linearly with the square root of time, and then saturates when equilibrium is reached, see Fig. 5.8. As shown in Fig. 5.8, Fickian model does not adequately describe the slow-saturation regime of water uptake. This two-phase water uptake (namely, simple diffusion followed by slow quasi-saturation) has been reported by many groups [139–141, 161, 162]. Therefore one needs an improved model that will capture both phases of water-intake.

'Bulk' Langmuir model

This model describes the diffusion of water molecules as they repeatedly react with polymer chains so that water molecules exist either in w, or in Y phases. The transport is described by Eq. 5.6.

$$\frac{\partial w}{\partial t} = \nabla \cdot (D_{\text{eff}} \nabla w) + r_{\text{w}} \tag{5.6a}$$

$$r_{\text{w}} = -r_{\text{Y}} = -k_{\text{F}} \cdot w + k_{\text{R}} \cdot Y \tag{5.6b}$$

where k_{F}, and k_{R} are forward and reverse reaction rates for the chemical reaction (i.e., $w \rightleftharpoons Y$), respectively. In this case, the water uptake analytical model can be shown by Eq. 5.7 [143].

$$\frac{M_{\text{t}}}{M_{\infty}} = 1 - \frac{k_{\text{F}}}{k_{\text{F}} + k_{\text{R}}} e^{-k_{\text{R}} t} - \frac{8 k_{\text{R}}}{(k_{\text{F}} + k_{\text{R}})\, \pi^2} \sum_{n=0}^{\infty} \frac{1}{(2n+1)^2} e^{\frac{-D_{\text{eff}} (2n+1)^2 \pi^2}{4L^2} t} \tag{5.7}$$

Langmuir model is widely used because it describes the quasi-saturation of the gravimetric curves [142, 143, 163, 164]. Indeed, many experiments have demonstrated

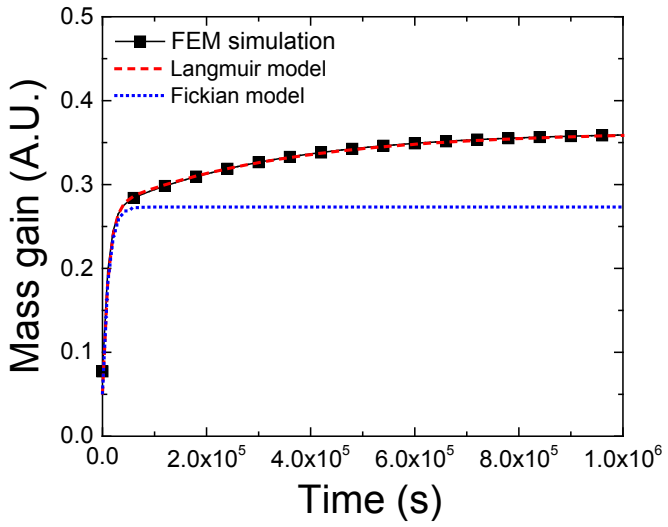

Fig. 5.8. Comparison between detailed FEM simulation [145], Fickian model, and Langmuir model based on the predefined parameters shown in the table 5.1.

a two-stage water uptakes behavior and many authors proposed several hypotheses [165–167] regarding the specific reactions involved. Although the hypotheses are not the same, however, there is a consensus that anomalous water diffusion must be described based on a diffusion-reaction scheme, such as Eq. 5.6.

Table 5.1.
Inputs parameters for simulation

Parameter	Value	Parameter	Value
Area, L $[cm^2, \mu m]$	$4.5^2, 750$	mass [g]	2.5
D_0 $[m^2 \cdot s^{-1}]$	5×10^{-12}	S_0 $[mol \cdot m^{-3} \cdot Pa^{-1}]$	5×10^{-3}
R_0 $[mol \cdot m^{-3}]$	1000	S_1 $[Pa^{-1}]$	1×10^{-6}
k_{F} $[s^{-1}]$	1×10^{-6}	k_{R} $[s^{-1}]$	3×10^{-6}

With the parameters shown in table 5.1, gravimetric curve by FEM simulation introduced in [145], and two analytical models are compared. Detail information regarding the parameters can be found in [145]. Even after the saturation, the additional mass gain due to the reaction is observed. By applying Langmuir model, the gravimetric curve can be estimated precisely for a MC whose parameters are predetermined. However, if the parameters are not known in advance due to different filler configuration or absolute relative humidity (RH), gravimetric curves cannot be predicted. In the following section, we will generalize the Langmuir model so that it can predict the water-uptake for MCs with arbitrary filler fraction, subjected to different RH.

5.3.2 Proposed generalized effective medium & solubility ($GEMS$) Langmuir model

If the chemical components composition of the polymer matrix (e.g., hardener, adhesion promoters, and other additives) is identical, then k_{F} and k_{R} would not change. Among other parameters, the amount of filler affects D_{eff} in MCs, environmental conditions affect the value of M_{∞}, as discussed below.

D_{eff} definition

Among analytical models discussed in sec. 5.2, we applied Eq. 5.3 for our $GEMS$-Langmuir model. Once we extract the D_{eff} of a composite material based on the gravimetric curve, we will be able to estimate D_{eff} of any MC with different filler fraction based on Eq. 5.3.

M_{∞} definition

The relationship between RH and the maximum water concentration (w_{Max}) in a mold can be determined by Henrys law ($w = S^{*} \cdot p_{\mathrm{w}}$, where S^{*}, and p_{w} are solubility of water in the polymer, and partial pressure in the environment, respectively). Once we know w_{Max}, M_{∞} can be calculated by multiplying water molar mass (18[g/mol]), and volume of the MC [cm^3] as shown in Eq. 5.8.

$$p_{\mathrm{w}} = a_{\mathrm{w}} \cdot e^{13.756 - \frac{m}{T}} \tag{5.8a}$$

$$W_{\infty} = S^{*} \cdot p_{\mathrm{w}} \cdot 18 \cdot V \tag{5.8b}$$

$$S^{*} = S^{\mathrm{ref}} \cdot \frac{1 - \phi_{\mathrm{f}}^{*}}{1 - \phi_{\mathrm{f}}^{\mathrm{ref}}} \tag{5.8c}$$

p_{w} [Pa] can be expressed by assuming the vapor pressure of water satisfies Rankines formula as shown in Eq. 5.8a (i.e., general equation), where m (5120 [145]) is a specific constant for each substance. Water activity factor (a_{w}) in the environment can be defined as 0.4, 0.6, and 0.9 for RH of 40%, 60%, and 85%, respectively, based

on the observation in the literature that shows a_{w} is always smaller than unity [145], and increases with as RH increases. In this work, $S^{*}\,[mol \cdot m^{-3} \cdot Pa^{-1}]$ is assumed to have a linear relationship with ϕ_m for a given unit volume of MC as shown in Eq. 5.8c. Once we obtain S^{ref} from the experiment data of the given sample ($\phi_{\mathrm{f}}^{\mathrm{ref}}$), we can estimate S^{*} of the any given MC (ϕ_{f}^{*}) with arbitrary ϕ_{f}.

Finally, D_{eff} and M_{∞} in Eq. 5.7 can be revised to Eq. 5.3, and Eq. 5.8b ($M_{\infty} = (W_{\infty} - W_0)\,/W_0$) that enclose the information of MCs filler configuration and RH of the environment. In this paper, we applied these revised parameters in conventional Langmuir model, and refer to $GEMS$-Langmuir model. In the following section, the analytical $GEMS$-Langmuir model is validated by detailed FEM simulation.

5.4 $GEMS$-Langmuir model validations

5.4.1 Numerical simulations

Detailed 2D FEM simulation based on the scheme described in [168] and $GEMS$-Langmuir model are compared as shown in Fig. 5.9. Different ϕ_{f} results in a different D_{eff}, so that at a certain time, the amount of water uptake is reduced if the ϕ_{f} is increased, as shown in Fig. 5.9a, top, where a fixed RH=85% is assumed. Also, different RH results in different water surface concentration so that higher RH results in a larger amount of diffused water at a given time, see Fig. 5.9a, bottom (fixed ϕ_{f}). If we plot a gravimetric curve for a longer timescale for every case, FEM simulation results and analytical $GEMS$-Langmuir model show a good match as reported in Figs. 5.9b and 5.9c. As a result, once we extract all the parameters from just one experiment, we can predict transient water uptake behavior for any given filler amount of MCs and RH in the environment. For a better appreciation of the model, we apply the model to the actual experimental data and reassessed.

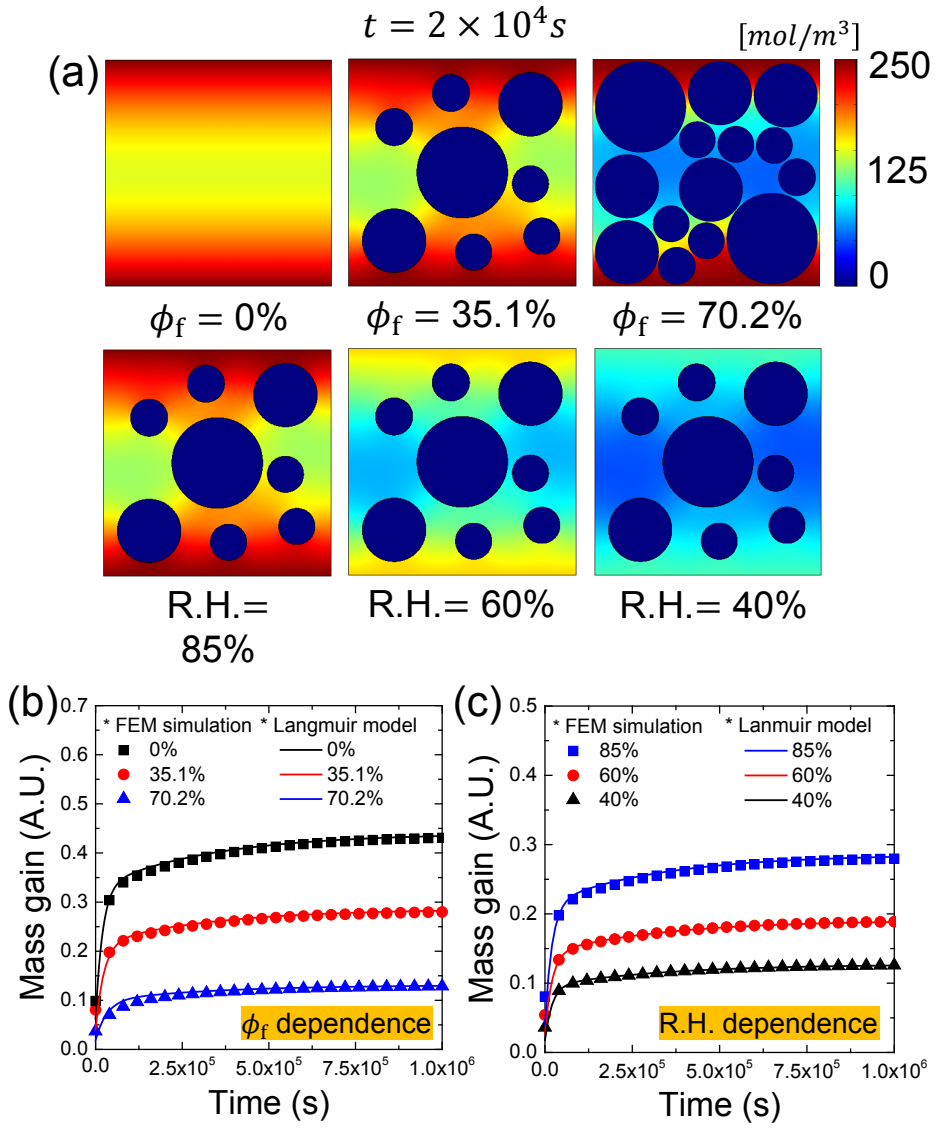

Fig. 5.9. Water (w) concentration comparison profile comparison for different ϕ_f, and RH at $t = 20000s$. Detailed FEM simulation and analytic gravimetric curve based on $GEMS$-Langmuir model comparison for different (a) ϕ_f, and (b) RH (ϕ_f=35.1% case).

5.4.2 Water uptake experiments

Different encapsulation materials have been used in this study to validate the proposed model. They are epoxy-based MCs employed in IC packaging, containing different fractions of silica micro-fillers. The weight in dry conditions of each sample

Table 5.2.
Filler configuration and geometric information of MCs used in this work for mass gain experiments.

	M73	M90	M91	MX87
Mass [g]	4.88	5.54	5.72	5.66
Size $[mm^3]$	$59 \times 64 \times 0.75$	$59 \times 64 \times 0.75$	$59 \times 64 \times 0.75$	$\pi 22.5^2 \times 2$
Filler amount [%]	73 / 60 (wt./vol.)	90 / 83 (wt./vol.)	91 / 84 (wt./vol.)	87 / 74 (wt./vol.)
Filler size $[um]$	∼20 / ∼75 (avg./max.)	∼25 / ∼135 (avg./max.)	∼20 / ∼75 (avg./max.)	∼20 / ∼75 (avg./max.)

is reported in Table 5.2, along with the dimensions of each measured bulk sample, and the different amount and size of the fillers. In this work, ϕ_f of the sample is varied from 60 to 84%. Polydisperse-size distribution of the fillers allows ϕ_f to reach up to 84% [157] which is much larger than that of the maximum ϕ_f (64%) in the case of monodisperse spheres system.

The moisture absorption of the EMCs has been investigated by our collaborator [169] using a climatic chamber (Genviro-060-C) to control the temperature and the relative humidity. Before moisturizing treatments, the samples have been dried at 125 °C for 24 hours to remove any residual humidity and weighted with an analytical balance (Sartorius CP 124 S) with an accuracy of 0.0001 g to determine their dry weight M_0. Subsequently, the samples have been placed into the climatic chamber at 85 °C with two different RH conditions (i.e., 60% and 85%) and periodically weighted until equilibrium was reached. The measurements have been carried out by following the test methods specified in [170].

In Eq. 5.3, k_F, k_R, D_{eff}, and S^* (included in M_∞) are empirical fitting parameters, and rest of other parameters (W_0, V, and p_w) can be known prior to an experiment. Based on our water uptake experiments, fitting parameters are extracted by a non-linear least squares regression curve fitting tool, available in MATLAB [171]. After parameters extraction, we predict gravimetric curve of different MCs under different humidity.

Relative humidity dependence

First, k_F, k_R, D_{eff}, and S^* of M90 are extracted based on experimental data at 85 °C and 85% of RH Based on $GEMS$-Langmuir model, we can now estimate water uptake behavior in a different condition. As shown in Fig. 5.10, experiments and analytic estimation for RH of 60% exhibit a good match. In the following section, the analytic estimation of MCs with different filler amount, and different size are done and compared with experiments.

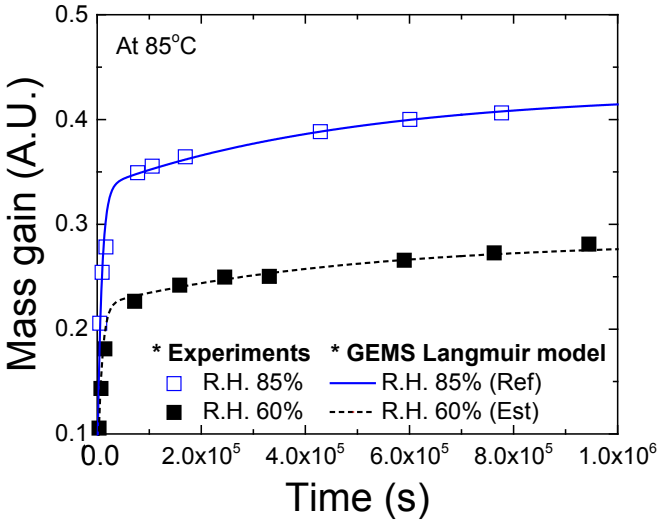

Fig. 5.10. Experimental validation of $GEMS$-Langmuir model when RH is varied.

Filler size and fill fraction dependence

The goal of this section is to show a single-sample analysis based on Eqs. 5.3 and 5.8 produces the equivalent information as many-sample analysis based on Eq. 5.7. Among the parameters of the Eq. 5.7, the four parameters (k_{F}, k_{R}, D_{eff} (ϕ_{f}), and S^{*}, included in M_{∞}) are obtained by fitting the experimental data for each sample (with known ϕ_{f}), while the remaining three parameters (W_0, V, and p_{w}) are known a-prior. All experiments are done at 85 °C and 85% of RH as shown in Fig. 5.11. The fitting parameters are extracted by a nonlinear least squares regression curve fitting tool, available in MATLAB [171]. These empirically fitted parameters are then compared with the predictions of *GEMS*-Langmuir model equations (i.e., Eq. 5.3, and Eq. 5.8b) to validate the model. Fig. 5.12 shows that *GEMS*-Langmuir model anticipates very well the parameters obtained by fitting the experimental data from many samples. Thus validated, *GEMS*-Langmuir model obviates the need for testing multiple samples. The fitting of the measured data by the generalized theory allows us to carefully explore the functional dependencies observed in the experiments, as follows.

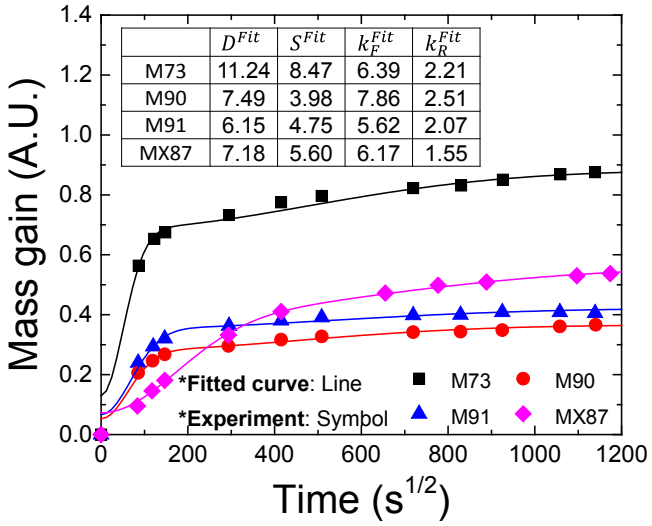

Fig. 5.11. water uptake experiment and fitted parameters of all MCs.

Extracted parameters

Surprisingly, even with different size distribution, the similarity of D_{eff} for M90 and M91 samples further validates the effective medium theory (EMT) which is used to calculate D_{eff} (ϕ_{f}) introduced in section 5.2.1, as shown in Fig. 5.12a. As we mentioned in sec. 5.2, the high-ϕ_{f} transition behavior (i.e., downward deviation from modified MG model) around p_{c} is well captured by GEM model developed by McLachlan [149–151]. Unlike D_{eff}, S^* defines the local maximum available water amount, and it is not the parameter that distorts the concentration field in a composite material. Consequently, as shown in Fig. 5.12b, we anticipate a simple linear relationship (e.g., the slope of 0.021) between ϕ_{f} and S^* as shown in Eq. 5.8c.

Before the chemical reaction reaches its equilibrium, the ratio k_{F} to k_{R}(i.e., $k_{\text{F}}/k_{\text{R}}$) indicates the efficiency of Y generation. k_{F} of all samples are nominally identical, see Fig. 5.12c. However, in the case of $k_{\text{F}}/k_{\text{R}}$, MX87 shows the largest value implying the concentration of Y is higher than the rest of the MCs as shown in Fig. 5.12d. This is caused by excess reactive sites due to the absence of the adhesion promoter. In conclusion, for the same chemical composition MCs, once we extract parameters from a gravimetric curve of a MC, we can predict water uptake behavior of other MCs with different ϕ_{f}, or under different RH In the following section, we investigate the optimization of filler configuration for reliable HV-ICs encapsulant based on parameters extracted based on $GEMS$-Langmuir model, and electric-field distribution simulation.

5.5 Fillers impact on dissipation factor and critical electric field

Among many reliability issues, the HV-ICs encapsulant has to meet both low electrical conductivity (σ) and high dielectric strength to sustain high voltage applied during operation [172]. It is important to lower σ of MCs for a better HV-ICs encapsulant because high σ may cause significant charge injection from electrodes [173], accelerated charges migration [174], and higher energy loss in AC circuit [175].

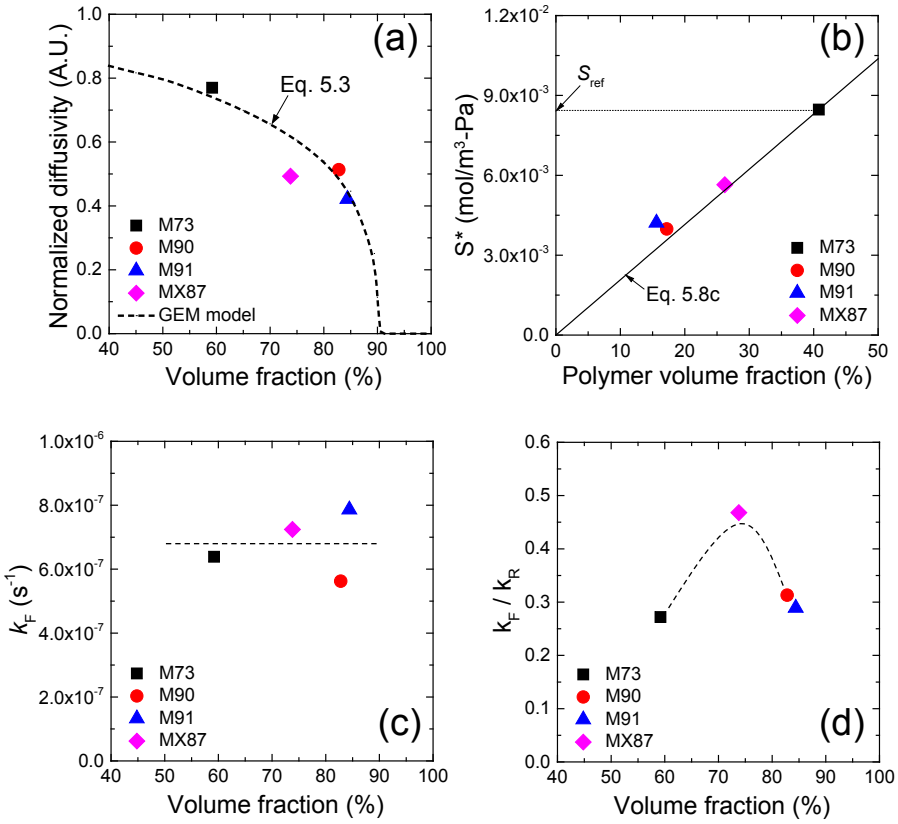

Fig. 5.12. (a) Extracted D_{eff} exhibits clear agreement with Eq. 5.3, where the value of s, t, and p_c are 0.3, 1, and 0.9, respectively. The correlation is similar to the work shown in [35,137,138]. (b) Validation of linear correlation between S^* and ϕ_m. (c) Extracted k_F exhibits similar for all MCs. (d) k_F/k_R for M73, M90, and M91 are similar, but differs from the sample without adhesion promoter (MX87).

5.5.1 Electrical conductivity

Electrical measurement experimental data is obtained from our collaborator [176]. In order to measure the steady state conductivity of the materials, a DC step voltage has been applied across the samples and the resulting current has been monitored with a Keithley-6514 electrometer for 1000 seconds into a thermostatic oven. The measurement time is long enough to separate polarization effects and carrier conduction, but short enough to avoid any significant moisture desorption during the

measurement. The conductivity has been extracted from the steady-state current I as: $\sigma = I \cdot h/(A \cdot V)$, where h, V, and A are the thickness of the sample, the applied voltage, and the area of the electrodes, respectively. All the measurements have been obtained by applying a step voltage of 3 kV, corresponding to an electric field of about $4kV/mm$ and the experimental setup allows to measure a minimum conductivity of about 10^{-19}S/cm. The analysis has been carried out on a sample of each material both in dry and under humidity in saturation conditions at the temperature of 25 °C.

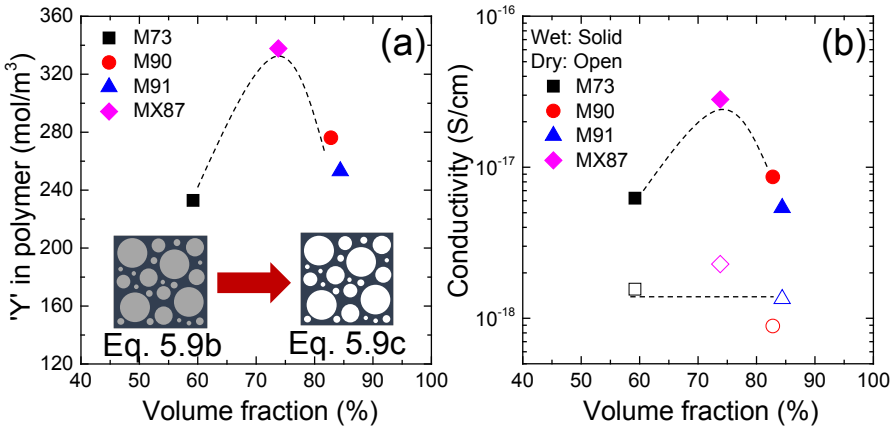

Fig. 5.13. (a) Actual calculated Y within mold by taking normalization of ϕ_{m} since Y cannot exist within filler. (b) σ extracted from DC current experiments. Considering log-scale, the difference between dry MCs is negligible. However, wet MX87 shows much higher σ than that of wet M73, M90, and M91 due to higher Y_{m}.

Although many experiments have focused on water uptake epoxy MCs, the role of water in defining σ is not fully understood [177, 178]. A recent work shows that hydrolysis, and the reaction between moisture and anhydride groups (Y) increase $\sigma(Y)$ significantly, whereas the effect of mobile water (w) is negligible [179]. In this work, we estimate Y concentration analytically and correlate the concentration to the

conductivity measurement. Based on the extracted parameters from section 5.4.2, we can calculate Y concentration as follows.

$$w + Y = \frac{W_\infty - W_0}{18 \cdot V} \tag{5.9a}$$

$$Y = (w + Y) \cdot \left(\frac{k_\mathrm{F}/k_\mathrm{R}}{1 + k_\mathrm{F}/k_\mathrm{R}} \right) \tag{5.9b}$$

$$Y_\mathrm{m} = \frac{Y}{1 - \phi_\mathrm{f}} \tag{5.9c}$$

where $W_\infty - W_0$ $[g]$, 18 $[gmol]$, and $V[m^3]$ are mass gain due to water, water molar mass, and sample volume, respectively. From mass gain experiments, we can calculate the sum of reacted and free water concentration ($w + Y\,[mol/m^3]$) within the MC, see Eq. 5.9a. Based on Eq. ($Y = w \cdot (k_\mathrm{F}/k_\mathrm{R})$, at steady state), Y concentration is obtained by multiplying the term in the second parenthesis of Eq. 5.9b. Finally, Eq. 5.9c determines Y within the mold (Y_m) by normalizing with $1 - \phi_\mathrm{f}$, since silica fillers are impermeable to water molecules. This explains why MX87 has the highest Y_m although M73 has the highest water gain (Fig. 5.11).

Adhesion promoter effect

Even though M73 show the highest absorbed water content, the σ measurements show the highest in MX87 as shown in Fig. 5.13b. Furthermore, Figs. 5.13 shows that Y_m calculated from theory and wet σ measured from the experimental data are directly correlated. Therefore, we conclude that adhesion promoter is essential to lower $\sigma(Y_\mathrm{m})$ by reducing available reactive sites, and Y byproduct after water uptake in a polymer-based encapsulant.

Filler volumetric fraction effect

In sec. 5.3, we observed the impact of ϕ_f on D_eff, and S^*. Thus, Y increasing over time before characteristic time (i.e., $0.67 \cdot L^2/D$, the time when water saturates the sample) also depends on ϕ_f. In a longer time scale, however, ϕ_f impact on Y_m

content is actually negligible as shown in Fig. 5.13a. In other words, the total water content is higher for MCs the lower ϕ_f, however, the concentration of Y_m in the polymer can eventually be quite similar. Thus, ϕ_f-optimization should focus on other properties (e.g., higher thermal conductivity, higher stiffness, and lower dielectric constant) rather than σ in a humid environment [180–182].

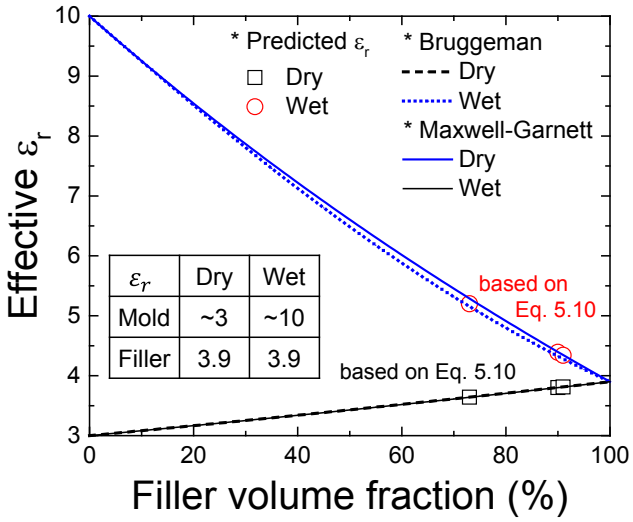

Fig. 5.14. Calculated ε_{eff} based on EMT model, validated in our previous work [41]. The difference between MG model, and Bruggeman model is insignificant due to small contrast ratio between ε_f, and ε_m. Thus, both model can be applied to estimate ε_{eff} of MCs.

5.5.2 Effective dielectric constant

Our previous experiments [41,183] have shown that an effective dielectric constant (ε_{eff}) of MC can be predicted by an appropriately generalized EMT model. There are

two widely known EMT models: Maxwell-Garnett (MG) model [31], and Bruggeman model [34] as shown in Eq. 5.10.

$$\varepsilon_{\text{eff}} = \varepsilon_{\text{m}} \left[1 + \frac{3\left(\varepsilon_{\text{f}} - \varepsilon_{\text{m}}\right)\phi_{\text{f}}}{\varepsilon_{\text{f}} + 2\varepsilon_{\text{m}} - \left(\varepsilon_{\text{f}} - \varepsilon_{\text{m}}\right)\phi_{\text{f}}} \right] \tag{5.10a}$$

$$\phi_{\text{f}} \frac{\varepsilon_{\text{f}} - \varepsilon_{\text{eff}}}{\varepsilon_{\text{f}} + 2\varepsilon_{\text{eff}}} + \left(1 - \phi_{\text{f}}\right) \frac{\varepsilon_{\text{m}} - \varepsilon_{\text{eff}}}{\varepsilon_{\text{m}} + 2\varepsilon_{\text{eff}}} = 0 \tag{5.10b}$$

where ε_{f}, and ε_{m} are dielectric constant of filler, and mold, respectively. The MG model calculates the filler polarization induced by the external field, and presumes the dipole on one quasi-spherical filler does not affect its neighbors. Thus, the model is accurate when ϕ_{f} is low. On the contrary, Bruggeman model accounts for the calculation at high ϕ_{f}, namely, aggregate structure. We note that Eq. 5.10b can be derived from Eq. 5.3 by putting 1, 1, and 1/3 into s, t, and p_{c}, respectively. Thus, Bruggeman model is appropriate for low-contrast systems where percolation behavior is insignificant. The difference between MG, and Bruggeman model becomes considerable when ε_{f} differs significantly from ε_{m}. In the case of typical commercial MC with SiO_2 fillers, the dielectric contrast is small for both dry and wet conditions. Thus, the two models result in almost identical curves as shown in Fig. 8. Therefore, we can estimate ε_{eff} of a MC either by the MG model or the Bruggeman model.

5.5.3 Dielectric strength of mold compounds

In order to study the impact of filler configuration on dielectric strength of MC, ($E_{\text{MC}}^{\text{Crit}}$ i.e., VL), we compare the local field distribution within each sample by FEM simulation [184–186]. The dielectric strength is an intrinsic property of a material (e.g., dielectric strength of SiO_2 ($E_{\text{f}}{}^{\text{Crit}}$), and epoxy ($E_{\text{m}}{}^{\text{Crit}}$) are $\sim 5MV/cm$ [187], and $\sim 0.5MV/cm$ [188], respectively). If the local maximum electric field inside the epoxy (E_{Max}) exceeds $E_{\text{MC}}^{\text{Crit}}$, the MC will break [189]. The E_{Max} will vary depending on the filler configuration so that comparison of electric field cumulative distribution function around E_{Max} ($F(E)$) is crucial to evaluate $E_{\text{MC}}^{\text{Crit}}$ for each MC with different fillers configuration, or different surrounding environment. For example, if $F(E)$ of

sample A exhibits less E_{Max} (i.e., electric field strength at the cumulative percentage of 100%) than that of sample B, $E_{\mathrm{MC}}^{\mathrm{Crit}}$ of sample A will be stronger. Simulated structures are constructed based on the actual configuration (e.g., ϕ_{f}, and the average diameter of the fillers) to emulate real samples as shown in Fig. 5.15a. This simplified geometry can be also used for the actual case studies based on the fact that nearest neighbor function between an actual and a simplified structure exhibits similarly [46].

Adhesion promoter effect

When the sample is dried, ε_{m}, and ε_{f} are $\sim$3.0, and 3.9, respectively, so that the ratio of ε_{f} to ε_{m} is greater than 1. However, when the sample is exposed to a humid environment, considering ε_{r} of water is around 80 at room temperature, the ratio will be smaller than 1. As more water is absorbed into the sample, smaller the ratio will be. Electric field distributions for the different ratio is shown in Fig. 5.15b. All situations exhibit two main peaks in the electric field distribution [190, 191]. The left and the right side peaks correspond to the region with higher ε_{r} and lower ε_{r} regions, respectively. As water content builds within the sample, we observe that the main peak gradually shifts to the right and the cumulative tail around E_{Max} gradually extends. Consequently, the water content $(w+Y)$ increases E_{Max} of the sample so that $E_{\mathrm{MC}}^{\mathrm{Crit}}$ will become weaker. In other words, reducing Y by adding adhesion promoter will further enhances $E_{\mathrm{MC}}^{\mathrm{Crit}}$.

Filler configuration effect

When the sample is dried, the experiments show a decrease in $E_{\mathrm{MC}}^{\mathrm{Crit}}$ with increasing ϕ_{f} [31,34]. Similarly, our simulations show that E_{Max} of M90, and M91 is higher than that of M73, see Fig. 5.15c. However, once ε_{m} becomes larger than that of ε_{f} due to water ingress, E_{Max} of M73 becomes higher than that of M90, and M91 as shown in Fig. 5.15d. Compared to the dry samples, electric field distribution under the wet condition is reversed as shown in Fig. 5.15a. Even if ϕ_{f} is the same, electric

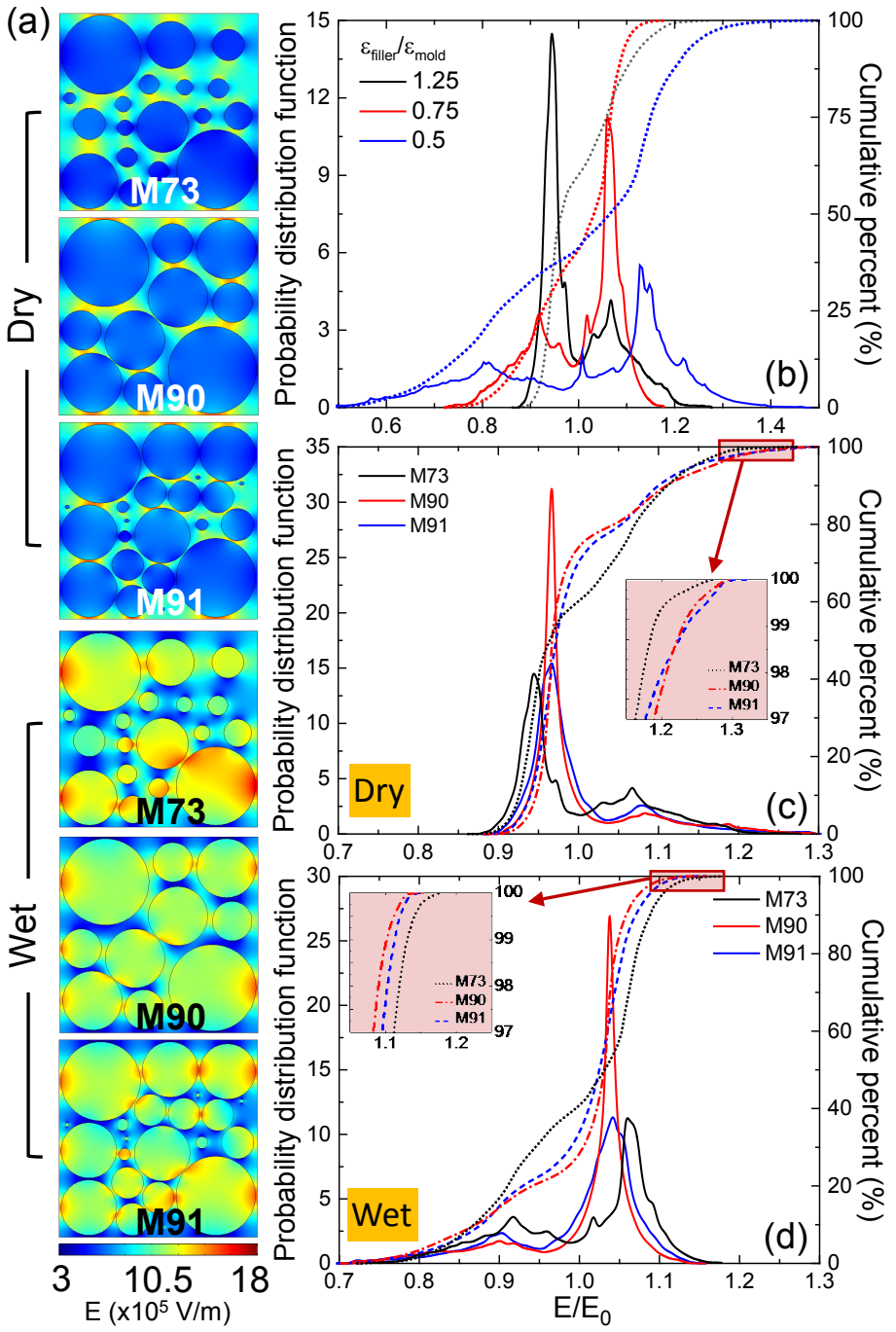

Fig. 5.15. (a) 2D FEM simulation showing electric field distribution. Comparison of electric field cumulative distribution depends on (b) different water amount in polymer (c) different MCs at dry condition (d) different MCs at wet condition. In dry case, lower ϕ_f (M73) exhibits the strongest E_{MC}^{Crit}. However, M73 shows the weaker E_{MC}^{Crit} when the MC absorbs moisture.

field distribution can be different if the size distribution is dissimilar. When the average radius is larger (e.g., M90), the distribution for the main peak in the filler-phase exhibits narrower peak. Based on the nearest surface distribution function, we realize that bigger particles have more probability of having more neighbors a shorter distance away [192], resulting in a concentrated distribution due to the filler phase. However, the tail of the right side distribution which determines maximum electric field does not change significantly with different filler-size distribution. Therefore, ϕ_{f} should be carefully optimized depending on the severity of humid environment: in a dry environment, lower ϕ_{f} samples are preferred, whereas, in a humid environment, higher ϕ_{f} samples would be more reliable.

5.6 Conclusions

Among many encapsulant properties, achieving lower dissipation factor, and higher $E_{\mathrm{MC}}^{\mathrm{Crit}}$ are important for HV-ICs applications. In this paper, we show $GEMS$-Langmuir model can predict the water uptake behavior for MCs with any filler configuration under a variety of environmental conditions. We also compared electric field distribution for each MC in both dry and wet environment. Based on the $GEMS$-Langmuir model and experiments, we find that 1) reacted water (rather than mobile water) plays a dominant role in determining σ of MCs; 2) adhesion promoter is essential for lower σ, and higher $E_{\mathrm{MC}}^{\mathrm{Crit}}$ in humid environment; 3) ϕ_{f} does not impact on σ significantly, however, it needs to be carefully optimized for higher $E_{\mathrm{MC}}^{\mathrm{Crit}}$ depends on the severity of humidity. Once all the parameters are known from mass gain experiments, $GEMS$-Langmuir model provides a deep and fundamental new insight regarding the physics of moisture transport in MCs. The model will also be useful initial optimization of MCs for other applications involving polymer encapsulants, e.g., solar cells and biosensors.

6. CHIP-PACKAGE INTERACTION: MOISTURE-ASSISTED ION TRANSPORT IN MOLD COMPOUNDS

6.1 Introduction

Space charge accumulation in an encapsulant distorts the internal electric field as shown in Fig. 6.1a-6.1d. The increased field can shorten dielectric lifetime by partial discharge, electrical tree growth, breakdown of the dielectric [193]. Ever since

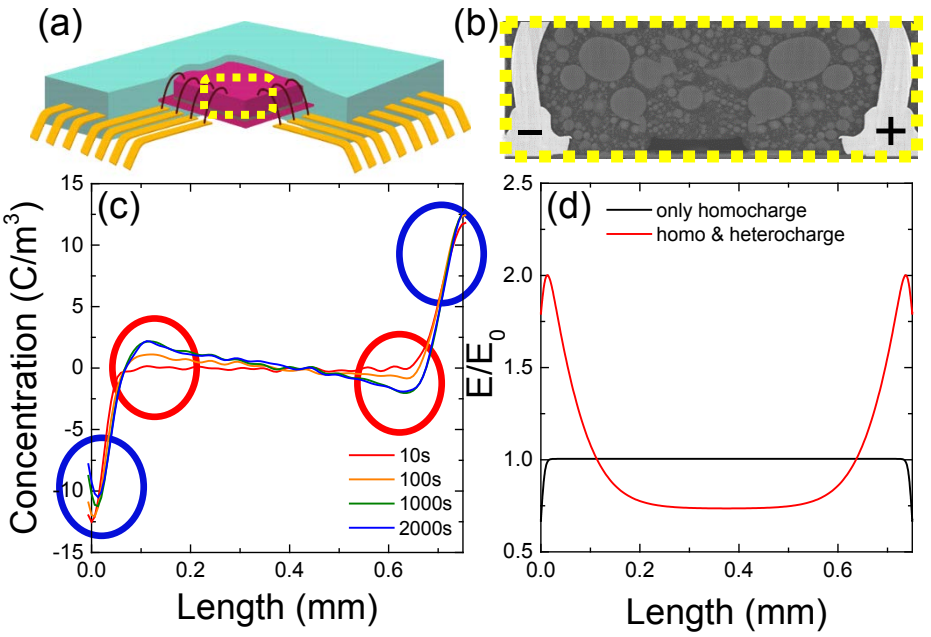

Fig. 6.1. (a) 3D schematic of Quad Flat Packaged device encapsulated with molding compounds. (b) SEM image of cross-section view of a commercial micro-composite material. (c) Example of PEA measurement data. Blue , and red circles indicates homo-charge, and hetero-charge, respectively. (d) Electric field distribution schematic in the case of different charge accumulation.

Langmuir [194] first recognized the existence of charges injection from electrode, these reliability problems due to space charge injection have been studied extensively by various groups. After the first establishment of non-desctructive method in 1976 [195], many measurement techniques (e.g. thermal, acoustic, and optical) have been invented, implemented, and validated [196]. Among them, the pulsed electro-acoustic (PEA) measurement is widely used due to its simplicity and robustness as well as its ability to map spatially-resolved time-dependent charge injection into the dielectric [197].

An example of the space charge distribution measured by the PEA technique is shown in Fig. 6.1c. Generally, once the voltage is applied, two types of charges (i.e. homo-charge and hetero-charge) may accumulate at the electrode/dielectric interface. The homo-charge (i.e., blue circles in Fig. 6.1c) refer to the charges having the same polarity of the electrode, and the hetero-charge (i.e., red circles in Fig. 6.1c) refer to charges having the opposite polarity. As shown in Fig. 6.1d, both charges can distort internal electric field considerably. Indeed, the hetero-charge leads to significant overstress at the electrode and can accelerates aging process. Therefore, it is important to know how charge packets evolve over time under different stress environments.

Based on an extensive literature review [198–204] and our PEA experiments, it is typical to find homocharge accumulation at the vicinity of the electrode. However, as shown in Fig. 6.2a and 6.2b, the transient evolution of homocharge packet and the amount of heterocharge accumulation depends sensitively on the filler loading and the humidity of the environment. Unfortunately, the origin of these differences have neither been explained nor modeled properly.

In this chapter, we (i) develop a compact analytical model to describe the time-evolution of the homocharge peak to explain the origin of charge packet development; (ii) investigate the effect of moisture ingress on the key transport parameters (i.e., mobility, trapping, and detrapping coefficient) by comparing experimental data and the newly developed numerical model; (iii) integrate a generalized random network

model ($RRNM$) [46] and an effective medium model to calculate the effective ion diffusivity ($D^{\mathrm{i}}_{\mathrm{eff}}$) for any given filler configuration; (iv) investigate how a specific filler configuration (e.g., average filler size, maximum filler size, ϕ_{f}) impacts $D^{\mathrm{i}}_{\mathrm{eff}}$, and finally (v) discuss the origin of homo- and heterocharges in a mold compound, and the key features of a "good encapsulant" for HV-ICs under humid environment.

6.2 A compact analytical model to describe ion-transport in mold compounds

6.2.1 Space-charge limited current transport in a trap-free material

A number of numerical studies [205–207] have interpreted the characteristic features of charge profiles obtained from non-destructive measurement techniques. These models self-consistently accounted for ion transport, flux continuity, and Poisson equation in an idealized, trap-free sample. The numerical models provide detailed information about spatio-temporal distribution of ions, however it lacks the insights

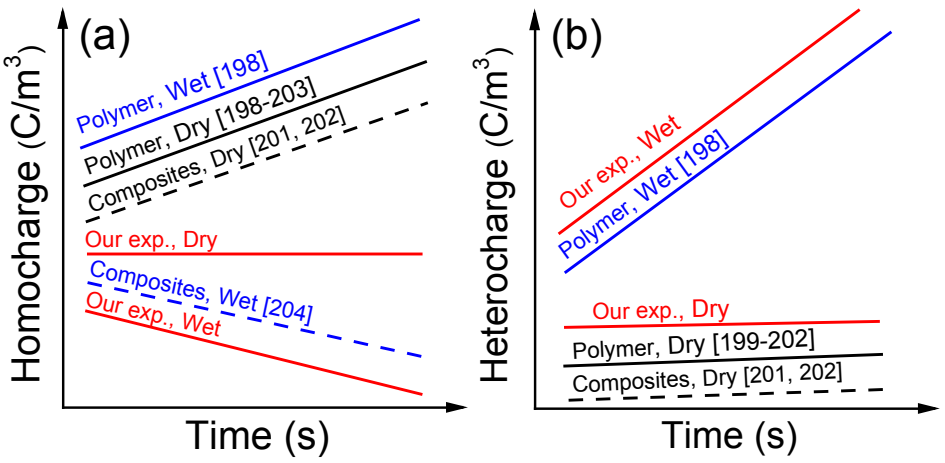

Fig. 6.2. Literature reviews of different charge transient behavior: (a) Homocharge, and (b) Heterocharge.

provided by an analytical model [208]. In this work, we integrate the effects of transient electric field ($\mathbf{E}(\mathbf{t})$) at the electrode, field-enhanced injection of ions into the dielectric, the drift-dominated transport of ions, and the continuity of ion fluxes, etc. to derive a simple physics-based analytical model for the overall phenomena. The model is validated by numerical simulation and experimental results.

A typical polymer dielectric is defective and involves trapping and detrapping processes. We will consider these issues later in the chapter, but let us begin by considering unipolar charge injection into a defect-free homogeneous dielectric. The flux injected into the electrode in response to the time-dependent electric field, $\mathbf{E}(\mathbf{t})$ can be calculated as follows.

Transient electric field on electrode

Once the voltage is applied between the electrodes, the instantaneous electric field ($E_{t=0}$) developed at the cathode injects charges into the polymer dielectric. The charge injection can be described by various models (e.g., Schottky emission [209], and Fowler-Nordheim injection [210]), and the self-consistent screening of the cathode electric field by the injected charges leads to the evolution of the cathode field, i.e. $\mathbf{E}(\mathbf{t})$. Since the homocharge accumulation is proportional to the time-integrated flux injected into the polymer (J_0), Gauss's law explains the time-dependent decrease of $\mathbf{E}(\mathbf{t})$ as shown in Eq. 6.1.

$$\mathbf{E}(\mathbf{t}) = E_0 - \frac{J_0 \cdot F \cdot t}{\varepsilon_\mathrm{r} \cdot \varepsilon_0} \tag{6.1a}$$

$$\frac{\mathbf{E}(\mathbf{t})}{E_0} = 1 - \frac{t}{t_\mathrm{c}}, \text{ where } \left(t_\mathrm{c} = \frac{\varepsilon_\mathrm{r} \cdot \varepsilon_0 \cdot E_0}{J_0 \cdot F} \right) \tag{6.1b}$$

where $J_0\,(mol/m^2 \cdot s)\,, F(C/mol), \varepsilon_\mathrm{r},$ and $\varepsilon_0(C/V \cdot m)$ respectively are the initial charge injection flux, the Faraday number, the dielectric constant of the polymer, and the DC permittivity. Equation 6.1b is the normalized (scaled) form of Eq. 6.1(a), with the characteristic time-constant t_c.

Transient charge injection on electrode

For an idealized trap-free material, the charge injection can be described by Schottky emission as shown in Eq. 6.2.

$$\frac{J(t)}{J_0} = A_0 \cdot T^2 \cdot \exp\left(\frac{-q \cdot \phi_{\mathrm{B}}}{kT}\right) \cdot \exp\left(\frac{q}{kT}\sqrt{\frac{q}{4\pi\varepsilon_{\mathrm{r}}\varepsilon_0}} \cdot \sqrt{\frac{\mathbf{E(t)}}{E_0}}\right) \tag{6.2}$$

where $A_0\,(A/m^2 \cdot K^2)\,, k(J/K), T(K)$, and $\phi_{\mathrm{B}}(eV)$ are the Richardson constant, the Boltzmann constant, ambient temperature, and the electrode-dielectric Shottky barrier height, respectively. Inserting Eq. 6.1 for $\mathbf{E(t)}$ into the flux-equation for $J(t)$, we can account for the time-evolution for homocharge buildup.

Transient space charge concentration

The continuity equation requires that the flux entering a local region (Eq. 6.2) must equal to the outgoing flux. For high-voltage applications ($V_{app} \gg k_B T/q$), we can neglect diffusion and focus exclusively on ion drift [208]. The drift-flux is given by $\mu_{\mathrm{n}} \cdot n_{\mathrm{m}}(t) \cdot \mathrm{E(t)}$, where μ_{n} is the carrier mobility and n_{m} is the electron concentration. Equating Eq. 6.2 and the drift term shown above, we obtain an expression for n_{m} as shown in Eq. 6.3.

$$n_{\mathrm{m}}(t) = \frac{J(t) \cdot F}{\mu_{\mathrm{n}} \cdot \mathbf{E(t)}} \tag{6.3}$$

In principle, we must iterate between $J(t)$, and $\mathbf{E(t)}$ to achieve self-consistently, in principle $t < t_{\mathrm{c}}$, the approximate final formula (Eq. 6.3) compares very well with the exact solution. The time derivative of Eq. 6.3 predicts time-dependence of n_{m}.

In practice, polymer encapsulants are highly defective. In the following section, we derive an expression for $n_{\mathrm{m}}(t)$ including the charges trapped into the defects ($n_{\mathrm{t}}(t)$).

6.2.2 Trapped space charge limited current case

Polymer defects include irregular topological structures and/or broken chemical bonds. The trapping and detrapping of mobile charges by these defects [211, 212]

fundamentally alters the the space charge evolution, and consequently, significantly modifies $E(x,t)$. The cathode field, $E(0,t)$, depends primarily on the injected mobile charge into the polymer so that Eqs. 6.1 6.2 are still valid. Assuming that the trapping is dominated by a shallow single level states, we can write the following expression for $n_{\mathrm{t}}(t)$:

$$\frac{\partial n_{\mathrm{t}}}{\partial t} = -\frac{\partial n_{\mathrm{m}}}{\partial t} = \tau_{\mathrm{T}} \cdot n_{\mathrm{m}} \cdot \left(1 - \frac{n_{\mathrm{t}}}{N_{\mathrm{t}}}\right) - \tau_{\mathrm{D}} \cdot n_{\mathrm{t}} \tag{6.4}$$

where $\tau_{\mathrm{T}}(1/s)$, $\tau_{\mathrm{D}}(1/s)$, and $N_{\mathrm{t}}\,(mol/m^3)$ are the trapping and detrapping coefficients, and the maximum trap concentration, respectively. Let us consider two special cases: fast trapping and slow trapping.

Slow trapping case

If the trapping is slow (i.e., small τ_{T} value), n_{t} increases at the rate of τ_{T} because we can neglect two terms: $1 - n_{\mathrm{t}}/N_{\mathrm{t}}$, and $\tau_{\mathrm{D}} \cdot n_{\mathrm{t}}$. In this case, $n_{\mathrm{t}}(t)$ is given by Eq. 6.5.

$$n_{\mathrm{t}}^{\mathrm{s}}(t) = n_{\mathrm{m}}(t) \cdot \tau_{\mathrm{T}} \cdot t \tag{6.5}$$

Fast trapping case

When trapping process is fast, we first calculate the steady-state n_{t} by setting Eq. 6.4 as zero, see Eq. 6.6.

$$n_{\mathrm{t}}(\infty) = n_{\mathrm{m}}(t) \cdot \left(\frac{\tau_{\mathrm{T}} \cdot N_{\mathrm{T}}}{\tau_{\mathrm{D}} \cdot N_{\mathrm{T}} + \tau_{\mathrm{T}} \cdot n_m(t)}\right) \tag{6.6}$$

The time-dependent $n_{\mathrm{t}}(t)$ is obtained by interpolating two curves (i.e., Eq. 6.5, and Eq. 6.6) as shown in Eq. 6.7.

$$n_{\mathrm{t}}(t) = \frac{n_{\mathrm{t}}^{\mathrm{s}}(t)}{\left(1 + \left(n_{\mathrm{t}}^{\mathrm{s}}(t)/n_{\mathrm{t}}(\infty)\right)^2\right)^{1/2}} \tag{6.7}$$

The space charge concentration at the electrode is given by the sum of Eq. 6.3 and Eq. 6.7. In the following section, the validate the analytical model by numerical simulation.

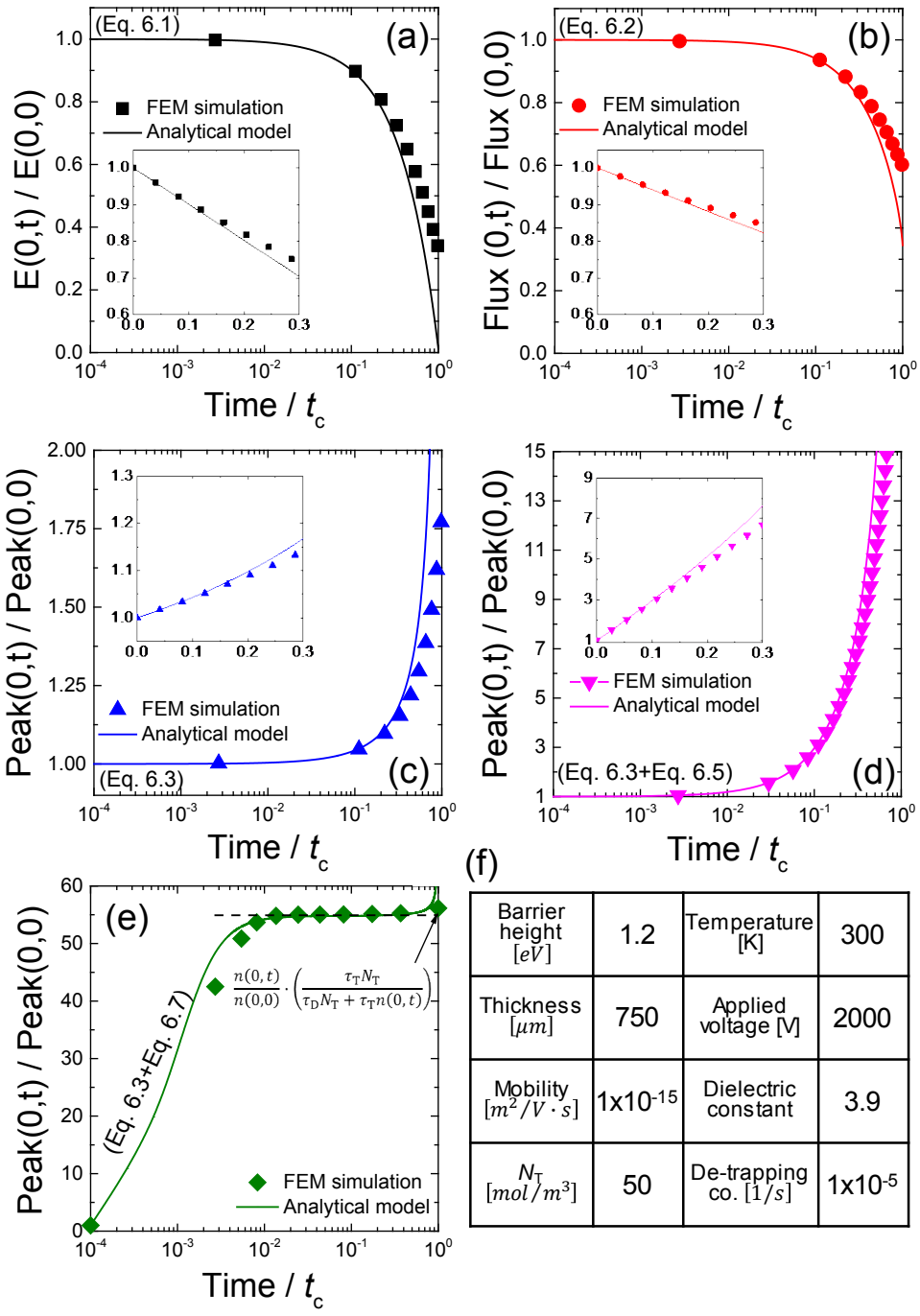

(f)

Barrier height $[eV]$	1.2	Temperature [K]	300
Thickness $[\mu m]$	750	Applied voltage [V]	2000
Mobility $[m^2/V \cdot s]$	1x10^{-15}	Dielectric constant	3.9
N_T $[mol/m^3]$	50	De-trapping co. $[1/s]$	1x10^{-5}

Fig. 6.3. Comparison between our derived compact analytical model and FEM simulation: (a) electric field at the electrode, (b) electrons injection flux at the electrode, (c) homocharge concentration at the electrode, (d) homocharge concentration when slow trapping occurs, (e) homocharge concentration when fast trapping occurs, (f) Parameter values for FEM simulation.

6.2.3 Model validation by numerical simulation

Our numerical simulation is based on simultananeous and self-consistent FEM solution of transport, continuity, and Poisson equations as shown in [205–207, 213]. The transport equations and the parameters used are summarized in table A.1, and A.2 in the Appendix. Fig. 6.3 shows that the analytical model compares resonably well with the FEM simulation. As $t \to t_c$, the results differ by 10% the electric field and injected fluxes are not fully self-consistent. Typically, $t_c > 10^4$, therefore the analytical model can be used to interpret PEA results within the time-window.

6.3 Revisiting the origin of space charge packets

6.3.1 PEA measurement data

The PEA technique was used The time-dependent evolution of the space charge profiles in dry and wet samples, as shown in Fig. 6.4, and 6.5. In both cases, we find considerable homocharge injection from the electrodes. For dry samples, the homocharge profiles do not change over time. For the wet samples, however, homocharge concentration *decays*, but heterocharge begins to build-up, with time. The heterocharge may either by injected from the opposite electrode and transported across the sample. Or, these pre-existing charges may have been uniformly distributed within the sample during the manufacturing process and attracted by field with opposite polarity. Next we will use the analytical model (Sec. 6.3.3) and the numerical model (Sec. 6.3.4) discussed above to interpret the PEA experimental results for dry and wet samples.

6.3.2 DC conductivity measurement data

Real-time characterization of encapsulant conductivity during moisture absorption and desorption cycles is shown in Fig. 4. The sample is prepared by drying them at 90°C for several hours. The samples are placed in a humidity chamber, with the

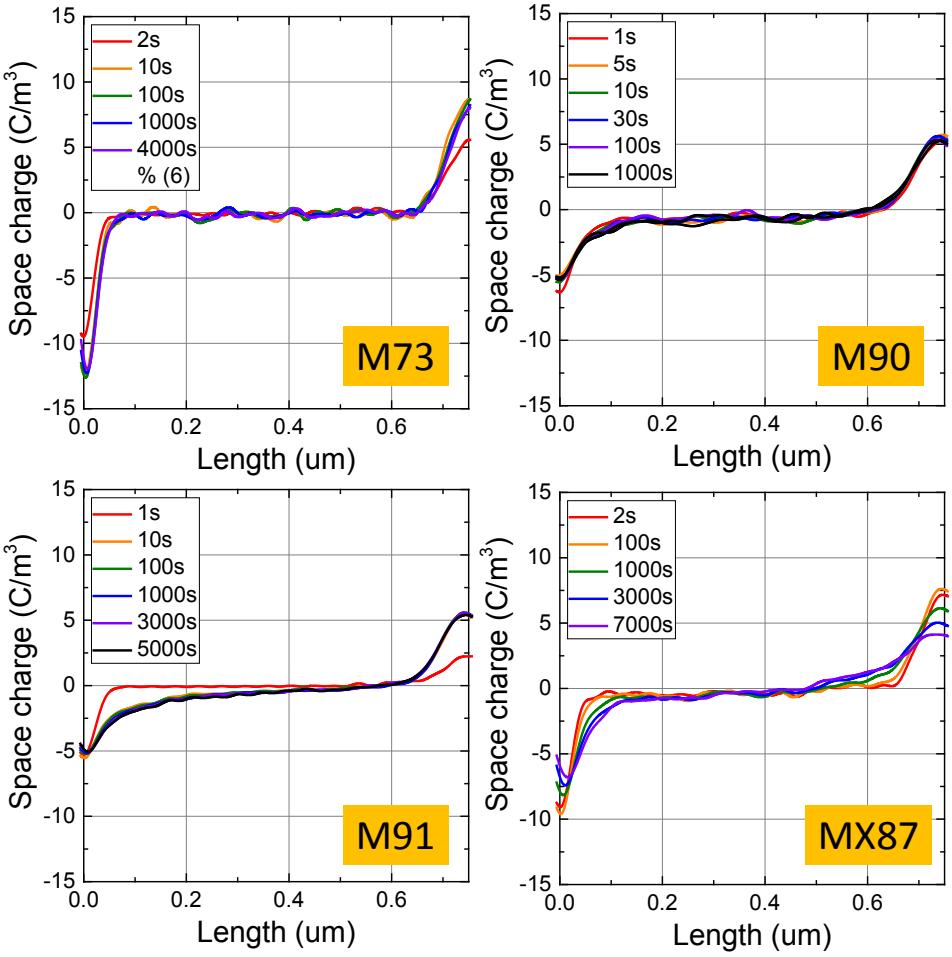

Fig. 6.4. Measured PEA measurement under dry condition.

relative humidity (RH) set to 90%. During the moisture absorption phase, the "leakage" current increases by more than two orders of magnitude. During desorption, the current decreases until the original current level is restored. The experiments suggest that conductivity depends strongly on the moisture content of the encapsulant. We have seen in Chapter 5 that the reacted water (rather than the mobile water) controls the conductivity of a sample. The increase and decreare of conductivity with moisture intake suggests that the water reaction is (essentially) reversible. Equation 6.8 empirically relates the sample conductivity and the reacted water content.

$$\sigma = \sigma_0 \cdot 10^{0.034 \cdot Y(x,t)} \tag{6.8}$$

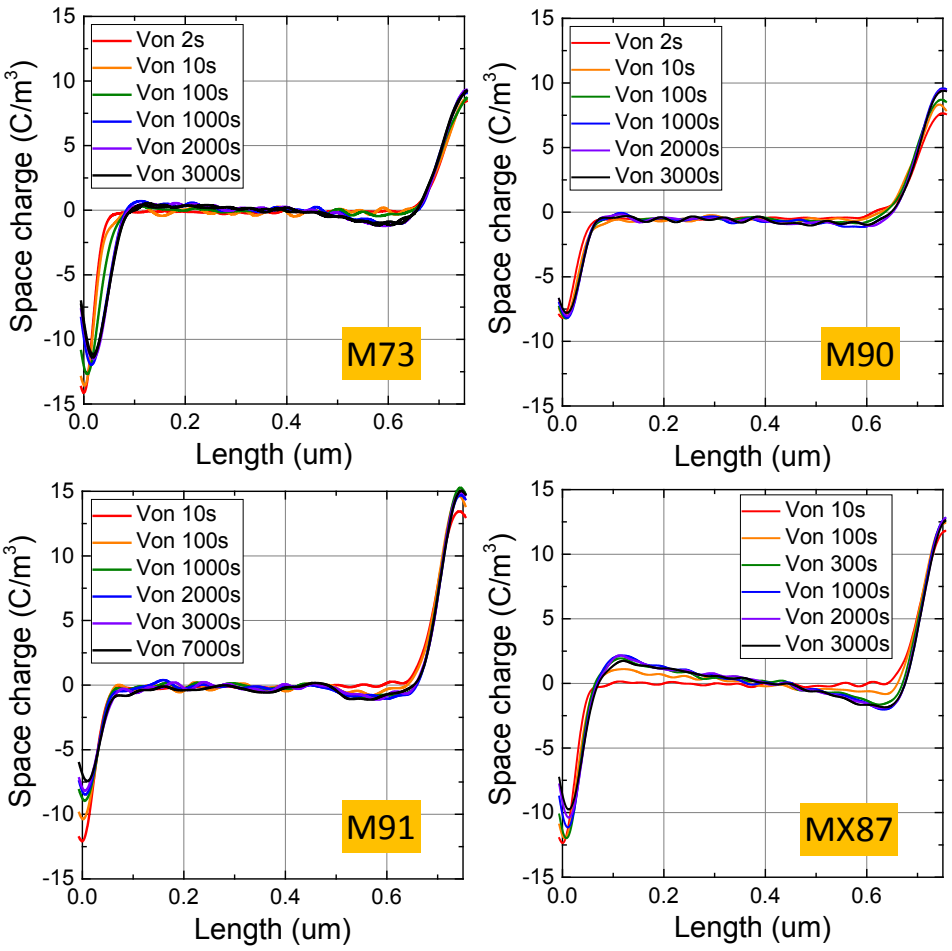

Fig. 6.5. Measured PEA measurement under humid condition (i.e., relative humidity is 85%.

where σ_0 is measured conductivity under dry condition.

6.3.3 Phenomenological study of heterocharge packet origin

Fig. 6.5 shows that the fast appearance of heterocharge packet in wet samples might be explained either by field-assisted separation of the pre-existing ionic impurities [214] or ultra-fast transport of charges injected from the opposite contact and transported through the sample [215, 216]. To characterize the essential features of hetero-charge transport, let us first analyze the PEA results by the analytical model.

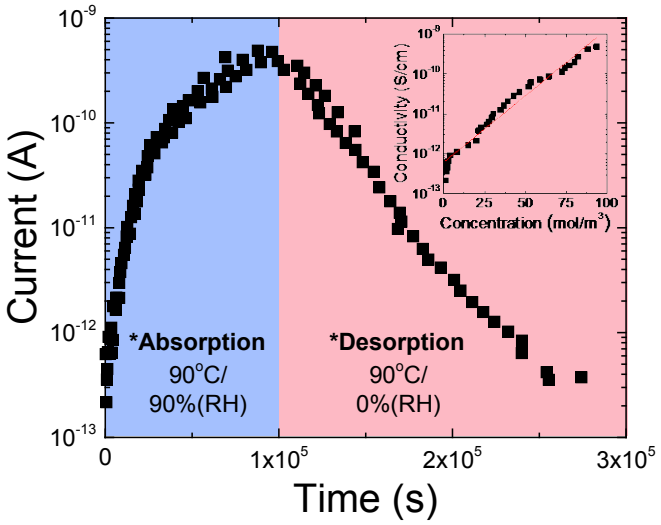

Fig. 6.6. Transient DC current measurement results. Initially, the sample is fully dried and exposed to humid condition. After 1×10^5s, the sample is dried again. (inset) Relationship between conductivity, and reacted water.

Home and heterocharge transport interpreted by the analytical model

The time-dependent decay of the homocharge can be understood by taking the time derivative of Eq. 6.3. The decay in the homocharge must satisfy the condition:

$$t_{\mathrm{C}} > 2\sqrt{t_{\mathrm{C}}\left(t_{\mathrm{C}} - t\right)} / \frac{q}{kT}\sqrt{\frac{q}{4\pi\varepsilon_{\mathrm{r}}\varepsilon_0}} + t \tag{6.9}$$

The only variable other than t_{c} in Eq. 6.9 is ε_{r}. When $t \ll t_{\mathrm{c}} \sim 100$s, Eq. 6.9 simplifies to $\sim 1.83 \times 10^6 > \varepsilon_{\mathrm{r}}$. Considering a typical ε_{r} value exhibits between 1 and 100, we conclude that homocharge injection alone cannot explain time-dependent reduction in space charge close to the electrode. Other factors, such as heterocharge accumulation, must be accounted for to explain the experimental observation. In the following paragraph, we compare the two mechanisms of heterocharge development interpret the experiments.

First, lets assume the origin of heterocharge packet (e.g., nearby anode) is due to the injected charges (e.g., electrons) from the opposite electrode (e.g., cathode). We

know that the mobility is given by: $\mu = L/(t \cdot E)$, where L, and t are the distance charge transit, and the time it takes, respectively. From Fig. 6.5, we estimate that $\mu \sim 1 \times 10^{-13}\,(m^2/V \cdot s)$, which is two orders of magnitude higher than the mobility needed to describe the homocharge behavior in dry samples. Also Eq. 6.3 suggests that the high mobility makes it impossible to accumulate homocharge density at the electrode. Thus, we conclude that the injected charge at the opposing contact cannot explain heterocharge accumulation.

As a different mechanism of ultrafast heterocharge accumulation, some researchers have proposed soliton-like charge propagation [216] across the sample. Our experiments do not satisfy the conditions for soliton propagation: Our electric field is too low (e.g. 2 MV/m $< 5-10$ MV/m) and the transit time too long ($\sim$ 1000s $\gg$ 100 ms) for experiments to be interpreted by soliton transport. Consequently, we conclude that the heterocharge observed in the PEA measurement is due to pre-existing ions (1$\sim$20 PPM) included in the encapsulant during the fabrication processes [214]. If the density of molding compounds is $2g/cm^3$, 10ppm corresponds to $0.9mM/m^3$ in the case of sodium ions. In the following section, we consider the role of the pre-existing ions to interpret the experimental data.

6.3.4 Revised FEM simulation set up

Based on the homocharge FEM simulation set up we applied in section 6.3, we added four additional species: mobile cation, mobile anion, and trapped cation, trapped anion. The mobilities and the capture cross-sections were adjusted to fit the experimental data. We need not consider field-induced ionization because the applied field is lower than the ionization threshold enough (i.e., $>$ 160MV/m) [217]. For simplicity, we assume a field-independent mobility, but the model can be easily generalized to include field-dependent mobiltiy associated with hopping and Poole-Frenkel conduction. Tables A.1 and A.2 summarizes the transport formula and the parameter values, respectively.

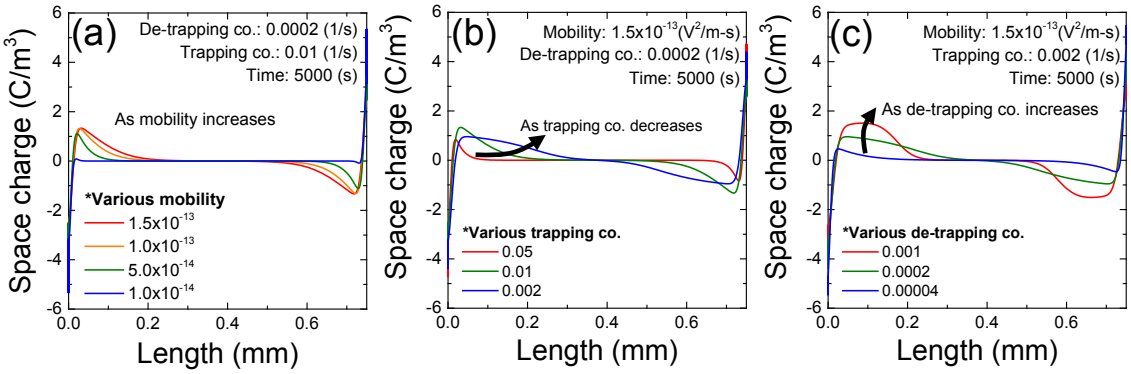

Fig. 6.7. FEM simulation results with electrons, holes, cations, and anions. Different variables have been changed to investigate their impact: (a) mobility, (b) trapping coefficient, (c) de-trapping coefficient.

Among the numerical models reported in the literature, few have considered transport of electrons, holes, and ionic impurities simultaneously and self-consistently. This is often justified by the fact that ion mobility is so low than that it cannot affect the space charge at short time scales. However, as the encapsulant is exposed to water and the effective ion mobility increase significantly, one must consider electron, hole and ion transport self-consistently. This generalized FEM model will provide new insights regarding the complicated dynamics of space charge transport. To this end, the correlation between ions' $D^{\mathrm{i}}_{\mathrm{eff}}$ and the corresponding filler configuration must be specified, especially for an wet mold compound. In the following section, we introduce a the predictive modeling framework for $D^{\mathrm{i}}_{\mathrm{eff}}$ estimation of pre-existing ions.

6.4 Effective diffusivity of ions, $D^{\mathrm{i}}_{\mathrm{eff}}$

As we mentioned in the Introduction of this chapter, the majority of microelectronic ICs are packaged by molding compounds (MC), i.e., silica-filled epoxy resins. The volumetric fraction of micro-fillers larger than 75% have been proposed recently to match coefficient of thermal expansion (CTE) with silicon and to avoid moisture

ingress [218]. However, considering the fact that the void percolation threshold (p_c) for mono-disperse spheres is only ∼3% [156], moisture will always transport into the MC and saturated unless the volume fraction of filler (ϕ_f) is over 97% (100%-void p_c). Even with poly-disperse spheres, maximum ϕ_f is ∼80% [157, 158]. Thus, we can realize that moisture would ingress and saturated someday within MC although we increase ϕ_f to delay water permeation.

When MC is exposed to a humid environment and after water saturates within the sample, PEA experimental data shown in Fig. 6.5 exhibits heterocharge development. In the previous section, I found out its origin is the pre-existing ions as shown in Fig. 6.8b. Heterocharge accumulation in an encapsulant distorts the internal electric field as shown in Fig. 6.8c, and cause detrimental ageing processes: partial discharge, electrical tree growth, and breakdown of dielectric [193]. In a dry environment, heterocharge is not developed as shown in Fig. 6.8b. Therefore, we can figure out that water within MC enhances the pre-existing ions diffusivity and results in heterocharge accumulation. Finally, the optimization of filler configuration (e.g., average filler size, maximum filler size, ϕ_f) that can suppress heterocharge accumulation under humid environment is a primary concern to enhance the reliability of microelectronics packaging material. In order to achieve this goal, we need to understand the connection between filler configuration and effective diffusivity of pre-existing ions within MC (D^i_{eff}) saturated with water.

In this section, I (i) develop revised random network model ($RRNM$) based on the conventional random network model for thermal transport issue [46] and effective medium model to calculate D^i_{eff} with any given filler configuration; (ii) investigate each filler configuration (e.g., average filler size, maximum filler size, ϕ_f) impact on D^i_{eff} and finally (iii) discuss the filler configuration conditions for small D^i_{eff} when MC is exposed to a humid environment. The conclusions shown in this section can also be considered to optimize filler conditions of the MC (e.g., High voltage DC cable, wind-turbine blade) exposed to a humid environment. Also, I believe $RRNM$ can be

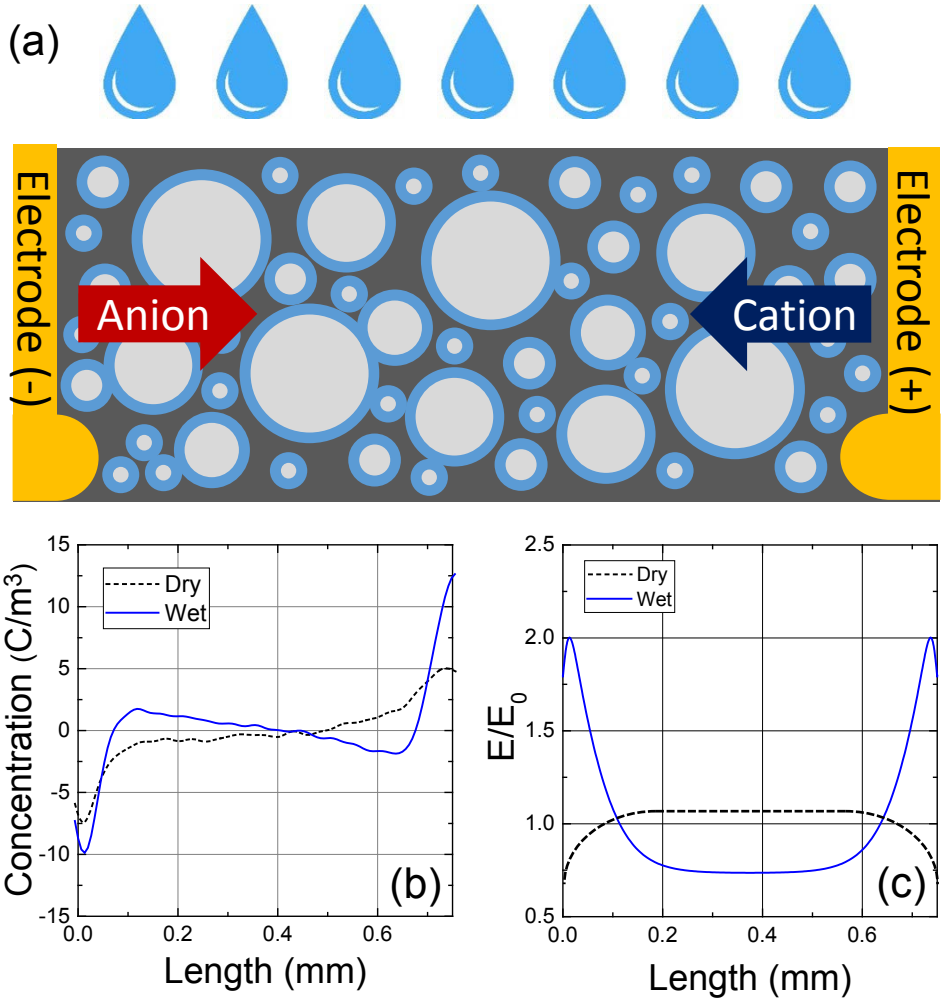

Fig. 6.8. (a) A schematic shows the formation of water shell layer around filler when the MC is exposed to a humid environment. (b) PEA measurements results of MX87 exhibiting space charge distribution at 3000s. Heterocharge is observed when the sample is wet, whereas only homocharge is observed under the dry condition. (c) Electric field distribution for the space charge shown in Fig. 6.8b. Electric field enhancement can be found due to heterocharge when sample is wet.

also applied to obtain the effective transport property for any composite system with spherical fillers coated by highly conducting layer.

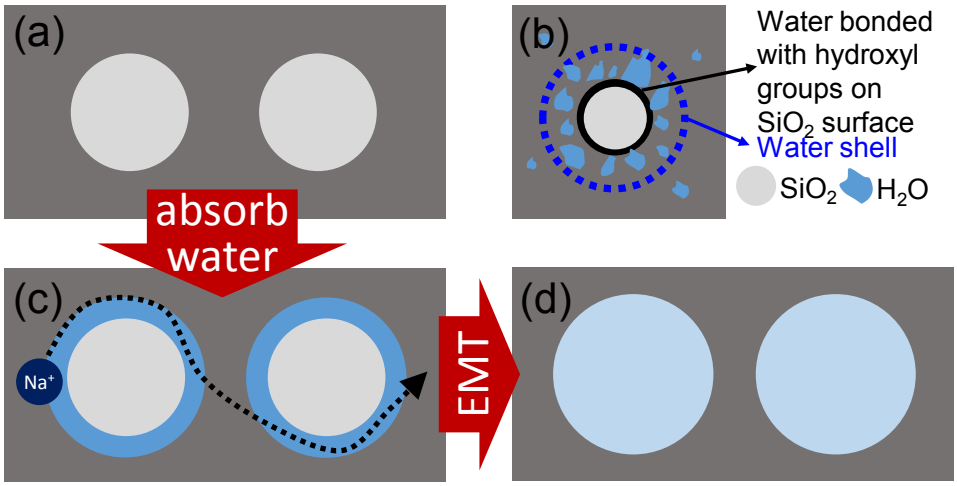

Fig. 6.9. (a) A schematic of MC when the sample is dried. (b) The actual water molecules distribution in MC when water ingress takes place. (c) Percolative paths formation due to water shell layer for ionic species. (d) Two heterogeneous regions (i.e., interface layer, and filler) can be replaced with one region based on EMT model.

6.4.1 Analytical model framework

When MC is exposed to a humid environment, our electrical conductivity measurement shows orders of magnitude conductivity increases compares to a dried MC as shown in Fig. 6.6. It is widely known that water molecules prefer to locate at the vicinity of the polymer and silica filler interface and forms water shell structure due to the hydrophilic nature of silica as shown in Fig. 6.9b [219–221]. Therefore, it can be presumed that the increase of electrical conductivity is due to the water shell layer which contains higher moisture content (which leads to higher conductivity) than that in the polymer. To our knowledge, there has no analytical methodology that can calculate the effective diffusivity of species with highly conducting interfacial region within the composite system. In the following sections, $RRNM$ derivation, and the validation are shown.

Revised Random Network Model ($RRNM$) with Effective Medium Theories (EMT)

As I mentioned in section 2.2, when a system size is much larger than the length scale of inhomogeneities, the heterogeneous material can be viewed as a homogeneous system with the effective physical property based on EMT model. In order to consider interfacial layer for the calculation, we apply EMT model to replace two regions (filler, and interfacial layer) with one effective region as shown in the schematic at the bottom of Fig. 6.9a. The radius of effective region is then the summation of the radius of filler and the thickness of interfacial region. The physical parameter value of effective region should be redefined based on the proper selection of EMT model (homogenization model). Different geometric arrangement can result in a different $D^{\mathrm{i}}_{\mathrm{eff}}$ value as described in section 2.2. Among various EMT models introduced in chapter 2, we can realize that upper HS bound and Wiener bound resembles our situation since insulating filler is covered by highly conductive interfacial layer. In the next section, numerical studies is done for the EMT model choice that can describe our case properly.

6.4.2 FEM studies for EMT model selection

In order to investigate $D^{\mathrm{i}}_{\mathrm{eff}}$ value that can replace filler and interfacial layer, two structure shown in Fig. 6.10a is simulated using commercial FEM tool, COMSOL. To obtain $D^{\mathrm{i}}_{\mathrm{eff}}$ by FEM simulation, we use the following algorithm. 1) Neighboring two hemispheres with interfacial layer is drawn (structure #1 in Fig. 6.10a), the radius of two hemispheres is fixed to 1, and interfacial layer thickness is varied; 2) Relevant diffusivity for each region is assigned, ions' diffusivity at filler ($D^{\mathrm{i}}_{\mathrm{f}}$), and at mold ($D^{\mathrm{i}}_{\mathrm{m}}$) are 0, and 1, respectively. Two values of ions' diffusivity at interfacial region ($D^{\mathrm{i}}_{\mathrm{int}}$) is done, 100 and 1000; 3) Diffusion equation is solved using a 3-D simulator, COMSOL as shown in Fig. 6.10b. The boundary conditions are: fixed concentration at red line, and blue line in Fig. 6.10a is 1 $[mol/m^3]$, and 0, respectively. Rest of all boundaries

are insulated; 4) Integrated normal diffusive flux $[mol/s]$ is evaluated; 5) Construct two hemispheres with one effective region (structure #2 in Fig. 6.10a), and perform the simulation with same conditions that we did for structure #1 and finally 6) Obtain D^{i}_{eff} value that gives the same integrated flux with that of structure #1 case. By changing interfacial layer thickness, we can perform the simulations for different volumetric fraction of interfacial region. As we presumed in the previous section, we

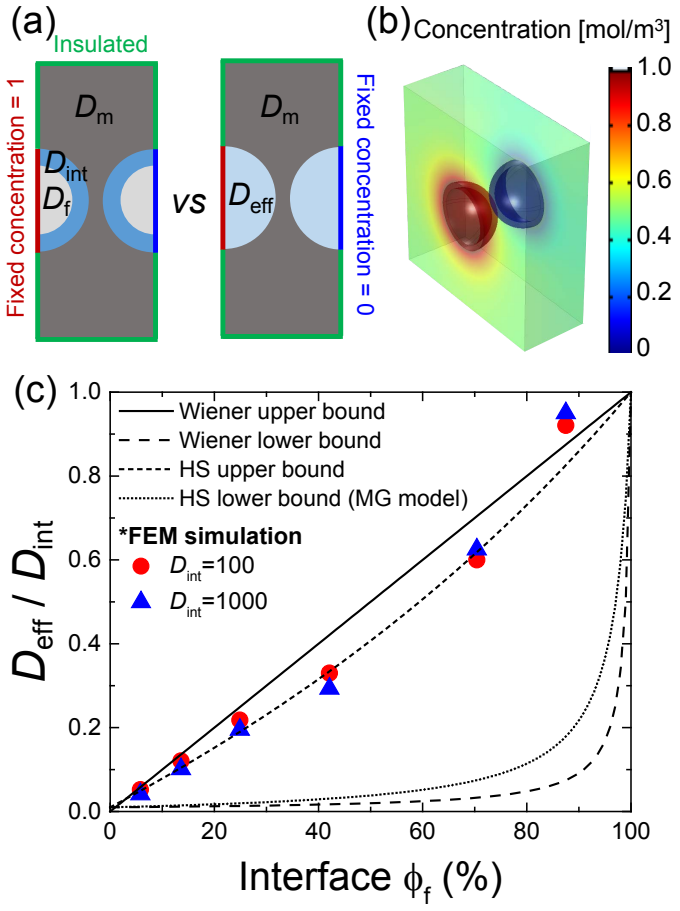

Fig. 6.10. (a) Performed two FEM simulation schematics for the modeling framework validation and boundary conditions. (b) Concentration distribution of simulated structure. (c) The correlation between D_{eff} and interface layer volumetric fraction follows Wiener upper bound, and HS upper bound.

can observe that calculated D^{i}_{eff} approximately follows Wiener upper bound and HS upper bound, see Fig. 6.10c.

In this work, we applied Wiener upper bound (Eq. 2.1a) for the EMT model. In Eq. 2.1a, we can regard D_1, D_2, and ϕ_f are ions diffusivity in the interfacial region, ions diffusivity in the filler (i.e., 0), and interfacial region volume fraction, respectively. As a results, Eq. 2.1a can be simplified as $D^{i}_{eff}=\phi_f \cdot D_1$. Thus, the larger the filler diameter, the smaller D^{i}_{eff} will be as ϕ_f of interfacial layer becomes smaller. After D^{i}_{eff} definition for an individual filler, we apply finite element method concept (RNM [46]) to calculate D^{i}_{eff} of whole system. The big difference between our *RRNM* and conventional RNM is that the D^{i}_{eff} between fillers with different radius is different for our model, however, the diffusivity of all fillers are the same for RNM [46]. After the redefinition of D^{i}_{eff} for each filler based on the given thickness value, we can calculate D^{i}_{eff} by the algorithm shown in the next section as shown in Fig. 6.11.

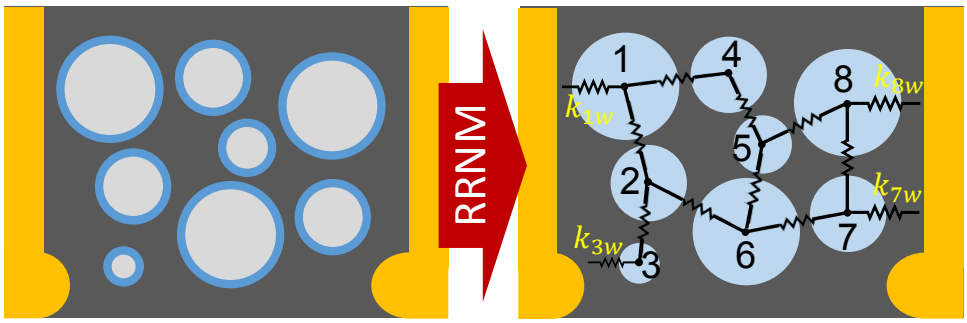

Fig. 6.11. Filler and interface layer regions can be replaced with an effective region based on HS model. Between neighboring effective regions, conductivity can be defined based on [29]. Then, D^{i}_{eff} of the whole system can be calculated using direct stiffness method (i.e., *RRN*-model).

6.4.3 Effective diffusivity calculation

In order to obtain $D_{\text{eff}}^{\text{i}}$ value, we apply one of the widely known FEM, direct stiffness method. Unlike the commercial FEM simulation tool, our method can set the node position only at the center of the fillers so that the computation load can be reduced dramatically. Firstly, direct stiffness method takes the following term shown in Eq. 6.10.

$$[K] \cdot \{u\} = \{F\} \tag{6.10}$$

where $[K]$, $\{u\}$, and $\{F\}$ are global stiffness matrix (can be constructed based on the conductivity information between nodes, m^3/s), nodal displacement (concentration at each node, mol/m^3), and nodal forces (net flux, mol/s), respectively. Once we define two matrices, $[K]$, and $\{F\}$, we can find out concentration at each node by multiplying inverse matrix of $[K]$ at both sides.

In order to construct $[K]$, conductivity calculation between two nodes needs to be done. Conductivity (diffusivity$\times$area$\div$length, m^3/s) calculation can be divided into two cases: between neighboring two spheres, and between the sphere and the wall. The formula for each case and more details are shown in appendix. Conductivity calculations were performed only if the distance between the centers of adjacent fillers is less than the distance defined by the radius of the two fillers ($R_1 \cdot R_2 / (R_1 + R_2)$). Now, $[K]$ can be constructed based on the algorithm shown below. 1) diagonal line, i.e., ii, consists of the sum of all the elements meeting at node i; 2) location ij consists of relating element joining node i to j. negative sign needs to be added; 3) Add zero for node that dont interact; 4) Add element that interact with wall at diagonal line and finally 5) Remove columns and rows with all zero element. Constructed $[K]$ for the given situation for Fig. 6.11 is shown in appendix B.

The next step is $\{F\}$ definition. $\{F\}$ is a single column matrix and n^{th} row indicates net flux at the specific node n. Therefore, for a node that does not interact with the wall, the element value is 0, and for the node interacting with the wall, the

element value is defined as multiplication between conductivity (between the sphere and the wall) and concentration of the wall.

Based on defined $[K]$, and $\{F\}$, we can get $\{u\}$ (i.e., concentration information at the specific node) by perfoming $[K]^{-1} \cdot \{F\}$ calculation. Finally, once we obtain concentration at all nodes, we can define $D^{\mathrm{i}}_{\mathrm{eff}}$ by adding all multiplication of the concentration difference between wall and the node that interacts with the wall, and conductivity between wall and the node. For example, in Fig. 6.11, if we set the concentration of the left-side wall as u_{LW}, and the other wall as u_{RW}, $D^{\mathrm{i}}_{\mathrm{eff}}$ is $k_{1w} \cdot (u_{\mathrm{LW}} - u_1) + k_{3w} \cdot (u_{\mathrm{LW}} - u_3)$. According to the continuity concept, $D^{\mathrm{i}}_{\mathrm{eff}}$ calculation by right-side wall should be same $(k_{7w} \cdot (u_7 - u_{\mathrm{RW}}) + k_{8w} \cdot (u_8 - u_{\mathrm{RW}}))$. In conclusion, based on $RRNM$, we can calculate $D^{\mathrm{i}}_{\mathrm{eff}}$ of water ingressed MC with any given filler configuration if we know each fillers coordinates, and radius information. In appendix C, a further RRNM validation is described in the case when the system size is expanded while keeping filler configuration same. We confirmed our model by checking the same calculated $D^{\mathrm{i}}_{\mathrm{eff}}$ regardless of different system size. In the following section, different filler configuration impact on pre-existing ions mobility is investigated based on our $RRNM$ and PEA measurement data.

6.5 Generation of Spheres packing

In order to study each filler configuration impact, we first generate prototype composites system within a cube (unit cell) with an edge length of $150\mu m$ based on the information shown in Table 6.1, see Fig. 6.12a. For each prototype MC, average filler size and maximum filler size are being kept same as our actual experimental sample. However, ϕ_{f} of generated structure (ϕ_{f} value of M73, M90, and M91 are 35, 44, and 45%, respectively) is lower than the actual case. Although ϕ_{f} is lower than that of the actual samples, we examined the generated structure to investigate each filler configuration impact on $D^{\mathrm{i}}_{\mathrm{eff}}$ altering tendency. The estimated $D^{\mathrm{i}}_{\mathrm{eff}}$ for each generated structure and the discussions on different filler configuration impacts

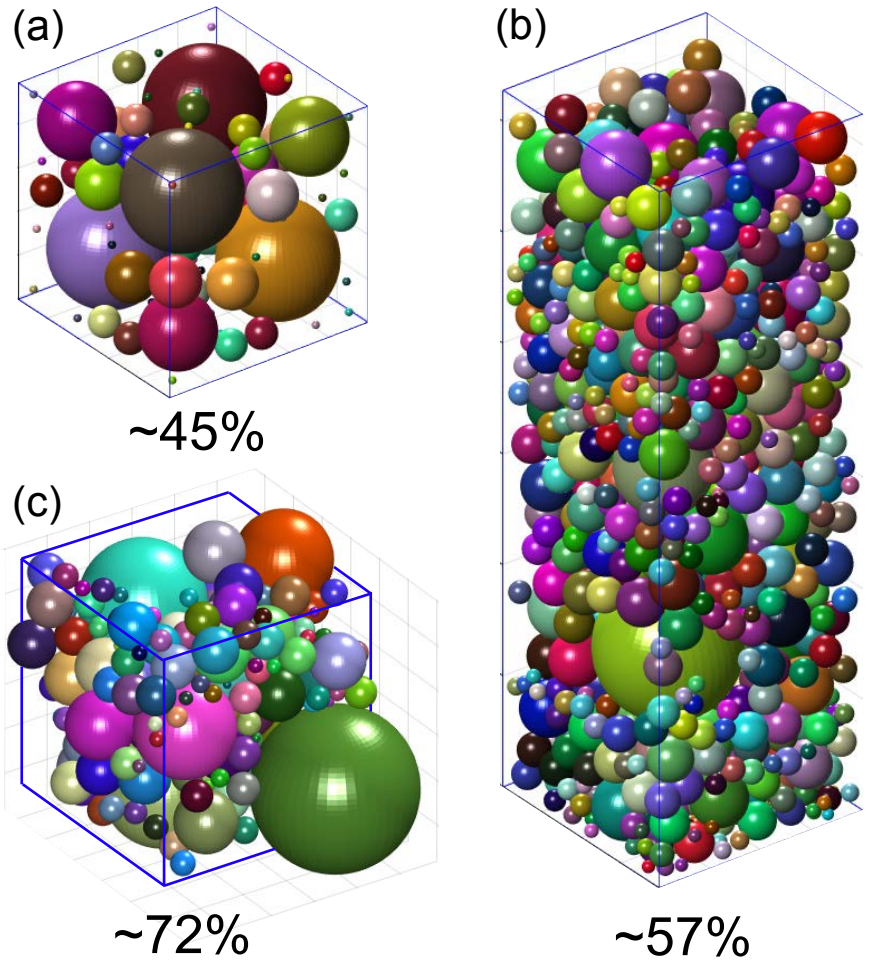

Fig. 6.12. Spheres packing simulation results and approximate ϕ_{f} for each methodology: (a) Manual packing, (b) Drop-fall-shake algorithm (by Huanyu Liao), and (c) Variation-cell method.

is shown in the following section (i.e., section 6.6). For $RRNM$ calculation, $D^{\mathrm{i}}_{\mathrm{f}}$, $D^{\mathrm{i}}_{\mathrm{m}}$, and $D^{\mathrm{i}}_{\mathrm{int}}$ are defined as 0, 1, and 1000, respectively.

Drop-fall-shake algorithm

In order to extend the ϕ_{f} value to an actual MC range (60∼80%), two methods have been used: Drop-fall-shake algorithm [222, 223], and variable-cell method [224,

225]. The first method is drop-fall-shake algorithm which allows us to generate the composite system with the required ϕ_f, and size distribution as shown in Fig. 6.12b. The specific algorithm is shown in [223]. In this thesis, the proto-type structure based on this algorithm is generated by Huanyu Liao in school of mechanical engineering at Purdue university.

Based on drop-fall-shake algorithm, two different maximum filler size cases (75, and 135 um) are considered and the rest of conditions (e.g., the number of spheres: 1000, standard deviation: 10, average sphere size: 25um, and ϕ_f) have been kept same. ϕ_f of the generated structures is between ∼52 and ∼ 59%. One limitation of drop-fall-shake algorithm is that all generated particles are confined within the box (i.e., no intersection between box boundaries and generated fillers) so that the maximum packing fraction is difficult to be attained. In order to attain larger ϕ_f, the box size needs to be much larger to mitigate the edge effects (i.e., the difficulty of filling a space between a box boundary and fillers on a boundary). If we want to generate the structure with higher ϕ_f, the number of spheres will be orders of magnitude larger than that of our current generated structures. For instance, more than 100,000 fillers would be required to reach more than 70% ϕ_f. Eventually, the increase number of spheres will result in the increase of computation load for the structure generation, and D^i_{eff} as well. When the number of spheres is fixed to 1000, ϕ_f of generated structure turns out to be between ∼52 and ∼59%. For this particular range of ϕ_f, I examined different maximum filler size impact on D^i_{eff} based on the generated structure by drop-fall-shake algorithm, and the discussions are shown in the section 6.6.

jamming algorithm

In order to achieve higher ϕ_f, I applied variable-cell method [225] which generates the structure based on athermal densification of soft, frictionless spheres from an initial sparsely connected phase to a mechanically stable, jammed phase. Packing

Table 6.1.
Simulation conditions for generated structures. Simulations are performed at [226].

	Mono-disperse	Bi-disperse (ratio=2)	Bi-disperse (ratio=3)	Poly-disperse
Sphere #	200	200	200	200
Sphere size (μm)	26.3	44.6(10%) & 22.3(90%)	54.0(10%) & 18.0(90%)	1∼85.7 (Fig. 6.14b)
Average size (μm)	26.3	24.5	21.6	20

simulation proceeds by reducing the unit cell size until the pressure of the system becomes larger than zero. Next, the unit cell slowly dilates until the pressure becomes zero, and we regard that state as jammed state. More detailed methodology and the physics of jamming is described in [224]. The simulations are performed at [226]. The big difference between this method and drop-fall-shake algorithm is that the allowance of the interaction between box boundaries and generated fillers. Thus, this method can generate higher ϕ_{f} structure compares to that of drop-fall-shake algorithm as shown in Fig. 6.12c. ϕ_{f} of generated structure is between ∼62 and ∼ 72%. Three different size distributions are generated: mono-disperse (i.e., single size sphere), bi-disperse (i.e., two-size spheres), and poly-disperse (i.e., log normal distribution) as shown in Fig. 6.13a. As we can see in Fig. 6.15, bi-disperse packing shows the highest ϕ_{f} since smaller fillers can fit into spaces left by mono-disperse fillers packing. In [155], a mathematical point of view of bi-disperse packing, and an accurate analytical compact model approximating the maximum ϕ_{f} is well explained. More details of generated structure is shown in table 6.2, and the size distribution of poly-disperse case is shown in Fig. 6.13b. Based on these generated proto-type structure, different filler configuration impact on ions' $D^{\mathrm{i}}_{\mathrm{eff}}$ is discussed in the following

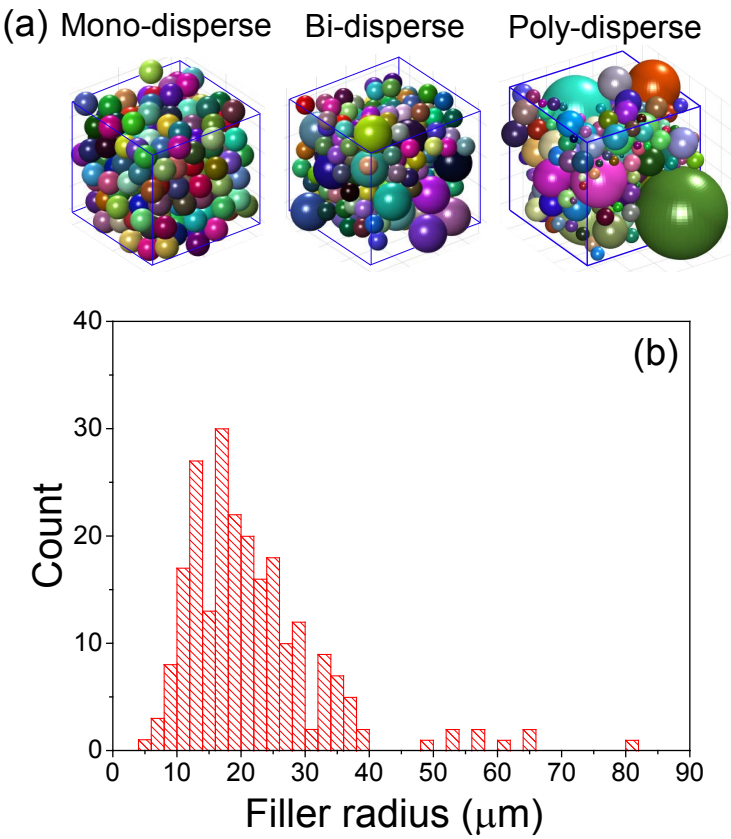

Fig. 6.13. (a) Examples of generated structure for each dispersity. (b) Size distribution histogram of poly-disperse packed case.

section. At last, the PEA experimental data is also analyzed to validate the tendency we observed based on RRN-model.

6.6 Different filler configurations impact on D^{i}_{eff}

6.6.1 Interfacial layer thickness (t_{int})

For the structure shown in Fig. 6.13(inset), t_{int} is varied from $10nm$ to $2\mu m$. One may easily can assume that as t_{int} becomes thicker, D^{i}_{eff} would also become larger. As shown in Fig. 6.13, D^{i}_{eff} becomes larger as t_{int} gets thicker. Of course, if the filler configuration is different, the increasing tendency of D^{i}_{eff} will not be the same.

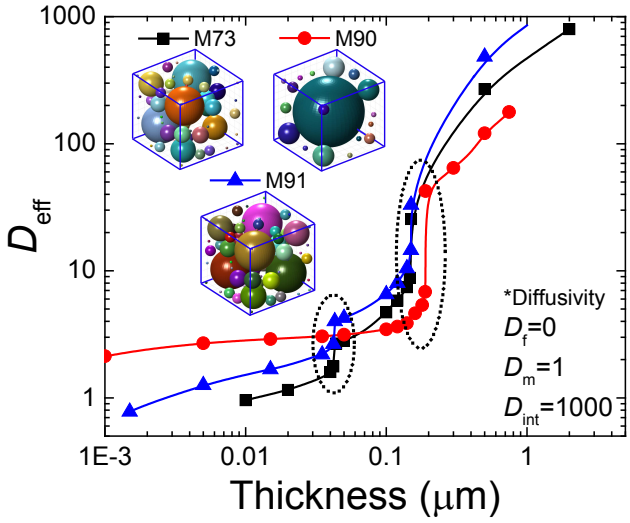

Fig. 6.14. Calculated D^{i}_{eff} as interface layer thickness varies for the structure shown by inset figure. Red arrows indicate the formation of percolative paths as thickness increases.

One interesting remark we find out is that approximate water shell layer isotherm for the modeling can be back estimated based on conductivity measurement result. As we observed the measured conductivity can increase 2 3 folds shown in Fig. 6.6, we can presumed that water shell thickness can be within several μm scale based on our calculated result. This remark is consistent with the recent published work of estimated water shell layer thickness in the case of glass/epoxy composites [221]. The further investigation of D^{i}_{eff} increasing behavior depending on various t_{int} is shown in Appendix C to confirm $RRNM$ validity.

6.6.2 Volumetric fraction

In order to investigate ϕ_f impact, first, we compared manually generated structure, ϕ_f of 35 (M73), and 45% (M91) cases. Both samples exhibit a same size distribution (same maximum, and average filler size) but different ϕ_f. For the calculation, the water shell layer thickness is set to $500nm$. Based on the assumed thickness value,

calculated $D^{\mathrm{i}}_{\mathrm{eff}}$ of M73, and M91 is 3.44, and 5.15, respectively. Thus, we can figure out that larger ϕ_{f} can result in a higher $D^{\mathrm{i}}_{\mathrm{eff}}$ value when a MC is exposed to a humid environment. Similarly, we can also find out in Fig. 6.15 that the same increasing trend for the samples generated by other algorithms: drop-fall-shake algorithm, and variable-cell method. One interesting remark in Fig. 6.15, is that $D^{\mathrm{i}}_{\mathrm{eff}}$ does not exhibits a considerable increase around $\sim 30\%$ (i.e., percolation threshold for 3D jammed spherical fillers [227]). This is because our assumed structure exhibits nonuniform conductivity depending on different filler size (larger the filler size, smaller the effective local conductivity) so that the increasing behavior is not same as proposed percolation threshold value for conducting spherical fillers [227]. Moreover, this increasing behavior is also different from the increasing behavior shown in Fig. 2.7a (in chapter 2) as the interfacial layer to matrix property ratio is different compares to the case shown in chapter 6. When the sample is dried, the conductivity difference between interfacial region and polymer is within one order so that it is not reasonable to describe the system based on percolation theory.

Measured heterocharge packet by PEA measurement also shows that more hetero charge accumulation in the case of M91 than that of M73 as shown in Fig. 6.16. This is because larger fillers content with highly conducting layers provide more percolative paths for the ions conduction. In conclusion, we can figure out when the size distribution is similar, $D^{\mathrm{i}}_{\mathrm{eff}}$ will be larger as ϕ_{f} increases.

6.6.3 Size distribution

First, the different size distribution impact is studied by comparing M90, and M91 samples. As shown in table 5.2, both samples show same ϕ_{f}, however, maximum, and average filler size of M90 is larger than that of M91. Based on the prototype structures, calculated $D^{\mathrm{i}}_{\mathrm{eff}}$ of M90, and M91 is 3.29, and 5.15, respectively. Therefore, we can figure out that the $D^{\mathrm{i}}_{\mathrm{eff}}$ value would be smaller if the filler size becomes larger. This result also coincides with the calculation of other generated structures

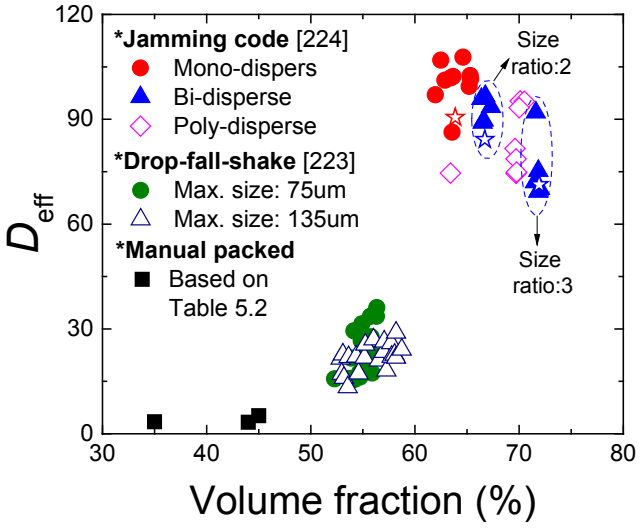

Fig. 6.15. Calculated $D^{\mathrm{i}}_{\mathrm{eff}}$ for different ϕ_{f} when the number of spheres is 200. Star symbols are based on the structures of 500 spheres. Simulation of poly-disperse when the number of spheres more than 250 is not performed due to the convergence issue.

by different algorithms as shown in Fig. 6.15. In the case of the structures by drop-fall-shake algorithm, we can find out that the samples with the larger maximum size filler shows less $D^{\mathrm{i}}_{\mathrm{eff}}$ value. The same trend can be also observed in the structures generated by variable-cell method. With the same number of fillers, mono-disperse structure shows even higher $D^{\mathrm{i}}_{\mathrm{eff}}$ value at lower ϕ_{f} than that of bi-disperse, and poly-disperse samples. Between two different bi-disperse samples, the sample with larger size distribution shows less $D^{\mathrm{i}}_{\mathrm{eff}}$.

Measured accumulated heterocharge of the actual MC in the case of M91 also shows larger than that of M90 due to the larger ions mobility as shown in Fig. 6.16. This is because large size fillers exhibit lower local $D^{\mathrm{i}}_{\mathrm{eff}}$ than that of smaller size fillers and the reason can be easily understood based on EMT model. With same thickness of interfacial region thickness, local $D^{\mathrm{i}}_{\mathrm{eff}}$ will be lower as filler size gets larger since the volume fraction of interfacial region will be smaller for larger filler size. In conclusion, we can realize deploying larger size distribution is more beneficial

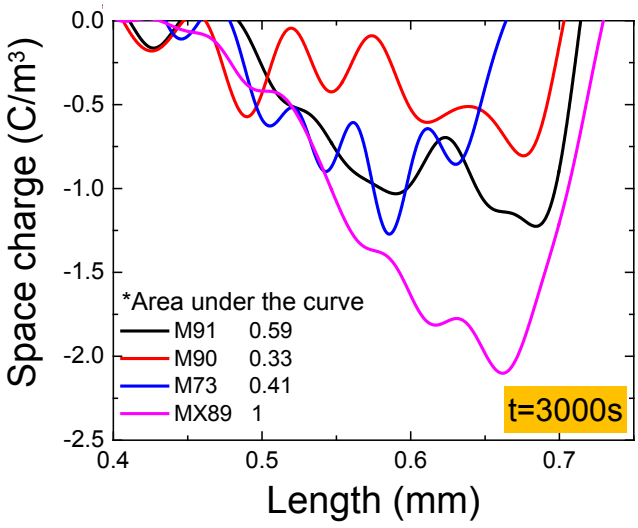

Fig. 6.16. Accumulated heterocharge comparison among different MCs based on measured PEA data. MX89 shows the maximum accumulated heterocharge and the area under the curve is normalized to 1.

to suppress heterocharge development when the packaging material is exposed to a humid environment.

6.6.4 Adhesion promoter

As shown in Fig. 6.16, MX89 shows much larger accumulated heterocharge (larger D^{i}_{eff} of ions) than that of M91 even though MX89 has smaller ϕ_f. In the previous section, we concluded that smaller ϕ_f would show smaller D^{i}_{eff} as smaller ϕ_f MC would exhibits less percolative paths. However, as we observed in chapter 5, the absence of adhesion promoter causes more reactive sites generation so that ions will be likely to transport through these sites. Thus, we can conclude that adhesion promoter is essential to lower D^{i}_{eff}, and in addtion, for more reliable encapsulant.

6.7 Filler configuration optimization

Other than the explicit variables (e.g., applied voltage, sample thickness, dielectric constant), mobility, trapping, and detrapping coefficient are the governing variables that impact on space charge behavior. Each variable impact on space charge behavior is studied to investigate how water influences on the heterocharge accumulation. As described in chapter 5, the reacted water (Y) has dominant impact on increasing conductivity (i.e., mobility). Similarly, we can figure out the mobility of ions also increases when water is present in the encapsulant based on space charge FEM simulation. We can investigate larger heterocharge packet as mobility of ions increases as shown in Fig. 6.16. As explained in section 5.5.1, the ions mobility increases due to hydrolysis that generates more polar, and hydrophilic ions (e.g., hydronium ions). Even though hydrolysis is somewhat suppressed by adding adhesion promoter, different filler configuration can result in a different heterocharge accumulation rate. In this section, we have shown that smaller ϕ_{f}, and larger size distribution are more beneficial to suppress heterocharge accumulation. Thus, a careful optimization is required not to sacrifice other important features of MC by following the conditions described above.

Different τ_{T}, and τ_{D} also cause considerable space charge behavior changes. As τ_{T} decreases, we can investigate broader heterocharge packet. When τ_{D} increases, we can observe more heterocharge buildup at the same given time. Based on our PEA measurement, we can figure out τ_{D} is increased due to water and results in more heterocharge buildup. Meanwhile, heterocharge packet width variation is not clearly observed in our PEA measurement which indicates inconsiderable changes of τ_{T} value.

In conclusion, we can figure out how transport input parameters change when MC is exposed to a humid environment as follows: (i) τ_{D}, and $\mu_{\mathrm{n,p}}$ increase. These two parameters increase result in larger heterocharge packet; (ii) N_{T} increase. Higher homocharge peak is caused by additional trapping sites generation; (iii) mobility

increase. Water forms highly conducting percolative paths so that pre-existing ions moves much faster than that of dry case. As a results, heterocharge development can be observed in wet samples, whereas not in dry samples. Each transport parameter impact on space charge can be also investigated based on an analytical model shown in appendix A.

Finally, based on our analytical model and discussions so far, we listed conditions for good encapsulant as follows.

- Small J_0 for less homocharge buildup: Wrap high voltage wire with an insulator or surface treatment to suppress charges injection.
- Larger ε_{r} for less homocharge buildup.
- Lower pre-existing ions for less heterocharge buildup.
- Lesser N_{T} to suppress homocharge buildup.
- Suppress water diffusion as it increases mobility of ions and develops heterocharge packet.
- If we can not avoid water ingression, smaller ϕ_{f}, and larger size distribution are better as these conditions result in less $D^{\mathrm{i}}_{\mathrm{eff}}$ of pre-existing ions.

6.8 Conclusions

Space charge distribution distorts the electric field inside an encapsulant and can cause severe reliability issues. Although the problem has been studied extensively, the origin of homocharge and heterocharge were not fully understood. In this chapter, we explained the key characteristics of commercial epoxy molding compounds as shown below based on our compact analytical model for homocharge behavior and new numerical transport model for ionic impurities.

- Homocharge decrease, and heterocharge accumulation are due to pre-existing ionic impurities.

- Smaller J_0, N_{T}, pre-existing ions, and larger ε_{r} are conditions for more reliable encapsulant for less space charge accumulation perspective.

- Water increases , and τ_{D} so that it causes heterocharge accumulation. we have to prevent water ingress to ensure long lifetime.

- Electrical conductivity of MC shows exponential relationship with Y concentration as shown in Eq. 6.8.

Our compact analytical model can be applied to analyze measured PEA data. In addition, RRN-model is suggested to estimate $D_{\mathrm{eff}}^{\mathrm{i}}$ when the sample is exposed to water and percolative paths are formed. Based on this new modeling frameworks, we optimized the filler configuration to suppress heterocharge buildup. The modeling framework developed in this chapter will give us new insights to understand complicated dynamics of space charge packets, and further suggest new opportunities for the better reliability optimization of an ICs encapsulant.

7. SUMMARY AND FUTURE WORK

7.1 Summary of thesis

The modeling microelectronics reliability in both Moore's law era and post-Moore's law era is difficult because it involves interactions among multiple competing, yet correlated, mechanisms involving a wide range of length (from nm to cm) and time scales (from ns to years). Among the variety of emerging reliability topics, in this thesis we have focused on two important concerns: transistor and interconnect self-heating involving electro-thermal transport, and chip package interaction issues involving correlated moisture and ion transport. Let us summarize the key conclusions related to these topics.

Summary and conclusions from Chapter 3

The main focus in chapter 3 was to develop a framework for multi-scale electro-thermal modeling in an IC. The analysis showed that SHE is an unfortunate corollary of the confined-gate transistors (e.g. FinFET; Nanowire-FET, NWFET; NanoSheet-FET, NSHFET) needed for the electrostatically-robust sub-10nm ICs. Many groups have developed tier-specific thermal models, which can neither predict the channel temperature (T_{C}) accurately, nor suggest innovative strategies to reduce T_{C} by identifying/removing thermal bottlenecks in the hierarchy. We have made the following contributions to the topic.

1. We have developed a FEOL level thermal compact model (TCM_{F}) based on 3D FEM transient thermal simulations.

2. We have investigated the multi-scale SHE effect by BSIM-CMG circuit simulation for ICs with a refined FEOL model.

3. We have proposed a BEOL level thermal compact model (TCM_{B}) by using image charge and EMT model. Then, we have integrated TCM_{F}, and TCM_{B} to predict T_{C} rise due to self-heated transistors.

4. We have also proposed a Variety of SHE mitigation strategies using thermal shunts.

The modeling frameowk allows us to conclude that:

1. SHE is more severe at high frequencies than anticipated by the traditional single-τ_{C} model. Thermal coupling of BEOL and self-heated transistors makes the situation worse.

2. NSHFET is a good candidate at sub-10nm nodes considering both lower subthreshold swing (SS) than that of FinFET and better reliability than that of NWFET.

Summary and conclusions from Chapter 4

The discussion in Chapter 3 focused on the calculation of the temperature distribution due to self-heated transistors. The additional temperature rise due to Joule heating within an interconnect was not considered. In chapter 4, front- and backend self- and mutual heating and its implications for the backend reliability were investigated. To summarize:

1. We derived a closed-form analytical formula to describe the transient temperature rise within an interconnect.

2. We applied the proposed compact model to predict the temperature distribution for any given circuits/systems.

3. We validated the proposed model by FEM simulations and experiments.

4. We compared the effectiveness of different interconnect materials and cooling strategies to reduce the interconnect Joule heating.

Based on these contributions, we concluded that:

1. Cobalt can replace Copper for the lower BEOL levels (e.g., M1-M3) due to its superior reliability, however, excessive heating in Cobalt makes Copper still a preferred option for the higher BEOL levels (e.g., M5-M10).

2. Between the two cooling strategies discussed in this chapter, increasing the wire size is more effective in Joule heating compared to than increasing the via density.

Summary and conclusions from Chapter 5

In chapters 5 and 6, we investigated electrical chip package interaction by focusing on moisture and ion transport within the packaging material. The modeling is nontrivial as charge transport involves multiple correlated phenomena, including moisture diffusion, electric potential redistribution, and self-heating due to transistors and interconnects. In chapter 5, we provided a fundamental understanding of moisture transport in mold compounds and suggested several strategies to suppress moisture diffusion. To summarize:

1. We developed a generalized EMT model to describe moisture diffusion as a function of fill-fraction, size-dispersion, shape, and topology of filler nanoparticles.

2. Our proposed generalized effective medium and solubility ($GEMS$) Langmuir model quantifies water uptake as a function of filler configuration and relative humidity.

3. We investigated the dominant impact of reacted-water on σ through numerical simulations, mass-uptake, and DC conductivity measurements.

4. We investigated electric field distribution to explain how moisture ingress reduces $E_{\mathrm{MC}}^{\mathrm{Crit}}$.

The proposed $GEMS$-Langmuir model is used to optimize filler configuration that can enhance the performance of MCs. The analysis allows us to conclude the following:

1. Reacted water (rather than mobile water) plays a dominant role in determining σ of MCs.

2. Adhesion promoter is essential for lower σ, and higher $E_{\mathrm{MC}}^{\mathrm{Crit}}$ in humid environment.

3. Filler volume fraction does not impact on σ significantly (i.e., more than an order of magnitude difference), however, it needs to be carefully optimized for higher $E_{\mathrm{MC}}^{\mathrm{Crit}}$ depending on the severity of moisture uptake.

Summary and conclusion from Chapter 6

Based on the fundamental understanding of moisture transport, and PEA measurement data, charges transport within MCs are also studied and modeled.

1. Derive physics-based compact analytical model of homocharge behavior and then the origin of homo-, heterocharge is investigated.

2. Suggest a new modeling framework (i.e., revised random network model ($RRNM$)) to predict effective ions diffusivity within the MC.

3. Clarify moisture impact on critical inputs (e.g., mobility, trapping coefficient) of the space charge behavior, and the important conditions for the better encapsulation for ICs are suggested.

Based on our new modeling framework, we reach the following conclusions regarding ion-transport in a mold compound.

1. The build-up of homocharges minimizes charge injection from the electrode.

2. Lowering pre-existing ions concentration is important to suppress heterocharge buildup.

3. One must suppress moisture ingress as it increases the mobility of the ions and favors development of the heterocharge packet.

4. If moisture ingress is unavoidable, smaller ϕ_f, and larger size dispersion of the fillers will suppress ion transport.

7.2 Future researches directions

7.2.1 Experimental Validation of the thermal compact model and its generalization to various circuits

A single transistor SHE behavior at either DC operation or AC operation under a constant frequency is quite straightforward. The SHE behavior of a digital circuit (i.e., ring oscillator), and analog circuit (i.e., amplifier) composed of multiple transistors has been also studied in this thesis based on our generalized FEOL compact model. The SHE behavior for these specific circuit configurations must still be validated experimentally. In particular, it will be important to validate SHE effect in the various digital circuits such as ring oscillator, NAND, AND, OR gates, etc, as well as the implications of the geometrical layout of the transistors and interconnects (i.e., electrode size, the distance between transistors).

7.2.2 Multi-physics modeling for 3D packaging configuration

As the industry moves on to 3D packaging strategies, there will be many thin layers of different material stacked together within an IC. As an IC undergoes thermal cycling due to SHE, warpage phenomenon due to the difference between the coefficient of thermal expansion cannot be ignored. Different stress on silicon substrate may change the mobility of the transistors, and the warpage can initiate cracks or voiding between board and IC. The multi-physics modeling among thermal, electrical, and mechanical dimensions should be also investigated.

7.2.3 Electrical chip package interaction at AC operating condition

In practice, many systems operate at moderate to high frequencies. In this thesis, DC operating condition is assumed. Considering the actual operating condition, the generalization of the proposed model to account for AC operating condition is also necessary. The algorithm developed for DC stress (e.g., EMT approximation, solution of transport equations, and coupling methodology for water and ions) can be appropriately revised for AC stress. Finally, the compact model can also consider SHE for high fidelity reliability prediction.

7.3 Concluding remarks

In this thesis, we have developed a variety of modeling methodologies to predict the reliability of modern ICs. The modeling of the reliability issues has been challenging because they involve multi-physics, multi-scale, coupled transport of several species. Our proposed modeling frameworks provide deep and fundamental insights regarding the reliability of microelectronic circuits and systems. In developing this modeling framework, we needed to generalize the EMT and random-resistor networks to anisotropic, multi-component system close to the jamming limit. The approach is general and therefore in addition to addressing the reliability concerns of the ICs, the techniques will apply to all electronic devices (e.g. solar cells, biosensors, etc.) that share similar reliability issues. I believe that creating a general framework is the ultimate achievement of this thesis.

REFERENCES

REFERENCES

[1] G. E. Moore, "Cramming more components onto integrated circuits, reprinted from electronics, volume 38, number 8, april 19, 1965, pp.114 ff." *IEEE Solid-State Circuits Society Newsletter*, vol. 11, no. 3, pp. 33–35, Sep. 2006.

[2] M. Bohr, "The evolution of scaling from the homogeneous era to the heterogeneous era," in *2011 International Electron Devices Meeting*, Dec 2011, pp. 1.1.1–1.1.6.

[3] H. M. Fahad and M. M. Hussain, "Are nanotube architectures more advantageous than nanowire architectures for field effect transistors?" *Scientific Reports*, vol. 2, p. 475, Jun 2012.

[4] A. Khakifirooz and D. A. Antoniadis, "Mosfet performance scalingpart ii: Future directions," *IEEE Transactions on Electron Devices*, vol. 55, no. 6, pp. 1401–1408, June 2008.

[5] S. Borkar, "Design challenges of technology scaling," *IEEE Micro*, vol. 19, no. 4, pp. 23–29, July 1999.

[6] J. D. Meindl, "Beyond moore's law: the interconnect era," *Computing in Science Engineering*, vol. 5, no. 1, pp. 20–24, Jan 2003.

[7] R. R. Tummala, "Moore's law meets its match (system-on-package)," *IEEE Spectrum*, vol. 43, no. 6, pp. 44–49, June 2006.

[8] E. Pop, "Energy dissipation and transport in nanoscale devices," *Nano Research*, vol. 3, no. 3, pp. 147–169, Mar 2010.

[9] H. Jiang, L. Shen, S. H. Shin, N. Xu, G. Du, B. . Nguyen, O. Faynot, M. A. Alam, X. Zhang, and X. Y. Liu, "Unified self-heating effect model for advanced digital and analog technology and thermal-aware lifetime prediction methodology," in *2017 Symposium on VLSI Technology*, June 2017, pp. T136–T137.

[10] U. S. Kumar and V. R. Rao, "A novel tcad-based thermal extraction approach for nanoscale finfets," *IEEE Transactions on Electron Devices*, vol. 64, no. 3, pp. 1404–1407, March 2017.

[11] M. Alam, H. Kufluoglu, D. Varghese, and S. Mahapatra, "A comprehensive model for pmos nbti degradation: Recent progress," *Microelectronics Reliability*, vol. 47, no. 6, pp. 853 – 862, 2007.

[12] S. Poli, S. Reggiani, G. Baccarani, E. Gnani, A. Gnudi, M. Denison, S. Pendharkar, R. Wise, and S. Seetharaman, "Investigation on the temperature dependence of the hci effects in the rugged sti-based ldmos transistor," in *2010 22nd International Symposium on Power Semiconductor Devices IC's (ISPSD)*, June 2010, pp. 311–314.

[13] E. Wu, J. Su, C. LaRow, and R. Dufresne, "Temperature dependence of tddb voltage acceleration in high-/ sio2bilayers and sio2gate dielectrics," in *2012 International Electron Devices Meeting*, Dec 2012, pp. 28.5.1–25.5.4.

[14] Y.-K. Cheng, *Temperature-dependent Electromigration Reliability*. Boston, MA: Springer US, 2002, pp. 121–155.

[15] A. H. Ajami, K. Banerjee, and M. Pedram, "Modeling and analysis of nonuniform substrate temperature effects on global ulsi interconnects," *IEEE Transactions on Computer-Aided Design of Integrated Circuits and Systems*, vol. 24, no. 6, pp. 849–861, June 2005.

[16] J. Lloyd and J. Clement, "Electromigration in copper conductors," *Thin Solid Films*, vol. 262, no. 1, pp. 135 – 141, 1995.

[17] A. Ghetti, *Gate Oxide Reliability: Physical and Computational Models*. Berlin, Heidelberg: Springer Berlin Heidelberg, 2004, pp. 201–258.

[18] M. Alam, B. Weir, J. Bude, P. Silverman, and A. Ghetti, "A computational model for oxide breakdown: theory and experiments," *Microelectronic Engineering*, vol. 59, no. 1, pp. 137 – 147, 2001.

[19] D. J. DiMaria and J. H. Stathis, "Non-arrhenius temperature dependence of reliability in ultrathin silicon dioxide films," *Applied Physics Letters*, vol. 74, no. 12, pp. 1752–1754, 1999.

[20] R. Degraeve, N. Pangon, B. Kaczer, T. Nigam, G. Groeseneken, and A. Naem, "Temperature acceleration of oxide breakdown and its impact on ultra-thin gate oxide reliability," in *1999 Symposium on VLSI Technology. Digest of Technical Papers (IEEE Cat. No.99CH36325)*, June 1999, pp. 59–60.

[21] C. Hsieh, C. Wu, and D. Yu, "Analysis and comparison of thermal performance of advanced packaging technologies for state-of-the-art mobile applications," in *2016 IEEE 66th Electronic Components and Technology Conference (ECTC)*, May 2016, pp. 1430–1438.

[22] B. Dang, M. S. Bakir, and J. D. Meindl, "Integrated thermal-fluidic i/o interconnects for an on-chip microchannel heat sink," *IEEE Electron Device Letters*, vol. 27, no. 2, pp. 117–119, Feb 2006.

[23] Y. J. Kim, Y. K. Joshi, A. G. Fedorov, Y.-J. Lee, and S.-K. Lim, "Thermal characterization of interlayer microfluidic cooling of three-dimensional integrated circuits with nonuniform heat flux," *Journal of Heat Transfer*, vol. 132, no. 4, pp. 041 009–041 009–9, Feb 2010.

[24] K. Tu, "Reliability challenges in 3d ic packaging technology," *Microelectronics Reliability*, vol. 51, no. 3, pp. 517 – 523, 2011.

[25] M. Uschitsky and E. Suhir, "Moisture diffusion in epoxy molding compounds filled with particles," *Journal of Electronic Packaging*, vol. 123, 03 2001.

[26] H. Ardebili, Ee Hua Wong, and M. Pecht, "Hygroscopic swelling and sorption characteristics of epoxy molding compounds used in electronic packaging," *IEEE Transactions on Components and Packaging Technologies*, vol. 26, no. 1, pp. 206–214, March 2003.

[27] G. Dummer, *Electronic inventions and discoveries : electronics from its earliest beginnings to the present day*, 3rd ed., ser. Pergamon international library of science, technology, engineering, and social studies. Pergamon Press, 1983.

[28] M. Sahimi, *Heterogeneous Materials I: Linear Transport and Optical Properties*, ser. Interdisciplinary Applied Mathematics. Springer New York, 2006.

[29] K. K. Karkkainen, A. H. Sihvola, and K. I. Nikoskinen, "Effective permittivity of mixtures: numerical validation by the fdtd method," *IEEE Transactions on Geoscience and Remote Sensing*, vol. 38, no. 3, pp. 1303–1308, May 2000.

[30] Z. Hashin and S. Shtrikman, "A variational approach to the theory of the effective magnetic permeability of multiphase materials," *Journal of Applied Physics*, vol. 33, no. 10, pp. 3125–3131, 1962.

[31] G. J. C. Maxwell and L. Joseph, "Xii. colours in metal glasses and in metallic films," *Philosophical Transactions of the Royal Society of London. Series A, Containing Papers of a Mathematical or Physical Character*, vol. 203, no. 359-371, pp. 385–420, Jan 1904.

[32] J. G. Berryman, "Bounds and estimates for transport coefficients of random and porous media with high contrasts," *Journal of Applied Physics*, vol. 97, no. 6, p. 063504, 2005.

[33] J. Helsing, "Bounds to the conductivity of some twocomponent composites," *Journal of Applied Physics*, vol. 73, no. 3, pp. 1240–1245, 1993.

[34] D. A. G. Bruggeman, "Berechnung verschiedener physikalischer konstanten von heterogenen substanzen. i. dielektrizittskonstanten und leitfhigkeiten der mischkrper aus isotropen substanzen," *Annalen der Physik*, vol. 416, no. 7, pp. 636–664, 1935.

[35] J. Kalnin, E. Kotomin, and J. Maier, "Calculations of the effective diffusion coefficient for inhomogeneous media," *Journal of Physics and Chemistry of Solids*, vol. 63, no. 3, pp. 449 – 456, 2002.

[36] A. Baji, Y.-W. Mai, Q. Li, and Y. Liu, "Electrospinning induced ferroelectricity in poly(vinylidene fluoride) fibers," *Nanoscale*, vol. 3, pp. 3068–3071, 2011.

[37] X.-L. Xie, Y.-W. Mai, and X.-P. Zhou, "Dispersion and alignment of carbon nanotubes in polymer matrix: A review," *Materials Science and Engineering: R: Reports*, vol. 49, no. 4, pp. 89 – 112, 2005.

[38] A. M. Mayes, "Softer at the boundary," *Nature Materials*, vol. 4, no. 9, pp. 651–652, 2005.

[39] S. Singha and M. J. Thomas, "Dielectric properties of epoxy nanocomposites," *IEEE Transactions on Dielectrics and Electrical Insulation*, vol. 15, no. 1, pp. 12–23, February 2008.

[40] I. V. Belova and G. E. Murch, "The effective diffusivity in polycrystalline material in the presence of interphase boundaries," *Philosophical Magazine*, vol. 84, no. 1, pp. 17–28, 2004.

[41] I. Imperiale, S. Reggiani, G. Pavarese, E. Gnani, A. Gnudi, G. Baccarani, W. Ahn, M. A. Alam, D. Varghese, A. Hernandez-Luna, L. Nguyen, and S. Krishnan, "Role of the insulating fillers in the encapsulation material on the lateral charge spreading in hv-ics," *IEEE Transactions on Electron Devices*, vol. 64, no. 3, pp. 1209–1216, March 2017.

[42] C.-W. Nan, R. Birringer, D. R. Clarke, and H. Gleiter, "Effective thermal conductivity of particulate composites with interfacial thermal resistance," *Journal of Applied Physics*, vol. 81, no. 10, pp. 6692–6699, 1997.

[43] S. Kanuparthi, M. Rayasam, G. Subbarayan, B. Sammakia, A. Gowda, and S. Tonapi, "Hierarchical field compositions for simulations of near-percolation thermal transport in particulate materials," *Computer Methods in Applied Mechanics and Engineering*, vol. 198, no. 5, pp. 657 – 668, 2009.

[44] S. Kanuparthi, G. Subbarayan, T. Siegmund, and B. Sammakia, "An efficient network model for determining the effective thermal conductivity of particulate thermal interface materials," *IEEE Transactions on Components and Packaging Technologies*, vol. 31, no. 3, pp. 611–621, Sep. 2008.

[45] B. Dan, S. Kanuparthi, G. Subbarayan, and B. G. Sammakia, "An improved network model for determining the effective thermal conductivity of particulate thermal interface materials," pp. 69–81, 2009. [Online]. Available: http://dx.doi.org/10.1115/InterPACK2009-89116

[46] P. K. Vaitheeswaran and G. Subbarayan, "Estimation of effective thermal and mechanical properties of particulate thermal interface materials by a random network model," *Journal of Electronic Packaging*, vol. 140, no. 2, pp. 020 901–020 901–7, May 2018.

[47] B. G. Keith and O. R. W., "Thermal or electrical conduction through a granular material," *Proceedings of the Royal Society of London. A. Mathematical and Physical Sciences*, vol. 355, no. 1682, pp. 313–333, Jul 1977.

[48] N. Pimparkar, C. Kocabas, S. J. Kang, J. Rogers, and M. A. Alam, "Limits of performance gain of aligned cnt over randomized network: Theoretical predictions and experimental validation," *IEEE Electron Device Letters*, vol. 28, no. 7, pp. 593–595, July 2007.

[49] A. Khakifirooz and D. A. Antoniadis, "The future of high-performance cmos: Trends and requirements," in *ESSDERC 2008 - 38th European Solid-State Device Research Conference*, Sep. 2008, pp. 30–37.

[50] Z. Liu, C. Hu, J. Huang, T. Chan, M. Jeng, P. K. Ko, and Y. C. Cheng, "Threshold voltage model for deep-submicrometer mosfets," *IEEE Transactions on Electron Devices*, vol. 40, no. 1, pp. 86–95, Jan 1993.

[51] G. Ghibaudo, "An analytical model of conductance and transconductance for enhanced-mode mosfets," *physica status solidi (a)*, vol. 95, no. 1, pp. 323–335, 1986.

[52] N. Singh, A. Agarwal, L. K. Bera, T. Y. Liow, R. Yang, S. C. Rustagi, C. H. Tung, R. Kumar, G. Q. Lo, N. Balasubramanian, and D. . Kwong, "High-performance fully depleted silicon nanowire (diameter /spl les/ 5 nm) gate-all-around cmos devices," *IEEE Electron Device Letters*, vol. 27, no. 5, pp. 383–386, May 2006.

[53] S.-M. Koo, Q. Li, M. D. Edelstein, C. A. Richter, and E. M. Vogel, "Enhanced channel modulation in dual-gated silicon nanowire transistors," *Nano Letters*, vol. 5, no. 12, pp. 2519–2523, Dec 2005.

[54] A. Danowitz, K. Kelley, J. Mao, J. P. Stevenson, and M. Horowitz, "Cpu db: Recording microprocessor history," *Queue*, vol. 10, no. 4, pp. 10:10–10:27, Apr. 2012.

[55] L. Shifren, R. Aitken, A. R. Brown, V. Chandra, B. Cheng, C. Riddet, C. L. Alexander, B. Cline, C. Millar, S. Sinha, G. Yeric, and A. Asenov, "Predictive simulation and benchmarking of si and ge pmos finfets for future cmos technology," *IEEE Transactions on Electron Devices*, vol. 61, no. 7, pp. 2271–2277, July 2014.

[56] P. Hashemi, T. Ando, S. Koswatta, K. . Lee, E. Cartier, J. A. Ott, C. . Lee, J. Bruley, M. F. Lofaro, S. Dawes, K. K. Chan, S. U. Engelmann, E. Leobandung, V. Narayanan, and R. T. Mo, "High performance and record subthreshold swing demonstration in scaled rmg sige finfets with high-ge-content channels formed by 3d condensation and a novel gate stack process," in *2017 Symposium on VLSI Technology*, June 2017, pp. T120–T121.

[57] E. Bury, B. Kaczer, P. Roussel, R. Ritzenthaler, K. Raleva, D. Vasileska, and G. Groeseneken, "Experimental validation of self-heating simulations and projections for transistors in deeply scaled nodes," in *2014 IEEE International Reliability Physics Symposium*, June 2014, pp. XT.8.1–XT.8.6.

[58] M. Jin, C. Liu, J. Kim, J. Kim, S. Choo, Y. Kim, H. Shim, L. Zhang, K. Nam, J. Park, S. Pae, and H. Lee, "Hot carrier reliability characterization in consideration of self-heating in finfet technology," in *2016 IEEE International Reliability Physics Symposium (IRPS)*, April 2016, pp. 2A–2–1–2A–2–5.

[59] H. Jiang, S. Shin, X. Liu, X. Zhang, and M. A. Alam, "The impact of self-heating on hci reliability in high-performance digital circuits," *IEEE Electron Device Letters*, vol. 38, no. 4, pp. 430–433, April 2017.

[60] A. D. D. Dwivedi, R. D'Esposito, A. K. Sahoo, S. Fregonese, and T. Zimmer, "A study on self-heating and mutual thermal coupling in sige multi-finger hbts," *Journal of Electronic Materials*, vol. 45, no. 11, pp. 5612–5620, Nov 2016.

[61] "http://ptm.asu.edu/."

[62] "http://bsim.berkeley.edu/models/bsimcmg/."

[63] D. Jang, E. Bury, R. Ritzenthaler, M. G. Bardon, T. Chiarella, K. Miyaguchi, P. Raghavan, A. Mocuta, G. Groeseneken, A. Mercha, D. Verkest, and A. Thean, "Self-heating on bulk finfet from 14nm down to 7nm node," in *2015 IEEE International Electron Devices Meeting (IEDM)*, Dec 2015, pp. 11.6.1–11.6.4.

[64] M. Ramdani, E. Sicard, S. Ben Dhia, and J. Catrysse, "Towards an emc roadmap for integrated circuits," in *2008 Asia-Pacific Symposium on Electromagnetic Compatibility and 19th International Zurich Symposium on Electromagnetic Compatibility*, May 2008, pp. 8–11.

[65] A. Majumdar, "Microscale heat conduction in dielectric thin films," *Journal of Heat Transfer*, vol. 115, no. 1, pp. 7–16, Feb 1993.

[66] M. Shrivastava, M. Agrawal, S. Mahajan, H. Gossner, T. Schulz, D. K. Sharma, and V. R. Rao, "Physical insight toward heat transport and an improved electrothermal modeling framework for finfet architectures," *IEEE Transactions on Electron Devices*, vol. 59, no. 5, pp. 1353–1363, May 2012.

[67] J. Cuffe, J. K. Eliason, A. A. Maznev, K. C. Collins, J. A. Johnson, A. Shchepetov, M. Prunnila, J. Ahopelto, C. M. Sotomayor Torres, G. Chen, and K. A. Nelson, "Reconstructing phonon mean-free-path contributions to thermal conductivity using nanoscale membranes," *Phys. Rev. B*, vol. 91, p. 245423, Jun 2015.

[68] M. Fulde, J. P. Engelstädter, G. Knoblinger, and D. Schmitt-Landsiedel, "Analog circuits using finfets: benefits in speed-accuracy-power trade-off and simulation of parasitic effects," *Advances in Radio Science*, vol. 5, pp. 285–290, 2007.

[69] Wei Huang, S. Ghosh, S. Velusamy, K. Sankaranarayanan, K. Skadron, and M. R. Stan, "Hotspot: a compact thermal modeling methodology for early-stage vlsi design," *IEEE Transactions on Very Large Scale Integration (VLSI) Systems*, vol. 14, no. 5, pp. 501–513, May 2006.

[70] J. Meng, K. Kawakami, and A. K. Coskun, "Optimizing energy efficiency of 3-d multicore systems with stacked dram under power and thermal constraints," in *Proceedings of the 49th Annual Design Automation Conference*, ser. DAC '12. New York, NY, USA: ACM, 2012, pp. 648–655.

[71] J. Yan, S. Jan, Y. Peng, H. H. Lin, W. K. Wan, Y. . Huang, B. Hung, K. . Chan, M. Huang, M. . Yang, and C. W. Liu, "Thermal resistance modeling of back-end interconnect and intrinsic finfets, and transient simulation of inverters with capacitive loading effects," in *2016 IEEE International Electron Devices Meeting (IEDM)*, Dec 2016, pp. 35.6.1–35.6.4.

[72] A. M. Thiele, A. Kumar, G. Sant, and L. Pilon, "Effective thermal conductivity of three-component composites containing spherical capsules," *International Journal of Heat and Mass Transfer*, vol. 73, pp. 177 – 185, 2014.

[73] B. A. Young, A. M. Fujii, A. M. Thiele, A. Kumar, G. Sant, E. Taciroglu, and L. Pilon, "Effective elastic moduli of core-shell-matrix composites," *Mechanics of Materials*, vol. 92, pp. 94 – 106, 2016.

[74] J. A. Davis, V. K. De, and J. D. Meindl, "A stochastic wire-length distribution for gigascale integration (gsi). i. derivation and validation," *IEEE Transactions on Electron Devices*, vol. 45, no. 3, pp. 580–589, March 1998.

[75] X. L, "Thermal conductivity modeling of copper and tungsten damascene structures," *Journal of Applied Physics*, vol. 105, no. 9, p. 094301, 2009.

[76] E. Hart, "On the role of dislocations in bulk diffusion," *Acta Metallurgica*, vol. 5, no. 10, p. 597, 1957.

[77] H. Xu, V. F. Pavlidis, and G. De Micheli, "Analytical heat transfer model for thermal through-silicon vias," in *2011 Design, Automation Test in Europe*, March 2011, pp. 1–6.

[78] Z. Liu, S. Swarup, S. X. . Tan, H. Chen, and H. Wang, "Compact lateral thermal resistance model of tsvs for fast finite-difference based thermal analysis of 3-d stacked ics," *IEEE Transactions on Computer-Aided Design of Integrated Circuits and Systems*, vol. 33, no. 10, pp. 1490–1502, Oct 2014.

[79] C. W. Chang, S. E. Liu, B. L. Lin, C. C. Chiu, Y. . Lee, and K. Wu, "Thermal behavior of self-heating effect in finfet devices acting on back-end interconnects," in *2015 IEEE International Reliability Physics Symposium*, April 2015, pp. 2F.6.1–2F.6.5.

[80] A. Jain, R. E. Jones, R. Chatterjee, and S. Pozder, "Analytical and numerical modeling of the thermal performance of three-dimensional integrated circuits," *IEEE Transactions on Components and Packaging Technologies*, vol. 33, no. 1, pp. 56–63, March 2010.

[81] D. Chiozzi, M. Bernardoni, N. Delmonte, and P. Cova, "A simple 1-d finite elements approach to model the effect of pcb in electronic assemblies," *Microelectronics Reliability*, vol. 58, pp. 126 – 132, 2016.

[82] C. Hau-Riege, G. Xu, Q. J. Zhang, Y. Yau, and H. Farr, "A study of self- and mutual-heating in wafer level packaging systems," in *2017 IEEE International Reliability Physics Symposium (IRPS)*, April 2017, pp. 4A–5.1–4A–5.6.

[83] K. R. Bagnall, Y. S. Muzychka, and E. N. Wang, "Analytical solution for temperature rise in complex multilayer structures with discrete heat sources," *IEEE Transactions on Components, Packaging and Manufacturing Technology*, vol. 4, no. 5, pp. 817–830, May 2014.

[84] S. Mahapatra, N. Goel, S. Desai, S. Gupta, B. Jose, S. Mukhopadhyay, K. Joshi, A. Jain, A. E. Islam, and M. A. Alam, "A comparative study of different physics-based nbti models," *IEEE Transactions on Electron Devices*, vol. 60, no. 3, pp. 901–916, March 2013.

[85] T. Grasser, K. Rott, H. Reisinger, M. Waltl, F. Schanovsky, and B. Kaczer, "Nbti in nanoscale mosfetsthe ultimate modeling benchmark," *IEEE Transactions on Electron Devices*, vol. 61, no. 11, pp. 3586–3593, Nov 2014.

[86] N. Parihar, N. Goel, A. Chaudhary, and S. Mahapatra, "A modeling framework for nbti degradation under dynamic voltage and frequency scaling," *IEEE Transactions on Electron Devices*, vol. 63, no. 3, pp. 946–953, March 2016.

[87] T. Grasser, W. Goes, Y. Wimmer, F. Schanovsky, G. Rzepa, M. Waltl, K. Rott, H. Reisinger, V. V. Afanas'ev, A. Stesmans, A. . El-Sayed, and A. L. Shluger, "On the microscopic structure of hole traps in pmosfets," in *2014 IEEE International Electron Devices Meeting*, Dec 2014, pp. 21.1.1–21.1.4.

[88] T. Grasser, M. Waltl, K. Puschkarsky, B. Stampfer, G. Rzepa, G. Pobegen, H. Reisinger, H. Arimura, and B. Kaczer, "Implications of gate-sided hydrogen release for post-stress degradation build-up after bti stress," in *2017 IEEE International Reliability Physics Symposium (IRPS)*, April 2017, pp. 6A–2.1–6A–2.6.

[89] A. Chaudhary, B. Fernandez, N. Parihar, and S. Mahapatra, "Consistency of the two component composite modeling framework for nbti in large and small area p-mosfets," *IEEE Transactions on Electron Devices*, vol. 64, no. 1, pp. 256–263, Jan 2017.

[90] N. Parihar, R. G. Southwick, U. Sharma, M. Wang, J. H. Stathis, and S. Mahapatra, "Comparison of dc and ac nbti kinetics in rmg si and sige p-finfets," in *2017 IEEE International Reliability Physics Symposium (IRPS)*, April 2017, pp. 2D–4.1–2D–4.7.

[91] J. Franco, B. Kaczer, A. Chasin, H. Mertens, L. . Ragnarsson, R. Ritzenthaler, S. Mukhopadhyay, H. Arimura, P. J. Roussel, E. Bury, N. Horiguchi, D. Linten, G. Groeseneken, and A. Thean, "Nbti in replacement metal gate sige core finfets: Impact of ge concentration, fin width, fin rotation and interface passivation by high pressure anneals," in *2016 IEEE International Reliability Physics Symposium (IRPS)*, April 2016, pp. 4B–2–1–4B–2–7.

[92] S. Mishra, H. Y. Wong, R. Tiwari, A. Chaudhary, R. Rao, V. Moroz, and S. Mahapatra, "Tcad-based predictive nbti framework for sub-20-nm node device design considerations," *IEEE Transactions on Electron Devices*, vol. 63, no. 12, pp. 4624–4631, Dec 2016.

[93] Chenming Hu, Simon C. Tam, Fu-Chieh Hsu, Ping-Keung Ko, Tung-Yi Chan, and K. W. Terrill, "Hot-electron-induced mosfet degradation - model, monitor, and improvement," *IEEE Journal of Solid-State Circuits*, vol. 20, no. 1, pp. 295–305, Feb 1985.

[94] F. . Hsu and K. . Chiu, "Temperature dependence of hot-electron-induced degradation in mosfet's," *IEEE Electron Device Letters*, vol. 5, no. 5, pp. 148–150, May 1984.

[95] H. S. Momose and H. Iwai, "Analysis of the temperature dependence of hot-carrier-induced degradation in bipolar transistors for bi-cmos," *IEEE Transactions on Electron Devices*, vol. 41, no. 6, pp. 978–987, June 1994.

[96] M. Jo, S. Kim, C. Cho, M. Chang, and H. Hwang, "Gate voltage dependence on hot carrier degradation at an elevated temperature in a device with ultrathin silicon oxynitride," *Applied Physics Letters*, vol. 94, no. 5, p. 053505, 2009.

[97] S. E. Rauch, F. J. Guarin, and G. LaRosa, "Impact of e-e scattering to the hot carrier degradation of deep submicron nmosfets," *IEEE Electron Device Letters*, vol. 19, no. 12, pp. 463–465, Dec 1998.

[98] S. Tyaginov, M. Jech, J. Franco, P. Sharma, B. Kaczer, and T. Grasser, "Understanding and modeling the temperature behavior of hot-carrier degradation in sion nmosfets," *IEEE Electron Device Letters*, vol. 37, no. 1, pp. 84–87, Jan 2016.

[99] H. Jiang, S. Shin, X. Liu, X. Zhang, and M. A. Alam, "Characterization of self-heating leads to universal scaling of hci degradation of multi-fin soi finfets," in *2016 IEEE International Reliability Physics Symposium (IRPS)*, April 2016, pp. 2A–3–1–2A–3–7.

[100] K. Hess, A. Haggag, W. McMahon, B. Fischer, K. Cheng, J. Lee, and J. Lyding, "Simulation of si-sio/sub 2/ defect generation in cmos chips: from atomistic structure to chip failure rates," in *International Electron Devices Meeting 2000. Technical Digest. IEDM (Cat. No.00CH37138)*, Dec 2000, pp. 93–96.

[101] K. Hess, A. Haggag, W. McMahon, K. Cheng, J. Lee, and J. Lyding, "The physics of determining chip reliability," *IEEE Circuits and Devices Magazine*, vol. 17, no. 3, pp. 33–38, May 2001.

[102] J. R. Black, "Mass transport of aluminum by momentum exchange with conducting electrons," in *6th Annual Reliability Physics Symposium (IEEE)*, Nov 1967, pp. 148–159.

[103] K. Lee, "Electromigration recovery and short lead effect under bipolar- and unipolar-pulse current," in *2012 IEEE International Reliability Physics Symposium (IRPS)*, April 2012, pp. 6B.3.1–6B.3.4.

[104] G. Posser, V. Mishra, P. Jain, R. Reis, and S. S. Sapatnekar, "Cell-internal electromigration: Analysis and pin placement based optimization," *IEEE Transactions on Computer-Aided Design of Integrated Circuits and Systems*, vol. 35, no. 2, pp. 220–231, Feb 2016.

[105] K. Lee, J. Kim, T. Jeong, Y. Zhao, Q. Yuan, A. Patel, Z. T. Mai, L. H. Brown, S. English, and D. Sawyer, "Effect of joule heating on electromigration in dual-damascene copper low-k interconnects," in *2017 IEEE International Reliability Physics Symposium (IRPS)*, April 2017, pp. 6B–6.1–6B–6.5.

[106] P. Jain, J. Cortadella, and S. S. Sapatnekar, "A fast and retargetable framework for logic-ip-internal electromigration assessment comprehending advanced waveform effects," *IEEE Transactions on Very Large Scale Integration (VLSI) Systems*, vol. 24, no. 6, pp. 2345–2358, June 2016.

[107] Y. Park, P. Jain, and S. Krishnan, "New electromigration validation: Via node vector method," in *2010 IEEE International Reliability Physics Symposium*, May 2010, pp. 698–704.

[108] Z. Guan, M. Marek-Sadowska, S. Nassif, and B. Li, "Atomic flux divergence based current conversion scheme for signal line electromigration reliability assessment," in *IEEE International Interconnect Technology Conference*, May 2014, pp. 245–248.

[109] G. Posser, V. Mishra, R. Reis, and S. S. Sapatnekar, "Analyzing the electromigration effects on different metal layers and different wire lengths," in *2014 21st IEEE International Conference on Electronics, Circuits and Systems (ICECS)*, Dec 2014, pp. 682–685.

[110] C. . Hu, L. Gignac, B. Baker, E. Liniger, R. Yu, and P. Flaitz, "Impact of cu microstructure on electromigration reliability," in *2007 IEEE International Interconnect Technology Conferencee*, June 2007, pp. 93–95.

[111] J. Lloyd, "Black's law revisitednucleation and growth in electromigration failure," *Microelectronics Reliability*, vol. 47, no. 9, pp. 1468 – 1472, 2007.

[112] "2013 international technology roadmap for semiconductors (itrs)."

[113] R. Shaviv, S. Gopinath, M. Marshall, T. Mountsier, G. Dixit, and Y. Jiang, "A comprehensive look at pvd scaling to meet the reliability requirements of advanced technology," in *2009 IEEE International Reliability Physics Symposium*, April 2009, pp. 855–860.

[114] J. A. Davis, R. Venkatesan, A. Kaloyeros, M. Beylansky, S. J. Souri, K. Banerjee, K. C. Saraswat, A. Rahman, R. Reif, and J. D. Meindl, "Interconnect limits on gigascale integration (gsi) in the 21st century," *Proceedings of the IEEE*, vol. 89, no. 3, pp. 305–324, March 2001.

[115] C. . Hu, J. Kelly, H. Huang, K. Motoyama, H. Shobha, Y. Ostrovski, J. H. Chen, R. Patlolla, B. Peethala, P. Adusumilli, T. Spooner, R. Quon, L. M. Gignac, C. Breslin, G. Lian, M. Ali, J. Benedict, X. S. Lin, S. Smith, V. Kamineni, X. Zhang, F. Mont, S. Siddiqui, and F. Baumann, "Future on-chip interconnect metallization and electromigration," in *2018 IEEE International Reliability Physics Symposium (IRPS)*, March 2018, pp. 4F.1–1–4F.1–6.

[116] V. Kumar, R. Sharma, E. Uzunlar, L. Zheng, R. Bashirullah, P. Kohl, M. S. Bakir, and A. Naeemi, "Airgap interconnects: Modeling, optimization, and benchmarking for backplane, pcb, and interposer applications," *IEEE Transactions on Components, Packaging and Manufacturing Technology*, vol. 4, no. 8, pp. 1335–1346, Aug 2014.

[117] N. Srivastava, R. V. Joshi, and K. Banerjee, "Carbon nanotube interconnects: implications for performance, power dissipation and thermal management," in *IEEE InternationalElectron Devices Meeting, 2005. IEDM Technical Digest.*, Dec 2005, pp. 249–252.

[118] J. W. McPherson, "Reliability trends with advanced cmos scaling and the implications for design," in *2007 IEEE Custom Integrated Circuits Conference*, Sep. 2007, pp. 405–412.

[119] F. Chen, M. Shinosky, J. Aitken, C. Yang, and D. Edelstein, "Temperature and field interrelation study of low-k tddb for cu interconnects with and without liner - new insights to the roles of cu for a competing breakdown process," in *2013 IEEE International Reliability Physics Symposium (IRPS)*, April 2013, pp. 2F.2.1–2F.2.7.

[120] Zhihong Li, Guoying Wu, Yangyuan Wang, Zhiguo Li, and Yinghua Sun, "Numerical calculation of electromigration under pulse current with joule heating," *IEEE Transactions on Electron Devices*, vol. 46, no. 1, pp. 70–77, Jan 1999.

[121] W. Wu, J. Yuan, S. Kang, and A. Oates, "Electromigration subjected to joule heating under pulsed dc stress," *Solid-State Electronics*, vol. 45, no. 12, pp. 2051 – 2056, 2001.

[122] S. Yokogawa, H. Tsuchiya, and Y. Kakuhara, "Effective thermal characteristics to suppress joule heating impacts on electromigration in cu/low-k interconnects," in *2010 IEEE International Reliability Physics Symposium*, May 2010, pp. 717–723.

[123] N. Rinaldi, "On the modeling of the transient thermal behavior of semiconductor devices," *IEEE Transactions on Electron Devices*, vol. 48, no. 12, pp. 2796–2802, Dec 2001.

[124] ——, "Generalized image method with application to the thermal modeling of power devices and circuits," *IEEE Transactions on Electron Devices*, vol. 49, no. 4, pp. 679–686, April 2002.

[125] A. Kim, B. Li, and B. Linder, "Transient self-heating modeling and simulations of back-end-of-line interconnects," in *2018 IEEE International Reliability Physics Symposium (IRPS)*, March 2018, pp. P–MR.2–1–P–MR.2–5.

[126] S. Lee and K. P. Moran, "Constriction/spreading resistance model for electronics packaging," *Proceedings of the 4th ASME/JSME Thermal Engineering Joint Conference*, vol. 4, 01 1995.

[127] D. Harmon, J. Gill, and T. Sullivan, "Thermal conductance of ic interconnects embedded in dielectrics," in *1998 IEEE International Integrated Reliability Workshop Final Report (Cat. No.98TH8363)*, Oct 1998, pp. 1–9.

[128] F. Chen, J. Gill, D. Harmon, T. Sullivan, A. Strong, B. Li, H. Rathore, and D. Edelstein, "Determination of the thermal conductivity of composite low-k dielectrics for advanced interconnect structures," *Microelectronics Reliability*, vol. 46, no. 2, pp. 232 – 243, 2006.

[129] M. H. Lin, W. S. Chou, Y. T. Yang, Y. C. Peng, and A. S. Gates, "Characterization of critical peak current and model of cu/low-k interconnects under short pulse-width conditions," in *2017 IEEE Electron Devices Technology and Manufacturing Conference (EDTM)*, Feb 2017, pp. 36–38.

[130] C. . Hu, J. Kelly, J. H. Chen, H. Huang, Y. Ostrovski, R. Patlolla, B. Peethala, P. Adusumilli, T. Spooner, L. M. Gignac, J. Bruley, C. Breslin, S. A. Cohen, G. Lian, M. Ali, R. Long, G. Hornicek, T. Kane, V. Kamineni, X. Zhang, F. Mont, and S. Siddiqui, "Electromigration and resistivity in on-chip cu, co and ru damascene nanowires," in *2017 IEEE International Interconnect Technology Conference (IITC)*, May 2017, pp. 1–3.

[131] L. T. Manzione, *Plastic packaging of microelectronic devices*. New York: Van Nostrand Reinhold, 1990.

[132] M. Uschitsky and E. Suhir, "Moisture diffusion in epoxy molding compounds filled with particles," *Journal of Electronic Packaging - J ELECTRON PACKAGING*, vol. 123, 03 2001.

[133] M. H. Shirangi and B. Michel, *Mechanism of Moisture Diffusion, Hygroscopic Swelling, and Adhesion Degradation in Epoxy Molding Compounds*. Boston, MA: Springer US, 2010, pp. 29–69.

[134] M. van Soestbergen, R. T. H. Rongen, L. J. Ernst, and G. Q. Zhang, "Modeling ion transport through molding compounds and its relation to product reliability," in *2008 International Conference on Electronic Packaging Technology High Density Packaging*, July 2008, pp. 1–8.

[135] G. Arienti, I. Imperiale, S. Reggiani, E. Gnani, A. Gnudi, G. Baccarani, L. Nguyen, A. Hernandez-Luna, J. Huckabee, and M. Denison, "Optimization of hv ldmos devices accounting for packaging interaction," in *2015 IEEE 27th International Symposium on Power Semiconductor Devices IC's (ISPSD)*, May 2015, pp. 305–308.

[136] N. Kinjo, M. Ogata, K. Nishi, A. Kaneda, and K. Dušek, "Epoxy molding compounds as encapsulation materials for microelectronic devices," in *Speciality Polymers/Polymer Physics*. Berlin, Heidelberg: Springer Berlin Heidelberg, 1989, pp. 1–48.

[137] D. Hlushkou, H. Liasneuski, U. Tallarek, and S. Torquato, "Effective diffusion coefficients in random packings of polydisperse hard spheres from two-point and three-point correlation functions," *Journal of Applied Physics*, vol. 118, no. 12, p. 124901, 2015.

[138] H. Liasneuski, D. Hlushkou, S. Khirevich, A. Hltzel, U. Tallarek, and S. Torquato, "Impact of microstructure on the effective diffusivity in random packings of hard spheres," *Journal of Applied Physics*, vol. 116, no. 3, p. 034904, 2014.

[139] G. LaPlante, A. V. Ouriadov, P. Lee-Sullivan, and B. J. Balcom, "Anomalous moisture diffusion in an epoxy adhesive detected by magnetic resonance imaging," *Journal of Applied Polymer Science*, vol. 109, no. 2, pp. 1350–1359, 2008.

[140] D. A. Bond, "Moisture diffusion in a fiber-reinforced composite: Part i nonfickian transport and the effect of fiber spatial distribution," *Journal of Composite Materials*, vol. 39, no. 23, pp. 2113–2141, 2005.

[141] L. L. Marsh, R. Lasky, D. P. Seraphim, and G. S. Springer, "Moisture solubility and diffusion in epoxy and epoxy-glass composites," *IBM Journal of Research and Development*, vol. 28, no. 6, pp. 655–661, Nov 1984.

[142] H. G. Carter and K. G. Kibler, "Langmuir-type model for anomalous moisture diffusion in composite resins," *Journal of Composite Materials*, vol. 12, no. 2, pp. 118–131, 1978.

[143] M. E. Gurtin and C. Yatomi, "On a model for two phase diffusion in composite materials," *Journal of Composite Materials*, vol. 13, no. 2, pp. 126–130, 1979.

[144] S. Roy, W. X. Xu, S. J. Park, and K. M. Liechti, "Anomalous moisture diffusion in viscoelastic polymers: Modeling and testing," *Journal of Applied Mechanics*, vol. 67, no. 2, pp. 391–396, Oct 1999.

[145] J. E. Yagoubi, G. Lubineau, F. Roger, and J. Verdu, "A fully coupled diffusion-reaction scheme for moisture sorptiondesorption in an anhydride-cured epoxy resin," *Polymer*, vol. 53, no. 24, pp. 5582 – 5595, 2012.

[146] X. Ma, K. M. B. Jansen, G. Q. Zhang, and L. J. Ernst, "Hygroscopic effects on swelling and viscoelasticity of electronic packaging epoxy," in *2006 7th International Conference on Electronic Packaging Technology*, Aug 2006, pp. 1–5.

[147] T. Braun, J. Bauer, L. Georgi, K. . Becker, M. Koch, T. Thomas, V. Bader, R. Aschenbrenner, and H. Reichl, "Nano- und micro sized filler particles for improved humidity resistance of encapsulants," in *2010 International Symposium on Advanced Packaging Materials: Microtech (APM)*, Feb 2010, pp. 22–28.

[148] D. Stauffer and A. Aharony, *Introduction to percolation theory*. Taylor & Francis, 1994.

[149] D. McLachlan, "A new interpretation of percolation conductivity results with large critical regimes," *Solid State Communications*, vol. 60, no. 10, pp. 821 – 825, 1986.

[150] D. S. McLachlan, "An equation for the conductivity of binary mixtures with anisotropic grain structures," *Journal of Physics C: Solid State Physics*, vol. 20, no. 7, pp. 865–877, mar 1987.

[151] D. S. McLachlan, M. Blaszkiewicz, and R. E. Newnham, "Electrical resistivity of composites," *Journal of the American Ceramic Society*, vol. 73, no. 8, pp. 2187–2203, 1990.

[152] Y. Chen, "Percolation and homogenization theories for heterogeneous materials," Ph.D. dissertation, massachusetts institute of technology, 01 2008.

[153] S. K. Sharma, R. P. Tandon, and V. K. Sachdev, "Pre-localized mwcnt network for a low percolation threshold in mwcnt/abs nanocomposites: experiment and theory," *RSC Adv.*, vol. 4, pp. 60 733–60 740, 2014.

[154] G. D. SCOTT, "Packing of spheres: Packing of equal spheres," *Nature*, vol. 188, no. 4754, pp. 908–909, 1960.

[155] S. Yamada, J. Kanno, and M. Miyauchi, "Multi-sized sphere packing in containers: Optimization formula for obtaining the highest density with two different sized spheres," *IPSJ Online Transactions*, vol. 4, pp. 126–133, 01 2011.

[156] Y. B. Yi, "Void percolation and conduction of overlapping ellipsoids," *Physical review. E, Statistical, nonlinear, and soft matter physics*, vol. 74, p. 031112, 10 2006.

[157] R. S. Farr and R. D. Groot, "Close packing density of polydisperse hard spheres," *The Journal of Chemical Physics*, vol. 131, no. 24, p. 244104, 2009.

[158] K. W. Desmond and E. Weeks, "Influence of particle size distribution on random close packing of spheres," *Physical Review E*, vol. 90, p. 022204, 09 2014.

[159] J. Crank, *The mathematics of diffusion / by J. Crank*. Oxford, 06 1975.

[160] C.-H. Shen and G. S. Springer, "Moisture absorption and desorption of composite materials," *Journal of Composite Materials*, vol. 10, no. 1, pp. 2–20, 1976.

[161] M. J. Adamson, "Thermal expansion and swelling of cured epoxy resin used in graphite/epoxy composite materials," *Journal of Materials Science*, vol. 15, no. 7, pp. 1736–1745, Jul 1980.

[162] D. Karalekas, J. Cugnoni, and J. Botsis, "Monitoring of hygrothermal ageing effects in an epoxy resin using fbg sensor: A methodological study," *Composites Science and Technology*, vol. 69, no. 3, pp. 507 – 514, 2009.

[163] M. A. Agwa, I. Taha, and M. Megahed, "Experimental and analytical investigation of water diffusion process in nano-carbon/alumina/silica filled epoxy nanocomposites," *International Journal of Mechanics and Materials in Design*, vol. 13, no. 4, pp. 607–615, Dec 2017.

[164] M. Barink, A. Mavinkurve, and J. Janssen, "Predicting non-fickian moisture diffusion in emcs for application in micro-electronic devices," in *2015 16th International Conference on Thermal, Mechanical and Multi-Physics Simulation and Experiments in Microelectronics and Microsystems*, April 2015, pp. 1–7.

[165] M. R. Vanlandingham, R. F. Eduljee, and J. W. Gillespie Jr., "Moisture diffusion in epoxy systems," *Journal of Applied Polymer Science*, vol. 71, no. 5, pp. 787–798, 1999.

[166] A. Tcharkhtchi, P. Bronnec, and J. Verdu, "Water absorption characteristics of diglycidylether of butane diol3,5-diethyl-2,4-diaminotoluene networks," *Polymer*, vol. 41, no. 15, pp. 5777 – 5785, 2000.

[167] S. Popineau, C. Rondeau-Mouro, C. Sulpice-Gaillet, and M. E. Shanahan, "Free/bound water absorption in an epoxy adhesive," *Polymer*, vol. 46, no. 24, pp. 10 733 – 10 740, 2005.

[168] G. van der Wel and O. Adan, "Moisture in organic coatings a review," *Progress in Organic Coatings*, vol. 37, no. 1, pp. 1 – 14, 1999.

[169] D. Cornigli, S. Reggiani, A. Gnudi, E. Gnani, G. Baccarani, D. Fabiani, D. Varghese, E. Tuncer, S. Krishnan, and L. Nguyen, "Electrical characterization of epoxy-based molding compounds for next generation hv ics in presence of moisture," *Microelectronics Reliability*, vol. 88-90, pp. 752 – 755, 2018.

[170] ASTM-D5229/D5229M-14, "Standard test method for moisture absorption properties and equilibrium conditioning of polymer matrix composite materials," *ASTM International*, 2004.

[171] "www.mathworks.com/products/curvefitting.html."

[172] M. L. White, "Encapsulation of integrated circuits," *Proceedings of the IEEE*, vol. 57, no. 9, pp. 1610–1615, Sep. 1969.

[173] J. A. van der Pol, R. Rongen, and H. Bruggers, "Model and design rules for eliminating surface potential induced failures in high voltage integrated circuits," *Microelectronics Reliability*, vol. 40, no. 8, pp. 1267 – 1272, 2000.

[174] T. Huang, P. Y. Chiang, C. C. Huang, P. C. Huang, K. H. Huo, R. Y. Su, J. R. Shih, F. . Chen, C. Chen, K. Chen, C. C. Chien, S. L. Hsu, M. Liu, J. Gong, and C. Tsai, "Mobile charge induced breakdown instability in 700v ldmosfet," in *2008 International Symposium on VLSI Technology, Systems and Applications (VLSI-TSA)*, April 2008, pp. 105–108.

[175] Y. Xie, Y. Yu, Y. Feng, W. Jiang, and Z. Zhang, "Fabrication of stretchable nanocomposites with high energy density and low loss from cross-linked pvdf filled with poly(dopamine) encapsulated batio3," *ACS Applied Materials & Interfaces*, vol. 9, no. 3, pp. 2995–3005, Jan 2017.

[176] D. Cornigli, S. Reggiani, A. Gnudi, E. Gnani, G. Baccarani, D. Fabiani, D. Varghese, E. Tuncer, S. Krishnan, and L. Nguyen, "Characterization of dielectric properties and conductivity in encapsulation materials with high insulating filler contents," *IEEE Transactions on Dielectrics and Electrical Insulation*, vol. 25, no. 6, pp. 2421–2428, Dec 2018.

[177] Y. Weitsman, "A continuum diffusion model for viscoelastic materials," *The Journal of Physical Chemistry*, vol. 94, no. 2, pp. 961–968, Jan 1990.

[178] J. Zhou and J. P. Lucas, "Hygrothermal effects of epoxy resin. part i: the nature of water in epoxy," *Polymer*, vol. 40, no. 20, pp. 5505 – 5512, 1999.

[179] G. Lubineau, A. Sulaimani, J. E. Yagoubi, M. Mulle, and J. Verdu, "Hysteresis in the relation between moisture uptake and electrical conductivity in neat epoxy," *Polymer Degradation and Stability*, vol. 141, pp. 54 – 57, 2017.

[180] G.-W. Lee, M. Park, J. Kim, J. I. Lee, and H. G. Yoon, "Enhanced thermal conductivity of polymer composites filled with hybrid filler," *Composites Part A: Applied Science and Manufacturing*, vol. 37, no. 5, pp. 727 – 734, 2006.

[181] W. Zheng, X. Lu, and S.-C. Wong, "Electrical and mechanical properties of expanded graphite-reinforced high-density polyethylene," *Journal of Applied Polymer Science*, vol. 91, no. 5, pp. 2781–2788, 2004.

[182] Z. Wang, J. K. Nelson, J. Miao, R. J. Linhardt, L. S. Schadler, H. Hillborg, and S. Zhao, "Effect of high aspect ratio filler on dielectric properties of polymer composites: a study on barium titanate fibers and graphene platelets," *IEEE Transactions on Dielectrics and Electrical Insulation*, vol. 19, no. 3, pp. 960–967, June 2012.

[183] E. Tuncer and I. Sauers, "Effective dielectric properties of binary dielectric mixtures on checkerboards," in *2012 Annual Report Conference on Electrical Insulation and Dielectric Phenomena*, Oct 2012, pp. 633–636.

[184] H. Cheng and S. Torquato, "Electric-field fluctuations in random dielectric composites," *Phys. Rev. B*, vol. 56, 10 1997.

[185] D. Cule and S. Torquato, "Electric-field distribution in composite media," *Physical Review B - PHYS REV B*, vol. 581, 11 1998.

[186] M. Barthelemy and H. Orland, "Local field probability distribution in random media," *Physical Review E - PHYS REV E*, vol. 56, pp. 2835–2840, 09 1997.

[187] W. M. Haynes, *CRC Handbook of Chemistry and Physics, 95th Edition.* Hoboken: CRC Press, 2014.

[188] G. Raju, *Dielectrics in electric fields, second edition*, June 2016.

[189] D. M. Hepburn, I. J. Kemp, A. J. Shields, and J. Cooper, "Degradation of epoxy resin by partial discharges," *IEE Proceedings - Science, Measurement and Technology*, vol. 147, no. 3, pp. 97–104, May 2000.

[190] J. P. Calame, "Finite difference simulations of permittivity and electric field statistics in ceramic-polymer composites for capacitor applications," *Journal of Applied Physics*, vol. 99, no. 8, p. 084101, 2006.

[191] O. S. Gefie, S. M. Lebedev, Y. P. Pokholkov, D. P. Agoris, and I. Vitellas, "Influence of polarisation on breakdown strength of polymeric composite dielectrics," *IEE Proceedings - Science, Measurement and Technology*, vol. 148, no. 3, pp. 125–128, May 2001.

[192] B. Lu and S. Torquato, "Nearest-surface distribution functions for polydispersed particle systems," *Phys. Rev. A*, vol. 45, pp. 5530–5544, Apr 1992.

[193] N. M. Chalashkanov, S. J. Dodd, L. A. Dissado, and J. C. Fothergill, "The role of bulk charge transport processes in electrical tree formation and breakdown mechanisms in epoxy resins," *IEEE Transactions on Dielectrics and Electrical Insulation*, vol. 23, no. 6, pp. 3256–3266, Dec 2016.

[194] I. Langmuir, "The effect of space charge and residual gases on thermionic currents in high vacuum," *Phys. Rev.*, vol. 2, pp. 450–486, Dec 1913.

[195] D. Darmon, P. Laurenceau, G. Dreyfus, and J. Lewiner, "Une methode non destructive de determination de la distribution spatiale des potentiels dans les dielectriques," *Journal of Electrostatics*, vol. 8, no. 1, pp. 75 – 79, 1979.

[196] A. Imburgia, R. Miceli, E. R. Sanseverino, P. Romano, and F. Viola, "Review of space charge measurement systems: acoustic, thermal and optical methods," *IEEE Transactions on Dielectrics and Electrical Insulation*, vol. 23, no. 5, pp. 3126–3142, October 2016.

[197] K. Fukunaga, "Progress and prospects in pea space charge measurement techniques - [feature article]," *IEEE Electrical Insulation Magazine*, vol. 24, no. 3, pp. 26–37, May 2008.

[198] A. Aragoneses, I. Tamayo, A. Lebrato, J. C. Canadas, J. Diego, D. Arencon, and J. Belana, "Effect of humidity in charge formation and transport ldpe," *Journal of Electrostatics*, vol. 71, 04 2013.

[199] G. Mazzanti, G. C. Montanari, and J. M. Alison, "A space-charge based method for the estimation of apparent mobility and trap depth as markers for insulation degradation-theoretical basis and experimental validation," *IEEE Transactions on Dielectrics and Electrical Insulation*, vol. 10, no. 2, pp. 187–197, April 2003.

[200] T. Fuqiang, Z. Lin, Z. Junliang, and P. Xiao, "Space charge and dielectric behavior of epoxy composite with sio2-al2o3 nano-micro fillers at varied temperatures," *Composites Part B: Engineering*, vol. 114, pp. 93 – 100, 2017.

[201] F. Magraner, A. Garca-Bernab, M. Gil, P. Llovera, S. J. Dodd, and L. A. Dissado, "Space charge measurements on different epoxy resin-alumina nanocomposites," in *2010 10th IEEE International Conference on Solid Dielectrics*, July 2010, pp. 1–4.

[202] Q. Wang and G. Chen, "Effect of nanofillers on the dielectric properties of epoxy nanocomposites," *Advances in materials Research*, vol. 1, 03 2012.

[203] N. Liu, M. He, H. Alghamdi, G. Chen, M. Fu, R. Li, and S. Hou, "An improved model to estimate trapping parameters in polymeric materials and its application on normal and aged low-density polyethylenes," *Journal of Applied Physics*, vol. 118, no. 6, p. 064102, 2015.

[204] M. Praeger, I. L. Hosier, A. F. Holt, A. S. Vaughan, and S. G. Swingler, "On the effect of functionalizer chain length and water content in polyethylene/silica nanocomposites: Part ii charge transport," *IEEE Transactions on Dielectrics and Electrical Insulation*, vol. 24, no. 4, pp. 2410–2420, 2017.

[205] D. Franceschetti and J. Macdonald, "Numerical analysis of electrical response: Statics and dynamics of spacecharge regions at blocking electrodes," *Journal of Applied Physics*, vol. 50, pp. 291 – 302, 02 1979.

[206] J. Zhao, G. Chen, and P. L. Lewin, "Investigation into the formation of charge packets in polyethylene: Experiment and simulation," *Journal of Applied Physics*, vol. 112, no. 3, p. 034116, 2012.

[207] J. Meng, Y. Zhang, S. HolÃ©, F. Zheng, and Z. An, "Charge mobility retrieval approach from apparent charge packet movements based on the negative differential resistance theory," *Scientific Reports*, vol. 8, no. 1, p. 5928, 2018.

[208] P. C. Arnett, "Transient conduction in insulators at high fields," *Journal of Applied Physics*, vol. 46, no. 12, pp. 5236–5243, 1975.

[209] F. Padovani and R. Stratton, "Field and thermionic-field emission in schottky barriers," *Solid-State Electronics*, vol. 9, no. 7, pp. 695 – 707, 1966.

[210] A. Heeger, I. Parker, and Y. Yang, "Carrier injection into semiconducting polymers: Fowler-nordheim field-emission tunneling," *Synthetic Metals*, vol. 67, no. 1, pp. 23 – 29, 1994.

[211] L. G. Kaake, P. F. Barbara, and X.-Y. Zhu, "Intrinsic charge trapping in organic and polymeric semiconductors: A physical chemistry perspective," *The Journal of Physical Chemistry Letters*, vol. 1, no. 3, pp. 628–635, Feb 2010.

[212] G. Blaise, "Charge localization and transport in disordered dielectric materials," *Journal of Electrostatics*, vol. 50, no. 2, pp. 69 – 89, 2001.

[213] G. Teyssedre and C. Laurent, "Charge transport modeling in insulating polymers: From molecular to macroscopic scale," *Dielectrics and Electrical Insulation, IEEE Transactions on*, vol. 12, pp. 857 – 875, 11 2005.

[214] L. Lantz and M. G. Pecht, "Ion transport in encapsulants used in microcircuit packaging," *IEEE Transactions on Components and Packaging Technologies*, vol. 26, no. 1, pp. 199–205, March 2003.

[215] D. Fabiani, G. C. Montanari, and L. A. Dissado, "Space charge accumulation due to ultra-fast charge packets in xlpe insulated cables: the effect of temperature and field," in *2009 IEEE 9th International Conference on the Properties and Applications of Dielectric Materials*, July 2009, pp. 337–340.

[216] L. A. Dissado, G. C. Montanari, and D. Fabiani, "Fast soliton-like charge pulses in insulating polymers," *Journal of Applied Physics*, vol. 109, no. 6, p. 064104, 2011.

[217] G. C. Montanari, "Bringing an insulation to failure: the role of space charge," *IEEE Transactions on Dielectrics and Electrical Insulation*, vol. 18, no. 2, pp. 339–364, April 2011.

[218] A. Garcia, N. Warner, N. Dsouza, E. Tuncer, L. Nguyen, M. Denison, and J. T. Fong, "Reliability of high voltage molding compounds: how particle size, curing time, sample thickness and voltage impacts on polarization," *IEEE Transactions on Industrial Electronics*, vol. 63, pp. 7104 – 7111, 11 2016.

[219] C. Zou, J. Fothergill, and S. Rowe, "The effect of water absorption on the dielectric properties of epoxy nanocomposites," *IEEE Transactions on Dielectrics and Electrical Insulation*, vol. 15, pp. 106 – 117, 03 2008.

[220] L. Hui, L. S. Schadler, and J. K. Nelson, "The influence of moisture on the electrical properties of crosslinked polyethylene/silica nanocomposites," *IEEE Transactions on Dielectrics and Electrical Insulation*, vol. 20, no. 2, pp. 641–653, April 2013.

[221] I. Rocha, S. Raijmaekers, F. Van der Meer, R. Nijssen, H. Fischer, and L. Sluys, "Combined experimental/numerical investigation of directional moisture diffusion in glass/epoxy composites," *Composites Science and Technology*, vol. 151, 08 2017.

[222] E. Santiso and E. A. Muller, "Dense packing of binary and polydisperse hard spheres," *Molecular Physics*, vol. 100, no. 15, pp. 2461–2469, Aug 2002.

[223] X. Zhang, "Constructive modeling strategies and implementation frameworks for optimal hierarchical synthesis," Ph.D. dissertation, Purdue University, December 2004.

[224] C. S. O'Hern, L. E. Silbert, A. J. Liu, and S. R. Nagel, "Jamming at zero temperature and zero applied stress: the epitome of disorder." *Physical review. E, Statistical, nonlinear, and soft matter physics*, vol. 68, p. 011306, 2003.

[225] K. C. Smith, I. Srivastava, T. S. Fisher, and M. Alam, "Variable-cell method for stress-controlled jamming of athermal, frictionless grains," *Phys. Rev. E*, vol. 89, p. 042203, Apr 2014.

[226] S. L. Pang, I. Srivastava, and T. Fisher, "Jamming of soft frictionless spheres," Oct 2012. [Online]. Available: https://nanohub.org/resources/jamming

[227] R. M. Ziff and S. Torquato, "Percolation of disordered jammed sphere packings," *Journal of Physics A: Mathematical and Theoretical*, vol. 50, no. 8, p. 085001, jan 2017.

APPENDICES

A. APPENDIX: APPLIED EQUATIONS FOR THE REVISED FEM SIMULATION SET UP

Equations for numerical simulation is shown below.

Table A.1.
Solved equations for revised space charge FEM simulations

Poisson equation: $-\varepsilon_r\varepsilon_0\frac{\partial}{\partial x}\left(\frac{\partial\varphi(x,t)}{\partial x}\right)=\rho_m(x,t)+\rho_t(x,t)$ $\rho_m(x,t)=q\left(p_m-n_m+i_m^+-i_m^-\right)$ $\rho_t(x,t)=q\left(p_t-n_t+i_t^+-i_t^-\right)$
Continuity equation (n_m, $p_m$cases are shown, same formula for other ionic species and mobility is zero for trapped species): $\frac{\partial n_m}{\partial t}+\frac{\partial}{\partial x}\left(\mu_n\cdot F\cdot n_m\cdot\frac{\partial\varphi(x,t)}{\partial x}\right)=R_{n_m}$ $\frac{\partial p_m}{\partial t}-\frac{\partial}{\partial x}\left(\mu_p\cdot F\cdot p_m\cdot\frac{\partial\varphi(x,t)}{\partial x}\right)=R_{p_m}$
Reaction equation (n_m, n_t cases are shown, same formula for other species, only τ_{T} and τ_{D} of ionic psecies is different.): $R_{n_m}=-R_{n_t}=-\tau_{\mathrm{T}}\cdot n_{\mathrm{m}}\cdot\left(1-\frac{n_{\mathrm{t}}}{N_{\mathrm{t}}}\right)+\tau_{\mathrm{D}}\cdot n_{\mathrm{t}}$
Boundary conditions (GND: x=0, HV:x=L): $\frac{\partial n_m(0,t)}{\partial x}=\frac{\partial p_m(L,t)}{\partial x}=\mathrm{Eq}\cdot 6.2$ $\frac{\partial n_m(L,t)}{\partial x}=\frac{\partial p_m(0,t)}{\partial x}=-\mu_n\cdot F\cdot n_m\cdot\frac{\partial\varphi(x,t)}{\partial x}$ $i_m^+(0,t)=i_m^+(L,t)=i_m^-(0,t)=i_m^-(L,t)=0$
Initial conditions: $n_m(x,0)=p_m(x,0)=n_t(x,0)=p_t(x,0)=i_m^-(x,0)=i_m^+(x,0)=0$ $i_t^-(x,0)=i_t^+(x,0)=4.2\left[C/m^3\right]$

Table A.2.
Defined input parameters and applied values in Fig. 6.7.

Symbol	**Meaning**	**Value**
L	Thickness of the sample	$750[\mu m]$
T	Temperature	333[K]
ε_r	Dielectric constant	3.9
V	Applied voltage	1500[V]
ϕ_{B}	Schottky barrier height	1.3[eV]
A_0	Richardson constant	$1200\left[\mathrm{Am^{-2}K^{-2}}\right]$
N_{t}	Trap density of electrons and holes	$50\lceil\mathrm{C/m^3}\rceil$
$N_{\mathrm{t}}^{\mathrm{i}}$	Trap density of ions	$10\lceil\mathrm{C/m^3}\rceil$
μ_n, μ_p	Electron and holes mobility	$5 \times 10^{-13}\,[\mathrm{m^2/V-s}]$
μ_i^+, μ_i^-	Ions mobility	$1.5 \times 10^{-13}\,[\mathrm{m^2/V-s}]$
τ_{T}	Trapping coefficient of electrons and holes	$1[\mathrm{s^{-1}}]$
τ_{T}^i	Trapping coefficient of ions	$0.01[\mathrm{s^{-1}}]$
τ_{D}	De-trapping coefficient of electrons and holes	$0.001[\mathrm{s^{-1}}]$
τ_{D}^i	De-trapping coefficient of ions	$0.0002[\mathrm{s^{-1}}]$

Analytical model for pre-existing ions transport with single trap level insulator is derived in [XX]. After the voltage is applied, the closed-form trapped ions concentration at x is shown in Eq. A1.

$$\frac{i_t^+}{N_t^i} = \left\{1 + \exp\left(\frac{x}{\tau_{\mathrm{T}} \cdot v_{\mathrm{th}}}\right)\left[\exp\left(\frac{\widehat{\sigma_{\mathrm{t}}} \cdot Q(t)}{q}\right) - 1\right]^{-1}\right\}^{-1} \tag{A.1}$$

where v_{th}, and $\widehat{\sigma_{\mathrm{t}}}$ are thermal velocity, and recombination cross section area multiplied by v_{th} over saturation velocity, respectively. As shown in Fig. A1, as τ_{T} is decreases, trap filling rate becomes faster at the specific position x. As more and more charges

fill up the trap sites, de-trapping rate becomes considerable and the velocity of the charge centroid can be describe as shown in Eq. A.2 [208].

$$\overline{v} = \frac{\tau_{\mathrm{T}} \cdot v_{\mathrm{th}}}{2\tau_{\mathrm{D}}} \tag{A.2}$$

Here, with same τ_{T}, we can see that lower τ_{D} results in faster heterocharge buildup. Both analytical formula shows same trend as we can observe from numerical simulations, shown in Fig.5. Although the analytical model gives us some intuitions, numerical simulation is necessary for:

- Considering proper electric field impact on the species flux both on electrodes and within bulk (analytical model assumes $\mu \cdot E$ term a constant value, saturation drift velocity).
- Including multiple species (i.e., electron, hole, and ions) simultaneously (Based on Poisson equation, E distortion at all position should be done by considering all polar species simultaneously).

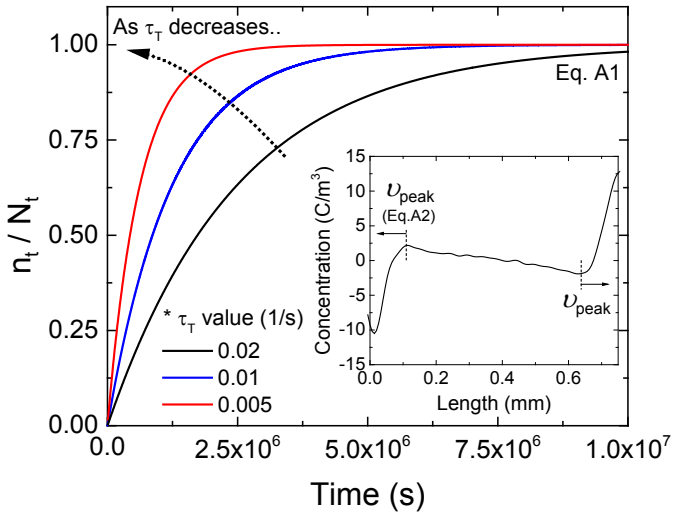

Fig. A.1. Trap site filling comparison between different trapping coefficient based on Eq. A1 [208]. (inset) Simple schematic of space charge centroid movement based on Eq. A2 [208].

- Including transient μ variation due to water absorption.

Thus, in order to study transient space charge behavior or extract parameters based on PEA measurements properly, we have to perform numerical analysis introduced in section 6.3.4.

B. APPENDIX: GLOBAL STIFFNESS MATRIX EXAMPLE (FOR FIG. 6.11)

$$\begin{bmatrix}
k_{12}+k_{14}+k_{1w} & -k_{12} & 0 & -k_{14} & 0 & 0 & 0 & 0 \\
-k_{12} & k_{12}+k_{23}+k_{26} & -k_{23} & 0 & 0 & -k_{26} & 0 & 0 \\
0 & -k_{23} & k_{23}+k_{3w} & 0 & 0 & 0 & 0 & 0 \\
-k_{14} & 0 & 0 & k_{14}+k_{45} & -k_{45} & 0 & 0 & 0 \\
0 & 0 & 0 & -k_{45} & k_{45}+k_{56}+k_{58} & -k_{56} & 0 & -k_{58} \\
0 & -k_{26} & 0 & 0 & -k_{56} & k_{26}+k_{56}+k_{67} & -k_{67} & 0 \\
0 & 0 & 0 & 0 & 0 & -k_{67} & k_{67}+k_{78}+k_{7w} & -k_{78} \\
0 & 0 & 0 & 0 & -k_{58} & 0 & -k_{78} & k_{58}+k_{78}+k_{8w}
\end{bmatrix}$$

C. APPENDIX: $RRNM$ VALIDATIONS

C.1 Different unit cell size

In order to validate the $RRNM$ by another way, we also performed $RRNM$ for different number of spheres (i.e., 500) while keeping the size of each filler size same as shown by star symbols in Fig. 6.15. As the number of fillers increases, the unit cell size is also increased. In order to compare with our 200 spheres cases, we need to normalize the final calculated $D^{\mathrm{i}}_{\mathrm{eff}}$ by increased unit cell area ratio (ΔA). As shown in Fig. 6.15, if the filler size is same, varying the number of fillers does not cause different $D^{\mathrm{i}}_{\mathrm{eff}}$.

C.2 $D^{\mathrm{i}}_{\mathrm{eff}}$ increasing tendency as t_{int} gets thicker

The correlation between an increasing behavior of $D^{\mathrm{i}}_{\mathrm{eff}}$ and t_{int} is investigated based on RRNM calculation for the structures shown in Fig. C.1. The filler configuration is predetermined: four smaller spheres, and two larger spheres form percolative paths when t_{int} is $100nm$, and $1\mu m$, respectively. Again, D_{f}, D_{m}, and D_{int} are defined as 0, 1, and 1000, respectively. As shown in Fig. A.2a, and A.2b, a sudden increase of $D^{\mathrm{i}}_{\mathrm{eff}}$ is observed when t_{int} is $100nm$, and $1\mu m$, respectively. The larger the size of fillers, the larger the degree of t_{int} increase. We can realize that t_{int} always represents the most percolating region within the system by observing the same behavior between the summation of curves shown in Fig. C.1a, and C.1b and the $RRNM$ calculation for the whole structure.

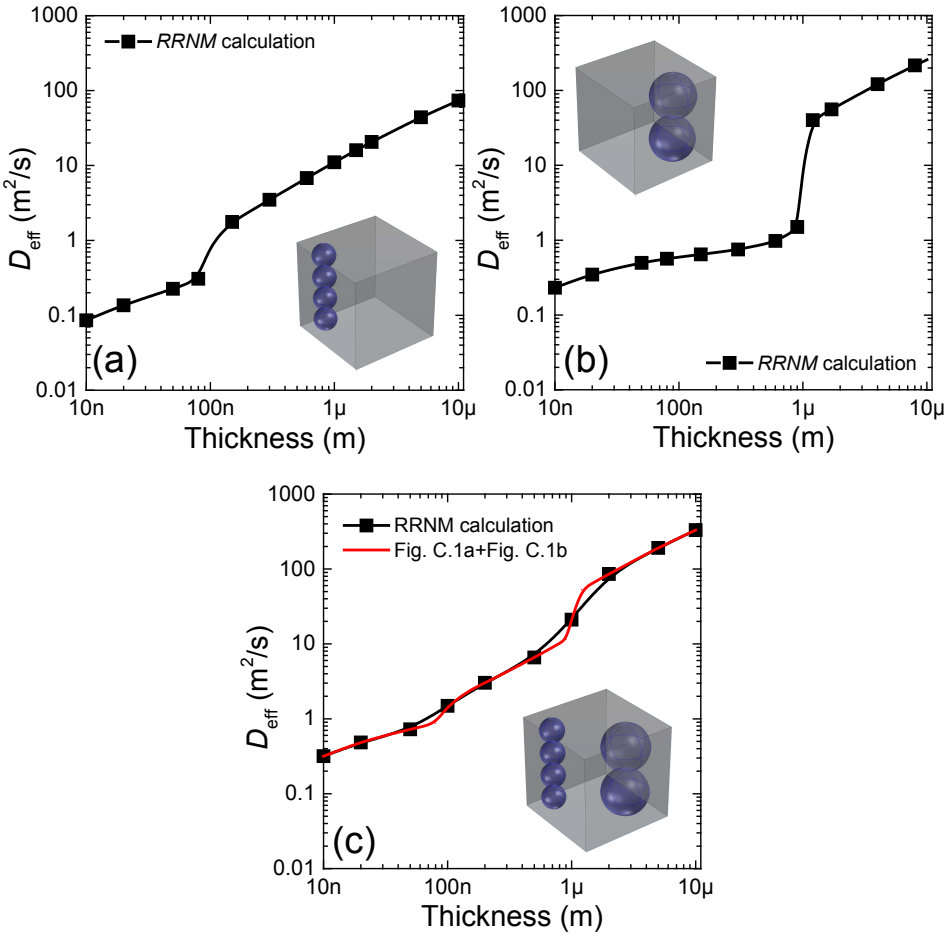

Fig. C.1. *RRNM* calculation results for the structure shown by inset image. The distance between neighboring filler in the case of (a), and (b) is $200nm$, and $2\mu m$ to form a percolative path when t_{int} is $100nm$, and $1\mu m$, respectively. (c) Combined structure of Fig. C.1a and C.1b.

VITA

VITA

Woojin Ahn was born in Daejeon, South Korea. He received the B.S. degree in electrical engineering from Hanyang University, Seoul, Korea, in 2011, and the M.S. degree in electrical engineering from Seoul National University, Seoul, Korea, in 2013. Since 2014, he is pursuing Ph.D. degree in electrical and computer engineering with Purdue University, IN USA. His research interests include compact modeling, numerical simulation, analytical skill, transistor fabrication and characterization to optimize performance and reliability of ICs. He has authored and co-authored more than 25 journals and conference papers. Since 2016, he has been an IEEE student member and serves as a reviewer for IEEE journals (e.g., Transactions on Nanotechnology and Transactions on Electron Devices). He has published his works several times to the most prominent conference, IEEE International Electron Devices Meeting (IEDM).